Taylor, B., Huchon, P., Klaus, A., et al., 1999
Proceedings of the Ocean Drilling Program, Initial Reports Volume 180

5. SITE 1108[1]

Shipboard Scientific Party[2]

SITE 1108

Hole 1108A (jet-in test only):
9°44.708′S, 151°37.514′E; 3162.7 mbsl
0–16.3 mbsf drilled without coring
Hole 1108B (RCB):
9°44.724′S, 151°37.543′E; 3177.2 mbsl
0–485.2 mbsf cored; 148.58 m recovered (30%)

Site 1108 is in the seismically active region of incipient continental separation 1 nmi ahead of the neovolcanic zone of the Woodlark Basin spreading center, Papua New Guinea. Here, a continental fault block (Moresby Seamount: summit 120 mbsl) forms the footwall to a low-angle normal fault imaged to 9 km that dips 25°–30° beneath a 3.2-km-deep, asymmetric rift basin with more than 2 km of sediment fill. At Site 1108 we sought to drill through ~900 m of the rift basin sediments, the low-angle normal fault zone, and into the footwall metamorphics. The primary objectives at this site were to (1) characterize the composition and in situ properties (stress, permeability, temperature, pressure, physical properties, and fluid pressure) of the active low-angle normal fault zone to understand how such faults slip and (2) determine the vertical-motion history of the hanging wall and the footwall as local ground truth for models of the timing and amount of continental extension before spreading initiation. Hole 1108A was a jet-in test in anticipation of reentry operations. Hole 1108B was rotary cored to 485 mbsf, with ~60 m of open-hole logging using the triple combo and temperature tools before unstable hole conditions terminated operations. The site was not deepened because of pollution prevention and safety concerns, and hence, the primary objectives were not met.

The first core contained upper Pleistocene nannofossil-bearing hemipelagic sediment: calcareous clay with minor volcaniclastic silt and

[1]Examples of how to reference the whole or part of this volume.
[2]Shipboard Scientific Party addresses.

Ms 180IR-105

sand. Talus from Moresby Seamount was recovered as isolated clasts from 14.5 to 62.7 mbsf and included dark siliciclastic sandstone and siltstone, volcanic breccia, microgranite, granodiorite, epidosite, greenschist mylonite, and biotite gneiss. Some glassy basalt fragments from submarine eruptions were incorporated in the same interval. Trace amounts of adhering sediments reveal biostratigraphic ages >1.25 Ma by 24.1 mbsf. Quartzo-feldspathic-lithic sand from 62.7 to 63.4 mbsf may relate to and herald the overlying talus. Gas observed bubbling out of the top of the core barrel for this interval may reflect penetration of a gas hydrate layer.

Terrigenous turbidites, now lithified to sandstones, siltstones, claystones, and minor conglomerates, constitute the remainder of the section 72.3–485.2 mbsf. Ages increase from 1.67 to 1.75 Ma at 82.8 mbsf to <3.35 Ma at the base. Sedimentation rates increase downsection, from 324 m/m.y. at 1.7–2.0 Ma to 400 m/m.y. at 2.60–3.2 Ma. Benthic foraminifers indicate deposition in deep water (lower bathyal: >2000 m), except for middle (500–2000 m) to lower bathyal conditions below 410 mbsf.

The majority of the turbidites comprise interbedded sandstones, siltstones, and claystones in which medium- to coarse-grained sediments dominate. The sandstones above ~330 mbsf contain a high proportion of metamorphic-derived lithoclasts, related mineral grains, and altered igneous-rock-derived grains (volcanic and ophiolitic), whereas those below contain large amounts of material derived from basic and acidic volcanic and minor plutonic rocks. Planktonic foraminifers and bioclasts of shallow-water origin are common to both sections.

A subunit from 139.4 to 200.2 mbsf comprises foraminifer-bearing clayey siltstone and silty claystone with occasional fine-grained sandstone. Bioturbation is common. Minor disseminated pyrite is suggestive of relatively low oxygen bottom conditions at times. Subunits of thin conglomerate were recovered near 313, 380, and 437 mbsf. The clayey siltstone subunit shows abundant evidence of brittle deformation characterized by bedding dips of up to 35°, low-angle shearing, brecciation, and ubiquitous slickensides. The faults dip at moderate angles (~45°), and most of the structures indicate normal senses of displacement in an extensional fault zone. The greatest frequency of fractures and faults is concentrated between 158 and 173 mbsf. Within this interval there is an age offset from 2.0 to 2.58 Ma between 159.6–164.8 and 172 mbsf. Based on the sedimentation rates above and below, ~200 m of section appears to be cut out by this normal fault near 165 mbsf.

Within the more competent lithologies below, the intensity of tectonic deformation falls off markedly and bedding is subhorizontal. However, below 350 mbsf the turbidites become finer grained (more claystones, siltstones, and fine sandstones), and the section is once more deformed with scaly fabrics, fractures, and evidence of shear along fault planes. Tectonic deformation appears to be concentrated in the finer grained units.

Porosities measured in the laboratory show an expected exponential decay with depth below ~160 mbsf, but the misfit of these values when extrapolated to the surface with the measured surface porosities indicates that at least 400 m of sediments has been removed. Half this amount may be associated with throw on the fault near 165 mbsf, the rest with erosion between the unconsolidated sands at 63 mbsf and the consolidated sandstones at 72 mbsf.

Temperature measurements suggest an average thermal gradient of 100°C·km^{-1} to 390 mbsf. Alternatively, the same data may be explained

by advection of fluids along the ~165-mbsf fault, and/or by a thermal gradient of 94°C·km^{-1} above 160 mbsf and 65°C·km^{-1} below 200 mbsf, with a 10°C offset formed in the last thousand years. Thermal conductivities in the upper several meters are 0.8–0.9 W·m^{-1}·°C^{-1} and are 1.0–1.7 W·m^{-1}·°C^{-1} below 130 mbsf.

Three processes appear to control the pore-water geochemistry. Bacterially mediated oxidation of organic matter depletes sulfate 75% by 83 mbsf (and totally below 172 mbsf), the depth where methane concentrations become elevated and there is a salinity minimum. The downhole decrease in K^+ and Mg^{2+} and the increase in salinity, Na^+, Cl^-, Ca^{2+}, Li^+, and Ca/Mg (locally modulated by the formation of calcite cements) are consistent with diagenesis of volcanic matter to form clay minerals. Depth profiles of all these ions show offsets or local deviations associated with the fault at ~165 mbsf.

Organic carbon contents average 0.5 wt%. The C/N ratios mainly between 8 and 20 suggest a mixed terrigenous and marine origin for the organic matter. Headspace gas data show a C_1/C_2 ratio decreasing from ~2000 at 335 mbsf to 138–195 in the deepest samples (467 and 476 mbsf). Starting at 391 mbsf, there is an increasing presence of higher chain volatile hydrocarbons indicative of thermogenically derived gas.

OPERATIONS

Port Call: Darwin

Leg 180 officially began with the first line ashore in Darwin, Australia, at 1630 hr on 7 June 1998. All times reported in the Leg 180 operations reports in this volume are local time (Universal Time Coordinated [UTC] + 10 hr). As soon as the ship was cleared through customs and immigration, the process of on- and offloading surface and air freight immediately began. Major items loaded included twenty 8¼-in drill collars, 41 joints of 16-in buttress casing, and 8 joints of 20-in buttress casing. Bulk products included 30 metric tons of sepiolite drilling mud, 15 metric tons of bentonite gel mud, and 1250 sacks of blended cement. In addition, 130 sacks of Kwikseal and 40 sacks of calcium carbonate lost-circulation material were put aboard along with an assortment of chemicals required for optimizing the cement program at proposed site ACE-8A.

Transit to Site 1108 (ACE-8A)

At 0715 hr on 11 June the last line was released and we departed Darwin for our first drill location, Site 1108 (proposed site ACE-8A). The transit was uneventful and excellent time was made (averaging 11.5 nmi/hr) in calm seas. Because we would be operating in Papua New Guinea (PNG) waters, we were required to clear PNG customs and immigration before drilling operations could begin. A helicopter rendezvous with the ship was scheduled to minimize the time necessary to complete this requirement. We had to arrive at the rendezvous location early on the morning of 16 June, but our transit speeds were better than expected. Therefore, on 15 June we reduced speed for several hours and used this time to pick up and space out drill collars—an operation that would otherwise have had to take place once we arrived at our first site.

The first helicopter landed on the ship on 16 June 1998 south of Alotau at 10°55.0′S, 150°20.0′E. Passengers on this flight included a

PNG customs agent, a PNG quarantine official, a representative from the Ocean Drilling Program's (ODP) agent in PNG, and the ODP logistics coordinator. After the helicopter landed we immediately resumed full speed for the second rendezvous location ~20 nmi to the east. The helicopter departed from the ship at 0655 hr for Alotau to pick up a second PNG observer who was due to arrive about 0800 hr. Following the formalities of clearing the ship into PNG waters, the PNG officials were given a tour of the ship's laboratory facilities. The helicopter returned for the second rendezvous (11°10.0′S, 150°50.0′E) at ~1000 hr that same morning. This time the pilot did not shut down his engines. After the second PNG observer (Paul Kia, Geological Survey of PNG) disembarked, the PNG customs and quarantine officials and ODP's PNG agent boarded the helicopter and departed. As soon as the helicopter lifted off, we resumed full speed for Site 1108.

We left the Coral Sea and turned north entering the Solomon Sea via the Jomard Passage picking up a favorable current along the way, which boosted our speed, temporarily at least, to nearly 14 nmi/hr. Overall, our transit speeds averaged 11.5 nmi/hr in calm seas. After arriving at the Global Positioning System (GPS) position for Site 1108, we lowered the thrusters/hydrophones and switched into dynamic positioning (DP) mode. After stabilizing on the GPS position, we deployed a Datasonic commandable positioning beacon at 0115 hr.

Hole 1108A

Hole 1108A was devoted to obtaining information on the seafloor sediments for a reentry cone deployment planned for later in the leg. We fit together a bottom-hole assembly (BHA) with an 18½-in tricone drill bit attached to the bottom stand of 8¼-in drill collars and lowered it to the seafloor. The subsea TV camera was deployed during the pipe trip, and while observing the seafloor we spudded Hole 1108A at 0815 hr on 17 June.

The 3.5-kHz depth recorder indicated a seafloor depth of 3157.4 meters below sea level (mbsl). We observed the drill bit tag the seafloor at 3162.7 mbsl. For the next 1 hr, 40 min we conducted a jet-in test into the moderately hard seafloor, eventually reaching a depth of 16.3 meters below seafloor (mbsf) (see Tables **T1, T2**). The test was suspended at that point because little progress was being made at flow rates of up to 110 strokes per minute (spm). The drilling assembly was pulled clear of the seafloor at 1000 hr, the subsea television camera was recovered, and the hole officially ended at 1530 hr when the bit cleared the rig floor.

T1. Site 1108 coring summary, **p. 109.**

T2. Site 1108 coring summary by section, **p. 111.**

Hole 1108B

We had originally planned Hole 1108B as an advanced piston corer/extended core barrel (APC/XCB) hole to ~600 mbsf. Because the jet-in test results indicated that APC coring was not possible and that XCB coring was unlikely to progress very far, we decided to start rotary core barrel (RCB) coring. After putting together an RCB drilling assembly (including a single stand of drill collars above a set of mechanical drilling jars), we lowered the drill string to the seafloor. During the pipe trip the ship was offset 50 m to the southeast on a bearing of 120°.

Upon reaching the 3162.7 mbsl, the seafloor depth of the previous hole, the driller had not recognized any indication of reaching bottom (reduction of total drill-string weight). Even after advancing another

single joint of pipe to a depth of 3172.0 mbsl, no weight loss was observed. We checked the driller's pipe tally that was verified as correct and recovered the core barrel, which was empty. After adding another joint of drill pipe, the seafloor indication was tagged at a depth of 3177.3 mbsl, or 14.6 m deeper than at the Hole 1108A jet-in test location.

Hole 1108B was officially spudded at 0100 hr on 18 June 1998 and continuous RCB coring began, using very little weight on bit (WOB) and slow revolutions per minute (RPM). We were forced to proceed cautiously because of the lack of stabilization for the BHA (it was above the seafloor) and the hard surface sediments. The upper 50 m of the borehole was characterized by erratic torque, overpull and drag, poor recovery (see Tables **T1, T2**), and low rates of penetration (ROP). Typically, 1–2 m of sediment filled the bottom of the borehole between connections. Liberal amounts of drilling mud (sepiolite) were used, and the hole condition gradually improved with depth. Because of the relatively unstable hole conditions and layers of semi-indurated sediments, we were unable to make temperature measurements in the formation.

At 91.3 mbsf (after Core 10R), we decided to make a wiper trip. The drilling of the last two cores indicated that the formation was getting more lithified and appeared to be more stable. Drilling parameters became more consistent and core recovery continued to improve. The partial wiper trip was strictly precautionary because the drilling jars and last stand of drill collars were about to go below the mudline. We raised the drill string to a depth of 42.7 mbsf. At 47.7 mbsf the driller noted 70,000 lb overpull and was unable to rotate the drill string. After working the pipe for a few minutes, it became unstuck and a sepiolite pill was circulated. This portion of the hole was reamed several times until there was no longer any indication of drag or overpull. We then proceeded with running the pipe to bottom, where we encountered 3 m of fill. Another sepiolite pill was circulated while drilling out the fill. All drilling conditions were normal and the hole appeared to be in excellent condition at that point. When the bit was back on the bottom, a portion of the hole again apparently collapsed, trapping the pipe. The pipe was worked free and another sepiolite pill was circulated. Coring resumed 2.75 hr later, after the wiper trip was completed and the hole appeared to be stabilized.

The RCB coring continued through Core 41R to a depth of 389.0 mbsf. Higher than normal core-barrel pump pressures (250–300 psi vs. normal values of 150 psi) and lower recovery led us to suspect that we might have lost some core in the pipe or that something was partially plugging the bit throat. A core barrel was pumped downhole and then recovered without advancing the drill bit. Upon recovery we found a small rock lodged in the lower core catcher. A bit deplugger with painted latch and landing shoulders (to document that it latched fully down and extended through the bit throat) was deployed. Once recovered, the deplugger indicated proper latching and pump pressures had returned to normal. The RCB coring progressed to 485.2 mbsf; however, core recovery and ROP deteriorated with depth, possibly because of an increase in the degree of fractures in the formation. Toward the bottom of the hole, hydrocarbon headspace C_1/C_2 was decreasing and higher molecular-weight hydrocarbons such as *n*-C_5 (pentane) started to appear. We wondered what impact this trend might have regarding our plan to advance a reentry hole down to a projected depth of 1150 mbsf.

At 1630 hr on 22 June, the hole collapsed just after we started to cut Core 52R. The top drive continually stalled out, and the pipe was pulled

free with 30,000 lb of overpull. At that point the annulus plugged off, preventing circulation. We pulled the pipe free again; this time with 110,000 lb overpull. Attempts to actuate the mechanical drilling jars were not successful, which led us to believe that the material holding the pipe had fallen in from above. The drilling assembly was literally dragged up the hole to 253.7 mbsf by using 20,000–60,000 lb overpull. At this depth we were able to resume circulation and torque/pump pressure returned to normal. We continued pulling the pipe to 114.7 mbsf without overpull. After recovering the core barrel (which had not been advanced before the pipe became stuck), we washed and drilled back to the bottom of the hole but could not pass 436.7 mbsf, which was 48.5 m above the bottom of the hole. At that point the hole packed off again, cutting off circulation and preventing top-drive rotation. The pipe was pulled back to 416.7 mbsf before we regained the ability to pump fluids and rotate the drill string. For the next several hours the pipe was cycled up and down in an unsuccessful attempt to get back to the original depth of the hole. Eventually, we decided that coring further in this hole was not possible. The pipe was placed at 379.0 mbsf and an Adara heat-flow shoe was deployed on a core barrel through the pipe to obtain a temperature gradient in the borehole. We knew that the data would not reflect accurate formation temperature but considered the data to be insurance in case the temperature-logging tool (TLT), which was to be run during the first wireline logging run, might not be able to be deployed very far into the hole. Temperatures were measured for 10 min at each interval of 0, 388, 300, 200, and 100 mbsf with the circulating pumps shut off. Results of the Adara temperature profile, inside the drill pipe, indicated a linear temperature gradient of ~35.4°C/km. We later determined this to be significantly lower than the actual gradient.

Once the Adara temperature measurements were completed, we made two wireline runs to activate the mechanical bit release (MBR) to drop the bit in the hole in preparation for logging. The hole was displaced with 150 bbl of sepiolite mud, and we pulled the drill string to a depth of 99.7 mbsf. During the pipe trip, the driller encountered overpulls of 20,000–40,000 lb up to a depth of 225.7 mbsf.

After rigging for logging, the triple combo with the TLT was assembled and run in the hole. Unfortunately, the logging tools were only able to reach 62 m below the end of the pipe in the open hole. This section of hole was logged twice, and the remaining logging program for the hole was abandoned. To displace the hole with weighted mud before abandoning this site, we attempted to lower the pipe farther into the hole, but it could not be lowered more than 0.5 m before encountering an obstruction. After the hole was filled with 31 bbl of 10½-ppg bentonite gel mud, the pipe was pulled clear of the seafloor at 0415 hr on 23 June. Hole 1108B ended when the bit cleared the rig floor at 0900 hr. The acoustic positioning beacon was left on the seafloor in an active mode because we were planning to return to this site after drilling Site 1109.

A total of 51 cores were recovered from 485.2 m of section with a recovery of 148.6 m (31%)(see Tables **T1, T2**). The average ROP was 12.3 m/hr.

LITHOSTRATIGRAPHY

The lithostratigraphic succession recovered from Hole 1108B consists of 485.2 m of sediments and sedimentary rocks of middle Pliocene to

late Pleistocene age. Four lithostratigraphic units were recognized on the basis of sediment or rock type, grain-size variations, sedimentary structures, color, smear-slide and thin-section compositions, bulk mineralogy (X-ray diffraction [XRD]), and calcium carbonate determinations. Only a small, upper part of the succession (60 m) was geophysically logged because of problems coring the hole.

The uppermost 10 m of the succession comprises nannofossil-bearing hemipelagic and pelagic sediment, defined as lithostratigraphic Unit I (see Fig. F1). This is underlain by an inferred unit of talus, represented by a number of sedimentary, metamorphic, and igneous clasts (Unit II) followed by inversely graded sand (Unit III). Beneath this, Unit IV comprises the greater part of the succession and is dominated by coarse- to medium-grained sand/sandstones, siltstones, and claystones. Unit IV is divided into three subunits, based on the predominate fine, medium, and coarse grain size. The succession is disrupted by a fault zone concentrated ~160–180 mbsf.

F1. Summary of lithologies recovered from Hole 1108B, p. 46.

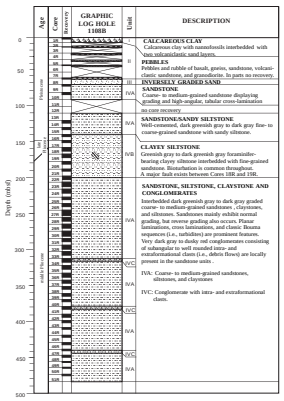

Lithostratigraphic Unit I

Description: calcareous clay with minor volcaniclastic silt and sand
Interval: Core 180-1108B-1R
Depth: 0–8.60 mbsf
Age: late Pleistocene

The recovery in Hole 1108B began with yellowish brown (10YR 5/6 and 6/6), to greenish gray (5G 6/1 and 7/1), slightly mottled nannofossil-bearing calcareous clay. The upper 18 cm of the core is highly disturbed and oxidized. In addition, dark yellowish brown volcaniclastic sand is present at interval 180-1108B-1R-1, 18–20 cm (Fig. F2). This layer has a sharp base and fines upward into very fine nannofossil ooze that is rich in planktonic foraminifers at the top. In addition, a thin layer of disturbed volcaniclastic sand occurs at interval 180-1108B-1R-2, 33–38 cm. Smear slides of the volcaniclastic layers contain common plagioclase, rare quartz, biotite, amphibole, pyroxene, volcanic glass (colorless and brown), rock fragments, carbonate, calcite, and opaque grains (see "Site 1108 Smear Slides" p. 53). The XRD analysis of Sample 180-1108B-1R-2, 18–19 cm, indicates the presence of calcite, quartz, plagioclase, and chlorite as major minerals and illite as a minor component (see Table T3). The biogenic component of Unit I is made up of abundant nannofossils, rare planktonic foraminifers, and diatoms. Two determinations of calcium carbonate indicate abundances of 28 and 31 wt% (see Table T4), and thus the sediment is classified as nannofossil clay rather than nannofossil ooze.

F2. Graded, volcaniclastic, sandstone over nannofossil, calcareous clay, p. 47.

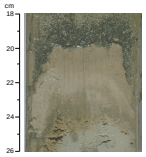

T3. Mineral composition by X-ray diffraction, p. 117.

T4. Carbon, calcium carbonate, nitrogen, and sulfur, p. 118.

Interpretation of Unit I

The calcareous clay is interpreted as deep-water hemipelagic and pelagic sediment with a high content of volcanogenic clay. The volcaniclastic beds are viewed as possible turbidites composed of redeposited volcaniclastic material (i.e., of epiclastic rather than primary pyroclastic origin). The sedimentation rate is estimated at 15 m/m.y., based on the microfossils present (see "Sediment Accumulation Rate," p. 27).

Lithostratigraphic Unit II

Description: clasts of plutonic and extrusive igneous rocks, metamorphic rocks, and sedimentary rocks
Interval: Core 180-1108B-2R through Section 8R-1, 0–26 cm
Depth: 8.6–62.96 mbsf
Age: not directly determined

Lithostratigraphic Unit II was recognized as the interval from Core 2R through Core 8R in which recovery was restricted to isolated clasts.

The following clast types were recognized in hand specimen: black vesicular basalt, volcanic breccia, granite, gneiss dolerite (metamorphosed to greenschist facies); mylonite (metamorphosed to greenschist facies); and dark volcaniclastic sandstone and siltstone.

Volcanic rocks include three types of basalt and a feldspar porphyry. The first basalt type has a glassy (tachylitic) groundmass. The second type of basalt has a fresh, pilotaxitic groundmass (containing plagioclase laths and rare olivine). The quench texture and freshness of the groundmass in both types imply a young age and submarine eruption. A third lithology is amygdaloidal aphyric basalt, containing chlorite and epidote. The feldspar porphyry contains phenocrysts of alkali feldspar, plagioclase, biotite, and hornblende in a quartzo-feldspathic groundmass, and may have originated as a dike rock.

Plutonic rocks include microgranite, granodiorite (or granite), and epidosite. The microgranite contains plagioclase, hornblende, and quartz, whereas the granodiorite contains plagioclase, quartz, and biotite replacing hornblende. The granodiorite contains chlorite and sericite alteration and has a mortar texture caused by brittle (low P,T) deformation. The epidosite consists primarily of epidote, sericite alteration, and actinolite needles within quartz grains. The granite clasts show a dominantly cataclastic texture.

Metamorphic rocks include mylonite, gneiss, and greenschist facies metadolerite. The mylonite contains stretched quartz, biotite, and chlorite in a very fine grained matrix. The gneiss contains plagioclase, quartz, biotite, apatite, sphene, and zircon. The gneiss also exhibits a foliation defined by biotite laths and shows evidence of shearing marked by sigmoidal porphyroblasts. The metadolerite contains altered feldspar and sporadic epidote.

In addition, the following information was obtained by study of thin sections of the sedimentary rocks recovered (see **"Site 1108 Thin Sections"**). Two sandstone pebbles (intervals 180-1108B-3R-CC, 0–4 cm [see Figs. **F3, F4, F5, F6,**] and 5R-CC, 6–8 cm [see Fig. **F7**]) are lithic sandstones with clasts of basalt, silicic extrusive rock, rare mica schist, quartzite, strongly altered basic extrusive rock, intrusive rock (granite?), and serpentinite. Mineral grains seen in thin section are fresh plagioclase, muscovite, quartz, and rare epidote. Bioclasts are mainly shell fragments and planktonic foraminifers. Another clast of sandstone is fine-grained, relatively well sorted micaceous lithic sandstone containing muscovite, quartz, plagioclase, chlorite, and opaque grains (interval 180-1108B-3R-CC, 16–20 cm). Numerous lithic fragments of basalt are seen. Bioclasts are present as numerous planktonic foraminifers. Scattered glauconite pellets are also seen.

F3. Digital photomicrograph of a clast of basalt with other clasts, **p. 48.**

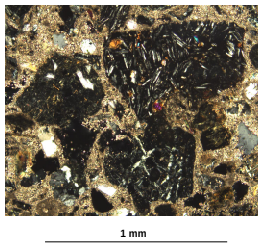

F4. Digital photomicrograph of a clast of glassy basalt with microphenocrysts, **p. 49.**

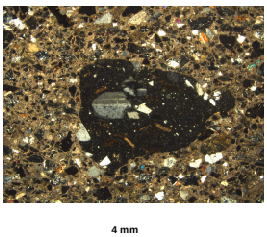

F5. Digital photomicrograph of foliated mica schist and volcanic grains, **p. 50.**

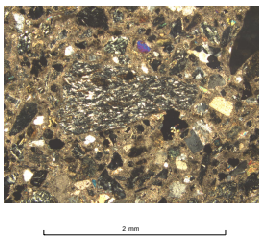

F6. Digital photomicrograph of serpentinite within a matrix of various grains, **p. 51.**

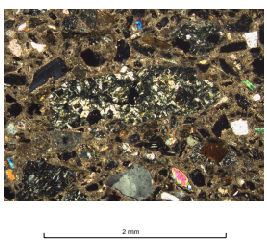

Interpretation of Unit II

All the clasts recovered are interpreted as talus (i.e., debris-flow or rock-fall deposits). No matrix was recovered, but it may have been washed out or lost during drilling. The probable source was a basement of plutonic igneous and metamorphic rocks combined with a lithified terrigenous sedimentary unit. The adjacent Moresby Seamount is an obvious suitable source location. The relatively fresh basic volcanic pebbles represent additional talus, or milled fragments derived from thin in situ, or local, flows that are probably related to the nearby Woodlark spreading center. The sedimentary rock fragments were possibly derived from the sedimentary cover of the Moresby Seamount, whereas the igneous and metamorphic rocks possibly originated in the underlying basement. The talus is much coarser than the underlying material recovered and may record a significant discrete gravity sliding event that was possibly triggered by movement along the Moresby extensional fault system, as imaged on multichannel seismic profiles. The faulting is assumed to have exhumed the greenschist facies rocks, either on land or on the seafloor, providing that the source material was talus emplaced by gravity flows.

F7. Digital photomicrograph of sandstone with various grains, p. 52.

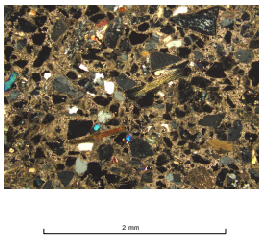

Lithostratigraphic Unit III

Description: inversely graded sand
Interval: Sections 180-1108B-8R-1, 26 cm, through 8R-2
Depth: 62.96–72.3 mbsf
Age: not determined

This unit ranges from fine- to coarse-grained unlithified sand, which was recovered beneath the inferred debris-flow deposits and talus of Unit II, but above well-cemented clastic sediments forming Unit IV (Fig. F1). This thin interval is recognized as a separate unit because it differs drastically from the overlying inferred talus in Unit II and the underlying well-lithified sandstones of Unit IV.

Unit III was recovered only in Core 8R. It consists of three inversely graded, medium-bedded sands. The unit comprises three beds. The first is dark gray (N4) silty sand and fine sand; this is followed by medium-grained sand that is, in turn, overlain by medium-grained to coarse-grained sand (Fig. F8). Components identified by visual inspection and XRD analysis are quartz, plagioclase, rock fragments, and shell fragments (<0.5 cm). Minor components are amphibole, chlorite, and probably smectite (see Table T3).

F8. Inversely graded sandstone, p. 53.

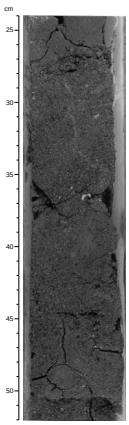

Interpretation of Unit III

The inversely graded nature of several of the beds in Unit III and the absence of tractional sedimentary structures is consistent with deposits from high-density turbidity currents. The uncemented nature indicates a much less diagenetically advanced state than that of the sedimentary rocks of Unit IV (see "Lithostratigraphic Unit IV," p. 10). It is possible that the sands relate to the inferred talus and debris of Unit II, possibly as precursor to its emplacement; however, data are inadequate to test this hypothesis.

Lithostratigraphic Unit IV

Description: graded sandstones, graded siltstones, nannofossil-rich claystones, and minor conglomerates
Interval: Cores 180-1108B-9R through 10R and 13R through 51R
Depth: 72.30–91.3 and 110.6–485.2 mbsf
Age: middle Pliocene–early Pleistocene

Substantial recovery of well-cemented, fine- to medium- and coarse-grained sandstone interbedded with claystones began in Core 9R (72.30 mbsf). Unlike Unit III, Unit IV is well lithified. Because the lithologic composition remains similar throughout, this entire interval is placed within a single lithostratigraphic unit (Fig. F1). However, there is sufficient variation in the relative abundances of different sedimentary rocks to recognize three different intercalated subunits within Unit IV as follows:

1. Subunit IVA is the volumetrically dominant sedimentary rock type and comprises interbedded sandstones, siltstones, and claystone in which medium- to coarse-grained sediments dominate.
2. Subunit IVB is mainly in the upper part of the succession and is made up of relatively fine grained clay-rich siltstone and fine-grained sandstone. Description of sedimentary features in the subunit is hampered by the occurrence of common structural deformation, related to a fault zone of mainly normal dip-slip type, concentrated ~160–180 mbsf (i.e., Cores 18R and 19R) (see "Structural Geology," p. 19, and Fig. F21).
3. Subunit IVC is composed of conglomerate and is restricted to the mid and lower parts of the recovered succession. The sandstones are cemented by calcite spar throughout Subunit IVA. The degree of lithification varies. In general, the sandstones are more cemented than the claystones. As a result of this, marked competency contrast in drilling disturbance (e.g., small high-angle faults) is locally observed at the contact between well-cemented sandstones and claystones.

The main characteristics of each of the three subunits are described below.

Lithostratigraphic Subunit IVA

Description: coarse- to medium-grained sandstones, siltstones, and claystones
Intervals: Cores 180-1108B-9R through 15R and Section 22R-3 through Core 51R (except intervals of Subunit IVC: 34R-2, 0–69 cm; 41R-1, 36–142 cm; and 47R-1, 29–66 cm to 47R-CC, 0–24 cm).
Depth: 72.30–139.4 and 200.2–485.2 mbsf
Age: middle Pliocene–Pleistocene

Lithostratigraphic Subunit IVA is characterized by sandstones that vary from coarse to fine grained, together with clay-rich siltstones and silty claystones. There was no recovery in Cores 11R and 12R. However, the base of Core 11R and all of Core 12R were geophysically logged (including gamma-ray, resistivity, and radioactivity logs). The log response of the missing interval (Cores 11R and 12R) indicates the presence of a

high porosity facies and is similar to the log response of the underlying interval of Subunit IVA recovered in Cores 14R and 15R, and the upper part of Core 16R. (Note: Only the interval from ~100 to 160 mbsf was logged because of problems in the hole; see "Downhole Measurements," p. 40.)

The sandstones typically contain 1.7–7.0 wt% calcium carbonate, whereas intercalated silty claystones are more calcareous (~15 wt%) (see Table T4 and "Organic Geochemistry," p. 33). In addition, a sample of clay-rich siltstone from near the base of the succession contains 39 wt% calcium carbonate. The XRD analyses indicate plagioclase and quartz as the major minerals (see Table T3).

Bedding Characteristics

Bedding in the sandstones is generally with sharp bases and gradational upper contacts. Colors are subdued, typically greenish gray and dark greenish gray (5Y 4/1 to 5GY 4/1), to a very rare bluish gray (5B 4/1). Bed thicknesses range from thin to thick. An example of a thick-bedded, coarse-grained sandstone is shown in Figure F9. Contrasting thin-bedded sandstones are shown in Figure F10. Commonly, the sandstones are discrete beds separated by silty claystone and clay-rich siltstone. However, repeated thin beds of sandstone of various thickness (<25 cm) were observed. Finer grained sandstones are commonly clay rich (usually termed clayey sandstone in the visual core descriptions).

Sedimentary Structures

The majority of the thicker bedded (>30 cm) and coarser grained sandstones are internally structureless. Some of the sandstones exhibit normal grading from coarse- or medium-grained sand to medium- or fine-grained sand. A relatively small number of sandstones show sequences of sedimentary structures that can be identified as the Ta, Tb, and Tc divisions of classical turbidites (Bouma, l962; e.g., Sections 20R-1 and 20R-2). Occasionally, complete Ta-Te divisions were noted within a single-graded sandstone bed (interval 180-1108B-24R-2, 4–36 cm). However, it must be emphasized that the majority of the sandstones defy simple classification using Bouma's (l962) scheme (see below).

Some graded units locally exhibit alternating low-angle planar lamination or cross lamination (e.g., interval 180-1108B-26R-1, 115–120 cm; Fig. F11). There are some exceptions where cross lamination is relatively steeply inclined (i.e., up to 35°, average <20°; e.g., interval 180-1108B-36R-2, 42–45 cm). Convolute lamination was also occasionally observed (e.g., intervals 180-1108B-26R-1, 112–114 cm, and 36R-3, 90–100 cm). A prominent additional feature of Subunit IVA is reverse-to-normal grading (reverse grading passing into normal grading within a single bed) within the medium- to thick-bedded sandstones. Reverse-to-normal grading is present throughout the unit but becomes more common below 245 mbsf. Commonly, individual beds exhibit reverse grading, from medium- to coarse-grained sand near the base, passing upward into normally graded coarse- to medium-grained sand. The reverse-graded intervals are typically structureless.

Intraformational and Extraformational Clasts

Rip-up clasts (i.e., intraformational) of mudstone are common within the graded sandstones and are concentrated near the top of individual depositional units (interval 180-1108B-26R-3, 70–80 cm). Mud clasts are typically less than several centimeters in size, but local larger mud clasts (up to 4 cm) were also noted (Fig. F12). In some places, it was unclear if a

F9. Sandstone with calcite veins, p. 54.

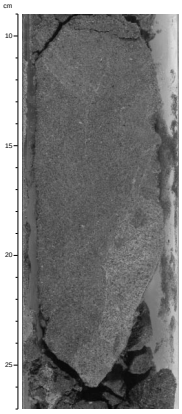

F10. Alternating beds of sandstone, siltstone, and claystone, p. 55.

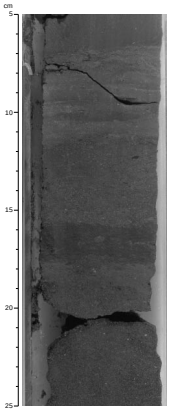

F11. Alternating parallel-wavy-laminated with ripple-laminated sandstone, p. 56.

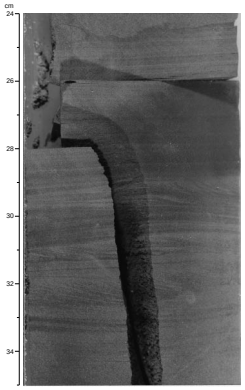

mud layer was part of a large mud clast or a discrete mudstone bed. Mud clasts are rarely concentrated in repeated thin beds to laminae (Section 32R-3, 86 cm, 105 cm, and 122 cm). Rip-up clasts in places are composed of siltstone rather than claystone (e.g., interval 180-1108B-32R-5, 33.5–83 cm).

In hand specimen the sandstones exhibit numerous angular, to subangular, extraformational lithic grains in the form of reddish lithic grains, quartz grains, and white detrital carbonate grains. The carbonate grains are fragments of bivalves, calcareous algae, bryozoans, echinoderms, and large (i.e., benthic) foraminifers. Coral fragments were rarely noted in Sections 32R-1, 32R-2, and 32R-5. In addition, occasional small intact gastropod shells are present (e.g., Section 15R-2, 109 cm). White, small tubular (noncalcareous) bioclasts (up to 0.8 cm in diameter) were observed locally but remain unidentified. These fossils range from spherical to elliptical in three dimensions with an internal cavity infilled by sediment.

Siltstones

Siltstones are commonly clay rich and occur as intercalated depositional units up to tens of centimeters thick. Colors typically range from dark greenish gray (5GY 4/1) to greenish gray (5BG 5/1). These siltstones exhibit parallel lamination, small-scale low-angle cross lamination, or are structureless. Some siltstones are sandy (Section 16R-1), whereas others are clay rich. Fragments of carbonized wood were locally observed (e.g., interval 180-1108B-15R-CC, 10–15 cm). The siltstones are similar to those described in more detail from Subunit IVB (see **"Lithostratigraphic Subunit IVB,"** p. 14).

Petrography of Sandstones and Siltstones

The compositions of a number of thin sections of the sandstones and siltstones studied are summarized in **"Site 1108 Thin Sections"**. All the sandstones are lithic; however, there is a marked difference in composition of the clasts and related mineral grains between sandstones in the upper and lower parts of the succession, with the change found at ~330 mbsf. However, it must be emphasized that this depth is only approximate as the change was observed in only a few thin sections of sandstone (see **"Site 1108 Thin Sections"**). There is no marked change in sedimentary structures, grain size, or physical properties. Also, there is no marked change in physical properties, corresponding to a depth of 330 mbsf (see **"Physical Properties,"** p. 35).

Sandstones in the upper part of Unit IVA (e.g., interval 180-1108B-15R-1, 11–14 cm) are lithoclastic, with small subangular to angular grains of fresh and altered basalt, schist, and altered siliceous extrusive igneous rock (Fig. **F13**). Common mineral grains are mainly quartz, feldspar (mostly plagioclase), muscovite, biotite, and epidote, set in a cement of fine calcite spar. Serpentinite lithoclasts and chromite are rarely observed.

Some of the sandstones (e.g., interval 180-1108B-26R-3, 7–16 cm) contain planktonic foraminifers as well as bioclasts of shallow-water origin, including calcareous algae and bryozoans. These biogenic components are in addition to numerous lithic grains of siliceous and calcareous schist, altered basalt, altered siliceous extrusive igneous rock, micritic carbonate (partly recrystallized), and mineral grains including fresh plagioclase, hornblende, biotite, quartz, and rare serpentinized olivine.

F12. Thick-bedded granule-pebble, very coarse-grained sandstone, **p. 57.**

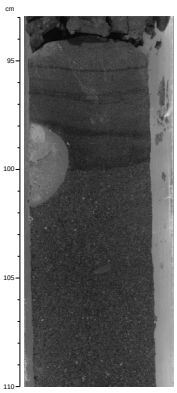

F13. Digital photomicrograph of a basaltic clast within a siliciclastic matrix, **p. 58.**

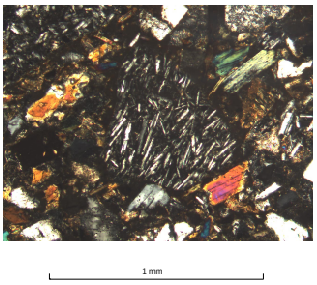

One other sandstone bed (interval 180-1108B-22R-6, 20.5–22.5 cm) includes rare grains of with a sheared mylonitic texture. These grains occur within a typical assemblage of relatively fresh basaltic grains, more altered silicic volcanic grains, mica schist, quartzite, and associated mineral grains (quartz, feldspar, and muscovite).

In several thin sections, grains of clinopyroxene were noted. They are probably associated with the basaltic clasts that commonly contain pyroxene phenocrysts (e.g., interval 180-1108B-23R-3, 35–36.5 cm). Indeed, an isolated clast of fresh olivine basalt was recovered in a nearby part of the succession (interval 180-1108B-26R-1, 0–2 cm). Elsewhere, the sandstones include well-rounded clasts of olivine basalt (e.g., interval 180-1108B-27R-5, 61–63 cm) in which the basalt grains show variable degrees of alteration. Basaltic grains, typically well rounded, were also observed to be abundant in several thin sections of sandstones that were recovered near the base of Subunit IVA (intervals 180-1108B-32R-3, 61–64 cm, and 34R-2, 126–128 cm).

By contrast, sandstones below ~330 mbsf (e.g., interval 180-1108B-36R-3, 52–56 cm) contain a mixture of lithoclasts of basalt, altered dolerite (epidote rich), acidic volcanic grains, chloritic grains (altered basic glass), rare coarse granitic rock fragments (characterized by intergrown quartz and feldspar, fresh and altered), plagioclase (commonly zoned), biotite, minor muscovite, hornblende, pyroxene, and rare olivine, together with bioclasts (e.g., bryozoans and calcareous algae), rare lithoclasts of quartzose siltstone, and diagenetic pyrite. In addition, microcrystalline quartz that may be chert was present but rare (e.g., interval 180-1108B-45R-CC, 8–10 cm). Planktonic foraminifers are also invariably present. Textures range from matrix to clast supported within individual sandstones, which are commonly poorly sorted with mainly angular grains.

In addition, a few thin sections of fine-grained sandstones were studied, mainly from the lower part of the Subunit IVA succession (e.g., interval 180-1108B-28R-3, 28–31 cm). They contain a mixed assemblage of planktonic foraminifers and detrital grains, including mineral and rock fragments set in a fine micritic matrix. These sediments are well sorted, with abundant small muscovite grains oriented parallel to lamination, and occasionally include benthic foraminifers (e.g., interval 180-1108B-39R-1, 94–96 cm).

In summary, sandstones from the upper part of Subunit IVA (i.e., above 350 mbsf) contain a high proportion of metamorphic-derived lithoclasts and related mineral grains (i.e., schist, quartzite, phyllite, polycrystalline quartz, muscovite, epidote, and rare chromite). Highly altered igneous-derived grains are also present. The lower ~150 m of the succession recovered contain large amounts of material derived from both basic and acidic volcanic rocks, with a minor contribution from both basic (dolerite) and acidic (granite) plutonic rocks. By contrast, metamorphic-derived material (e.g., schist, polycrystalline quartz) is greatly diminished relative to the above 330 mbsf (see **"Site 1108 Thin Sections"**).

Silty Claystones

Silty claystones are common and range in color from greenish gray and dark greenish gray (5Y 4/1 to 5GY 4/1), to dark gray (N4), to olive gray (5Y 5/4), and black (5Y 2.5/2). The silty claystones are mainly structureless, but they are commonly bioturbated to variable extent, giving rise to a distinctive mottled appearance. Discrete silt laminae are rarely present. Planktonic foraminifers are commonly scattered

throughout (e.g., interval 180-1108B-19R-1, 43–80 cm). The darkish claystones are commonly massive and devoid of trace fossils (e.g., interval 180-1108B-23R-4, 83–150 cm). In addition, the lower part of the subunit includes rare thin (<20 cm) intervals of reddish brown claystones (e.g., interval 180-1108B-36R-4, 21–23 cm; 2.5YR 4/4). The claystones are similar to those described in more detail from Subunit IVB (see "Lithostratigraphic Subunit IVB," p. 14).

Pebbles

Two pebbles of medium- to coarse-grained sandstone were recovered in Core 13R. This was the entire recovery in the core and, thus, it is unclear if the pebbles were derived from an interbedded conglomerate, if they fell from above (i.e., from Unit II), or if they represent drilling artifacts (i.e., pieces of sandstone milled to clasts by rotary drilling). For this reason, the pebbles in Core 13R are included within Subunit IVA (i.e., mainly coarse clastic sediments) rather than with Subunit IVC (see conglomerates discussion in "Lithostratigraphic Subunit IVC," p. 16).

The sandstones locally contain scattered granule-sized clasts. These occur exclusively within the thicker (>30 cm), coarser grained sandstones that are common near the base of individual beds. For example, a rounded pebble (2 cm × 3.5 cm) of coarse- to very coarse-grained, well-cemented sandstone was recovered in Core 13R. This sandstone contains clasts of quartz and rock fragments. In addition, rare small clasts of reddish, altered basalt clasts were also noted (e.g., interval 180-1108B-13R-CC, 0–7 cm).

Volcaniclastic Layers

Relatively homogeneous volcaniclastic layers are very rare, but local thin-bedded siltstones are rich in volcaniclastic material. For example, a thin bed of light gray (5YR7/1) sandy, silty volcaniclastic material is in interval 180-1108B-14R-2, 54–59 cm. Smear-slide analysis of this layer revealed common colorless glass, rare brown glass, and common bioclasts (e.g., echinoderm fragments). A large amount of colorless (rhyolitic) glass shards is present together with bioclasts, including planktonic foraminifers. Elsewhere, volcaniclastic material forms a subordinate constituent of thin-bedded (<5 cm) siltstones (e.g., Sample 180-1108B-23R-1, 99.5–100.5 cm) as documented by smear-slide analysis (see "Site 1108 Smear Slides," p. 53).

Lithostratigraphic Subunit IVB

Description: foraminifer-bearing clayey siltstone
Interval: Cores 180-1108B-16R through 22R-2
Depth: 139.4–200.2 mbsf
Age: middle to late Pliocene

Subunit IVB is distinguished from Subunit IVA by greenish gray to dark gray and black foraminifer-bearing clay-rich siltstone interbedded with thin- to medium-bedded, mainly fine- to medium-grained sandstone. The XRD analysis documents the presence of chlorite, illite, and smectite as the clay minerals present (see Table T3). Determinations of calcium carbonate indicate that the fine-grained sediments of this subunit are highly calcareous, with $CaCO_3$ values >25 wt% recorded (see Table T4).

The part of the succession between 140 and 200.2 mbsf shows abundant evidence of tectonic deformation within mainly silty claystone

and clay-rich siltstone, characterized by bedding dips up to 35°, low-angle shearing, brecciation, and ubiquitous slickensides that are commonly concentrated along joints and lithologic boundaries (see "Structural Geology," p. 19). The structural deformation has particularly distorted bedding contacts and disrupted depositional units. A combination of structural, paleomagnetic, and physical properties evidence indicates that an important, inclined, predominantly dip-slip fault zone is present and is concentrated ~158–173 mbsf (Cores 18R and 19R). The orientation of this fault zone is unknown. However, it is probable that up to 200 m of the succession were cut out by faulting. Below 200.2 mbsf, within more competent lithologies, the intensity of tectonic deformation falls off markedly, although occasional (normal) faults cut the succession.

The following lithologies are present in Subunit IVB:

Clay-Rich Siltstone and Silt-Rich Claystone

These sediments are greenish gray (5GY 4/1), bioturbated (with variable intensity) and contain scattered planktonic foraminifers (e.g., interval 180-1108B-19R-1, 0–43 cm). There are subtle differences between the relative abundance of claystone and siltstone, as observed both within and between individual depositional units.

The clay-rich siltstones are typically present as relatively thin to medium beds <15 cm thick. These sediments are commonly strongly sheared and tectonically fragmented, obscuring primary sedimentary structures. Chondrite burrows are ubiquitous throughout many of the claystones (e.g., Section 16R-1). In addition, large *Zoophycos*-type horizontal burrows are locally present (e.g., Sections 19R-2 and 19R-3). In places, entire intervals, including successive beds, are bioturbated (e.g., interval 180-1108B-16R-1, 0–84 cm). Darker (organic-rich?) layers are mainly claystones with minimal silt and are mainly devoid of trace fossils (e.g., interval 180-1108B-19R-4, 82–100 cm).

The clay-rich siltstones and silt-rich claystones are mainly structureless (e.g., interval 180-1108B-19R-4, 0–20 cm), but are locally graded (e.g., interval 180-1108B-20R-1, 10–23 cm), cross laminated (e.g., interval 180-1108B-16R-2, 102–115 cm), convolute laminated (e.g., interval 180-1108B-26R-1, 112–121 cm), or parallel laminated (e.g. interval 180-1108B-20R-1, 130–145 cm; Fig. **F14**).

Some siltstones are packed with planktonic foraminifers (e.g., interval 180-1108B-19R-2, 35–39 cm). Pyrite concretions occur locally (interval 180-1108B-18R-4, 0–67 cm). Also, some small woody fragments were noted. Chemical analysis indicates that the calcareous claystones of Subunit IVB are rich in organic matter, which is probably of terrestrial origin (see "Organic Geochemistry," p. 33).

In thin section the typical foraminifer-rich silty claystone was seen to comprise abundant planktonic foraminifers set in a muddy micritic matrix. The XRD analysis of Sample 180-1108B-17R-2, 70–73 cm, shows calcite as the major mineral and quartz and plagioclase as minor minerals (see Table **T3**). In addition, a fine-grained foraminifer-rich calcareous interval from Subunit IVA (interval 180-1108B-16R-CC, 1–3 cm) comprises planktonic foraminifer packstone with a calcite spar cement. Small detrital grains of quartz, feldspar, plagioclase, muscovite, and biotite are also present. Pyrite was noted within individual foraminifer tests.

F14. Sandstone, parallel- and climbing-ripple laminated under parallel-laminated siltstone, p. 59.

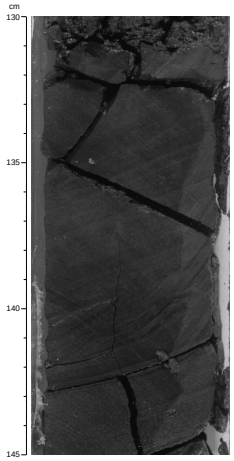

Sandstones

Sandstones are mainly fine to medium grained and thin to medium bedded and are intercalated with the silty claystones and clay-rich siltstones. The majority of the sandstones are graded, with sharp bases (commonly scoured) and gradational tops. They are very similar to the sandstones described above from Subunit lVA and are, therefore, not described in detail here. Partial Bouma sequences were rarely observed and in places show amalgamation (interval 180-1108B-20R-2, 16.5–25 cm). Typical sedimentary structures within the thin- to medium-bedded sandstones are shown in Figures **F14, F15, F16,** and **F17.** In addition to siliciclastic sediment, local disseminated volcanic clasts (Fig. **F18**) and glass shards (brown and colorless) were identified by use of a hand lens (e.g., interval 180-1108B-16R-2, 0–14 cm), and in a number of the smear slides (see **"Site 1108 Smear Slides,"** p. 53).

Rare, very coarse grained sandstone (up to 2 mm) was recovered in interval 180-1108B-16R-2, 14–19.5 cm. This sandstone forms the base of relatively thick, graded sandstone beds, and is included within Subunit IVB rather than within the conglomerate forming Subunit IVC.

Lithostratigraphic Subunit IVC

Description: conglomerates
Intervals: intervals 180-1108B-34R-2, 0–69 cm; 41R-1, 36–142 cm; and 47R-1, 29–66 cm through 47R-CC, 0–24 cm
Depth: 313.34–314.04; 379.7–380.80; and 437.39–438.06 mbsf
Age: middle Pliocene–late Pliocene

First, a distinctive horizon of granule-sized conglomerate is present in interval 180-1108B-34R-2, 0–69 cm. This is a single sharp-based unit of granule conglomerate, grading into coarse sandstone at the top (Fig. **F19**). This interval is structureless and contains shell fragments. The color is subdued dark gray (5Y 4/1).

In the lower part of Unit IV, a second conglomerate interval is interbedded with the succession (interval 180-1108B-41R-1, 36–142 cm). This interval is composed of matrix-supported sandstone strewn with subrounded to rounded lithic fragments that are concentrated near the base of the unit. Clast sizes range from coarse-grained sand to pebble with most being in the 3–5 mm grain-size range. Sedimentary clasts are more rounded relative to igneous ones. In addition to lithogenous clasts, shell fragments and other calcareous fossil clasts are scattered through the conglomerate. Colors of this conglomerate are red, black, white, and green. The matrix is more grayish in color.

A third, thin conglomeratic interval is present lower in the lower part of Unit IV (interval 180-1108B-47R-1, 29–66 cm, through 47R-CC, 0–24 cm). This comprises 0.2 m of polymict paraconglomerate containing both intraformational and extraformational clasts. The base of this unit was not recovered by drilling, whereas the top of the paraconglomerate is directly overlain by fine-grained sandstone. In marked contrast to Subunit IVA, colors are dark gray to dark red and very dark gray. The extraformational clasts include subangular, subrounded to subangular, to locally rounded basalt, and other altered extrusive igneous rocks. The intraformational clasts are coaly fragments of small pebble size. In addition, large shell fragments were observed only in the working half of the core. The matrix to the paraconglomerate is fine-grained sandstone.

F15. Normally graded sandstone displaying cross and parallel-wavy laminations, **p. 60.**

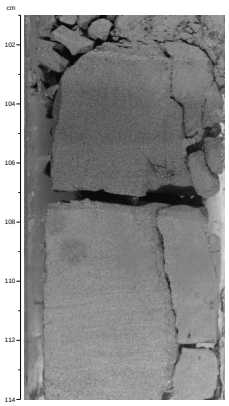

F16. Laminated clayey siltstone with foraminifers, **p. 61.**

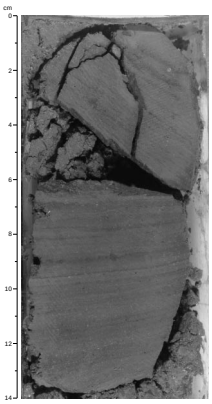

F17. Bioturbated sandy silty claystone with foraminifers and pyrite concretions, **p. 62.**

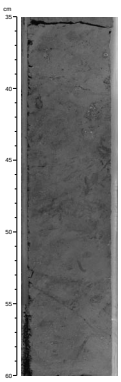

Interpretation of Unit IV

Unit IV is interpreted as a single depositional unit, which on land would correspond to a single lithostratigraphic formation. This conclusion was reached for the following reasons: (1) sediments of similar type (i.e., lithology and sedimentary structures) are present throughout the entire unit; (2) the study of thin sections shows that all levels of Unit IV exhibit similar composition, although the relative abundances of constituents vary locally; and (3) all the sediments are well cemented by calcite and exhibit a similar diagenetic state.

Notwithstanding the above similarities, the relative abundances of coarse-, medium-, and fine-grained sediments vary systematically throughout Unit IV and allow us to subdivide them into three subunits as described previously.

We interpret all of the sandstones as turbidites. These predominate in Subunit IVA but are also a subordinate component of Subunit IVB. A deep-water origin is indicated by a well-preserved, diverse fauna of benthic foraminifers that indicate bathyal depths (>1000 m; see "Benthic Foraminifers," p. 26). A relatively small number of Bouma sequences (Bouma, l962) were identified: either complete Ta–Te or partial Tb–Te, or rarely Tc–Te divisions. However, such classical turbidites are rare. More commonly sandstones are massive, show irregular cross lamination, or reverse-to-normal grading on different scales. In addition, rare amalgamated beds may record deposition from successive turbidity currents. Provisionally, these sandstones are interpreted as deposits from high-density turbidity currents, and they require further postcruise study. In addition, a small number of structures (e.g., sharp-topped planar laminae) are suggestive of deposition under the influence of bottom currents (cf. Pickering et al., l989).

Within Subunit IVB, the succession is considerably finer grained and more calcareous, with abundant silty claystone and clay-rich siltstone, rich in nannofossils, dispersed planktonic foraminifers, and (inferred) organic matter. We interpret this interval as mainly hemipelagic silts and clays. The sandstones with partial Bouma divisions (Tb, Tc, and Td) are interpreted mainly as classical turbidites, whereas the thinner bedded more silty beds are viewed as deposits from low-density turbidity currents (cf. Piper, l978). The subdued hues of gray green and gray to black, with minor disseminated pyrite, are suggestive of relatively low-oxygen bottom conditions at various times. The presence of relatively fine grained sediments in Subunit IVB could relate to factors that include sediment input from the source area, relative sea-level change, or autocyclic effects (i.e., evolution of the depositional system).

The three coarser grained intervals of conglomerate that form Subunit IVC are provisionally interpreted as high-density turbidity current and/or debris-flow deposits. Possible reasons for their occurrence could include relative sea-level change, increased clastic sediment input to the basin, or concentration in local channelized units.

The provenance of all the clastic sediments of Unit IV was from a continental area exposing mainly extrusive igneous and metamorphic rocks. Plutonic igneous and ophiolitic rocks (i.e., indicated by rare chromite grains and serpentinite fragments) were also present in the source region. Possible source areas are Moresby Seamount, Normanby Island, adjacent islands, and areas generally to the west that are now submerged but were land during the Pliocene, including the mainland of Papua New Guinea. The ubiquitous reddened lithic grains may well represent material weathered by laterization on land. The calcareous

F18. Digital photomicrograph of acidic volcanic clast with other grains, p. 63.

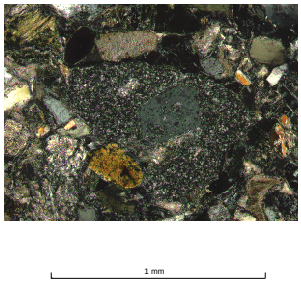

F19. Graded, granule-pebble, matrix-supported paraconglomerate, p. 64.

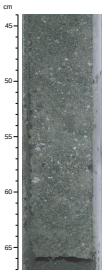

bioclast fragments were derived from shallow-marine (e.g., coral and algae) and shelf depths (e.g., benthic foraminifers), and then redeposited into a deep-marine setting.

Finally, based on evidence of microfossils (see "Biostratigraphy," p. 24), the sedimentation rate of the uppermost part of Subunit IVA (90–155 mbsf) is estimated as 324 m/m.y. (see Fig. F30). An apparent sedimentation rate for Subunit IVB (155–200 mbsf) is estimated as 18 m/m.y. but is probably due to the removal of as much as 200 m of the succession by the fault (see "Structural Geology," p. 19). The lower sandstones and conglomerates of Subunits IVB and IVC accumulated at ~409 m/m.y. It is notable that the apparently slow depositional rate of Subunit IVB is an artifact of faulting that cut out up to 200 m of the succession. On the other hand, an original difference in sedimentation rates between the finer grained Subunit IVB and the coarser grained Subunit IVA above and below may have existed but cannot be quantified

Summary of Depositional History

A generalized downhole variation in grain size is shown in Figure F20. Sedimentation recorded at Site 1108 began in the middle to late Pliocene with very rapid accumulation (409 m/m.y.) of fine-, medium-, and coarse-grained sandstones, and minor conglomerate, interpreted as mainly deposits from turbidity currents and debris flows. The composition of the sandstones is dominated by clasts and mineral grains derived from basic and acidic volcanic rocks, with a minor contribution from both basic and acidic plutonic rocks (dolerite and granite). Shallow-water-derived carbonate and quartzose siltstone are also present. A possible source of the shallow-water-derived sediments is the upper crustal units of the Moresby Seamount, assuming it was then exposed above sea level. However, this was possibly too small to provide all the clastic material and may not have existed as a discrete feature. It is probable that sediment was also contributed from the present areas of the D'Entrecasteaux Islands (e.g., Normanby Island), where a similar range of rock types is exposed (Hill et al., 1992), and from any adjacent emergent areas. An alternative possible source for shallow-water carbonate might have been the Trobriand Platform or Ergun Reef to the north. However, these settings are unlikely because the carbonates recovered at Site 1108 are invariably mixed with abundant lithic clasts, including metamorphic constituents, for which a westerly or southwesterly derivation is likely, as discussed above.

Above 330 mbsf there is a marked incoming of metamorphic rock fragments and related mineral grains, in addition to the igneous and other grains summarized above. A possible explanation for the change in composition is that sediments were derived from source areas that experienced pervasive extensional faulting (i.e., detachment faulting) such that deeper, metamorphic levels of the crust were exposed through time (i.e., high-level extrusive and intrusive rocks were unroofed and eroded first, whereas deeper metamorphic rocks were not unroofed until later) resulting in an overall "reverse stratigraphy" of composition as observed in Hole 1108B.

In addition, the serpentinite and rare chromite grains that occur throughout the middle to upper Pliocene succession are assumed to have been derived from ultramafic ophiolitic rocks of the Papuan ophiolite belt (Davies and Jaques, 1984). Also, the metamorphic rocks can possibly be correlated with the Kagi metamorphics that regionally underlie the Papuan ophiolite belt and are interpreted as a lower Ter-

F20. Summary of grain-size variation in Hole 1108B, p. 65.

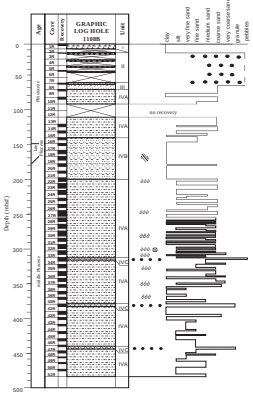

tiary subduction-accretion complex (Rogerson et al., l987). The shallow-water bioclastic debris (including algae and bryozoans) presumably accumulated at shelf depth and were then mixed with land-derived clastic sediment. Some of the lithic grains were clearly rounded in a fluvial or shallow-marine setting.

From ~1.95 to 2.58 Ma (late Pliocene) there was an apparent drop in sedimentation rate to ~24 m/m.y., corresponding to an interval of finer grained deposits from turbidity currents (Subunit IVB). However, this is probably an effect of faulting.

Later, during the time interval 1.71–1.95 Ma (late Pliocene), represented by the upper part of Subunit IVA, the sedimentation rate increased markedly to ~324 m/m.y. and then reduced slightly to an estimated 138 m/m.y. from 1.25 to 1.71 Ma (see **"Sediment Accumulation Rate,"** p. 27). During this entire time interval, there was a return to predominant deposition from high-density turbidity currents.

Following, at ~60 mbsf, there is an abrupt change from well-consolidated lithologies to completely unconsolidated sand (Unit III). To explain this sudden change in degree of consolidation, sediment may have been deposited then eroded, possibly by mass flow processes, gravity flows, or bottom currents.

This was then followed by emplacement of talus as thick as ~50 m. The coarse, angular nature of the clasts recovered, including basalt, metadolerite, mylonite, and gneiss, suggests that the obvious provenance relates to the proximity of the Moresby Seamount. In addition, the commonly cataclastically deformed and sheared nature of some of the clasts, including mylonite and gneiss, suggests the Moresby detachment fault system as the specific source. As noted above, metamorphic rocks probably became available for erosion following exhumation related to extensional faulting. The time of emplacement of the talus is only poorly constrained by the late Pleistocene age of Unit I above (to 1.25 Ma) and the late Pliocene–early Pleistocene age (1.25–1.71 Ma) of the upper part of Unit IV beneath (see **"Biostratigraphy,"** p. 24). The talus differs strongly from the relatively well sorted predominantly silt-sand grain size of the mainly Pliocene succession beneath, suggesting that it might relate to a discrete tectonic event (e.g., a pulse of movement along the Moresby extensional detachment system).

Finally, during the late Pleistocene (to 1.25 Ma) deposition was restricted to calcareous, nannofossil-rich clay with minor silt and sand containing a high content of volcanic ash. This is assumed to be pyroclastic ash derived from the Trobriand volcanic arc (including the Amphetts Islands and Egum Atoll) or rift-related volcanoes in Dawson Strait. The ash is mainly reworked, reflecting a gravitationally unstable setting adjacent to Moresby Seamount. Sedimentation rates are very much lower (15 m/m.y.) than for most of the Pliocene succession (Unit lV), despite the additional input of pyroclastic ash and proximity to Moresby Seamount. This area was possibly submerged during this time, and thus, not a significant sediment contributor, or the basin had become isolated from surrounding land areas by formation of tectonic barriers (i.e., sub-basins and highs related to rifting).

STRUCTURAL GEOLOGY

The sedimentary succession cored at Site 1108 penetrated about half of the local thickness of the hanging-wall sequence of a detachment fault adjacent to the Moresby Seamount, as inferred from seismic data

(see "Leg 180 Summary" chapter). Structural observations and measurements made at Site 1108 are summarized in Figure F21. In the following text, the sections' depths (in mbsf) refer to their respective tops.

F21. Summary log of structural features measured at Site 1108, p. 66.

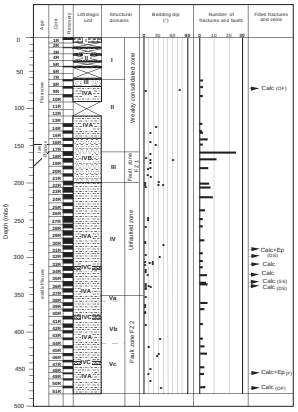

Structural Subdivisions

The 485-m-thick section of Holocene–middle Pliocene sediments drilled at Site 1108 (see "Biostratigraphy," p. 24) can be subdivided into five distinct structural domains on the basis of marked variations in both lithologies and types of deformation.

Domain I is represented by a thin sequence of clay-bearing ooze and recovered pebbles (lithostratigraphic Units I and II; see "Lithostratigraphic Unit I," p. 7, and "Lithostratigraphic Unit II," p. 8), extending from the seafloor to the top of Core 180-1108B-8R (62.7 mbsf). Recovery was very low; therefore, the primary or reworked origin of the pebbles recovered cannot be firmly elucidated.

Domain II consists mainly of unconsolidated sand (lithostratigraphic Unit III) overlying a more lithified sandstone sequence (lithostratigraphic Subunit IVA) that shows some evidence for brittle deformation, including fractures and micro-normal faults. This domain extends from the top of Core 180-1108B-8R down to the top of Core 18R (158.6 mbsf).

Domain III is an interval marked by considerable faulting, extending from Core 180-1108B-18R to the top of Core 22R (197.2 mbsf). Within this interval of semilithified claystones to sandstones (lithostratigraphic Subunit IVB) stress led predominantly to brittle failure.

Domain IV comprises little-deformed turbiditic sandstones (lithostratigraphic Subunit IVA) that are present between the top of Core 180-1108B-22R and the top of Core 38R (350.5 mbsf). Brittle deformation is expressed only by a few minor normal faults.

Domain V encompasses the lower part of lithostratigraphic Unit IV. It is observed from Core 180-1108B-38R to the base of Hole 1108B (i.e., 485 mbsf). The mainly fine grained silty material in this interval shows intense deformation, including scaly fabrics, fracturing, and shear along fault planes.

The majority of the structures observed at Site 1108 are thought to be real tectonic features, although drilling-induced fracturing cannot be ruled out for some. In fact, the RCB drilling process was partly hindered by the well-cemented rock in that the core rotated in the barrel for a considerable length of time. This problem has been pointed out previously (Lundberg and Moore, 1986). The causes of subhorizontal fragmentation is thus unclear. Nevertheless, most of the brecciation and normal faulting cannot be explained as an artifact of drilling; therefore, the features are inferred to relate to tectonics.

In the following section, the deformational structures of the abovementioned domains are described mainly in terms of fault/fracture frequency, with peculiar attention to the fault zone of structural Domain III.

Domain I

Within the undeformed, soft sediments at the top of the succession (Domain I; see Fig. F21), no structures other than horizontal bedding planes are observed.

Domain II

Beneath Domain I and throughout Domain II, the bedding dips vary considerably, ranging from 0° to 75° with an average attitude in the interval 10°–20° (Fig. F22). Some of these bedding planes have been reactivated as slip planes (e.g., Sections 180-1108B-8R-1 [62.7 mbsf] and 9R-1 [72.3 mbsf]). Also, faults intersecting bedding planes at high angles are in evidence, as illustrated in Figure F23 by a steeply inclined dip-slip fault in Section 180-1108B-10R-1 (81.9 mbsf). At Section 180-1108B-17R-1 (149.0 mbsf), the observation of staircase-like morphologies along a system of minor steeply dipping slip planes indicates reverse faulting. Brittle deformation is also illustrated by intense fragmentation of intervals composed of centimeter-sized angular blocks of siltstone (Sections 180-1108B-9R-1, and 10R-1).

Domain III

The top of Domain III is defined by a sharp change in both lithology and deformational style, as mirrored by intensely fractured clays and claystones. However, the exact nature of the contact between Domains II and III remains uncertain because of poor core recovery. The abrupt increase in fracturing within Domain III is clearly shown on the frequency distribution curve in Figure F21. Domain III typically shows alternations of extensive intervals of unbroken material, up to 1 m long (Sections 180-1108B-18R-1 [158.6 mbsf] and 18R-4 [163.1 mbsf]), and highly strained zones. Within the unbroken intervals, bedding is often preserved and, where measured, is inclined ~10° on average (Fig. F22).

Coherent pieces of silty material are consistently cut by various sets of planar-type fractures, including both open fractures with no indication of movement, and minor fault surfaces marked by slickenlines. The entire fracture population identified throughout Domain III dips at moderate angles, clustered around 45° (Fig. F24). However, both shallow- and high-angle normal faults (Section 180-1108B-20R-1 [178.0 mbsf]) are also well documented. Analysis of the plunge of the slickenline data set indicates a dominantly dip-slip direction of displacement (~75% of the data collected), but some oblique-slip and pure strike-slip faults are also documented (Fig. F25). Very few indications of sense of movement have been recorded, and most of the few apparent millimeter-scale offsets directly measured on the core face indicate normal sense of displacement (Section 180-1108B-19R-1 [168.3 mbsf]).

The general arrangement of the deformed zones is dominated by brecciated zones that are largely developed throughout Domain III. They comprise centimeter to decimeter-sized angular fragments of fine-grained siltstone and clay with polished surfaces, lying in a random orientation on the observed core surfaces.

A gradual vertical transition from coherent, or slightly fractured, core pieces to progressively broken intervals was observed at Sections 180-1108B-18R-1 (158.6 mbsf), 18R-3 (161.6 mbsf), and 19R-4 (171.3 mbsf); these, in turn, pass into individual rock fragments whose size diminishes gradually <1 cm (Fig. F26). Because no significant variation in lithology is observed, the brecciation process can be assigned to disaggregation of an original coherent material in response to increasing brittle fracturing. As stated before, the inferred primary fault-related brecciation may have been later emphasized during drilling operations.

F22. Histograms of bedding dips within four structural domains at Site 1108, p. 67.

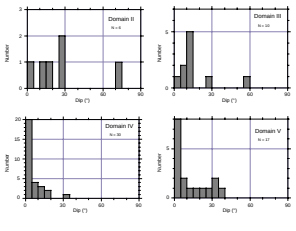

F23. Steep dip-slip fault cutting lithologic boundaries, p. 68.

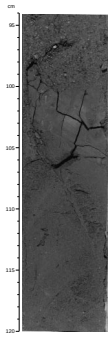

F24. Fracture/fault population at Site 1108, p. 69.

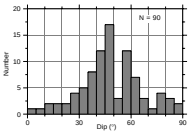

F25. Dip of fault vs. plunge of corresponding slickenlines at Site 1108, p. 70.

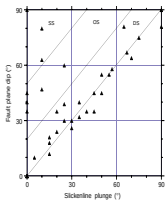

F26. Diagram of vertical transition from intact silty material to fragmented facies, p. 71.

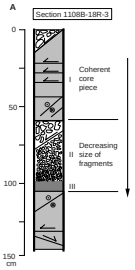

Domain IV

The boundary between Domains III and IV also corresponds to a well-marked lithologic and deformational limit. In Domain IV, the coarser grained and more competent turbiditic sandstones of lithostratigraphic Subunit IVA (Fig. F21) exhibit less intense fracturing and dip at shallower angles (<10°) (Fig. F22). As a result, Cores 180-1108B-22R through 37R (197.2 to 350.5 mbsf) show intervals of mostly coherent and intact sandstones as long as 50 cm. Along this zone the only significant deformation consists of a system of horizontal joints that are likely to represent drilling-induced disturbances, probably reactivating primary sedimentary anisotropies.

From Section 180-1108B-36R-1 (331.3 mbsf) to the top of Section 38R-1 (350.5 mbsf), the basal part of Domain IV is characterized by an increase in minor brittle fracture deformation. In some places, the core surface splits into coherent pieces, a few decimeters in length, along striated vertical fault planes displaying either dip-slip or strike-slip displacements (Sections 180-1108B-36R-2 [332.3 mbsf], 37R-2 [342.1 mbsf], and 37R-3 [343.5 mbsf]). The limit between Domains IV and V is placed on top of Section 180-1108B-38R-1 (350.5 mbsf), below which we note a significant change in the density of the brittle structures, as well as a pronounced lithologic variation, passing downward from coarse-grained sandstones into fine-grained silt/clay material (see "Lithostratigraphy," p. 6).

Domain V

Domain V can be subdivided into three structural subdomains according to lithologic and tectonic criteria.

Subdomain Va, restricted to Section 180-1108B-38R-1, corresponds to a highly fragmented zone that contains randomly arranged decimeter- to centimeter-sized angular blocks of fine-grained silt/clay material. This brecciated zone comprises two decimeter-thick horizontal bands showing a strongly preferred orientation of fissility or fracture planes. These pervasive flat-lying surfaces enclose centimeter- to millimeter-thick pieces of clay with polished and highly striated surfaces. This fabric is similar to scaly fabrics that might result from a horizontal layer-parallel shearing, coeval with brittle normal faulting.

Subdomain Vb extends from Section 180-1108B-39R-1 (360.1 mbsf) to Section 44R-1 (408.2 mbsf) and comprises horizontally bedded, dominantly coarse-grained sandstones exhibiting little tectonic deformation. A few examples of normal faults were observed, such as a minor steeply dipping fault set, as illustrated in Figure F27 (Section 180-1108B-44R-1). In fact, the most prominent structures of Subdomain Vb correspond to curve-shaped fractures, largely developed at Sections 180-1108B-39R-1, 40R-1 and 40R-2 (370.7 mbsf), 42R-4 (391.0 mbsf), and 44R-1 (408.2 mbsf); these are likely to be drilling induced.

Subdomain Vc extends from Core 180-1108B-45R (417.8 mbsf) to the base of the cored section. It is composed of coarse-grained sandstones, locally highly fragmented, with an average dip of ~15° (Fig. F22). The nature of the transition from this inclined sequence to the almost horizontal overlying series is not clear, but it may represent a progressively fanning dip pattern, or an abrupt fault-induced feature.

We observed only a few examples (~10) of filled vein/fracture structures cutting through the section drilled at Site 1108. These structures are expressed by either millimeter-thick open fractures or normal and

F27. Array of dipping normal faults in laminated sandstone, p. 73.

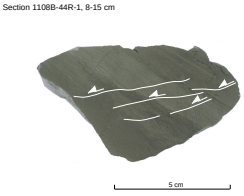

strike-slip fault planes commonly filled with carbonates in association with epidote. Figure F21 shows that most of the filled vein/fracture pattern occurs in the basal half of the unfaulted Domain IV. So far, no particular spatial or time relationships have been observed between the different vein/fracture-filled systems.

Discussion

The 485-m-long vertical section drilled at Site 1108 penetrated two structural domains that exhibit typical characteristics of fault zones, namely the Domains III and V. According to the kinematics of most of the core-scale structures observed within these two fault zones, they are both confidently interpreted as dominantly extensional. A schematic structural diagram of the entire drilled section is shown in Figure F28A. Because of poor core recovery along the faulted contacts, the exact nature and geometry of these fault zones remain conjectural.

F28. Sketch of a vertical section drilled at Site 1108, p. 74.

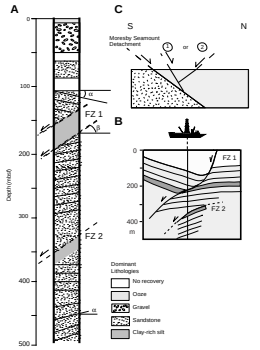

Domain III forms the shallowest fault zone (labeled FZ1), is ~40 m thick, and is developed throughout a fine-grained, clay-rich silty sequence separating two thick packages of less deformed and more competent sandstones. At a first approximation, its specific location with respect to the general lithostratigraphy illustrates that, as usually stated for any given deformed rocks, grain size represents an important factor in the distribution of brittle strain, the finer grained material being the locus of major deformation. Postcruise physical properties measurements should help to determine the extent to which additional factors such as the porosity (function of the ratio clast/matrix) have played a key role in the deformation process. Within the fault zone itself, deformation is mainly accommodated by brittle failure along discrete moderately dipping normal faults. The close association of this extensive fault/fracture network with widely distributed brecciated facies, of supposed tectonic origin, suggests a heterogeneous vertical distribution of brittle strain toward narrow, higher strained bands.

Quite similar conclusions can be reached about the second fault zone (FZ2), the base of which should occur below the end of the drilled section (Fig. F28A). First, its upper limit is also seen to put into contact the little-deformed sandstones series of its hanging wall with highly deformed clayey silts lying in the footwall. There, the occurrence of two thin flat-lying bands with more pervasive "scaly" fabric that pass vertically into highly brecciated levels, and then into fragmented material, leads us to suggest a model of brittle deformation involving a concentration of strain along discrete zones, probably reactivating primary sedimentary planar anisotropies. The development of these flat-lying deformed bands within the FZ2 extensional fault zone remains to be explained.

For both FZ1 and FZ2, the top of the fault zone coincides with a pronounced change in some physical properties measurements, as indicated, for example, by a decrease of the bulk density (see "Physical Properties," p. 35). On the other hand, the importance of FZ1 is emphasized (1) by the anomalous trend of the depth/porosity curve, indicating that part of the upper stratigraphic units at Hole 1108B has probably been removed by both erosion and faulting (see "Physical Properties," p. 35); (2) by an inflection of the in situ temperature curve in the depth interval 100–164 mbsf (see "In Situ Temperature Measurements," p. 42); and (3) by a 0.6-Ma age offset in the magnetostratigraphy between Cores 180-1108B-18R and 19R (see

"Magnetostratigraphy," p. 29), which have the greatest number of fractures and microfaults (Fig. F21).

On the interpretative model of Figure F28B, the highest dips measured in the hanging wall of FZ1 are tentatively interpreted in terms of tilt-related rotations, although the mutual relationships between the boundary fault plane and the hanging-wall inclined strata are difficult to determine because of poor recovery.

Interpretation of paleomagnetic measurements might supply reliable constraints for reorienting the core structures to geographical coordinates. These constraints could more specifically determine the synthetic or antithetic position of the faults identified at Site 1108 with respect to the Moresby Seamount detachment system (Fig. F28C).

BIOSTRATIGRAPHY

Introduction

Biostratigraphic assignments were made to core-catcher and other selected samples using calcareous nannofossils and planktonic foraminifers. Figure F29 shows a summary of biozonal assignments. Paleobathymetry estimations were made using benthic foraminifer assemblages (see "Biostratigraphy," p. 18, in the "Explanatory Notes" chapter).

F29. Planktonic foraminifer and calcareous nannofossil zones, Hole 1108B, p. 75.

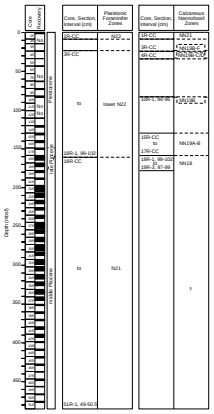

Calcareous Nannofossils

Abundance and Preservation

Samples from Core 180-1108B-1R contain common to abundant, well-preserved nannofossils. Core 180-1108B-2R was not recovered. Samples 180-1108B-3R-CC and 4R-CC contain rare to few, moderately to poorly preserved, nannofossils. Samples 180-1108B-5R-CC, 8R-CC, and 9R-CC are barren, and there was no recovery of sediment in Cores 180-1108B-6R and 7R. Core 180-1108B-10R contains a rare, moderately to poorly preserved assemblage. There was no recovery in Cores 180-1108B-11R, 12R, and 13R; and Sample 180-1108B-14R-CC is barren. Nannofossils in Cores 180-1108B-15R to 19R range from rare to abundant (mostly few) and are moderately preserved. Nannofossil abundance and quality of preservation decline markedly from Core 180-1108B-20R downward. Samples containing nannofossils are mostly rare to few in abundance, with an occasional sample containing common nannofossils. Preservation is moderate to poor. Numerous barren samples, or samples with only trace amounts of nannofossils, occur in the interval from Core 180-1108B-20R downward.

We noted a normal amount of reworking of older species throughout the sampled interval (Cores 180-1108B-1R through 51R).

Zonation

Table T5 shows the distribution of the index species and other selected species. This table was prepared during shipboard investigation and does not list all species present in a given sample. The uppermost core, 180-1108B-1R, is in nannofossil Zone NN21, based on the presence of *Emiliania huxleyi* (Fig. F29). Sample 180-1108B-3R-CC contains *Gephyrocapsa oceanica* and *Pseudoemiliania lacunosa,* indicating the Pleis-

T5. Distribution of calcareous nannofossils, p. 119.

tocene Subzonal interval NN19B–F. We found single specimens of *Discoaster brouweri* (Pliocene), *Sphenolithus abies* (Pliocene), and *Calcidiscus macintyrei* (early Pleistocene) in this sample, which we consider to be reworked. Sample 180-1108B-4R-CC is in the Subzone NN19B-C/D interval based on the last occurrence (LO) of *Helicosphaera sellii*.

Calcidiscus macintyrei and *G. oceanica* co-occur in Sample 180-1108B-10R-1, 94–96 cm, indicating Subzone NN19B. We assign Samples 180-1108B-15R-CC to 17R-CC to the subzonal interval NN19A–B, based on the presence of *C. macintyrei, Gephyrocapsa caribbeanica, G.* aff. *G. oceanica* (early, nontypical forms), and the absence of *D. brouweri*. The first downhole *D. brouweri* is found in Sample 180-1108B-18R-1, 99–102 cm. This LAD of *D. brouweri* marks the top of Zone NN18 (late Pliocene). Zone NN18 is present from Section 180-1108B-18R-1 down to Sample 180-1108B-19R-3, 97–99 cm. Specific zonal indicators are absent below that level because of generally poor preservation of the assemblages.

Planktonic Foraminifers

Preservation and Abundance

Planktonic foraminiferal assemblages varied from well preserved and abundant in Sample 180-1108B-1R-CC to recrystallized, poorly preserved, and rare in Sample 180-1108B-31R-CC, with the majority of the assemblages size sorted toward the larger specimens, moderately preserved, and common to few in abundance. The core catchers of Cores 180-1108B-2R, 4R, 5R, 19R, 22R, 23R, 36R, 38R, 42R, 43R, 45R, and 49R through 51R were barren of foraminifers. Cores 180-1108B-6R, 7R, and 11R through 13R were not recovered.

Zonation

Table T6 shows the stratigraphic distribution of species. The planktonic foraminiferal zonation is presented in Figure F29 and described below:

T6. Distribution of planktonic foraminifers, p. 121.

- Zone N23 (late Pleistocene–Holocene) is recognized in Sample 180-1108B-1R-CC by the presence of *Bolliella calida* and *B. adamsi*. *Globorotalia truncatulinoides* is rare in Sample 180-1108B-1R-4, 4–6 cm.
- Zone N22, lower part (early Pleistocene or late Pliocene) is recognized in Sample 180-1108B-3R-CC through 18R-1, 99–102 cm, by the spotty occurrences of *Globorotalia crassaformis hessi* with *G. tosaensis* and *G. truncatulinoides*. The last occurrence of *Globigerinoides fistulosus* (LAD 1.6 Ma) in Sample 180-1108B-16R-CC, 7–10 cm, lies just above the Pliocene/Pleistocene boundary.
- Zone N21 (middle to late Pliocene) is recognized from Sample 180-1108B-18R-CC through Sample 180-1108B-51R-1, 49–50.5 cm, the bottom of the hole. The upper boundary is drawn below the first occurrence of *Globorotalia truncatulinoides*. *Globorotalia tosaensis* occurs throughout this interval to the bottom of the hole.

Benthic Foraminifers

Paleobathymetry

Hole 1108B was drilled in a water depth of 3177 m. Coring revealed a benthic foraminiferal assemblage consistent with this lower bathyal depth in the youngest foraminiferal zone, N23 (Sample 1108B-1R-CC). Species represented include *Fontbotia wuellerstorfi, Melonis affinis, Neouvigerina ampullacea, Nuttallides umbonifera, Parrelloides bradyi, Pseudoparrella exigua,* and *Pullenia bulloides*. This full complement of lower bathyal species was not found in the remainder of the cores from this site, principally because of size sorting and the admixture of shallower dwelling species transported in turbidites, and possibly a different paleoenvironment in the lowest part of the cored section.

Interspersed with samples in which the benthic foraminifers are predominantly shelf (neritic) or higher slope (upper and middle bathyal) species are samples containing lower bathyal species, which indicates that the turbidites were deposited in deep water. The planktonic assemblages, which are mostly size sorted, contain species such as *Sphaeroidinella dehiscens* and *Globorotalia tumida* that live at 200–300 m depth in the upper water column. These species do not occur in inner neritic deposits, thus supporting the interpretation presented here that no part of the recovered section is indicative of shallow-water paleodepths.

A brief summary of the in situ and derived assemblage paleobathymetry of samples recovered from Hole 1108B and the key species upon which the interpretation is based follows:

- Sample 180-1108B-1R-CC (N23). Lower bathyal (>2000 m) in situ benthic foraminifers as described above, with no admixture of species from shallower water.
- Sample 180-1108B-10R-CC (lower N22). *Bolivina robusta* and *B. karreriana* transported from middle bathyal (~500–1500 m).
- Samples 180-1108B-14R-CC through 16R-CC (lower N22). Species transported from inner neritic depths (<50 m) include those of *Amphistegina, Baculogypsina, Calcarina, Elphidium, Heterostegina,* and *Operculina*.
- Samples 180-1108B-17R-CC, 18R-1, 99–102 cm (lower N22), and 18R-CC (N21). In situ lower bathyal species of *Fontbotia, Hoeglundina, Laticarinina,* and *Oridorsalis*.
- Sample 180-1108B-20R-CC (N21). Species transported from inner neritic depths, including those of *Amphistegina, Calcarina, Elphidium,* and the miliolids.
- Samples 180-1108B-21R-CC, 24R-CC, and 25R-CC (N21). Rare benthic foraminifers.
- Samples 180-1108B-26R-CC through 33R-CC (N21). Transported inner neritic *Amphistegina, Elphidium, Operculina,* miliolids, *Pseudorotalia,* and *Lugdunum schwagerianum* (Samples 180-1108B-26R-CC and 32R-CC). Admixture with bathyal species *Globocassidulina subglobosa* in Sample 180-1108B-27R-CC.
- Sample 180-1108B-34R-2, 91–92 cm (N21). In situ lower bathyal species, including *Ceratobulimina pacifica, Fontbotia wuellerstorfi, Gyroidinoides* sp., *Pullenia bulloides,* and *Uvigerina hispida*.
- Samples 180-1108B-36R-CC, 37R-CC, and 40R-CC (N21). Species transported from inner neritic depths including those of *Amphistegina, Elphidium,* and *Operculina,* admixed with bathyal *Fontbotia, Globocassidulina,* and *Oridorsalis* in Sample 180-1108B-40R-CC.

Sample 180-1108B-44R-1, 84–85 cm (N21). Low-oxygen/high–organic carbon environment dominated by globobuliminids.
Sample 180-1108B-44R-CC (N21). Middle to lower bathyal benthic assemblage with *Ceratobulimina pacifica*, *Gyroidinoides*, and *Pyrgo*.
Sample 180-1108B-48R-2, 6–8 cm (N21). Low-oxygen/high–organic carbon environment dominated by globobuliminids.

Sediment Accumulation Rate

Figure **F30** shows the estimated sediment accumulation rate at Site 1108, based on foraminiferal and nannofossil datums and magnetic chrons and subchrons. The calculated sedimentation rate for the interval from the present to 1.25 Ma is 15 m/m.y. However, much of the section may be missing in this interval (removed by erosion or slumping; see **"Erosion Estimates,"** p. 20 in the "Leg 180 Summary" chapter), making the actual sedimentation rate higher. The rate from 1.25 to 1.71 Ma is estimated to be 138 m/m.y.; the rate from 1.71 Ma to 1.95 is estimated to be 324 m/m.y. The apparent sedimentation rate from 1.95 to 2.58 Ma is 18 m/m.y., but the presence of a normal fault at ~165 mbsf between Cores 180-1108B-18R and 19R (inferred from structural, temperature, and inorganic geochemistry measurements) and the high sedimentation rates surrounding this interval, make the interpretation that ~200 m of section has more likely been displaced by the fault. Excluding this discontinuity, the sedimentation rates progressively increase downsection. From 2.58 to 3.04 Ma, the rate is estimated to be 409 m/m.y.; from 3.04 to 3.22 Ma, it is estimated to be 378 m/m.y.

F30. Age-depth relationship at Site 1108, **p. 76.**

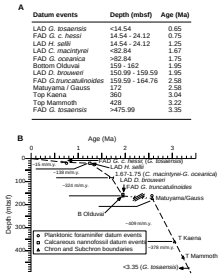

PALEOMAGNETISM

The investigation of magnetic properties at Site 1108 included the measurement of bulk susceptibility of whole core sections, point susceptibility and remanent magnetization of archive-half core sections, and magnetic susceptibility and its anisotropy and remanent magnetization of discrete samples. The RCB drilling throughout the hole prevented orientation of cores using the tensor tool. There was no recovery from Hole 1108A; only data from Hole 1108B are reported here.

Magnetic Susceptibility

Magnetic susceptibility measurements were made on whole core sections as part of the MST analysis (see **"Magnetic Susceptibility,"** p. 39). Susceptibilities (bulk volume; uncorrected) were relatively high, on the order of 10^{-3} SI. Some horizons showed higher values on the order of 10^{-2} SI. Susceptibility spikes throughout the hole correlated well with medium- to coarse-grained layers (see **"Physical Properties,"** p. 35). In general, susceptibility data from the MST and AMST analyses agreed; differences in magnitude can be attributed to volume differences for the uncorrected data (Fig. **F31**).

Initial mean susceptibilities of discrete samples were generally on the order of 10^{-3} SI, consistent with the MST and AMST data on long cores. The mean susceptibility, the degree of anisotropy (P_j) and the shape parameter (T) for the susceptibility ellipsoid (Jelinek, 1981), and the inclination of the minimum axis of the susceptibility ellipsoid (K_{min}) with bedding dips are shown vs. depth in Figure **F32.** Above ~140 mbsf, P_j values were ~1.05 and increased slightly with depth. Below ~200

F31. Susceptibility data for Hole 1108B from long-core measurements, **p. 77.**

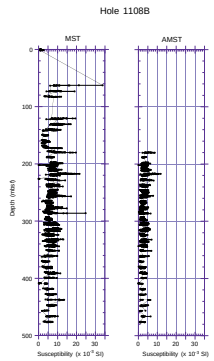

F32. AMS data for discrete samples from Hole 1108B, **p. 78.**

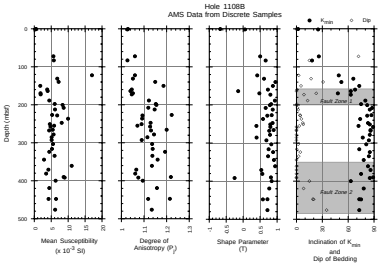

mbsf, P_j values remained relatively constant, ranging between 1.05 and 1.20, which reflected a relatively high degree of anisotropy. Nearly all samples showed positive T values higher than ~0.5, which indicated an oblate ellipsoid. Prolate ellipsoids were indicated for four samples with negative or near-zero T values. Two of the samples with prolate ellipsoids were from sections showing drilling-related deformation (flow-in) near the top of the cores. The remaining two from ~160 and 390 mbsf, respectively, were located within fault zones that were interpreted from structural data (see "Structural Geology," p. 19). Bedding dips and inclinations of K_{min} axes without structural correction showed a strong correlation: K_{min} was very steep where bedding was horizontal, and shallowed where bedding steepened (Fig. F32). All samples between ~200 and 400 mbsf showed very steep K_{min} axes and, with the exception of the anomalous ones at 160 mbsf and 390 mbsf, showed oblate ellipsoids, which suggested that the anisotropy data dominantly reflected a primary magnetic fabric related to sediment compaction (Tarling and Hrouda, 1993).

Remanent Magnetization

Measurement of remanent magnetization was made on all but the most disturbed archive-half core sections recovered from Hole 1108B. Forty-four discrete samples from working-half sections were demagnetized by alternating field (AF) in six steps up to 25 mT.

Demagnetization behavior of discrete samples generally showed two components of magnetization (Fig. F33). The soft component, which was removed by 20 mT AF demagnetization, showed inclinations that were either steep downward or shallow downward, which probably represents an overprint acquired from the drill string (Fig. F33A, F33B, F33D). For some samples with a reversed polarity characteristic remanent magnetization (ChRM) (i.e., downward inclination; Fig. F33C), an overprint from the present dipole field (PDF; I ~–32° based on the 1980 isocline chart shown in Merrill and McElhinny, 1983, p. 19) or from the geocentric axial dipole (GAD) field (I ~–19°) could have contributed to the shallow and down direction of the soft component.

Intensity of remanent magnetization of long cores after AF demagnetization at 20 mT increases with depth between ~120 and 200 mbsf, from values on the order of 10^{-3} A·m^{-1} up to values on the order of 10^{-2} A·m^{-1}; after which the intensity decreases to values on the order of 10^{-3} A·m^{-1} with a few narrow horizons showing higher values. Intensities of discrete samples were consistent with those from long cores (Fig. F34A). A similar trend was not observed in the magnetic susceptibility, which decreased from ~120 to 175 mbsf, and then abruptly increased around 180 mbsf and again around 220 mbsf, punctuating lower susceptibilities between these depths (Fig. F31). Other horizons below 220 mbsf also show abrupt susceptibility increases, most of which seem to correlate with the occurrence of coarser grained horizons (see "Magnetic Susceptibility," p. 39). The disagreement between the trends of remanent intensity and magnetic susceptibility suggests that the magnetic minerals that carry the remanent magnetization differ from those that dominate the magnetic susceptibility.

Although intensities were high, poor recovery from an unstable depositional environment (i.e., turbidites and faults), coupled with extensive core disturbance related to RCB drilling, precluded the compilation of a complete magnetostratigraphy. However, relatively undisturbed

F33. AF demagnetization behavior of discrete samples from core sections, p. 79.

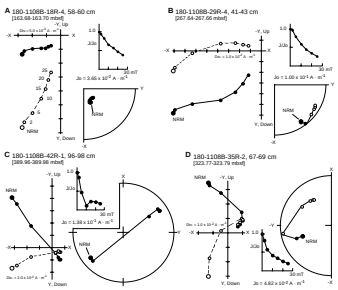

F34. Downhole plots of magnetostratigraphic and paleontologic data, Hole 1108B, p. 80.

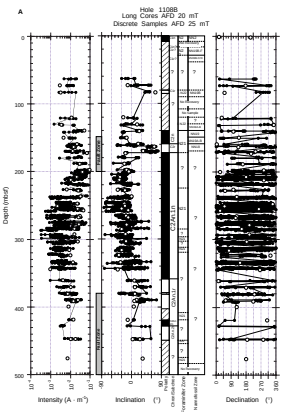

segments of lithified sediment from many core sections yielded a stable magnetic component after AF demagnetization that allowed magnetic polarities to be determined.

Inclinations of the remanent magnetization show relatively large scatter, particularly between sections and occasionally within sections. In addition, inclinations expected at the site from a GAD field are shallow (~19°) so that incomplete removal of secondary components or tilting of bedding could affect the polarity interpretation. Declinations are highly scattered, primarily as the result of the RCB drilling process, which precluded their use for magnetostratigraphic interpretation.

Magnetostratigraphy

The polarity of the remanent magnetization after AF demagnetization at 20 mT was determined primarily from the inclinations. Although scatter between sections was relatively high, biases within the inclination data from long cores, corroborated by discrete sample analysis, facilitated the polarity interpretation. The time scale used was that of Berggren et al. (1995).

Interpreting polarities based on inclinations was hampered because of many factors: (1) the low latitude of this site (an inclination of ±19° is expected from the geocentric axial dipole model); (2) the possible incomplete removal of a steep downward magnetic overprint; (3) the unstable nature of the depositional environment (i.e., turbidites and faults); (4) the core disturbance caused by RCB drilling; (5) the lack of transition data exacerbated by generally poor recovery; and (6) the lack of dip azimuth and core orientation information. In spite of these obstacles, polarity zones could be assigned to much of the section below 150 mbsf, based primarily on inclination data in conjunction with the paleontologic data (see **"Biostratigraphy,"** p. 24).

The Brunhes/Matuyama polarity transition (0.78 Ma) was not preserved in these sediments. Limited data between 0 and 120 mbsf was due to extremely low core recovery. Paleomagnetic data showed steep negative directions attributed to flow-in disturbance throughout Core 180-1108B-1R. Therefore, interpretation of a small portion of the Brunhes at the top of the hole was based solely on the paleontologic data (Figs. **F34A, F34B**).

Above ~140 mbsf, polarity interpretation was generally unclear (Fig. **F34A**); however, reversed polarities were observed between ~82 and 84 mbsf. In conjunction with the paleontologic data, the interval between ~30 and 140 mbsf was interpreted as part of the Matuyama reversed polarity chron, which ranges in age between 0.78 and 1.77 Ma (C1r). The base of the upper Matuyama Chron, however, was not clearly defined. The normal polarity zone between 142 and 159–162 mbsf probably represents part of the Olduvai Subchron (C2n; 1.77 to 1.95 Ma), which is consistent with the paleontologic data. The termination of the Olduvai Subchron, however, is not clearly defined. Reversed polarities occur between 159–162 and 172 mbsf, which lies within the zone of a normal fault (see **"Structural Geology,"** p. 19). The simplest interpretation based on the paleomagnetic data and the paleontologic data suggests that this region lies within the lower part of the Matuyama reversed polarity chron (C2r), which ranges in age between 1.95 and 2.58 Ma. Unexpectedly steep inclinations in the 159–172 mbsf interval might be related to tilting associated with faulting.

Between ~172 and 345 mbsf, a dominantly normal polarity interval occurs. The paleontologic data are sporadic throughout this interval,

but they indicate an extended N21 zonation (see "Biostratigraphy," p. 24). Of key importance for interpreting the magnetostratigraphy is the occurrence of nannofossil Zone NN18 near the top of the 172–345 mbsf interval, with Zones NN19A–B directly above Zone NN18. Consequently, this interval probably represents the upper part of the Gauss normal polarity chron (C2An.1n; 2.58 to 3.04 Ma).

Shallow reversed polarities are found between ~360 and 400 mbsf, which lies partially within and directly above another fault zone (see "Structural Geology," p. 19); however, bedding attitudes in this zone were horizontal, suggesting that little deformation has occurred. The top of this interval may represent the termination of the Kaena Subchron (C2An.1r; 3.04 Ma), which is consistent with the paleontologic data. At ~428 mbsf, normal- to reversed-polarity transitional data were observed; this may represent the transition between C2An.2n and C2An.2r (termination of the Mammoth Subchron; 3.22 Ma), below which apparently reversed polarities occur.

INORGANIC GEOCHEMISTRY

The interstitial water (IW) sampling program at Site 1108 was initially designed to obtain a high-resolution profile of pore-water constituents throughout the sedimentary column. However, poor recovery, the occurrence of heavily indurated sediments, and subsequent drilling difficulties deeper downhole resulted in the collection of only 13 whole-round samples. The 5-cm whole rounds that were collected rapidly became insufficient to produce enough IW to conduct the routine shipboard analyses, therefore, as much as 15-cm whole rounds were collected from cores recovered in the deeper portions of the hole. Three whole-round core samples failed to produce any pore water, even upon extended squeezing (12–24 hr) at the maximum pressure available on the Carver press.

Results

The IW was analyzed for salinity, pH, alkalinity, major cations (Na^+, K^+, Ca^{2+}, Mg^{2+}) and anions (Cl^-, SO_4^{2-}), SiO_2, Sr^{2+}, and Li^+. Because generally less than 10 mL of IW was recovered from the whole-round core sections, the alkalinity was only determined in four samples to allow time for other more critical analyses. Results of shipboard inorganic chemical analyses are presented in Table T7. For reasons described in "Interstitial Water Sampling and Geochemistry," p. 23, in the "Explanatory Notes" chapter, pH measurements presented here should be considered only semiquantitative.

T7. Hole 1108B interstitial water geochemistry, p. 122.

The titration alkalinity at Site 1108 is near 3.2 meq/L in the shallowest two core samples (Cores 180-1108B-1R and 10R) and then drops to ~1 meq/L in the two other samples analyzed for this constituent (Table T7).

Salinity decreases between 0.7 and 83 mbsf and then increases downhole with a maximum of 39 observed at ~392 mbsf. The slightly lower salinity (33) observed at 83 mbsf can be attributed primarily to a depletion of SO_4^{2-} because no decrease in Na^+ or Cl^- is observed in this section. Sulfate displays a rapid depletion downhole, with 75% depletion observed by 83 mbsf, the depth where headspace analyses reveal that CH_4 concentrations become elevated (see "Organic Geochemistry,"

p. 33). Although SO_4^{2-} returns to near 18 mM at 164 mbsf, complete depletion of this constituent is observed below this depth. The IW analysis at 164.5 mbsf also corresponds to the core in which the $CaCO_3$ maximum was observed (see "Organic Geochemistry," p. 33) and is within the fault zone identified between 160 and 220 mbsf ("Structural Geology," p. 19); this anomalous SO_4^{2-} concentration is puzzling and may be related to a fluid input along the fault zone.

Concomitant with the increase in salinity observed downhole, Na^+ and Cl^- concentrations increase, reaching maxima of ~500 and 678 mM, respectively, at 392 mbsf. (Fig. F35). Dissolved K^+ concentrations, however, decrease downhole from near seawater values (12 mM) immediately below the mudline to a minimum of 2.7 mM at 304 mbsf, then fluctuate slightly below this depth.

The dissolved Li^+ profile at Site 1108 shows substantial variations over the range of 20–136 µM (Table T7; Fig. F35). Immediately below the mudline, near-seawater concentrations decrease to a minimum of 20 µM at 83 mbsf. Elevated values (43–63 µM) are observed in sediments near the fault zone identified between Cores 180-1108B-18R and 19R, but Li^+ concentrations subsequently decrease to near-seawater values by 202 mbsf. Below this depth, Li^+ increases steadily downhole and reaches a maximum of 135 µM at 392 mbsf. Within sediments near the fault zone, the Li^+ concentration is relatively low (43 µM) in the interval coinciding with the $CaCO_3$ maximum, but nearly 50% more concentrated (62 µM) immediately below in the interval containing approximately half as much $CaCO_3$ (see "Organic Geochemistry," p. 33).

Calcium (Fig. F35) increases from a near-seawater concentration in the first IW sample to a local maximum of 46.4 mM at 267 mbsf, with a slight reversal noted in Section 180-1108B-33R-1 (304 mbsf). Magnesium generally displays a trend opposite that of Ca^{2+}, decreasing from a near-seawater value at 0.7 mbsf to a minimum of 18.4 mM at 267 mbsf. A slight reversal of the concentration trend for these constituents is observed below this depth, but the initial trend returns in the deeper portion of the hole. The Sr^{2+} profile exhibits an order of magnitude increase between the mudline and 202 mbsf, with the largest increase to 759 µM between 165 and 202 mbsf. Below this depth, Sr^{2+} concentrations decrease to 225 µM in the deepest sample analyzed for this constituent (344 mbsf).

Dissolved SiO_2 displays a substantial increase over seawater below the mudline, reaching 374 µM at 83 mbsf, then decreases downhole, remaining in a narrow range of 140–180 µM to the bottom of the hole.

F35. Interstitial water constituents, Site 1108, p. 83.

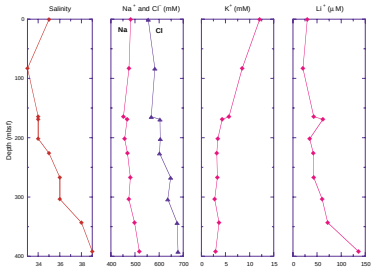

Discussion

Although insufficient inorganic geochemical data were collected to fully characterize sedimentary diagenesis caused by a paucity of available fluid, the SO_4^{2-} profile, when combined with the CH_4 profile obtained in the upper section of Hole 1108B by the organic geochemistry program, indicates that these constituents reflect bacterially mediated oxidation of organic matter (e.g., Claypool and Kaplan, 1974; see "Microbiology," p. 34). Extensive depletion of SO_4^{2-} below 83 mbsf coincides with the rise in CH_4 concentrations observed in headspace analyses (see "Organic Geochemistry," p. 33). The 18-mM SO_4^{2-} concentration observed at 164 mbsf, however, is difficult to explain in terms of an input of seawater because other major dissolved constituents do

not display more seawater like signatures. However, an input of previously altered seawater extant within the fault could readily explain the anomalous concentrations observed here. Furthermore, all IW constituent profiles, except salinity, display an offset at 169 mbsf relative to the 164 mbsf sample, attesting to nonsteady state or normal diffusive profiles within this active zone.

The characteristics of the IW at Site 1108 suggest sedimentary diagenesis under a mildly elevated temperature regime (see **"In Situ Temperature Measurements,"** p. 42). The principal processes at Site 1108 responsible for the observed pore-water profiles include the alteration of volcanic matter and the formation of clay minerals. Evidence in support of this hypothesis includes an increasing Ca/Mg value (Fig. **F36**) with increasing depth below seafloor attributable to a release of Ca^{2+} from the alteration of plagioclase and a concomitant uptake of Mg^{2+} from pore water during the formation of chlorite/smectite (McDuff and Gieskes, 1976; McDuff, 1981; Martin et al., 1995), and increasing dissolved Li^{+} concentrations in the deeper portions of Hole 1108B. Although the slight reversal in the trend of decreasing Mg^{2+} and increasing Ca^{2+} concentrations observed at 303 mbsf could possibly arise from contamination with seawater during drilling; a lack of a return to more seawater-like concentrations of other pore-water constituents in this interval suggests this is not the case. Rather, the presence of calcite cements in various portions of the cores suggests that precipitation of this mineral may have influenced the concentration of dissolved Ca^{2+}. A continued influence of volcanic matter on the alkaline earth profiles downhole is suggested by the return to the original trend observed above 303 mbsf. A generally linear decrease in the concentration of K^{+} downhole is consistent with its uptake from pore water during the formation of clay minerals resulting from the alteration of volcanic matter (Gieskes, 1981). The large increase in dissolved Sr^{2+} at Site 1108 can be attributed to either (1) release to pore water during the recrystallization of biogenic carbonate, especially aragonite (Baker, 1986), and/or (2) release during the alteration of volcanic ash/glass (Gieskes, 1981). Aragonite is not particularly abundant in the sediments of Site 1108, but the dissolved Sr^{2+} maximum at 202 mbsf is consistent with the presence of shell fragments within Core 180-1108B-22R (see **"Lithostratigraphy,"** p. 6). Nonetheless, alteration of volcanic minerals dispersed throughout the sediments also likely contributes some of the dissolved Sr^{2+} in the pore water from Site 1108. The downhole decrease in Sr^{2+} observed in IW from the lower portion of the sedimentary column is consistent with a lack of ash layers that could act as source material for this constituent, although plagioclase remains an important mineral constituent throughout the sedimentary column (see **"Lithostratigraphy,"** p. 6).

Variations in SiO_2 concentrations often reflect reactions under local lithologic control to a much greater extent than those of other IW constituents such as Mg^{2+}, Ca^{2+}, and Sr^{2+}, which often display diffusion-controlled profiles and reflect diagenesis of the sedimentary column as a whole (McDuff, 1981). Although high dissolved SiO_2 concentrations often arise when volcanic glass is altered in sediments, IW from Site 1108 generally contains <200 µM SiO_2, except in the upper 100 mbsf. Dissolved SiO_2 concentrations in marine sediments can reflect diagenesis of biogenic silica with conversion of Opal-A to Opal-CT, followed by recrystallization to quartz, as well as reactions involving the alteration of volcanic ash/glass (Gieskes, 1981). Additionally, the local lithology

F36. Ca/Mg ratios as a function of depth in interstitial water, Site 1108, **p. 85.**

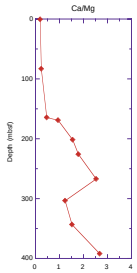

can exert a strong influence on dissolved SiO_2 profiles. Often SiO_2 profiles reveal an initial increase immediately below the mudline to ~400–600 µM that reflects dissolution of biogenic silica (Opal-A). Subsequently, recrystallization to Opal-CT and/or the alteration of volcanic glass result in elevated concentrations that can exceed 1 mM, before recrystallization to quartz or uptake by clay mineral formation removes most of the dissolved SiO_2 from the pore water. No large increase in dissolved SiO_2 is observed deeper downhole at Site 1108. The highest concentrations are observed immediately below the mudline in the sediments of lithostratigraphic Units I and II (see **"Lithostratigraphic Unit I,"** p. 7, and **"Lithostratigraphic Unit II,"** p. 8); they subsequently drop to <200 µM in lithostratigraphic Units III and IV. This observation may be consistent with removal of a significant portion of the sedimentary column at Site 1108 (see **"Lithostratigraphy,"** p. 6, **"Biostratigraphy,"** p. 24, and **"In Situ Temperature Measurements,"** p. 42), in which dissolution and recrystallization of Opal-CT and the alteration of volcanic glass/ash layers would dominate SiO_2 profiles. The abundance of clay minerals in the deep sediments at Site 1108 is also consistent with low dissolved SiO_2 concentrations (Gieskes, 1981). Although uptake of dissolved SiO_2 also occurs during precipitation of quartz (e.g., De Carlo, 1992, and references therein), it is not possible to distinguish between this process and uptake by formation of clay minerals at Site 1108 without further knowledge of the origin of the quartz found in the deeper portions of the sedimentary column.

Lithium is another element that can reflect both overall sedimentary diagenesis and localized reactions. Dissolved Li^+ generally increases with depth in deep-sea sediments (Gieskes, 1981). It is released during the diagenesis of biogenic silica and the alteration of fresh volcanic matter and can be removed from solution during the formation of clay minerals. At Site 1108 we observe fluctuations that are interpreted to derive from a combination of reactions involving clay minerals and local lithologic control, including the alteration of volcanic layers. Gieskes et al. (1983) have attributed coincident dissolved Li^+ and SiO_2 fluctuations to the diagenesis of opaline silica and an alteration of volcanic materials. However, no such correlation exists in the sediments at Site 1108. Rather, the highest dissolved Li^+ concentrations, with the exception of the local submaximum within sediments of the fault zone, occur in the deepest sections of Hole 1108B. It is thus likely that this trend reflects deep-seated water-rock reactions under an increasing thermal regime. Hydrothermal alteration of basalt, for example, is known to release Li^+ to the aqueous phase (Edmond et al., 1979). Downhole temperature measurements (see **"In Situ Temperature Measurements,"** p. 42) are consistent with this observation.

ORGANIC GEOCHEMISTRY

At Site 1108, the shipboard organic geochemistry analyses consisted of determinations of total organic carbon (TOC), inorganic carbon, total carbon, total nitrogen, and total sulfur in sediments in addition to the routine hydrocarbon gas safety monitoring procedure. The analytical techniques used are outlined in **"Organic Geochemistry,"** p. 25, in the "Explanatory Notes" chapter.

Volatile Hydrocarbons

Because of poor sediment recovery in the top section of Hole 1108B, the headspace hydrocarbon gas profiles were poorly resolved between 0 and 100 mbsf (Table T8; Fig. F37). Very low methane concentrations (~3 ppmv) were found between 0 and 72 mbsf. Below 120 mbsf, the methane levels increased to ~1000 to 60,000 ppmv and remained relatively constant throughout the rest of the hole to the last sample measured at a depth of 476 mbsf. Small quantities of ethane and propane were also detected below 120 mbsf and increased with depth (Fig. F37). Below ~400 mbsf, traces of branched and straight chain C_4 and C_5 components were detected. The increase in methane below 120 mbsf coincided with the disappearance of sulfate in the pore water (Fig. F35). This is indicative of biogenic methane. Traces of higher chain volatile hydrocarbons, together with the decrease in the C_1/C_2 headspace ratio below ~300 mbsf, indicated that a thermogenically derived gas input was present, either being generated in situ or by migration from source.

T8. Headspace gas in sediments, Hole 1108B, p. 123.

F37. C_1, C_2, and C_3 hydrocarbon profiles, p. 86.

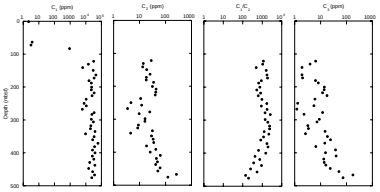

$CaCO_3$, Sulfur, Organic Carbon, and Nitrogen

Concentration of $CaCO_3$ was found to be generally below 10 wt% throughout the core, with the exception of the surface and peaks at ~150, 250, and 475 mbsf (Fig. F38). These correlate with the observed lithology. Sulfur was very low throughout the hole, averaging ~0.2 wt% (Table T4). Organic carbon was also low throughout the core, averaging ~0.5 wt%, although a peak (1.1 wt%) was seen at 131 mbsf (Fig. F38). The C/N ratio ranged mainly between 8 and 20 throughout the hole, indicating a mixed terrigenous and marine origin for the organic matter. The peak of 34 at 131 mbsf indicates a terrigenous source for the organic material. This, accompanied by the peak in organic carbon (1.1 wt%), correlates with the occurrence of fibrous material thought to be wood recovered in Section 180-1108B-15R-CC (see "Lithostratigraphy," p. 6), which could explain these excursions.

F38. $CaCO_3$, organic carbon, and C/N ratio profiles, p. 87.

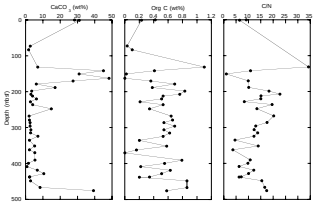

MICROBIOLOGY

Only six samples were obtained from Hole 1108B for microscopic determination of total bacterial populations. One sample was taken from the surface core, Core 180-1108B-1R, at 0.99 mbsf; poor core recovery (<4%) then precluded further sampling until Core 10R at a depth of 83.16 mbsf. Below this depth an increasing degree of induration meant that further samples were obtained from only 132.04, 150.07, 164.54, and 189.06 mbsf before microbiological sampling ceased.

Bacteria were present in all samples examined (Table T9; Fig. F39); their numbers decreased rapidly with increasing depth. In near-surface sediment, total bacterial numbers were $2.67 \cdot 10^8$ cells/cm^3 at 0.99 mbsf. Total organic carbon at 1.14 mbsf was 0.23 wt% (Table T4). Near-surface bacterial populations in Hole 1108B are similar to those at other sites with similar overlying water depths and near-surface organic carbon concentrations (Table T10).

Geochemical data provide evidence for bacterial activity in Site 1108 sediments. Pore-water sulfate was 75% depleted by 83 mbsf in Hole 1108B (Fig. F35), whereas methane concentrations increased rapidly below 121 mbsf (Fig. F37). Depletion of sulfate allows methanogenic

T9. Bacterial populations and dividing and divided cells, p. 124.

F39. Hole 1108B bacterial populations and dividing and divided cells, p. 88.

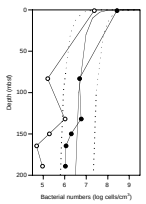

T10. Bacterial populations, depth, and organic carbon, p. 125.

bacteria to outcompete sulfate-reducing bacteria for available carbon sources. Furthermore, C_1/C_2 ratios indicate that gas production in at least the upper 350 mbsf of sediments at Site 1108 is biogenic (Table T8).

A peak in total bacterial populations, and in the number of dividing and divided cells, was observed at 132 mbsf (Fig. F39) coincident with a peak in TOC at 131.39 mbsf (1.1%; Fig. F38). The frequency of dividing and divided cells peaking at 17.6% in this depth horizon is indicative of an active bacterial community. Below this depth, organic carbon concentrations were very low (<0.02 wt% between 150 and 165 mbsf; 0.38 wt% at 189 mbsf) in a zone of calcium carbonate sandstones (17–48 wt% calcium carbonate; Table T4). Total bacterial numbers in Hole 1108B sediments were lower than the general model for bacterial populations in deep-sea sediments (Parkes et al., 1994), although still within the 95% prediction limits. Low bacterial numbers were also characteristic of low organic carbon carbonate deposits in sediments recovered from the Japan Sea during Leg 128 (Cragg et al., 1992) and the Lau Basin, Leg 135 (Cragg, 1994).

Only one whole-round core was obtained for microbiological analysis in Hole 1108B; further shore-based processing is planned to measure potential bacterial activities and cultural microorganisms.

Samples taken at Site 1108 represent the first RCB core samples analyzed for bacterial populations, and thus concerns about contamination of samples during the RCB coring process, for example by drilling mud, need to be addressed. Although acridine orange staining and subsequent epifluorescent microscopic examination of a sepiolite drilling mud sample showed that particles of sepiolite fluoresce green, as do bacterial cells, sepiolite particles and cells are easily distinguished visually. The results of microscopic enumeration of both total and dividing and divided bacteria correlate well with previously published results, which suggests that cores obtained by RCB are comparable to APC and XCB cores for microbiological studies.

PHYSICAL PROPERTIES

Introduction

At Site 1108, a comprehensive downhole profile of physical properties measurements was obtained on whole cores using the MST and on discrete samples from split cores. Even though MST data are reliable only in APC and nonbiscuited XCB and RCB cores, MST measurements were nevertheless made on all 51 RCB cores from Site 1108, irrespective of core condition. Our rationale was to obtain physical properties data in the event that geophysical logging of the borehole ultimately proved to be impossible or limited, as was the case for this site. Depending on the induration of the sediment, thermal conductivity was measured from either unconsolidated whole cores or rock slices.

Density and Porosity

Bulk density, grain density, and porosity were calculated from the wet mass, dry mass, and dry volume of each sample using the moisture and density (MAD) method for soft and semilithified sediment in Cores 180-1108B-1R through 18R (0–156.3 mbsf). Below this depth, the index properties were determined through the MAD hard-rock method. All

data are presented in Table T11 (also in also in ASCII format in the TABLES directory).

The MAD-determined bulk densities of the two near-seafloor samples (lithostratigraphic Unit I; see "Lithostratigraphic Unit I," p. 7) are 1.44 and 1.48 g·cm^{-3} (Fig. F40). Lack of recovery prevented measurement of index properties from 1.43 to 63.13 mbsf (lithostratigraphic Unit II). From 63.13 to 83 mbsf (lithostratigraphic Unit III and Subunit IVA), bulk densities were significantly higher, averaging 2.03 g·cm^{-3}. Following an interval of no recovery between 91.3 and 110.6 mbsf, bulk densities decrease to an average 1.92 g·cm^{-3} within Cores 180-1108B-16R and 17R (130–158.6 mbsf; Fig. F40), coinciding with the upper limits of an observed brittle fault zone (see "Structural Geology," p. 19). Below this depth, bulk densities increase slightly downhole. A second interval of lower bulk density is present between 350 and 400 mbsf (average values of 2.18 g·cm^{-3}) and coincides with the top of another zone of brittle deformation (see "Structural Geology," p. 19).

Little correlation exists between the bulk densities derived from direct measurement (i.e., MAD-derived densities) and the gamma-ray attenuation porosity evaluator (GRAPE) derived densities. This lack of correlation is likely a function of core fracturing, biscuiting, and a reduced core diameter, all of which affect the GRAPE-derived densities. Nevertheless, restoring the MAD-derived bulk densities onto the GRAPE-derived densities (Fig. F41) indicates that the maximum GRAPE-derived densities agree reasonably well with the MAD-derived densities, especially above ~200 mbsf. From 220 mbsf to the base of the borehole (485.2 mbsf), the maximum GRAPE-derived densities appear to be systematically lower than the MAD-derived densities by 0.2–0.3 g·cm^{-3} although the same general trends exist (e.g., the local minimum at 360–375 mbsf). We conclude that despite the large scatter within the GRAPE-derived density measurements, the maximum value either underestimates or approximates the bulk sediment density. A full compilation of GRAPE data is presented with the MST measurement data set (in also in ASCII format in the TABLES directory) on the accompanying LDEO CD-ROM.

Based on the index properties measurements, the average grain density is 2.72 g·cm^{-3} with minimum and maximum grain densities of 2.62 and 2.80 g·cm^{-3}, respectively (Fig. F40). Maximum sediment grain densities exist over a depth range of 230–300 mbsf and correlate with the thick, high-frequency, volcanogenic turbidites of lithostratigraphic Subunit IVA (see "Lithostratigraphy," p. 6). Grain densities show large scatter in the interval from 100 to 170 mbsf, varying from 2.62 to 2.75 g·cm^{-3}. Much of this scatter is attributed to variations in carbonate content (see "Organic Geochemistry," p. 33). From 170 to 270 mbsf, grain densities increase toward a maximum of 2.80 g·cm^{-3}, after which they decrease back to the average value of 2.72 g·cm^{-3} (i.e., from 270 to 380 mbsf). Below 380 mbsf, the grain density is nearly constant to the bottom of Hole 1108B (485.2 mbsf). Although thin carbonate-rich layers exist within the section, for example, at 220 and 250 mbsf (see "Lithostratigraphy," p. 6), the general variation in grain density with depth does not show a relationship with carbonate content.

Increased turbidite frequency within lithostratigraphic Subunit IVA indicates the rapid input of clastic material, as shown by the large sediment accumulation rates over the 200–380 mbsf interval (see "Sediment Accumulation Rate," p. 27). The steady increase in the percentage of relatively high density material of 2.8–3.04 Ma age

T11. Index properties, Site 1108, p. 126.

F40. Site 1108 MAD-determined porosity, bulk density, and grain density, p. 89.

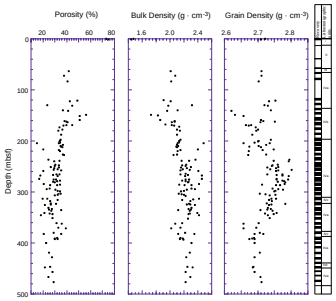

F41. Density derived from GRAPE and index properties measurements, p. 90.

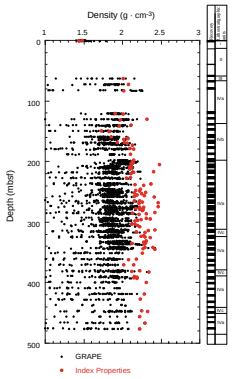

between 250 and 350 mbsf (see "Biostratigraphy," p. 24) possibly indicates the input of clastics from a different source area, such as the unroofing of the metamorphic core complexes of the D'Entrecasteaux Islands or the first denudation of mafic-rich ferromagnesium rocks from the forearc sequences (see "Lithostratigraphy," p. 6).

Porosity is calculated from the MAD index properties measurements used to determine bulk density and grain density. Consequently, the porosity curve as a function of depth mirrors that of the bulk density, with minor differences caused by variations in grain density. Porosity varies from 38% to 49% at depths of 63–122 mbsf to 20%–30% toward the base of Hole 1108B (Fig. F40). The general behavior of porosity as a function of depth for Hole 1108B is consistent with the expected negative exponential variation that characterizes normally compacting sediments. This empirical relationship is termed Athy's Law (Athy, 1930). Fitting a least-squares exponential curve to the observed porosity-depth relationship, the predicted surface porosity is 48% with a compaction decay constant of 0.0016 m^{-1} (Fig. F42A; correlation coefficient of 0.68). The inverse of the decay constant (617 m) can be physically interpreted as the depth over which porosity is reduced by a factor of ~⅓ (i.e., 1/e) of its initial value, that is, a compaction "decay depth." It is clear from this figure that the depth-porosity behavior of the deeper sediments is not consistent with the surface porosity. Further, if the surface porosity is constrained to be 78%, then the compaction decay depth must vary between 120 and 200 m to envelope the scatter of porosity with depth. Such compaction constants are unrealistically low.

Based on the regression least-squares curve shown in Figure F42A, the porosity data from Hole 1108B show an obvious discontinuity between the near-surface sediments and the remainder of the data set beginning at 63.13 mbsf. Core recovery within the 14.5–63.13 mbsf zone was poor, consisting of pebbles and rubble of basalt, gneiss, granodiorites, and sandstones (see "Lithostratigraphy," p. 6). Sediments below 63.13 mbsf have porosities inconsistent with their depth, suggesting that they may have been compacted by the weight of overlying units that have since been eroded. Sediment erosion is consistent with (1) the interpretation of reflection seismic data indicating the truncation of reflectors at the seafloor (see "Miocene–Quaternary Arc and Forearc," p. 4, in the "Background and Regional Setting" chapter) and (2) the measured high sediment velocities (e.g., 2024–2713 $m \cdot s^{-1}$ at depths of 70–130 mbsf) beneath the inferred unconformity at 62.7 mbsf. Sediment erosion could also contribute to the apparent low sedimentation rate derived from biostratigraphy (see "Sediment Accumulation Rate," p. 27). To estimate the thickness of eroded sediment, we recalculated a least-squares exponential curve, using only the porosity data between 63.13 and 485.2 mbsf. For this case, the least-squares fit predicts an initial surface porosity of 44% and the compaction decay constant translates to a decay depth of 740 m (see Fig. F42B; correlation coefficient of 0.58). Extrapolation of this porosity-depth relationship to the surface, assuming an initial porosity of 73%–75% (i.e., equal to the near-surface sediments from Hole 1108B), implies that ~385 m of sediment has been removed from a section that once existed above lithostratigraphic Unit IV in Hole 1108B.

F42. Regression least-squares exponential curves of porosity, Hole 1108B, p. 91.

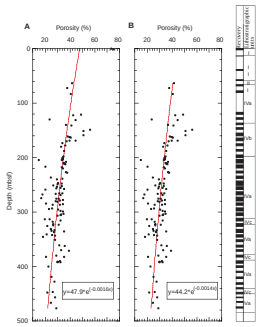

Compressional Wave Velocity

The PWS1 and PWS2 insertion probe system was used to measure the transverse (i.e., perpendicular to the core axis) and longitudinal (i.e.,

along the core axis) *P*-wave velocities in unconsolidated sediments. Sediment velocities obtained from the upper several meters of Core 180-1108B-1R (0–8.6 mbsf) yielded values between 1518 and 1527 m·s^{-1}, as expected for unconsolidated surficial sediments (Fig. F43). The PWS3 contact probe system was used to measure the *P*-wave velocity of ~10-cm^3 cube samples of semilithified and lithified sediments cut from the RCB cores. Velocities were measured in the x and y (transverse) and z (longitudinal) directions (Fig. F43). The *P*-wave logger (PWL) measured velocities from MST measurements on unsplit cores do not correlate well with those measured using the PWS1, PWS2, and PWS3 system and show extreme scatter, possibly caused by drilling disturbance. Because of the poor quality of the PWL-measured velocities, only PWS1-, PWS2-, and PWS3-derived velocities are discussed further. Below ~150 mbsf, longitudinal velocities increase from an average of 2250 to ~3000 m·s^{-1} at 380 mbsf. Curiously, velocities abruptly decrease to an average of ~2600 m·s^{-1} below 380 mbsf. High velocities, particularly those in excess of 3000 m·s^{-1}, correlate strongly with the existence of carbonate and siliceous cements (e.g., 220 and 380 mbsf). Triaxial seismic velocity measurements indicate that transverse and longitudinal velocities typically vary by less than 20%. The bias is toward lower longitudinal velocities compared to transverse velocities (i.e., across bedding, positive anisotropies; Fig. F44). A compilation of the PWS1, PWS2, and PWS3 data is located in Table T12 and in also in ASCII format in the TABLES directory.

Thermal Conductivity

As described in "Thermal Conductivity," p. 30, in the "Explanatory Notes" chapter, methods for measuring thermal conductivity depended on the degree of induration of the sediment cored. The needle probe full-space method was applicable only to Core 180-1108B-1R. Between Cores 180-1108B-2R and 14R, measurements were either not possible because of lack of recovery or unsuccessful because of the disrupted nature of the cores. From Core 180-1108B-15R to the bottom of Hole 1108B, thermal conductivity was determined using the half-space method. Because the measurements were time consuming, the number of measurements per core was reduced from one per section to one every two sections after Core 180-1108B-20R. In addition, the number of measurement repetitions on each sample was reduced from four to two in cases where results from the first two repeat measurements varied by less than 1%. The reported value is an average of the repeat measurements. Refer to Table T13 (also in also in ASCII format in the TABLES directory) for thermal conductivity data.

In the upper several meters of sediment (Core 180-1108B-1R; 0–8.6 mbsf), measured thermal conductivities were 0.8–0.9 W·m^{-1}·°C^{-1} (Fig. F45). As core conditions became conducive to preparing half-space samples for thermal conductivity measurement (i.e., deeper than 121.64 mbsf), thermal conductivities routinely exceeded 1.0 W·m^{-1}·°C^{-1}. The thermal conductivities show an overall increase downhole to ~322 mbsf, where values reach 1.7 W·m^{-1}·°C^{-1}. Below this peak, thermal conductivities remain nearly constant or decrease slightly with depth. In addition to the large-scale trends, the thermal conductivity data show variations that are probably related to lithostratigraphic changes within the turbidite sequences.

F43. Site 1108 *P*-wave transverse (x, y) and longitudinal (z) velocities, p. 92.

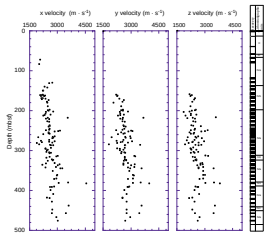

F44. Longitudinal velocity vs. the average transverse velocity, p. 93.

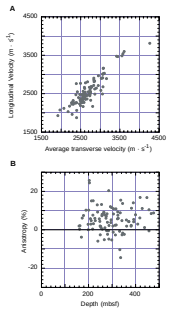

T12. Longitudinal and transverse velocities, Site 1108, p. 129.

T13. Thermal conductivity values, Site 1108, p. 131.

F45. Site 1108 thermal conductivity, p. 94.

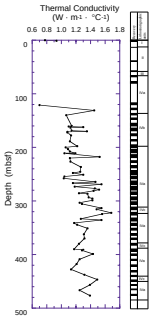

Magnetic Susceptibility

Magnetic susceptibility reflects changes in magnetic mineralogy and, as a result, is widely used as a proxy for lithostratigraphic variations. The quality of these data are degraded in XCB and RCB sections where the core may be undersized with respect to the liner diameter and/or disturbed. Nevertheless, the general downhole trends can be useful for stratigraphic correlations. The MST and AMST susceptibility data are shown in Figure F31 and the full magnetic susceptibility meter (MSM) data set can be found as part of the MST compilation (in also in ASCII format in the TABLES directory) on the accompanying LDEO CD-ROM. The AMST susceptibilities are termed point values because a smaller volume is measured compared with the MST, which uses the full uncut cores (see "Paleomagnetism," p. 27). This volume difference also explains the variation in the susceptibility amplitude between the two measurement procedures. The close correlation between the two verifies that both the spatial variation and amplitude are being successfully measured.

By comparing the magnetic susceptibility with the remanent magnetization intensity (see "Paleomagnetism," p. 27), it is possible to determine if the minerals carrying the magnetic remanence are also responsible for the susceptibility. Whereas magnetite and hematite are commonly the carriers of magnetic remanence, it is usually the clay minerals and clay content that dominate the susceptibility. The ferromagnesium–rich clays are smectite and, less frequently, chlorite. To evaluate this association for Site 1108, the magnetic susceptibility, natural gamma ray (NGR), and remanent intensity were compared (Fig. F46). No clear relationship was found between these parameters. For example, the remanent intensity maximum at 200 mbsf is not reflected in either the NGR, which increases from 190 to 210 mbsf, or the susceptibility, which tends to be relatively constant over the 190 to 215 mbsf interval. Some minor correlations do exist, such as the high susceptibility and remanence peaks at ~218 mbsf. From Figure F46 we conclude that, in general, the minerals controlling the magnetic susceptibility are different from those controlling the remanent magnetic intensity. Further, the lack of correlation between NGR and the magnetic susceptibility suggests that the clays and sands containing radioactive material are distinct from those units rich in ferromagnesium minerals.

Comparing the grain-size distribution, magnetic susceptibility, and remanent intensity on an expanded scale allows us to (1) investigate the cause of magnetic susceptibility variations, and (2) determine if a relationship exists with grain size, an observation that was made on various ODP cruises (e.g., Leg 169; Fouquet, Zierenberg, Miller, et al., 1998). In Figure F47A, the general decrease in magnetic susceptibility from 217.5 to 218.5 mbsf and many of the individual peaks appear to correlate with the location of fine to coarse sands, whereas the silts and clays tend to be associated with relatively lower values of magnetic susceptibility. Little relationship exists between the remanent magnetic intensity and magnetic susceptibility. Given that we should not expect any relationship between susceptibility and grain size, per se, Figure F47A implies that the sand fraction of the turbidite sequences most likely contains magnetic material derived from a different source region than the intervening clays. However, it is clear from Figure F47B that the sands do not always induce high magnetic susceptibility. For example, whereas the sands at 255–256.5 mbsf and 256.5–256.8 mbsf have relatively high magnetic susceptibility, the sands at 257.8–257.9 mbsf

F46. Site 1108 magnetic profiles, p. 95.

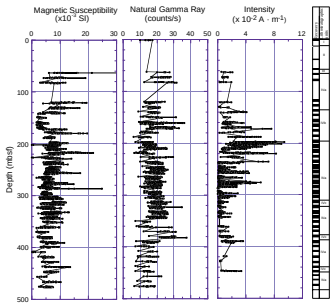

F47. Comparison between grain size and magnetic susceptibility, p. 96.

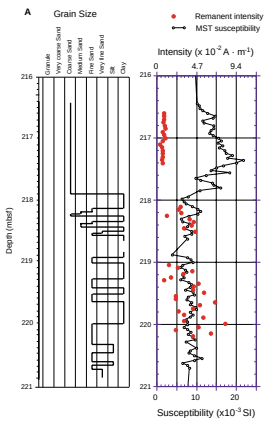

and 258–259 mbsf show no such correlation. It would seem that both the clays and the sands can contain magnetic material: smectite, chlorite, and pyritic clays, and magnetite within the sands. The mixing between magnetic and nonmagnetic clays and sands implies sediment input from multiple provenances. Magnetic and nonmagnetic carrying provinces are likely represented by the New Guinea mainland and associated islands (e.g., D'Entrecasteaux Islands) and the carbonate banks of the Trobriand platform and the Egum reef, respectively.

Natural Gamma Ray

The NGR count was recorded on the MST. A full compilation of NGR values is presented with the MST measurement data set in ASCII format on the accompanying LDEO CD-ROM. Clay minerals, being charged particles, tend to attract and bond with K, U, and Th atoms so that an increasing NGR count typically correlates with increasing clay/shale content. In contrast, sand-prone and carbonate units usually tend to be characterized by low NGR counts. These relationships can be used to define the location of shale-prone and sand-prone formations down the borehole. However, this relationship will begin to break down in poorly sorted sequences, such as volcaniclastic units and/or with peculiarities in the source region mineralogy.

The NGR data are rather noisy even though the sampling period was intentionally set high (at 28 s) to increase precision. Nevertheless, the NGR profile shows a number of general trends (Fig. **F46**). From 62 to 160 mbsf and from 170 to 200 mbsf, there are two segments of downward-decreasing NGR count separated by an abrupt increase in the NGR count between 155 and 165 mbsf. This same location has been subjected to brittle deformation (see **"Structural Geology,"** p. 19). From 200 to 250 mbsf the NGR count generally increases, followed by a segment from 250 to 340 mbsf in which the NGR count at first decreases and then increases. There is a decrease in the NGR count at 350–360 mbsf followed by an increasing segment to 380 mbsf. From 385 to 400 mbsf, there is a rapid decrease in the NGR count after which the average trend steadily decreases to the bottom of the hole (485.2 mbsf). The NGR count minimum at 180–200 mbsf and maximum at 370–380 mbsf correlate with clays at the base of lithostratigraphic Subunit IVB (see **"Lithostratigraphy,"** p. 6), and the sands and conglomerates of lithostratigraphic Subunits IVA and IVC, respectively (Figs. **F48A, F48B**). However, the clay units between 160 and 170 mbsf are also characterized by a high NGR count (Fig. **F48A**). This implies that both radioactive mineral-bearing sands and clays exist in the section. Consequently, in contrast to the typical relationship of NGR count and grain size, a decreasing NGR count with depth may indicate a coarsening upward sequence and an increasing NGR count with depth may indicate a fining-upward sequence at Site 1108. Note that other factors can also affect NGR count, such as variations in the calcium carbonate content and specifics of the clay mineralogy.

F48. Comparison between grain size and NGR, **p. 98.**

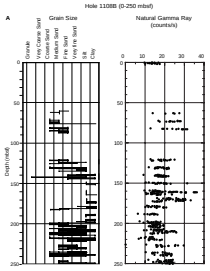

DOWNHOLE MEASUREMENTS

Only one logging run was attempted in Hole 1108B. The pipe was raised to 100 mbsf and a triple combo string with the dual induction tool (DIT) (Table **T7,** p. 74, Fig. **F15,** p. 66, both in the "Explanatory

Notes" chapter) was lowered downhole. The mudline depth determined by the drill pipe (drill-pipe depth) was at 3188.3 mbrf (3177 mbsl).

The count recorded downward from 2979 mbrf identified the mudline wireline depth at 3188 mbrf, and this value was used to convert mbrf to mbsf (Fig. F49). The logging string was stopped for 3 min at mudline to provide a depth reference for the TLT log. Upon reaching open hole at 115 mbsf, the tool string encountered some resistance causing cable tension to drop by ~5 kN (1000 lb). This was finally overcome after working the tool string up and down. The tool string then reached 165 mbsf, where the same problem arose again. Despite numerous attempts, the tool string did not go deeper.

The log was then run from 165 to 125 mbsf at 550 m/hr mainly to acquire caliper data and investigate borehole size. The accelerator porosity sonde (APS) minitron source was not activated so that subsequent passes could record NGR. This first pass revealed a very rough hole with diameters varying from drill-bit size (25.1 cm [9⅞ in]) to more than 42 cm at 135 mbsf, where the caliper arm was fully extended (Fig. F50). The tool was then lowered again but still could not go below 165 mbsf.

A second logging pass was then recorded up from 163 mbsf at 525 m/hr with the APS source activated. This pass was stopped at 120 mbsf, which is below the upper level of downgoing resistance, and the tool brought down again to record a slower, third upgoing pass.

The third pass was run from 163 mbsf at 225 m/hr to record high-resolution (5-cm vertical sampling) APS data up to the base of the pipe. This pass continued to acquire NGR inside the pipe up to the mudline where the tool string was again stopped for 2 min, 45 s to provide a second TLT depth reference. The tool was then brought up to 3150 mbrf, where it was stopped again for calibration before being pulled out of the hole.

The caliper data from the three passes are consistent (Fig. F50) and suggest that the downward progression of the tool may have been hampered by the difficulty of finding a normal-size hole when passing through the bottom of a large washout area.

The NGR readings from the third pass are distorted between 160 and 110 mbsf by the formation activation by the APS during the second pass (Fig. F50). As a result, there is a gap in the usable NGR between 110 and 120 mbsf, because this interval was logged only during pass 3 where the formation was still strongly influenced by the former pass APS activation (Fig. F51).

The APS data (Fig. F51) show very high porosities, which are above the highest values of comparable physical properties measurements from core. This is typical in clayey formations but may also be caused by hole size and roughness.

The low resistivity values seem consistent with the inferred high porosity.

The TLT was set to start recording temperature at 200 m above the seafloor and kept on recording until the return to the drill floor (Fig. F52). The depth shift applied to its data to obtain mbsf is 3186.7 m. The highest recorded temperature was 16°C, which corresponds to the deepest point of the log at 165 mbsf (Fig. F53). Circulation is typically maintained as the hole is being prepared for logging. It is then stopped when the logging strings are rigged up. This helps explain the warming observed in the borehole during logging. Further time-dependent analysis is included in the temperature measurements section. The warmer water temperature encountered while running in pipe when

F49. Hole 1108B total gamma ray (HSGR) from the HNGS, p. 100.

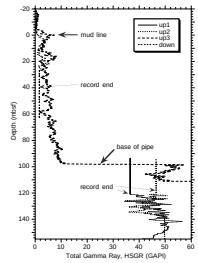

F50. Hole 1108B caliper data (LCAL) from the lithodensity tool (HLDT), p. 101.

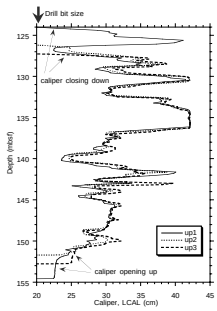

F51. Hole 1108B composite log, p. 102.

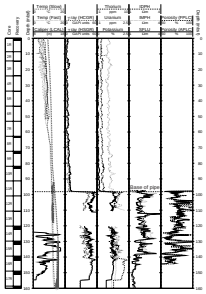

F52. Temperature data from TLT in and above Hole 1108B, p. 103.

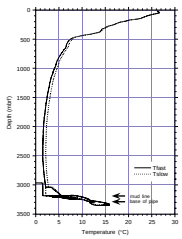

coming out the hole (Fig. F52) may be related to water upwelling caused by the tool movement.

IN SITU TEMPERATURE MEASUREMENTS

An in situ thermal measurement was attempted using the Davis-Villinger temperature probe (DVTP) (Davis et al., 1997) after retrieving Core 180-1108B-3R. Deployment into the formation was prevented by fill within the borehole. Difficult drilling conditions and indurated formation precluded further deployment of the DVTP.

Because of the lack of in situ temperature data, an open-hole temperature record was obtained using the Adara temperature tool (Adara) after coring operations had ended (Fig. F54). The Adara was lowered in the drill pipe and held for temperature measurements at 390 mbsf for ~10 min, and at 300, 200, and 100 mbsf for ~6 min each. Measured temperature at mudline was 2.5°C. Downhole equilibrium temperatures were approximated by plotting the temperature as a function of $\ln[t/(t-s)]$, where t is the total time elapsed since the drill bit penetrated that depth, and s is the total time elapsed between the initial penetration and the cessation of circulation (Fig. F55). The line was then extrapolated to infinite time (where $\ln[t/(t-s)] = 0$). This method was introduced by Bullard (1947) and previously applied to open-hole temperature measurements from ODP Leg 123 (Castillo, 1992). Because the approximation considers only conductive thermal transport, and recovery duration of the Hole 1108B was very limited, these data cannot be considered as accurate as in situ temperature determinations.

The data from the Adara run were supplemented by measurements taken by the TLT (see "Downhole Measurements," p. 40). Temperature data points between 159.5 and 160.5 mbsf were selected for estimation of in situ temperature at that depth (Fig. F56). For this approximation, circulation was assumed to persist for the entire period from the time that the depth was first penetrated until circulation ended as the logging tools left the bottom of pipe (105 hr). Interruptions in circulation, such as for the Adara run, were considered to be of sufficiently short duration relative to total circulation time that they could be neglected.

The profile of temperature with depth indicates a discontinuity between 160 and 200 mbsf (Fig. F57). This depth is coincident with a fault zone near 165 mbsf (see "Structural Geology," p. 19) and observed perturbations in inorganic geochemical profiles (see "Inorganic Geochemistry," p. 30). The estimated thermal gradient depends on whether all data points are considered or individual intervals are examined. Linear regression of all the approximated equilibrium temperatures from both the Adara and TLT runs indicates a thermal gradient of 100°C·km^{-1} if the line is required to pass through the measured mudline temperature (Fig. F57). Alternatively, gradients can be interpreted as 94°C·km^{-1} above 160 mbsf, 24°C·km^{-1} between 160 and 200 mbsf, and 65°C·km^{-1} below 200 mbsf, as indicated by the dashed lines on Figure F57.

It is possible that normal fault movement has caused the discontinuity in thermal gradient. Calculations using the one-dimensional thermal transport equation suggest that the discontinuity can be reasonably reproduced by a 200-m vertical displacement, if the initial thermal gradient was 65°C·km^{-1}. However, the offset would need to be rapid because thermal conduction would significantly reduce the discontinuity in less than a few 1000 yr. An alternative explanation for the

F53. Borehole temperature in Hole 1108B from TLT, p. 104.

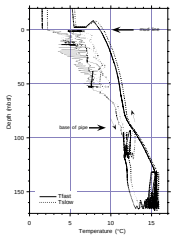

F54. Temperature as a function of time for Adara temperature run, p. 105.

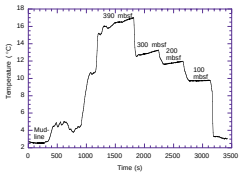

F55. Temperature vs. $\ln[t/(t-s)]$ for Adara depth stations, p. 106.

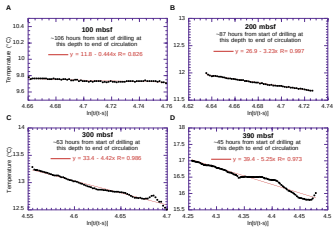

F56. Temperature vs. $\ln[t/(t-s)]$ for TLT tool during logging run, p. 107.

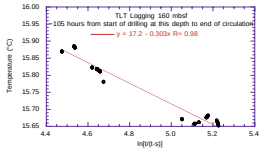

F57. Approximated temperature as a function of depth, and best-fit regression, p. 108.

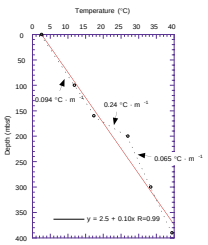

observed thermal discontinuity may be advection of warm fluids along the fault zone.

REFERENCES

Athy, L. F., 1930. Density, porosity, and compaction of sedimentary rocks. *AAPG Bull.,* 14:1–24.

Baker, P.A. 1986. Pore-water chemistry of carbonate-rich sediments. Lord Howe Rise, Southwest Pacific Ocean. *In* Kennett, J.P., von der Borch, C.C., et al., *Init. Repts. DSDP,* 90: Washington (U.S. Govt. Printing Office), 1249–1256.

Berggren, W.A., Kent, D.V., Swisher, C.C., III, and Aubry, M.-P., 1995. A revised Cenozoic geochronology and chronostratigraphy. *In* Berggren, W.A., Kent, D.V., Aubry, M.-P., and Hardenbol, J. (Eds.), *Geochronology, Time Scales and Global Stratigraphic Correlation*. Spec. Publ.—Soc. Econ. Paleontol. Mineral. (Soc. Sediment. Geol.), 54:129–212.

Bouma, A.H., 1962. *Sedimentology of Some Flysch Deposits: A Graphic Approach to Facies Interpretation:* Amsterdam (Elsevier).

Bullard, E.C., 1947. The time necessary for a borehole to attain temperature equilibrium. *Mon. Not. R. Astron. Soc., Geophys. Suppl.,* 5:127–130.

Castillo, D.A., 1992. Thermal and hydrologic properties of old oceanic crust in Hole 765D, Argo Abyssal Plain, Indian Ocean. *In* Gradstein, F.M., Ludden, J.N., et al., *Proc. ODP, Sci. Results,* 123: College Station, TX (Ocean Drilling Program), 515–522.

Claypool, G.E., and Kaplan, I.R., 1974. The origin and distribution of methane in marine sediments. *In* Kaplan, I.R. (Ed.), *Natural Gases in Marine Sediments:* New York (Plenum), 99–139.

Cragg, B.A., 1994. Bacterial profiles in deep sediment layers from the Lau Basin (Site 834). *In* Hawkins, J., Parson, L., Allan, J., et al., *Proc. ODP, Sci. Results,* 135: College Station, TX (Ocean Drilling Program), 147–150.

Cragg, B.A., Harvey, S.M., Fry, J.C., Herbert, R.A., and Parkes, R.J., 1992. Bacterial biomass and activity in the deep sediment layers of the Japan Sea, Hole 798B. *In* Pisciotto, K.A., Ingle, J.C., Jr., von Breymann, M.T., Barron, J., et al., *Proc. ODP, Sci. Results.,* 127/128 (Pt. 1): College Station, TX (Ocean Drilling Program), 761–776.

Davies, H.L., and Jaques, A.L., 1984. Emplacement of ophiolite in Papua New Guinea. *Spec. Publ.—Geol. Soc. London,* 13:341–350.

Davis, E.E., Villinger, H., MacDonald, R.D., Meldrum, R.D., and Grigel, J., 1997. A robust rapid-response probe for measuring bottom-hole temperatures in deep-ocean boreholes. *Mar. Geophys. Res.,* 19:267–281.

De Carlo, E.H., 1992. Geochemistry of pore water and sediments recovered from the Exmouth Plateau. *In* von Rad, U., Haq, B.U., et al., *Proc. ODP, Sci. Results,* 122: College Station, TX (Ocean Drilling Program), 295–308.

Edmond, J.M., Measures, C., McDuff, R.E., Chan, L.H., Collier, R., and Grant, B., 1979. Ridge crest hydrothermal activity and the balances of the major and minor elements in the ocean: the Galapagos data. *Earth Planet. Sci. Lett.,* 46:1–18.

Fouquet, Y., Zierenberg, R.A., Miller, D.J., et al., 1998. *Proc. ODP, Init. Repts.,* 169: College Station, TX (Ocean Drilling Program).

Gieskes, J.M., 1981. Deep-sea drilling interstitial water studies: implications for chemical alteration of the oceanic crust, layers I and II. *In* Warme, J.E., Douglas, R.G., and Winterer, E.L. (Eds.), *The Deep Sea Drilling Project: A Decade of Progress*. Spec. Publ.—Soc. Econ. Paleontol. Mineral., 32:149–167.

Gieskes, J.M., Elderfield, H., and Nevsky, B., 1983. Interstitial water studies, Leg 65: *In* Lewis, B.T.R., Robinson, P., et al., *Init. Repts. DSDP,* 65: Washington (U.S. Govt. Printing Office), 441– 449.

Hill, E.J., Baldwin, S.L., and Lister, G.S., 1992. Unroofing of active metamorphic core complexes in the D'Entrecasteaux Islands, Papua New Guinea. *Geology,* 20:907–910.

Jelinek, V., 1981. Characterization of the magnetic fabric of rocks. *Tectonophysics,* 79:63–67.

Lundberg, N., and Moore, J.C., 1986. Macroscopic structural features in Deep Sea Drilling Project cores from forearc regions. *In* Moore, J.C. (Ed.), *Structural Fabric in Deep Sea Drilling Project Cores From Forearcs*. Mem.—Geol. Soc. Am., 166:13–44.

Martin, J.B., Kastner, M., and Egeberg, P.K., 1995. Origins of saline fluids at convergent margins. *In* Taylor, B., and Natland, J. (Eds.), *Active Margins and Marginal Basins of the Western Pacific*. Geophys. Monogr., Am. Geophys. Union, 88:219–239.

McDuff, R.E., 1981. Major cation gradients in DSDP interstitial waters: the role of diffusive exchange between seawater and upper oceanic crust. *Geochim. Cosmochim. Acta,* 45:1705–1713.

McDuff, R.E., and Gieskes, J.M., 1976. Calcium and magnesium profiles in DSDP interstitial waters: diffusion or reaction? *Earth Planet. Sci. Lett.,* 33:1–10.

Merrill, R.T., and McElhinny, M.W., 1983. *The Earth's Magnetic Field: Its History, Origin, and Planetary Perspective:* London (Acad. Press).

Parkes, R.J., Cragg, B.A., Bale, S.J., Getliff, J.M., Goodman, K., Rochelle, P.A., Fry, J.C., Weightman, A.J., and Harvey, S.M., 1994. A deep bacterial biosphere in Pacific Ocean sediments. *Nature,* 371:410–413.

Pickering, K.T., Hiscott, R., and Hein, F.J., 1989. *Deep-marine Environments: Clastic Sedimentation and Tectonics:* London (Unwin Hyman).

Piper, D.J.W., 1978. Turbidite muds and silts on deepsea fans and abyssal plains. *In* Stanley, D.J., and Kelling, G. (Eds.), *Sedimentation in Submarine Canyons, Fans and Trenches:* Stroudsburg, PA (Dowden, Hutchinson and Ross), 163–175.

Rogerson, R., Hilyard, D., Francis, G., and Finlayson, E.J., 1987. The foreland thrust belt of Papua New Guinea. *Proc. Pac. Rim Congr.,* 87:579–583.

Tarling, D.H. and Hrouda, F., 1993. *The Magnetic Anisotropy of Rocks:* London (Chapman and Hall).

Figure F1. Summary of the lithologies recovered from Hole 1108B. Note that lithologies are inevitably generalized in view of the very limited, or absent, recovery of some intervals. See Fig. F2, p. 52, in the "Explanatory Notes" chapter for key to symbols, and "Core Descriptions" contents list for visual core descriptions.

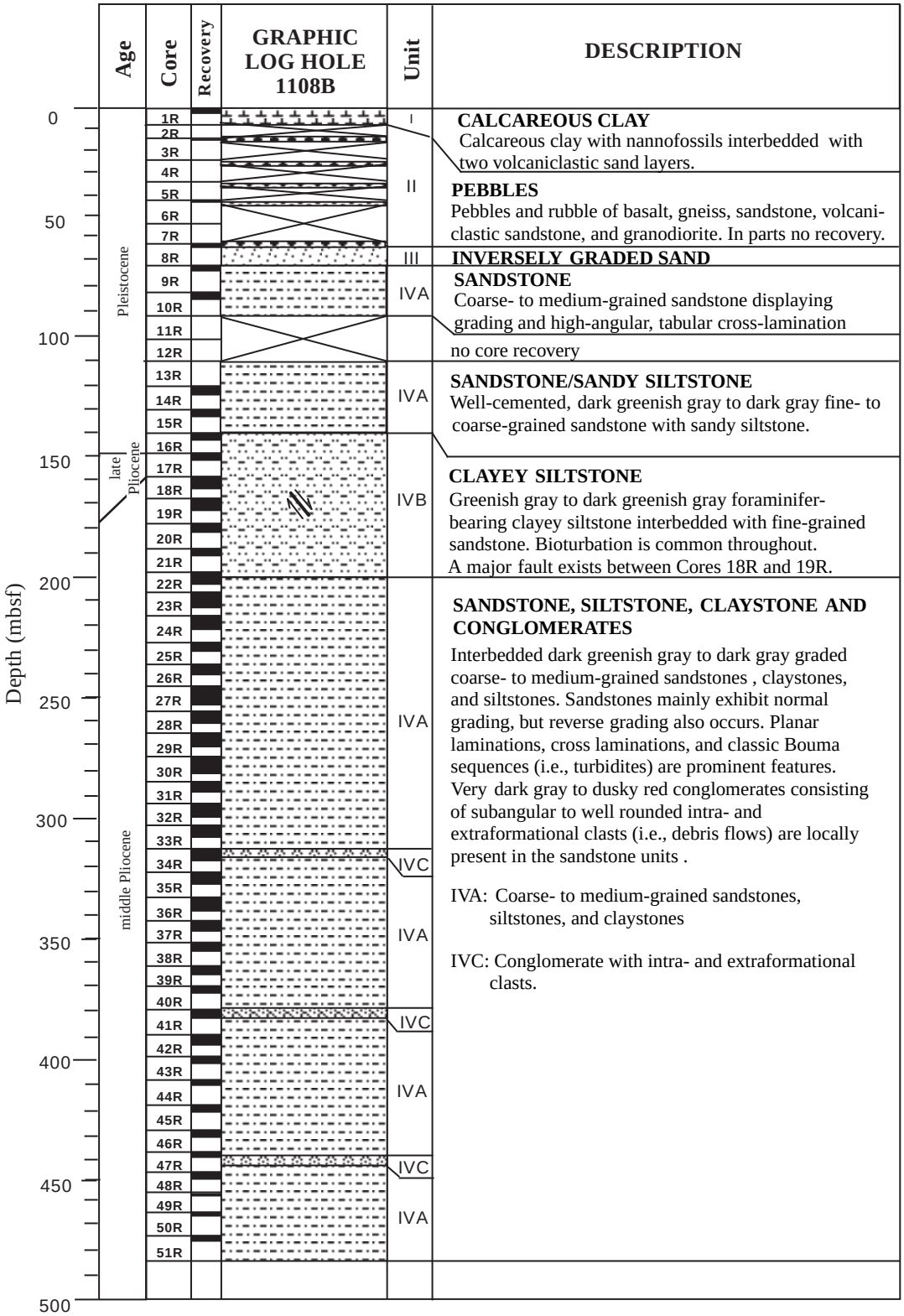

Figure F2. Normally graded, volcaniclastic, very thin sandstone bed (at 18–20 cm) sharply overlying a calcareous clay with nannofossils (at 20.0–25.0 cm; interval 180-1108B-1R-1, 18–26 cm).

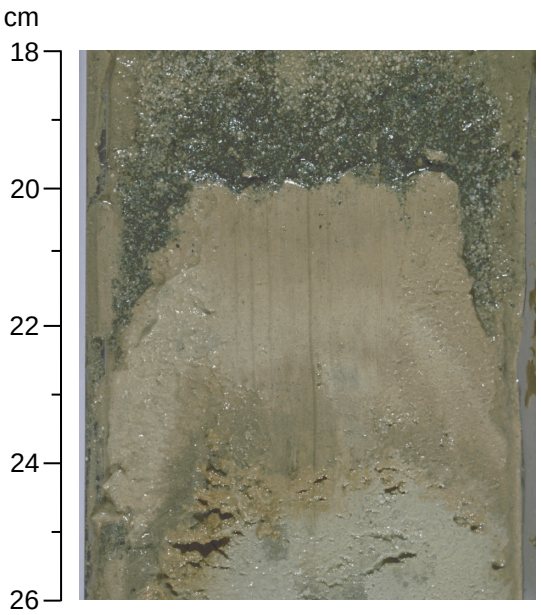

Figure F3. Digital photomicrograph (crossed nicols) showing a subrounded clast of basalt with plagioclase microphenocrysts (right); an acidic volcanic clast (left) and a clast of serpentinite (bottom). Surrounding grains include quartz and feldspar set in a calcite cement (interval 180-1108B-3R-CC, 0–4 cm).

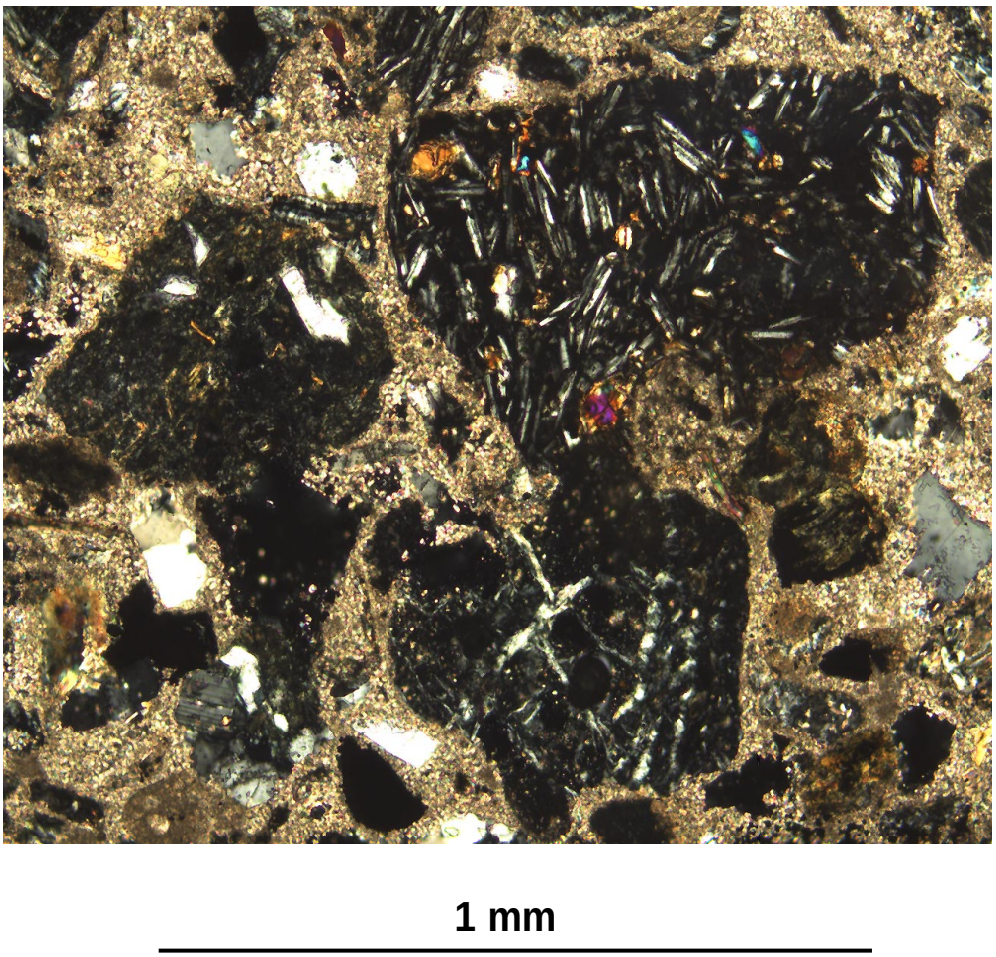

Figure F4. Digital photomicrograph (crossed nicols) showing a well-rounded clast of fresh glassy basalt with plagioclase and biotite microphenocrysts set in a calcite cement including volcanic and metamorphic grains (interval 180-1108B-3R-CC, 0–4 cm).

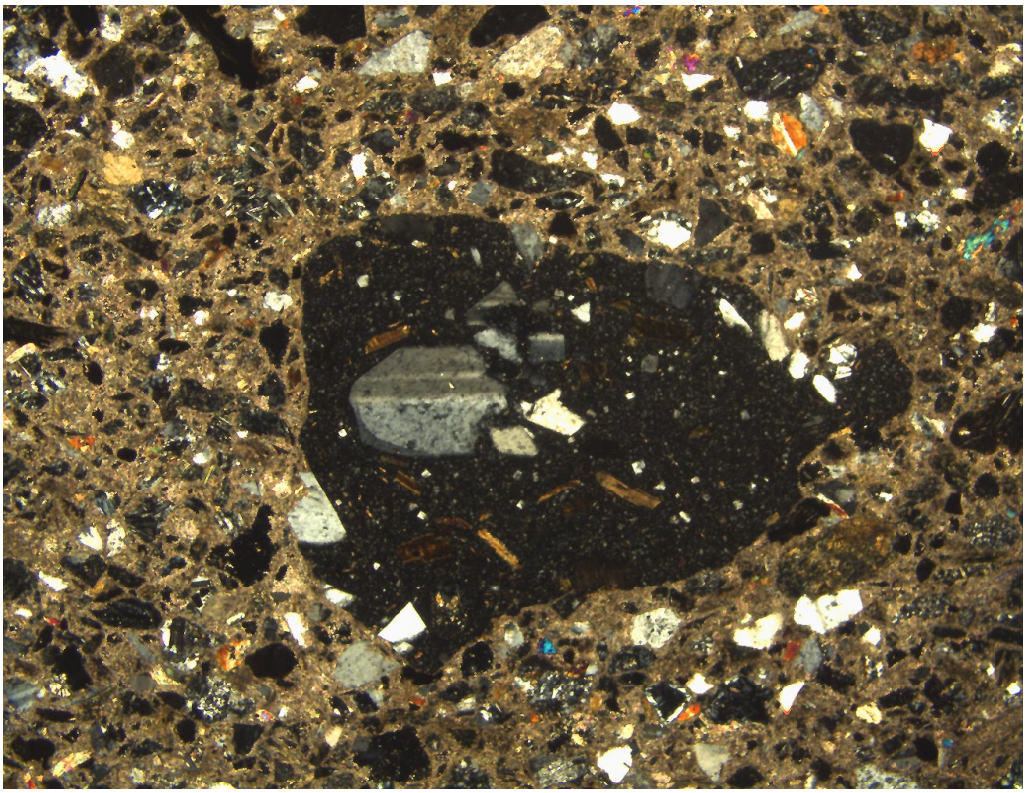

Figure F5. Digital photomicrograph (crossed nicols) showing a subangular grain of foliated mica schist set in a calcareous cement with grains of quartz, feldspar, small basic and acidic volcanic grains, and rare serpentinite (interval 180-1108B-3R-CC, 0–4 cm).

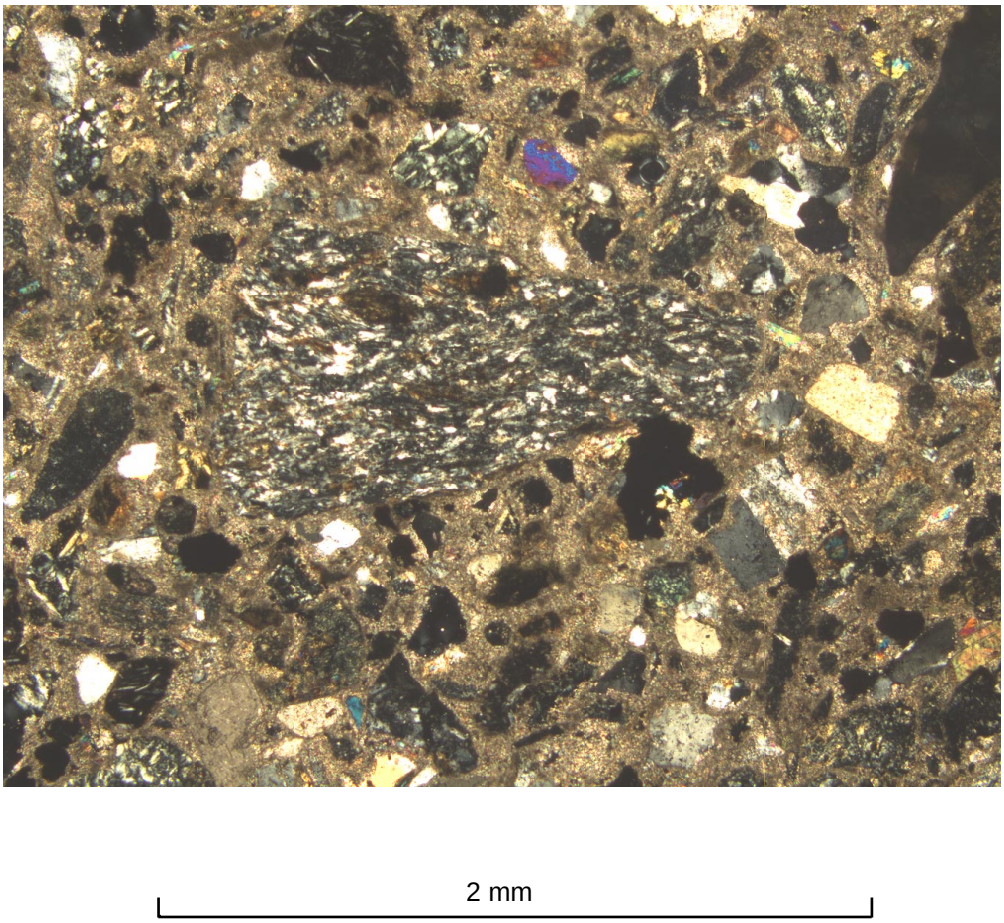

Figure F6. Digital photomicrograph (crossed nicols) showing a well-rounded grain of serpentinite surrounded by quartz, feldspar, and basic and acidic volcanic rock grains set in a calcite cement (interval 180-1108B-3R-CC, 0–4 cm).

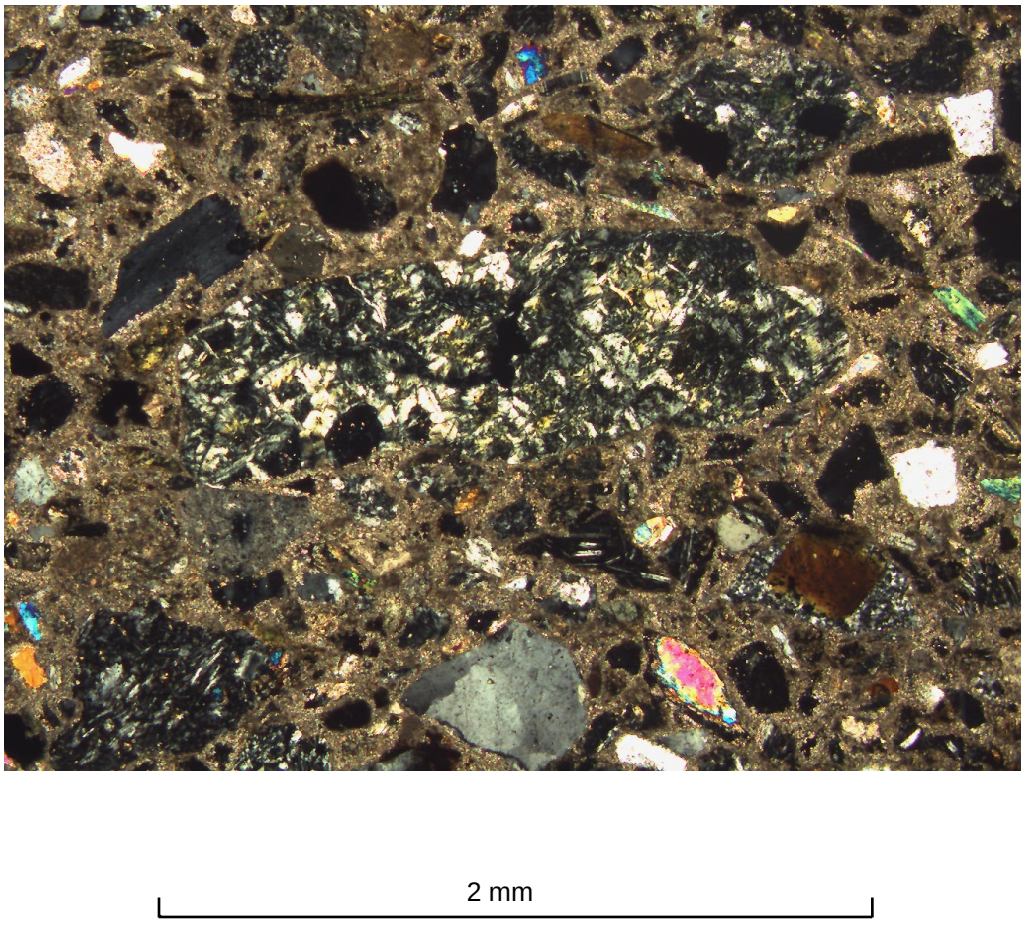

Figure F7. Digital photomicrograph (crossed nicols) showing a medium-grained sandstone with angular grains of feldspar, quartz, biotite, and volcanic rock fragments (acidic and basic) (interval 180-1108C-5R-CC, 6–8 cm).

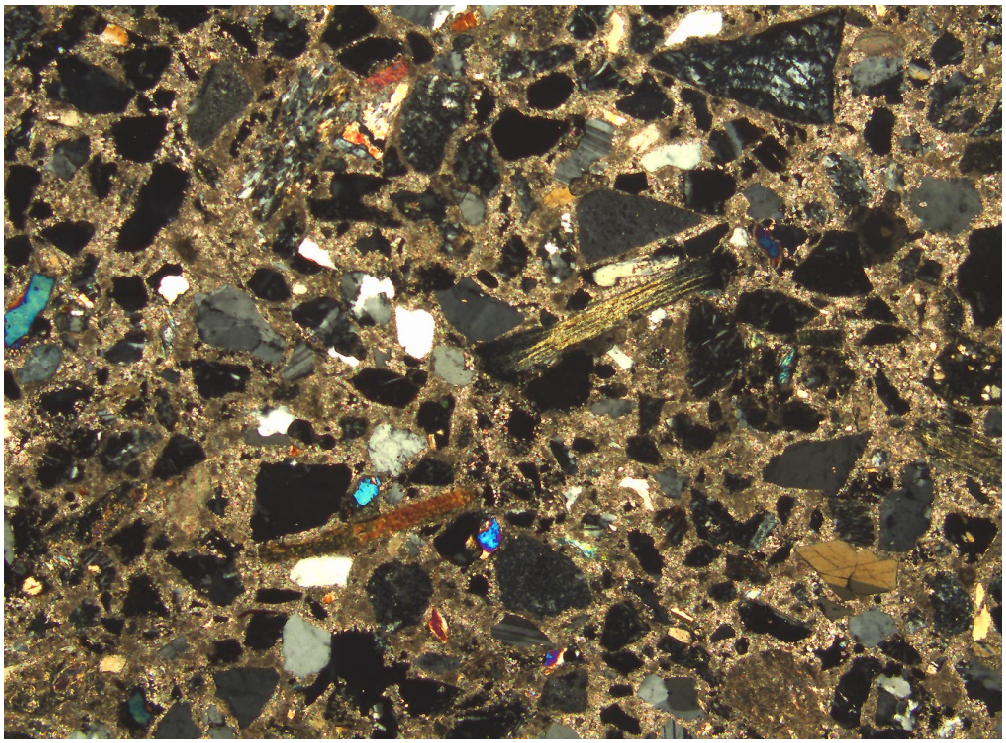

Figure F8. Inversely graded medium- to coarse-grained sandstone (26–50.5 cm). This bed shows sharp lower (50.5 cm) and upper (26.0 cm) contacts (interval 180-1108B-8R-1, 24–52 cm).

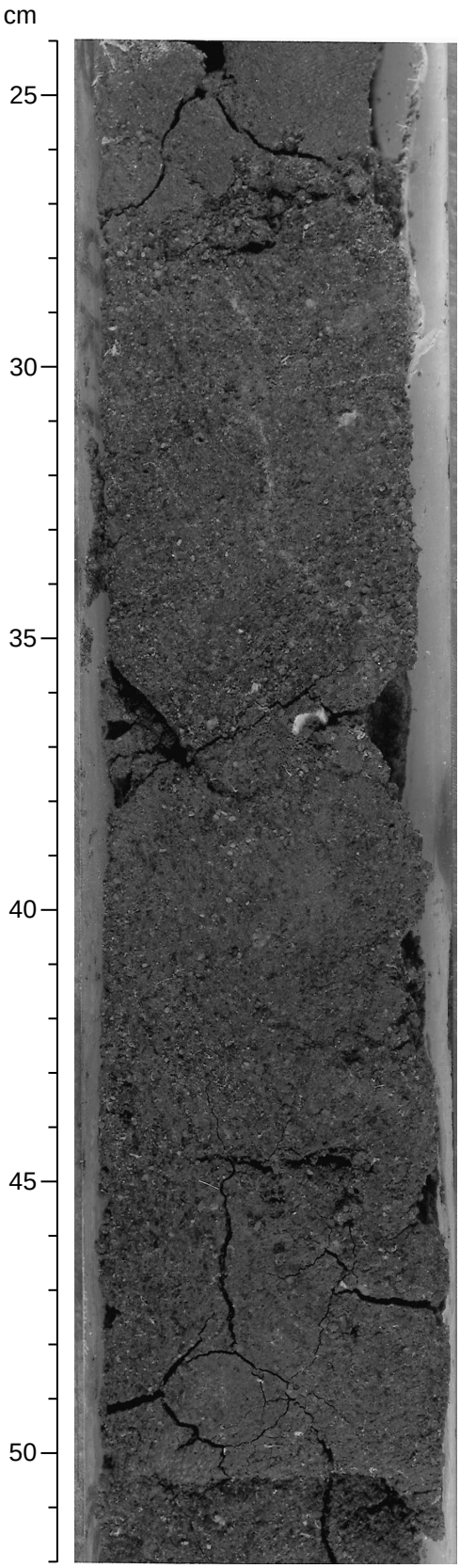

Figure F9. Coarse-grained sandstone with calcite veins. In the lower part the pores are filled with calcite. The calcite veining relates to tectonic deformation of this interval of Subunit IVA (interval 180-1108B-15R-1, 9–27 cm).

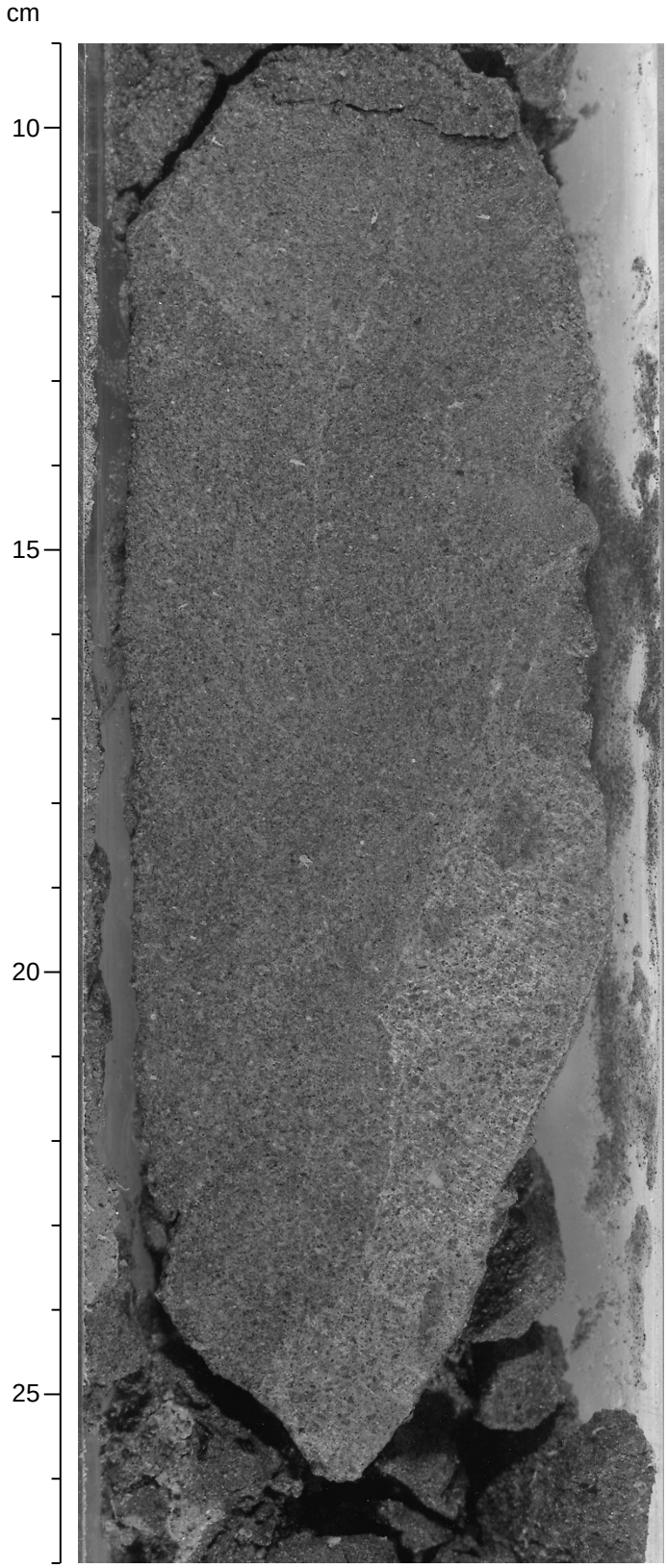

Figure F10. Alternating thin and very thin beds of sandstone, siltstone, and claystone. Most of these beds have sharp upper and lower contacts and are moderately to highly bioturbated (interval 180-1108B-26R-3, 5–25 cm).

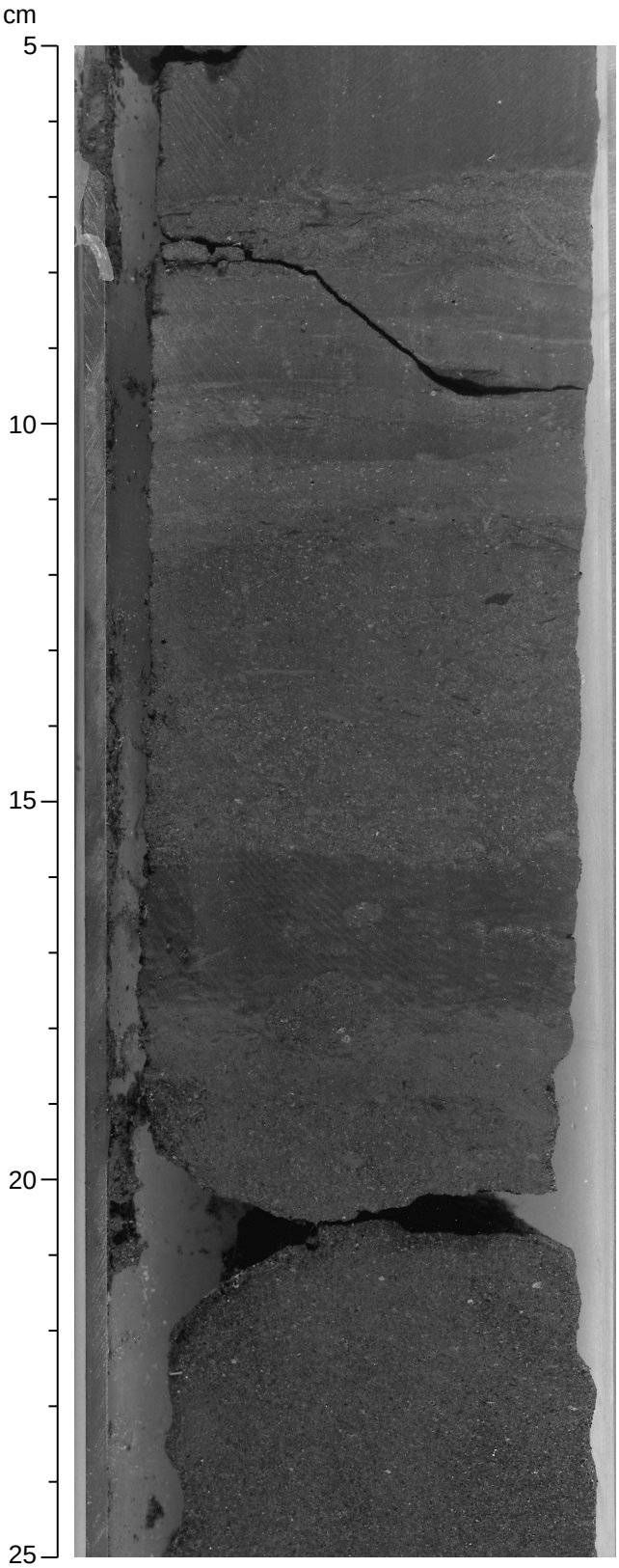

Figure F11. Alternating parallel-wavy-laminated (at 33–35, 32–31.5, 29.5–31, and 29–25 cm) with ripple-laminated (at 31.8–32.8, 31–31.5, and 29–29.5 cm) fine-grained sandstone. This sandstone underlies another fine-grained sandstone with a sharp erosional contact marked by scours (interval 180-1108B-34R-4, 24–35 cm).

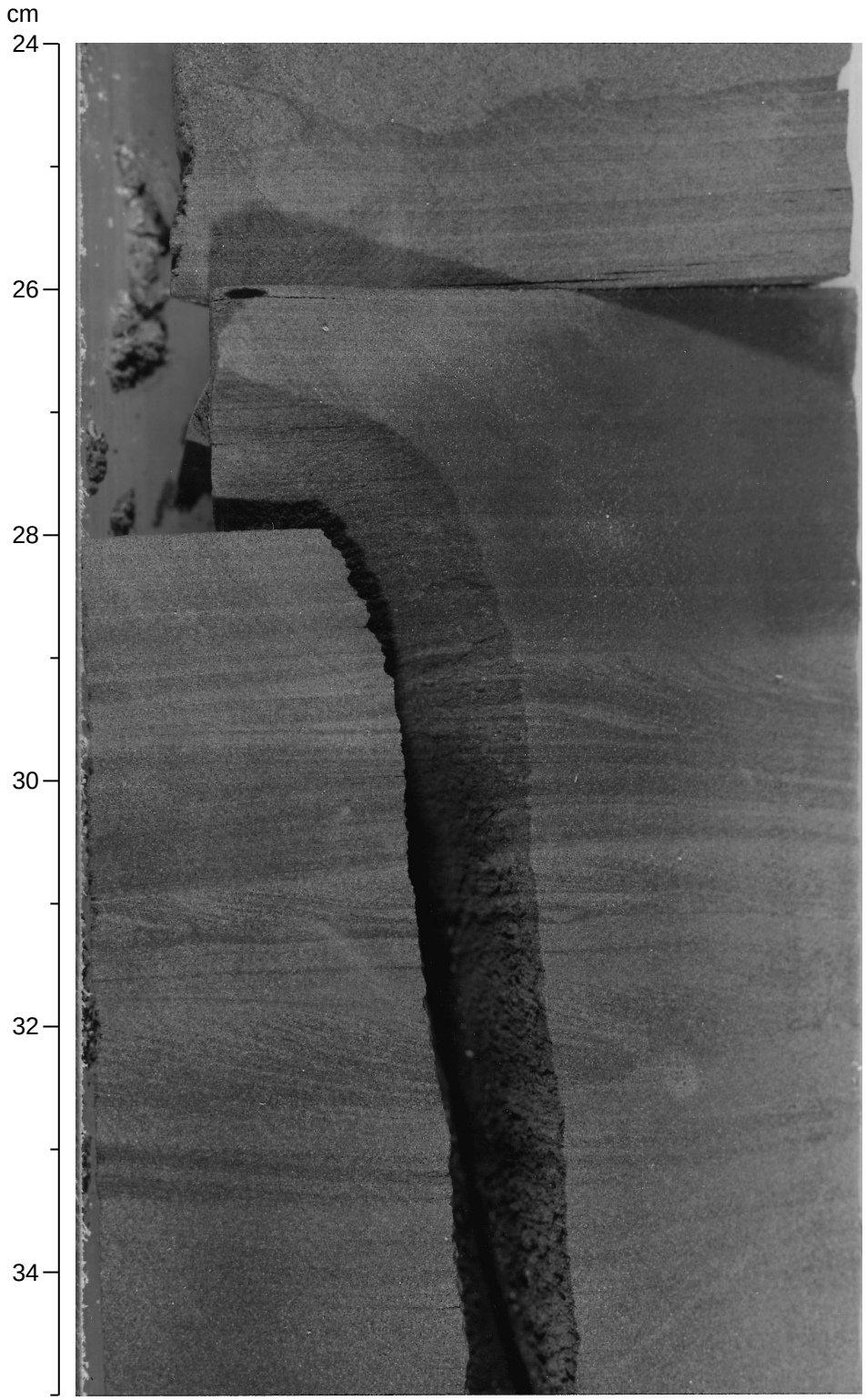

Figure F12. The upper part of a thick-bedded granule-pebble, very coarse grained sandstone (100–110 cm). Note the very well rounded calcareous claystone clast at the top of the bed (98–102 cm) that projects above into a fine-grained sandstone, which also exhibits climbing ripples (interval 180-1108B-37R-3, 93–110 cm).

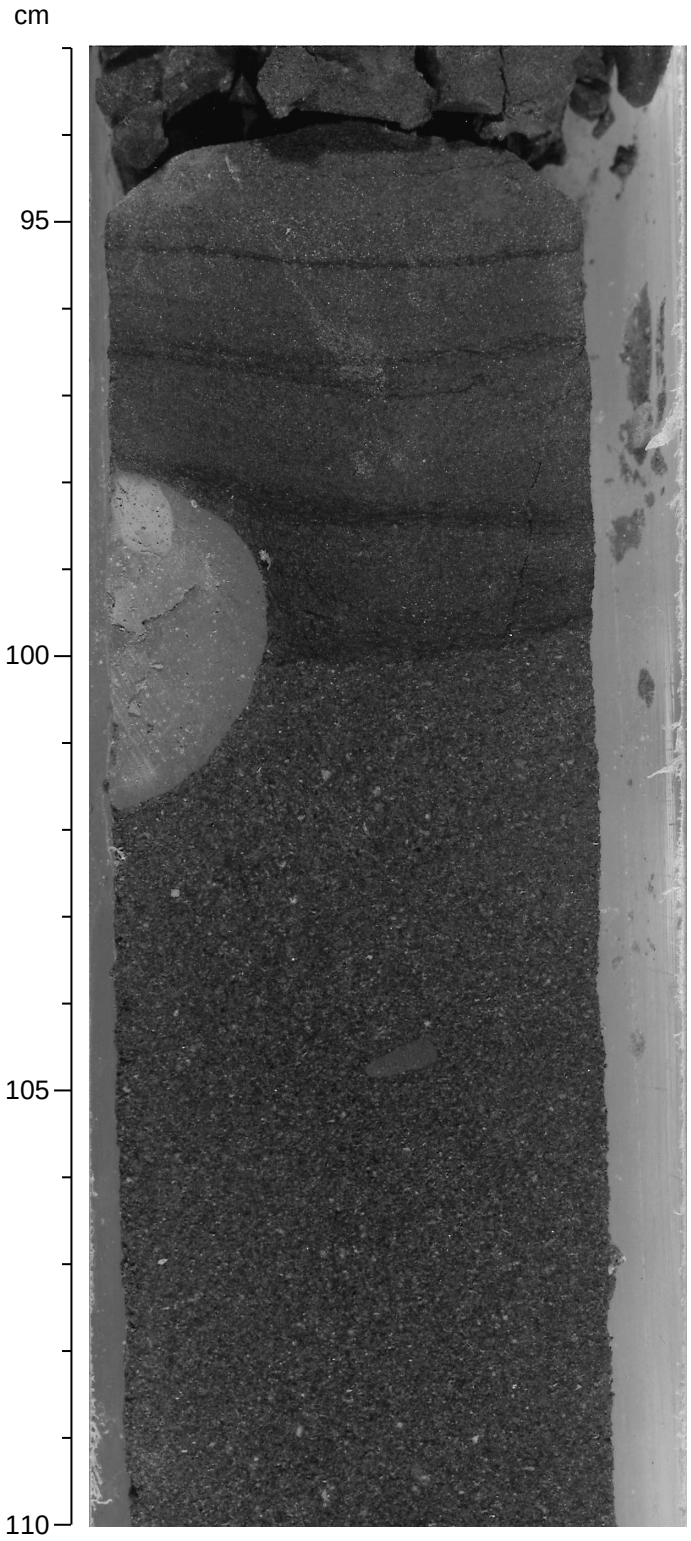

Figure F13. Digital photomicrograph (crossed nicols) showing a basaltic clast set within a siliciclastic matrix (interval 180-1108B-34R-2, 126–128 cm).

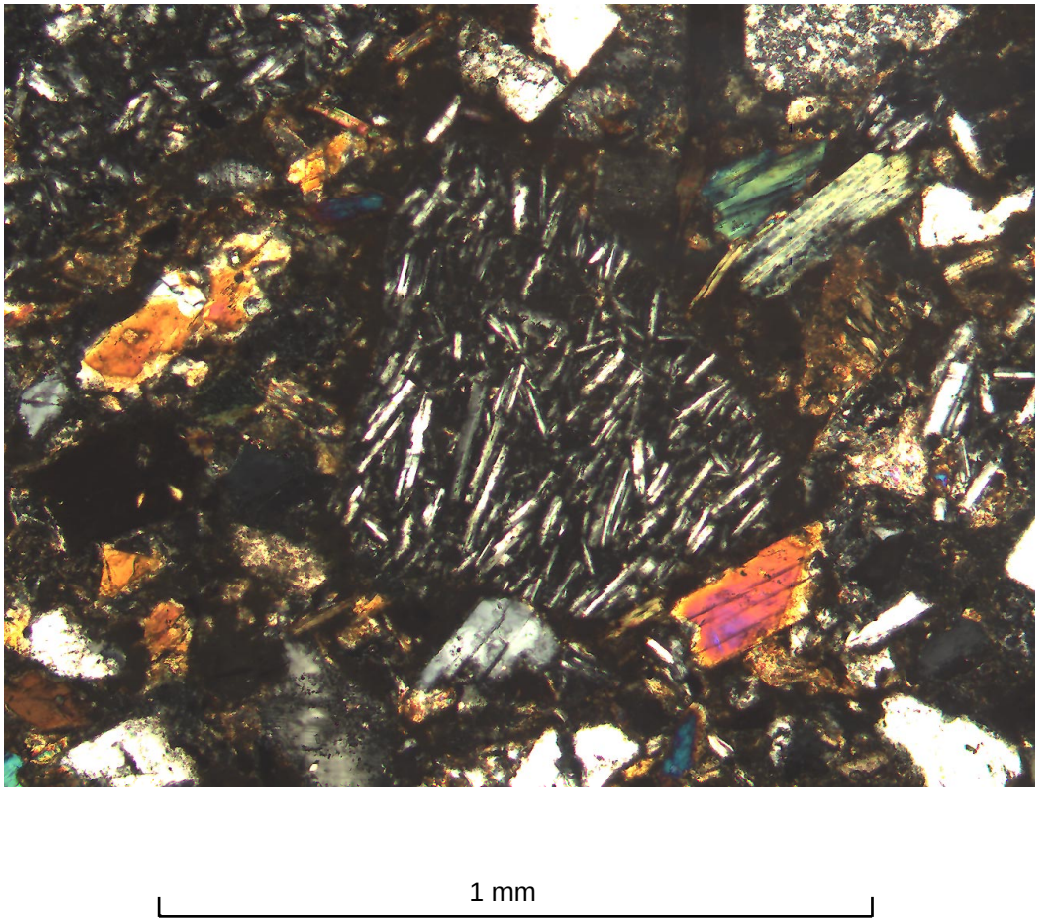

Figure F14. Normal-graded, medium-bedded, silty sandstone bed (140.5–145 cm) displaying a lower parallel laminated interval (142.5–145 cm) followed by a climbing ripple-lamination interval (140.5–142 cm), in turn followed by parallel-laminated clayey siltstone that gradually becomes massive and finer grained toward the top. The dip of the bed is probably not primary, but instead is related to tectonic tilting (interval 180-1108B-20R-1, 130–145 cm).

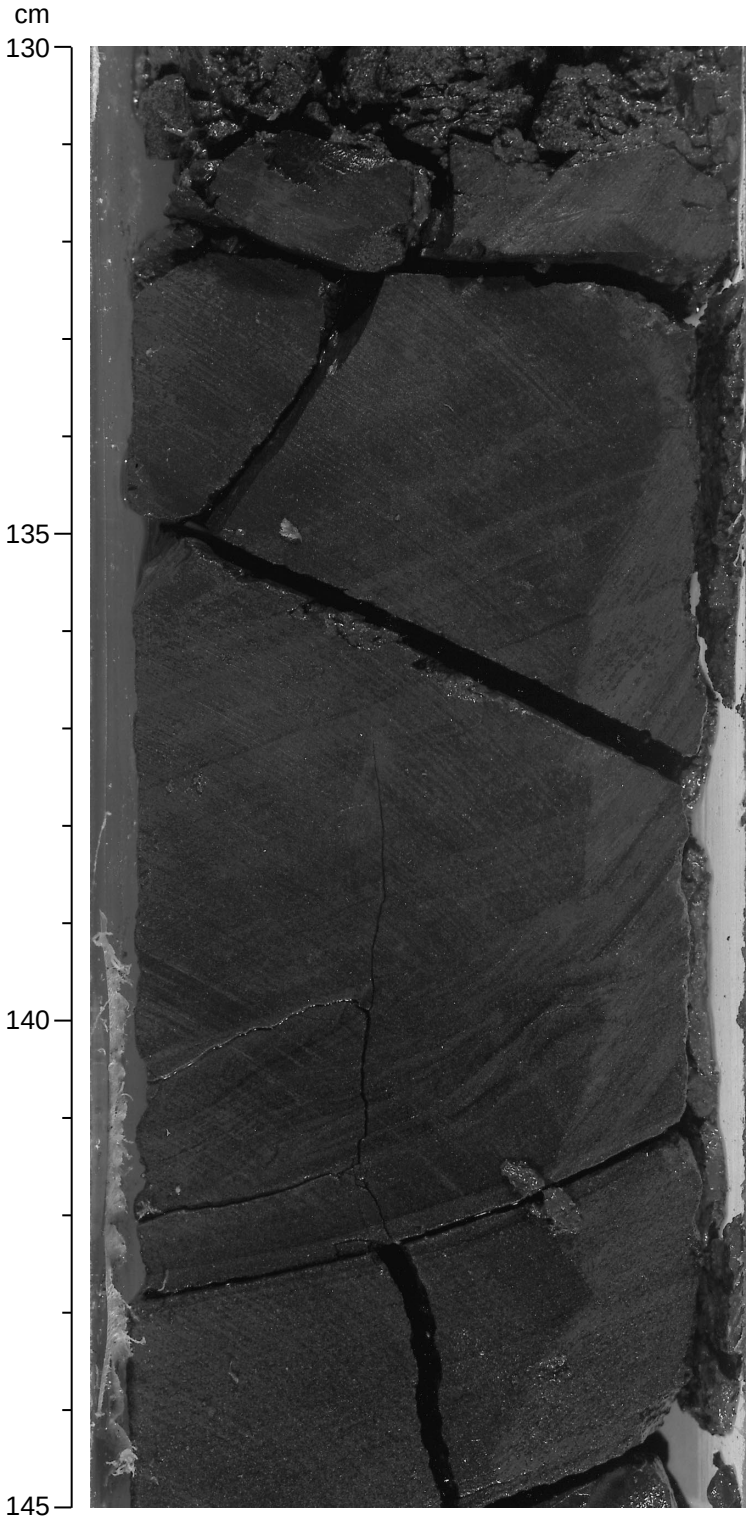

Figure F15. Normally graded, thin-bedded sandstone bed displaying cross laminations (112–114 cm) and parallel-wavy lamination (105–111 cm; interval 180-1108B-16R-2, 101–114 cm).

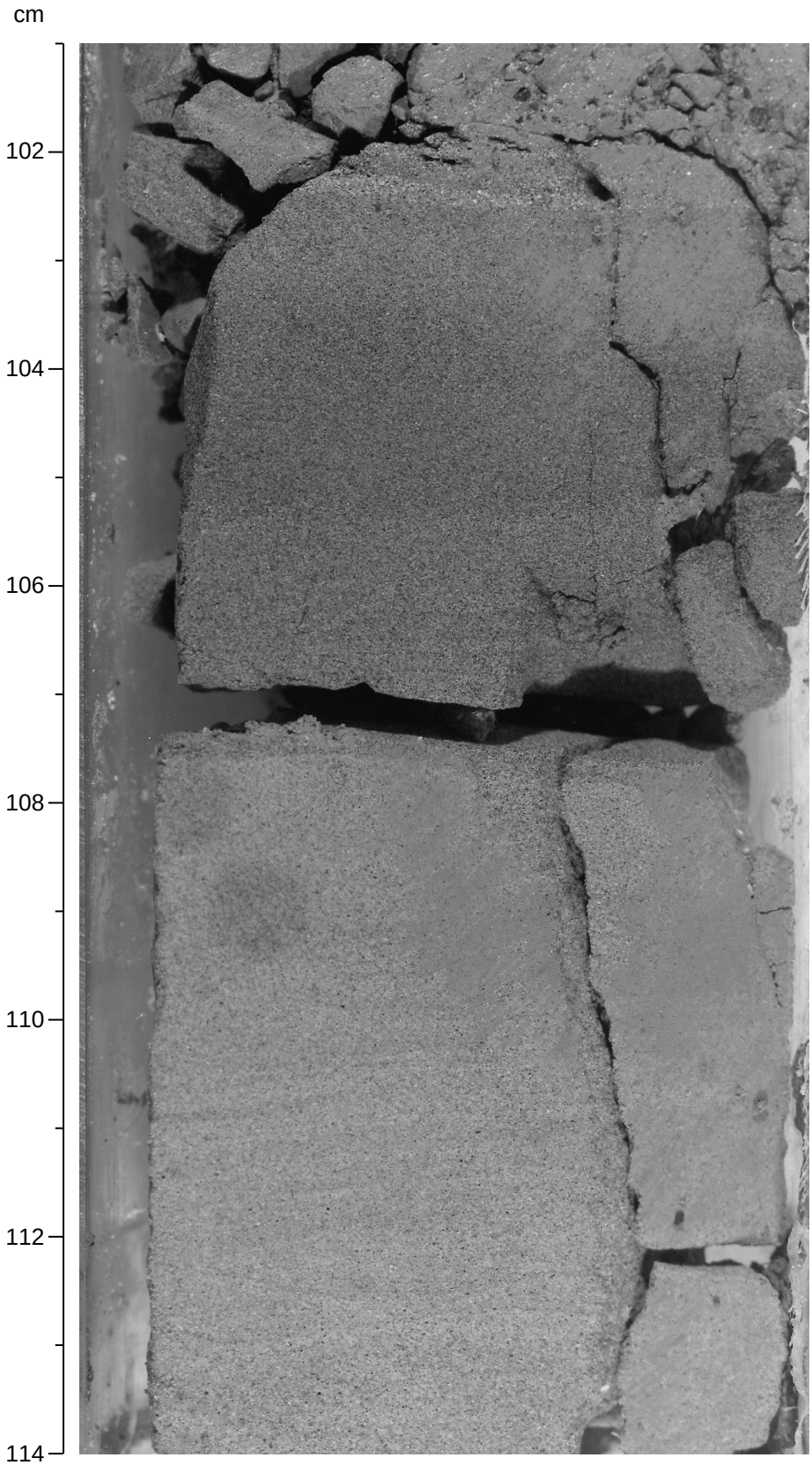

Figure F16. Thinly laminated clayey siltstone with abundant foraminifers (6–14 cm; interval 180-1108B-17R-CC, 0–14 cm).

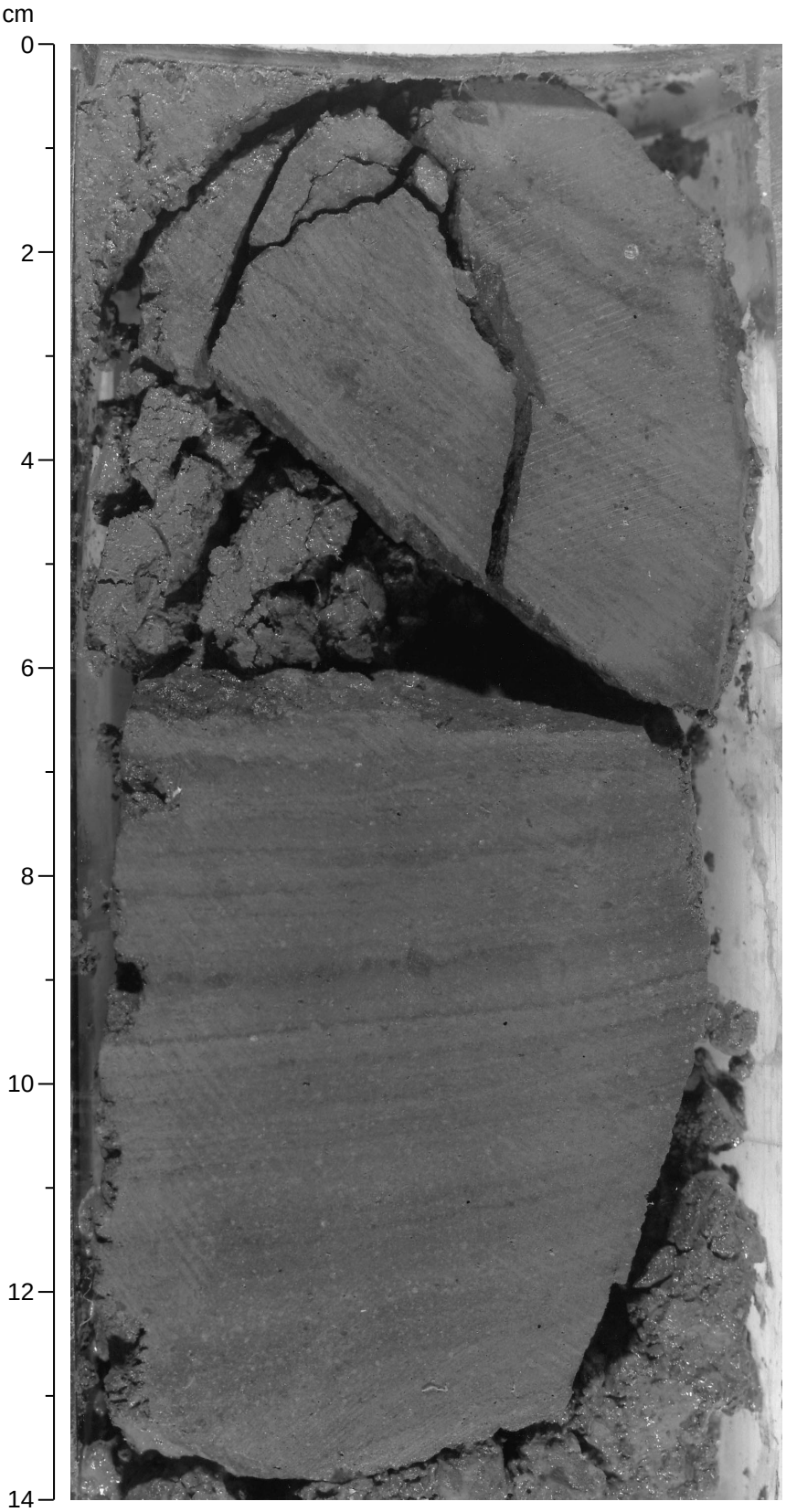

Figure F17. Intensely bioturbated sandy silty claystone with abundant foraminifers and pyrite concretions (at 41 cm; interval 180-1108B-18R-4, 35–60 cm).

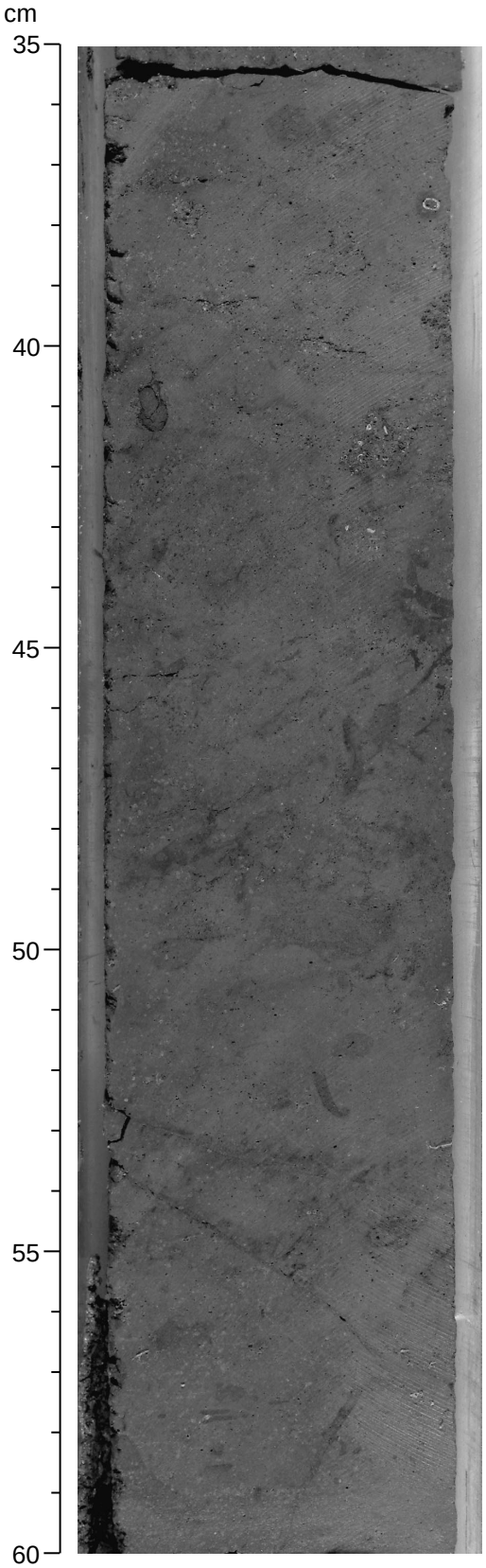

Figure F18. Digital photomicrograph (crossed nicols) showing a clast of acidic volcanic rock with plagioclase phenocrysts surrounded by clastic grains including feldspar, quartz, and mica. The texture is grain supported (interval 180-1108B-20R-CC, 0–3 cm).

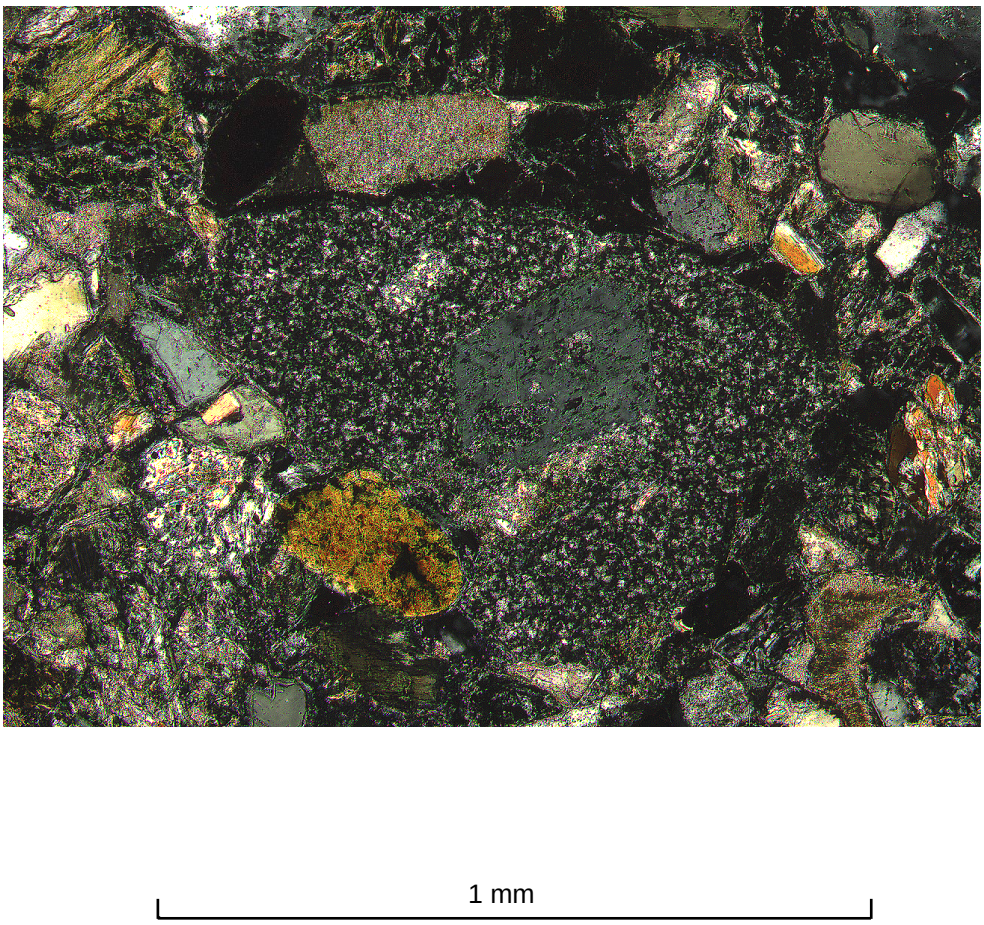

Figure F19. Inverse- to normal-graded granule-pebble, matrix-supported paraconglomerate (44–64 cm; interval 180-1108B-34R-2, 44–67 cm). Refer to **"Lithostratigraphic Subunit IVC,"** p. 16, for further discussion.

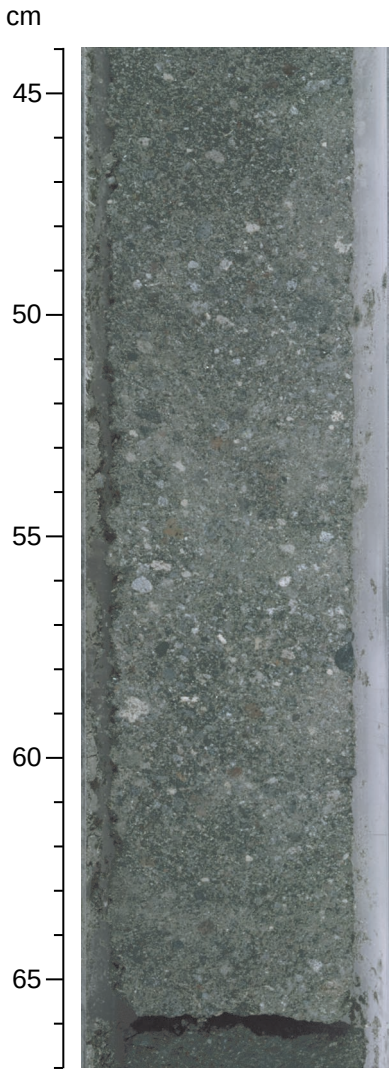

Figure F20. Summary of grain-size variation in Hole 1108B. The plot is smoothed to show the main variation, which is based on information summarized in the barrel sheets. Note that the variation may not be representative of the actual recovery within intervals of low recovery. See Figure F2, p. 52, in the "Explanatory Notes" chapter for symbol definitions.

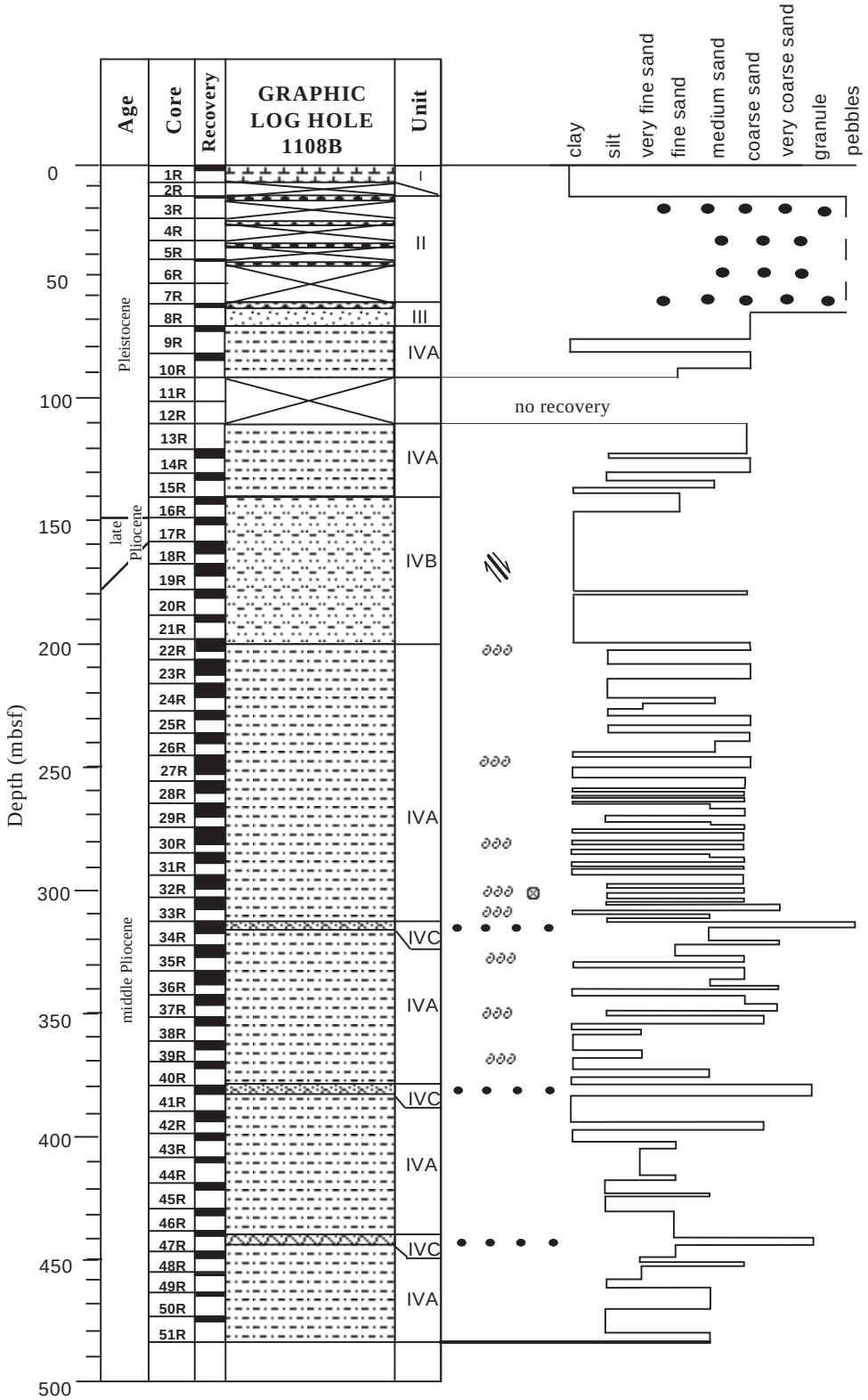

Figure F21. Summary depth log of the main structural features measured at Site 1108. Lithostratigraphic Units I through IV: see **"Lithostratigraphy,"** p. 6, for discussion. Calc = calcite; Ep = epidote; DS = dip-slip fault; F = fault; OF = open fractures; SS = strike-slip fault.

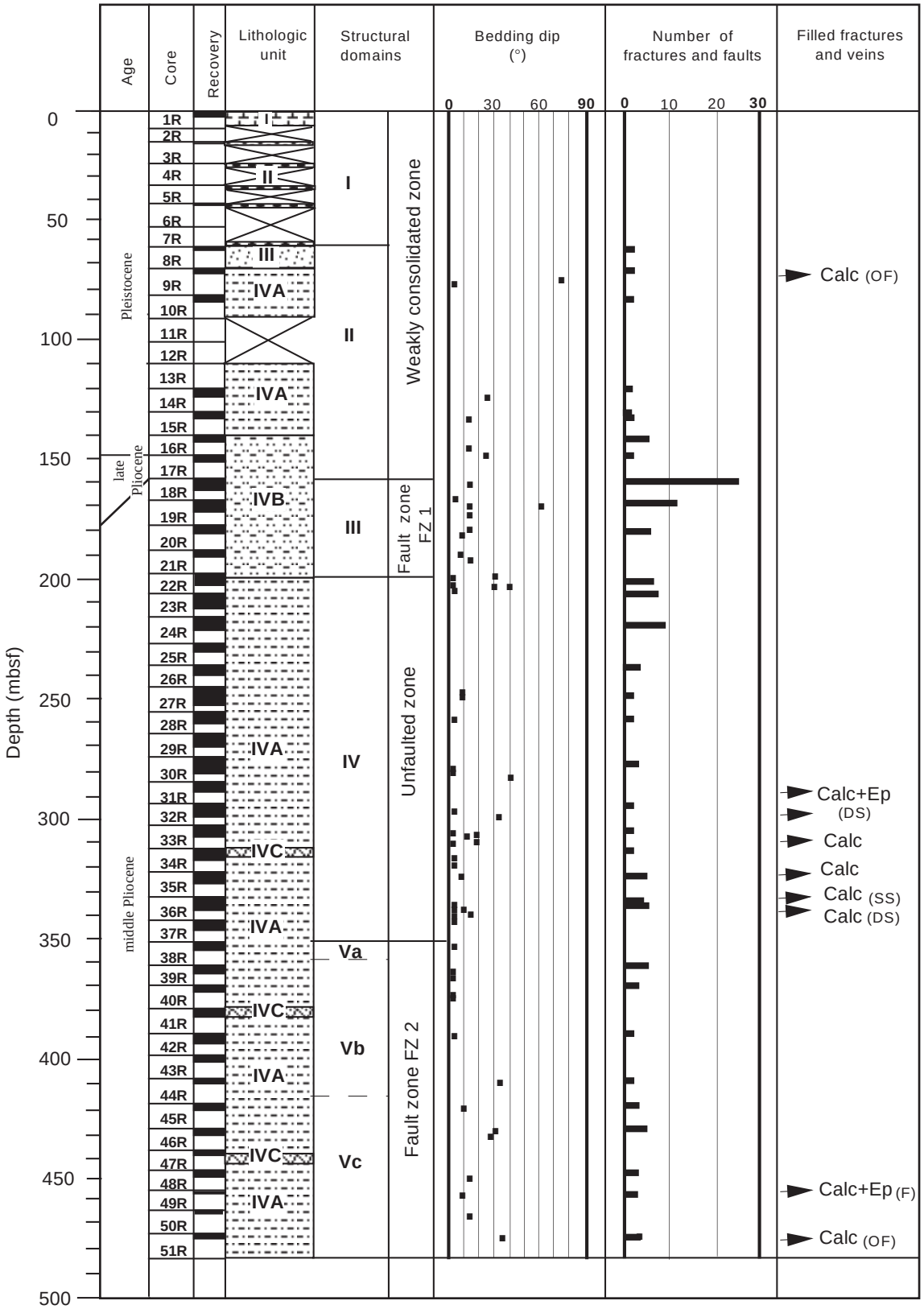

Figure F22. Histograms of bedding dips measured within four of the five structural domains identified at Site 1108. N = number of collected data.

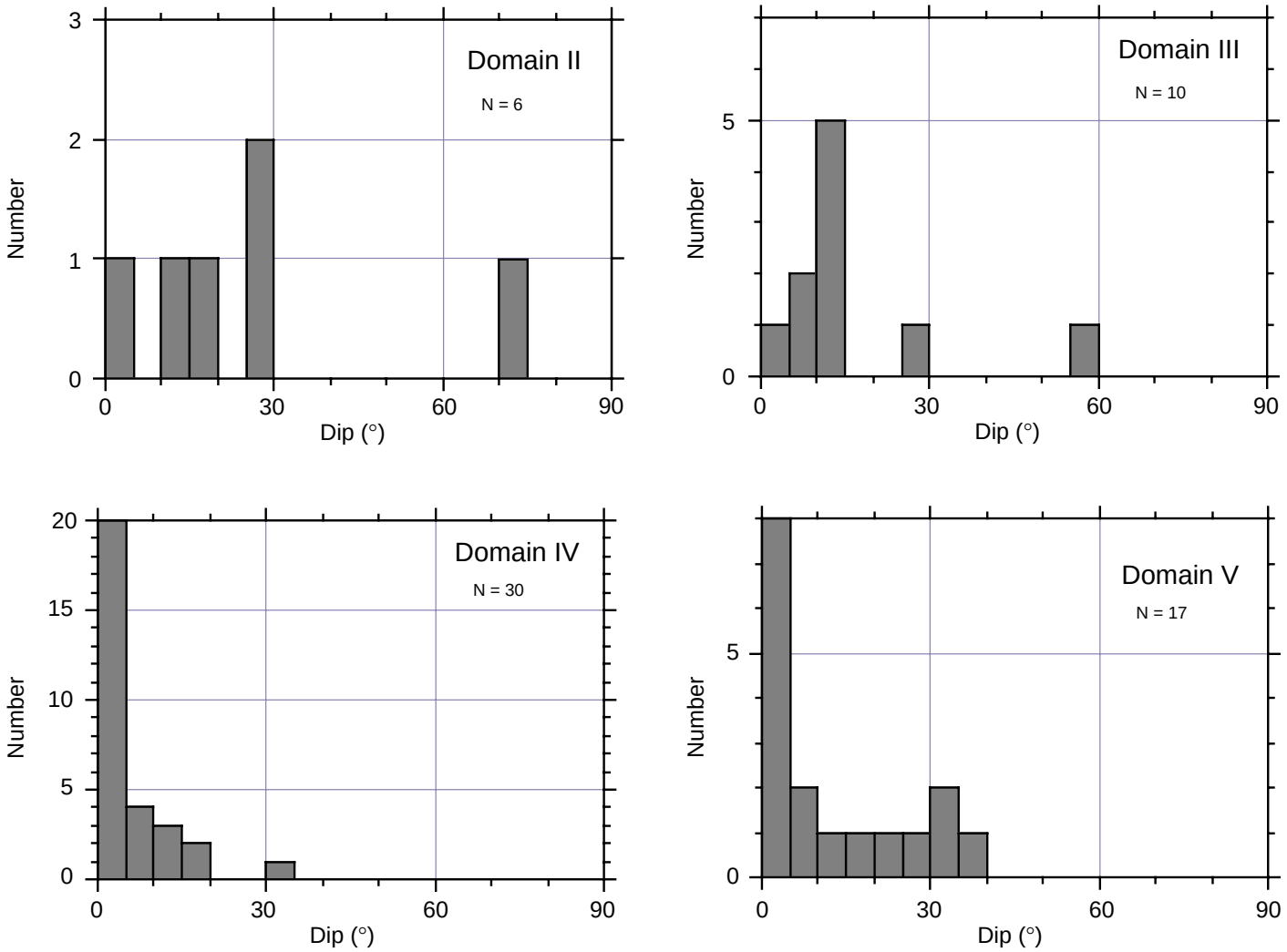

Figure F23. Example of steep dip-slip (normal?) fault cutting through lithologic boundaries (interval 180-1108B-10R-1, 94–120 cm).

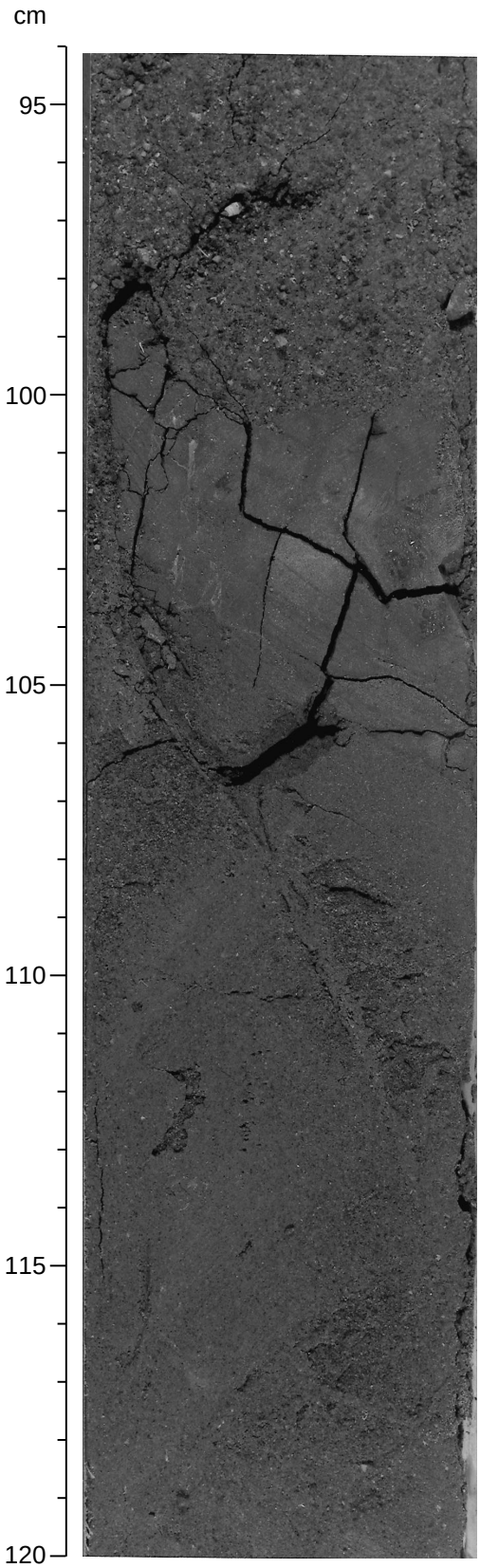

Figure F24. Histogram of the total fracture/fault population measured at Site 1108. N = number of collected data.

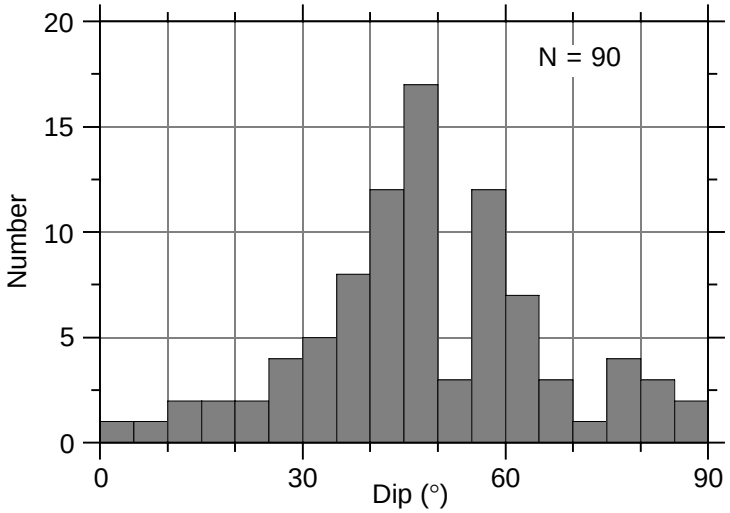

Figure F25. Diagram of dip of fault vs. plunge of the corresponding slickenlines. The linear correlation is typical of pure dip-slip fault kinematics. SS = strike slip; OS = oblique slip; DS = dip slip.

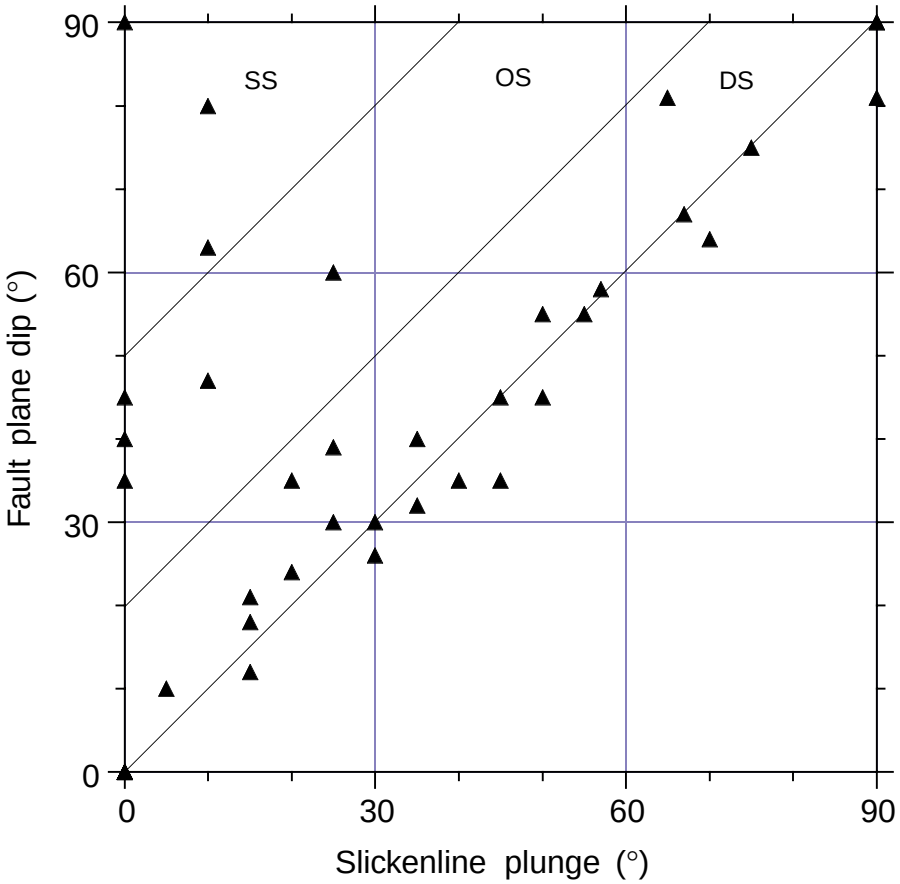

Figure F26. A. Diagram of Section 180-1108B-18R-3 showing the gradual vertical transition from intact unbroken silty material to progressively fragmented facies (fault Domain III). (Continued on next page.)

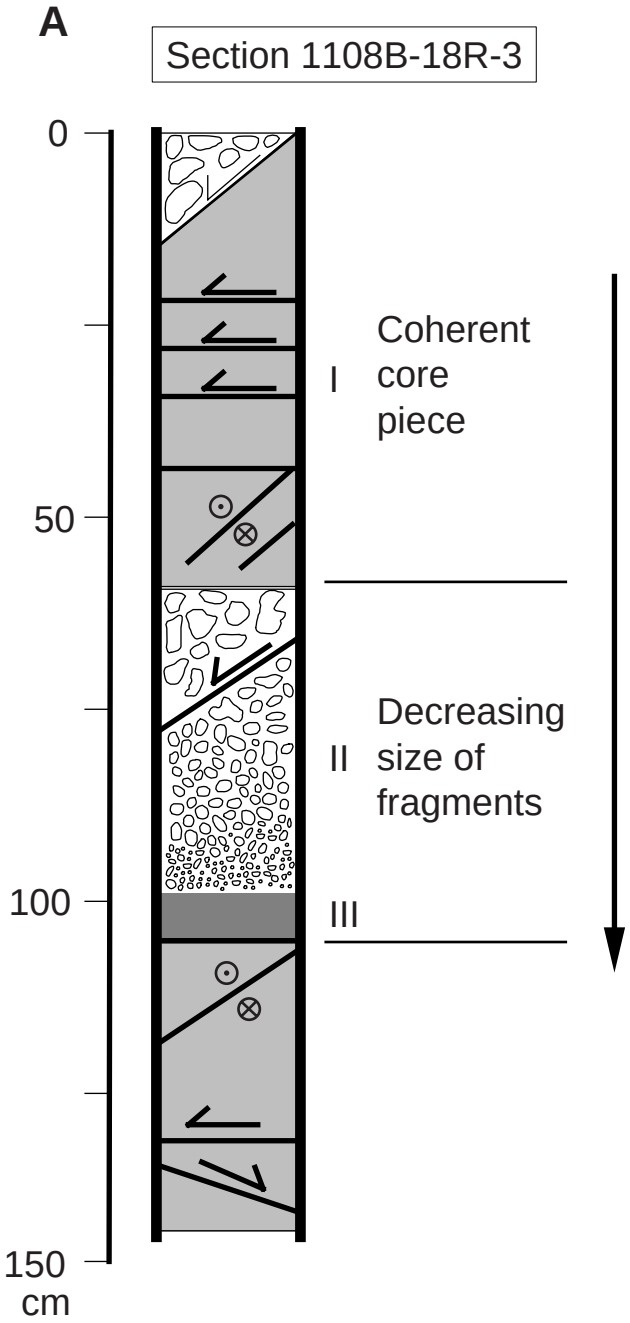

Figure F26 (continued). B. Diagram of Section 180-1108B-19R-4 showing the gradual vertical transition from intact unbroken silty material to progressively fragmented facies (fault Domain III).

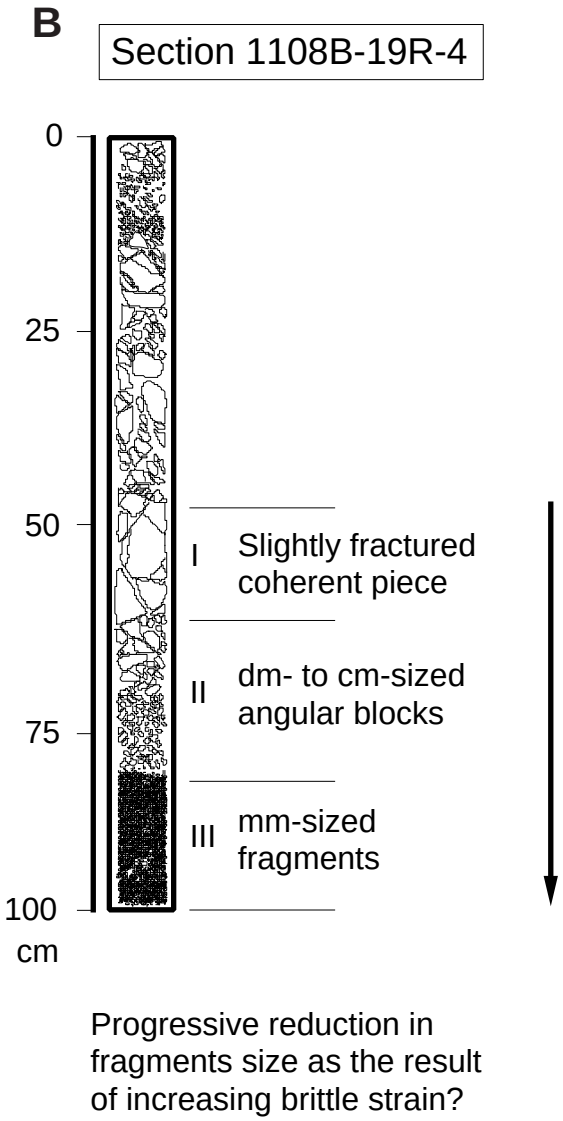

Figure F27. Example of an array of moderately dipping normal faults involving laminated fine-grained sandstones of lithostratigraphic Subunit IVA (interval 180-1108B-44R-1, 8–15 cm).

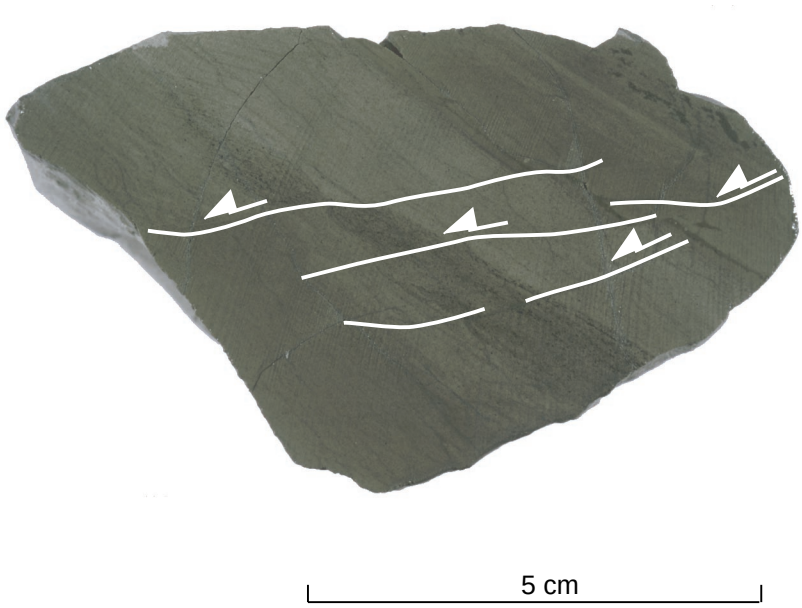

Figure F28. A. Structural sketch of the vertical section drilled at Site 1108. Dip of the fault zones is only indicative. The FZ1 and FZ2 fault zones are described in "Discussion," p. 23. α = bedding dip, ß = fault dip. **B.** Simplified interpretative model for Site 1108 showing the two main normal fault zones (FZ1 and FZ2) developed into the sedimentary sequence. **C.** Simplified interpretative model for possible synthetic or antithetic position of the fault zone at Site 1108 with respect to the Moresby Seamount detachment system.

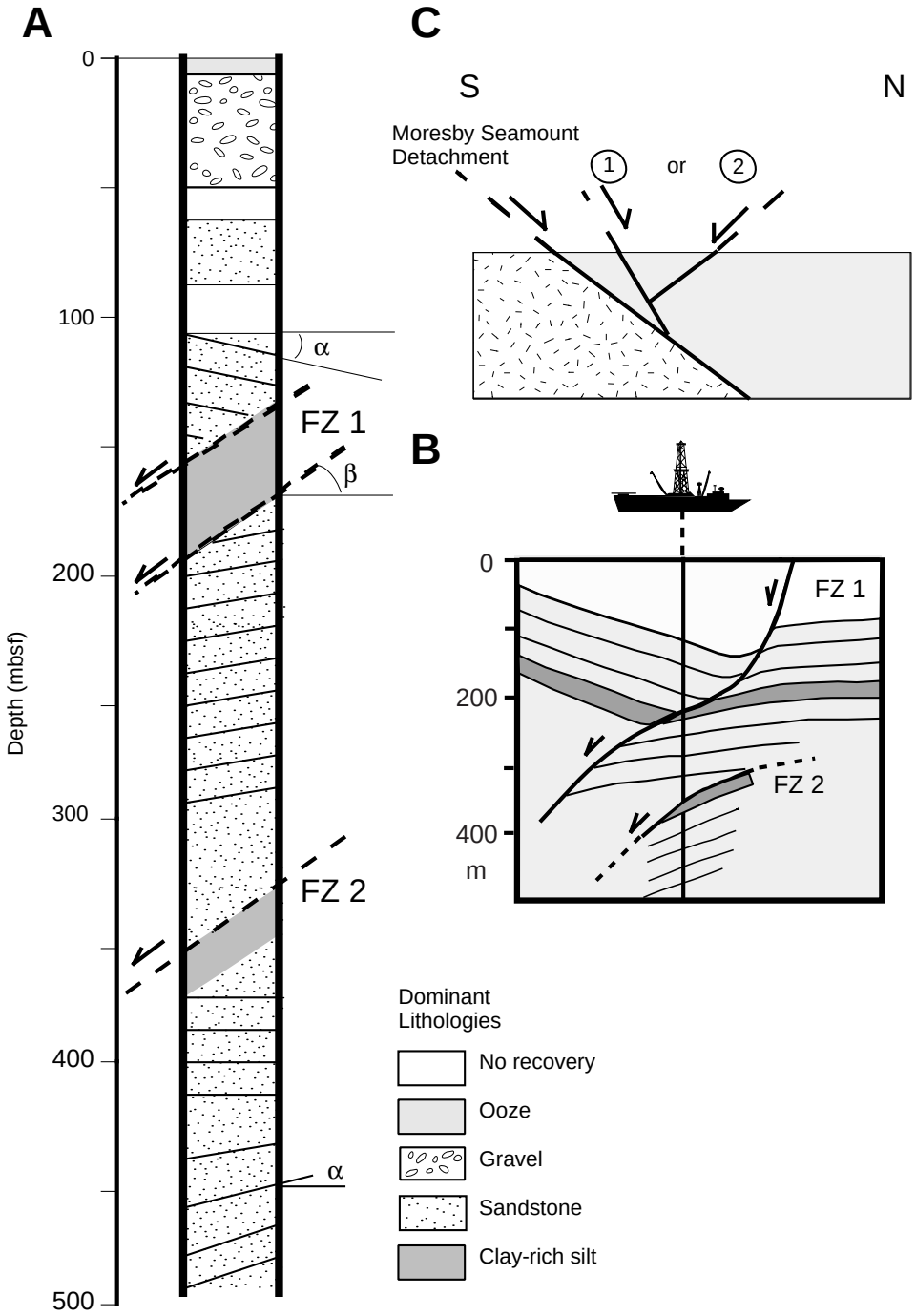

Figure F29. Planktonic foraminifer and calcareous nannofossil zones plotted against age and cores recovered from Hole 1108B. Dashed lines indicate the true zonal boundary may be above or below this level.

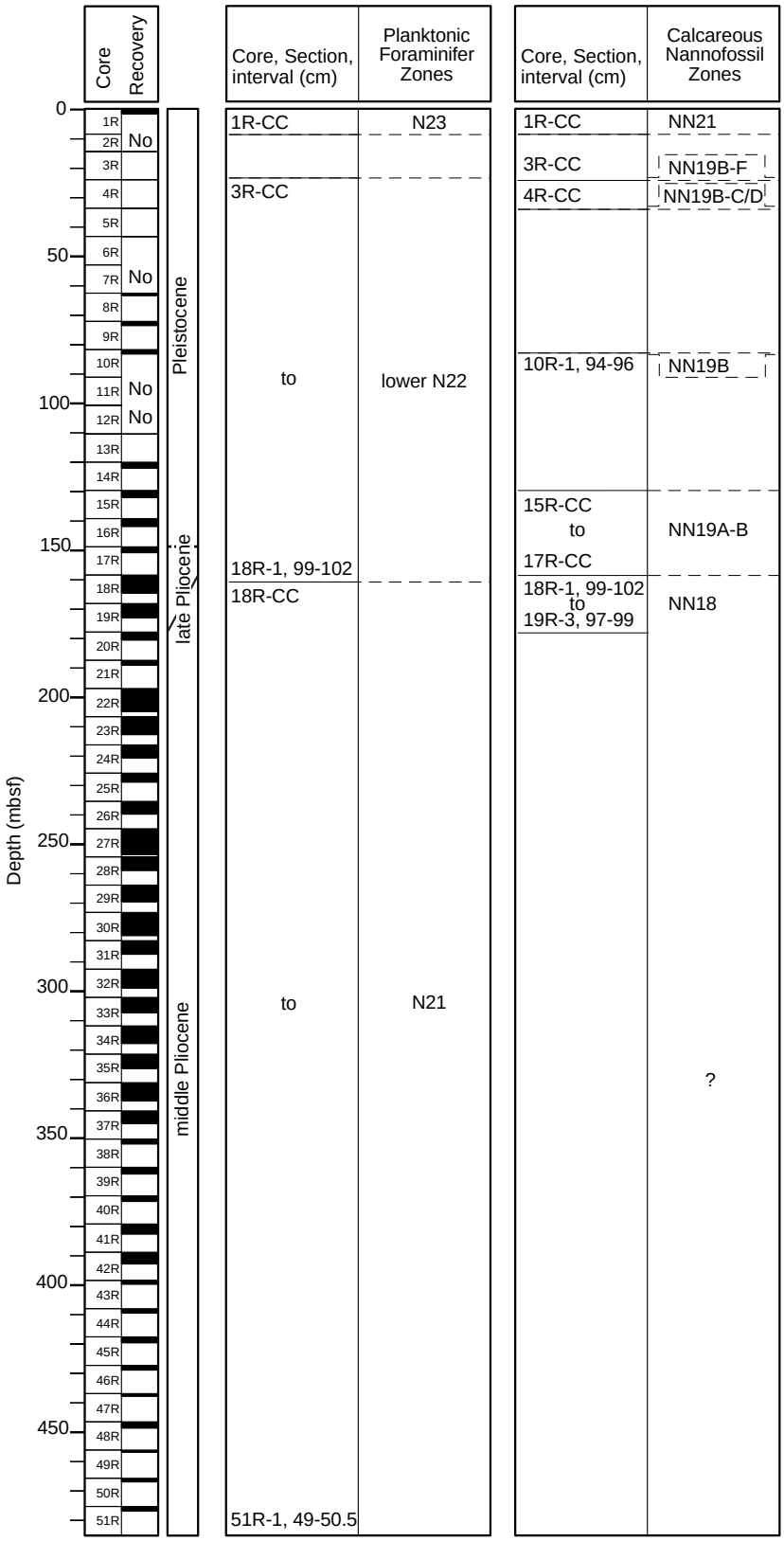

Figure F30. Planktonic foraminifer and calcareous nannofossil **(A)** Sediment accumulation rates estimated in m/m.y., LAD = last-appearance datum, FAD = first-appearance datum; and **(B)** datum events and chron and subchron boundaries plotted against age and depth in Hole 1108B.

A

Datum events	Depth (mbsf)	Age (Ma)
LAD *G. tosaensis*	<14.54	0.65
FAD *G. c. hessi*	14.54 - 24.12	0.75
LAD *H. sellii*	14.54 - 24.12	1.25
LAD *C. macintyrei*	<82.84	1.67
FAD *G. oceanica*	>82.84	1.75
Bottom Olduvai	159 - 162	1.95
LAD *D. brouweri*	150.99 - 159.59	1.95
FAD *G.truncatulinoides*	159.59 - 164.76	2.58
Matuyama / Gauss	172	2.58
Top Kaena	360	3.04
Top Mammoth	428	3.22
FAD *G. tosaensis*	>475.99	3.35

B

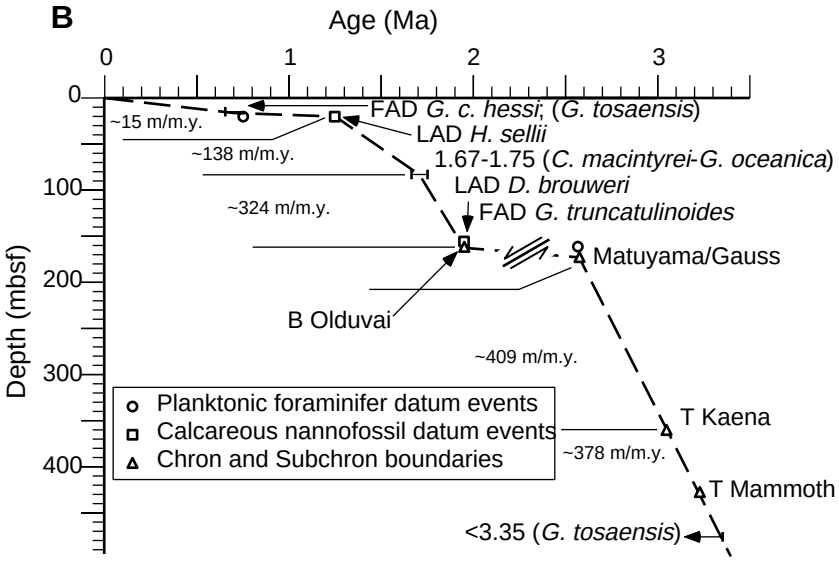

Figure F31. Comparison of susceptibility data (uncorrected for volume) for Hole 1108B from long-core measurements using the MST and AMST.

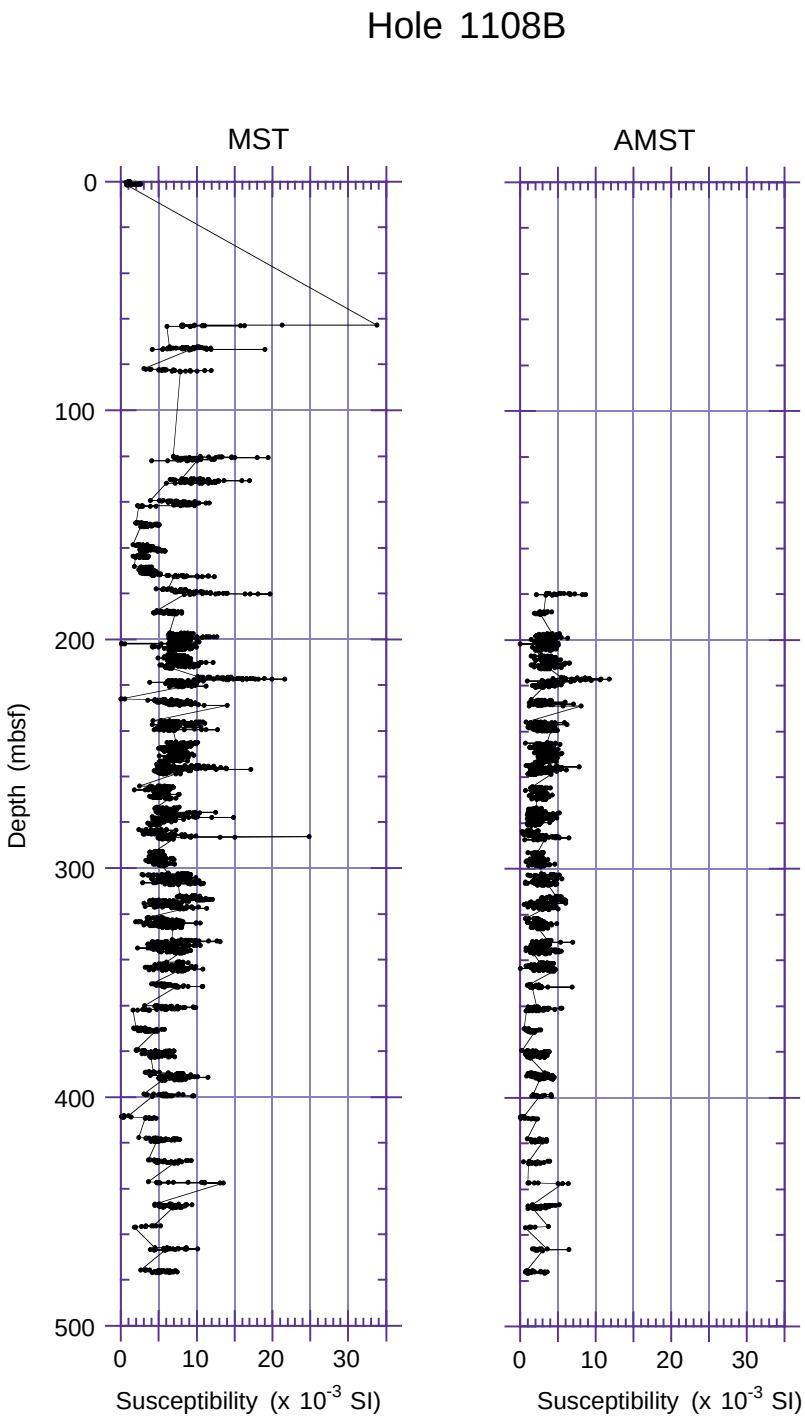

Figure F32. Magnetic susceptibility and its anisotropy (AMS) data for discrete samples from Hole 1108B. Degree of anisotropy (P_j) and the shape parameter (T) calculated according to Jelinek (1981). For fault zones (shaded areas), see **"Structural Geology,"** p. 19.

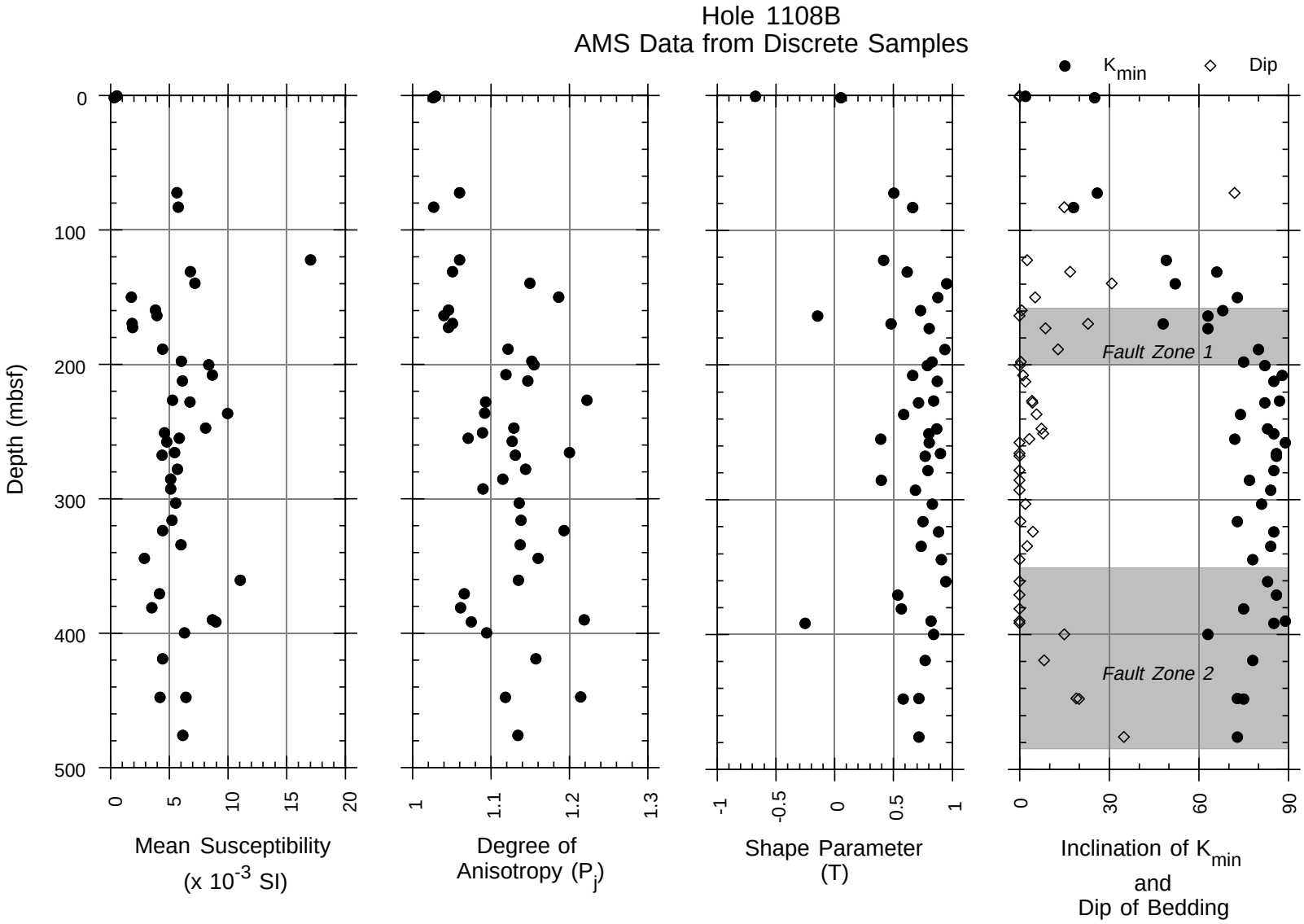

Figure F33. AF demagnetization behavior of discrete samples from working halves of core sections. **A.** Sample 180-1108B-18R-4, 58–60 cm (163.68–163.70 mbsf). Steep downward direction; this sample was from within a fault zone. **B.** Sample 180-1108B-29R-4, 41–43 cm (267.64–267.66 mbsf). Shallow downward overprint. **C.** Sample 180-1108B-42R-1, 96–98 cm (389.96–389.98 mbsf). Reversed polarity ChRM. **D.** Sample 180-1108B-35R-2, 67–69 cm (323.77–323.79 mbsf). Normal polarity ChRM. Vector plots: horizontal component = filled circles; vertical component = open circles. Stereonet plots: lower hemisphere = filled circles; upper hemisphere = open circles. NRM = natural remanent magnetization; Div. = division; Jo = NRM intensity.

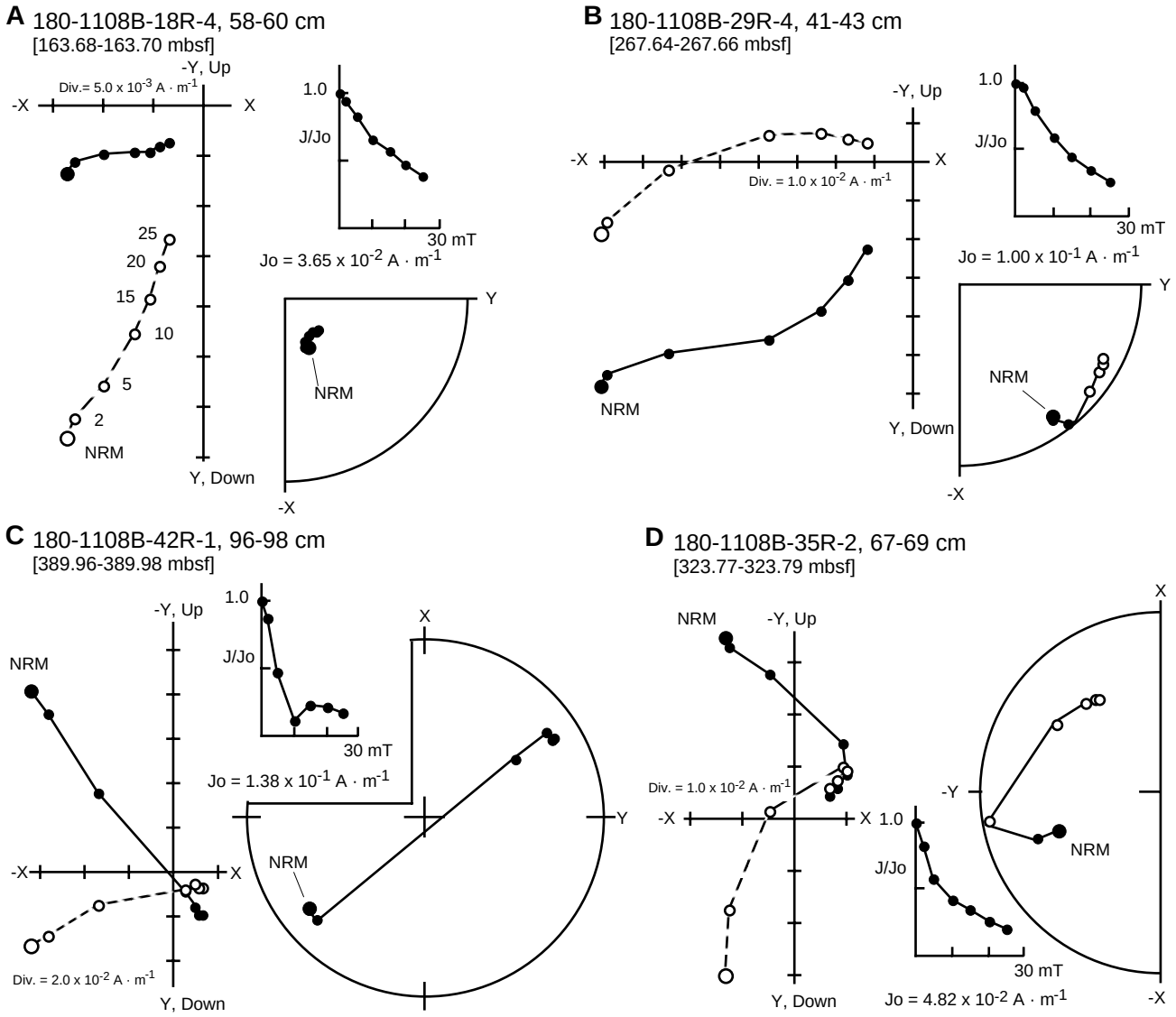

Figure F34. Downhole plots of intensity, inclination, declination, magnetostratigraphic interpretation, and paleontologic data from Hole 1108B. **A.** Data from long cores after AF demagnetization at 20 mT shown as filled circles; data from discrete samples after AF demagnetization at 25 mT shown as open circles. Chrons: C1n = Brunhes (0.0–0.78 Ma); C1r = upper part of the Matuyama (0.78–1.77 Ma); C2n = Olduvai (1.77–1.95 Ma); C2r = lower part of the Matuyama (1.95–2.58 Ma); C2An.1n = upper part of the Gauss (2.58–3.04 Ma); C2An.1r = Kaena (3.04–3.11 Ma); C2An.2n = middle part of the Gauss (3.11–3.22 Ma); C2An.2r = Mammoth (3.22–3.33 Ma). Ages according to Berggren et al. (1995). For paleontologic zonations, see **"Biostratigraphy,"** p. 24. **(Figure shown on next two pages.)**

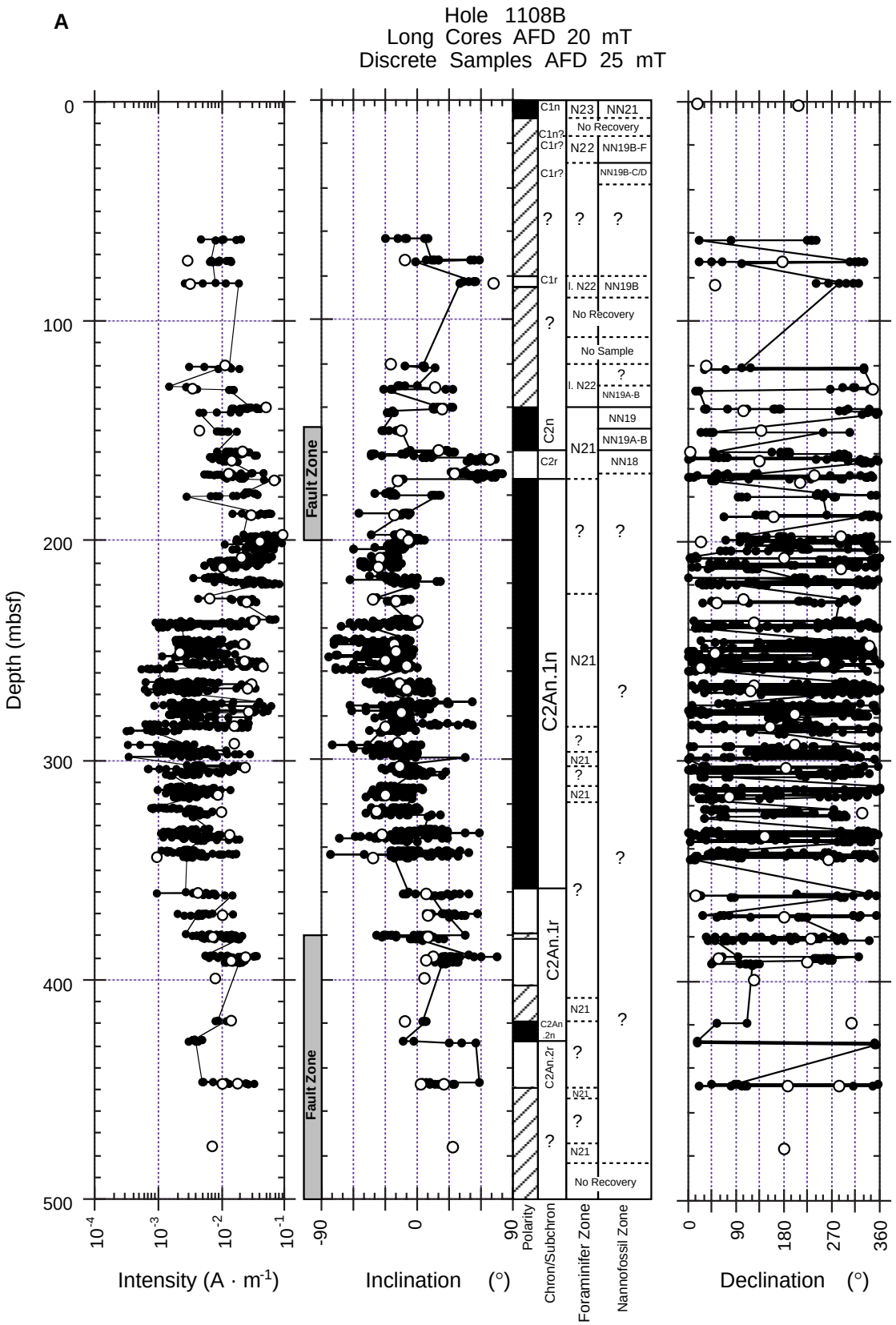
A
Hole 1108B
Long Cores AFD 20 mT
Discrete Samples AFD 25 mT
Depth (mbsf)
0
100
200
300
400
500
Fault Zone
Fault Zone
C1n
C1n?
C1r?
C1r?
C1r
C2n
C2r
C2An.1n
C2An.1r
C2An .2n
C2An.2r
N23
NN21
No Recovery
N22
NN19B-F
NN19B-C/D
l. N22
NN19B
No Recovery
No Sample
l. N22
NN19A-B
NN19
NN19A-B
N21
NN18
N21
N21
N21
N21
N21
No Recovery
10-4
10-3
10-2
10-1
Intensity (A · m-1)
-90
0
90
Inclination (°)
Polarity
Chron/Subchron
Foraminifer Zone
Nannofossil Zone
0
90
180
270
360
Declination (°)

Figure F34 (continued). B. Data from discrete samples after AF demagnetization at 25 mT: in situ data shown as filled circles, tilt-corrected data shown as open boxes. Polarity: black = normal; white = reversed; diagonal lines = undetermined.

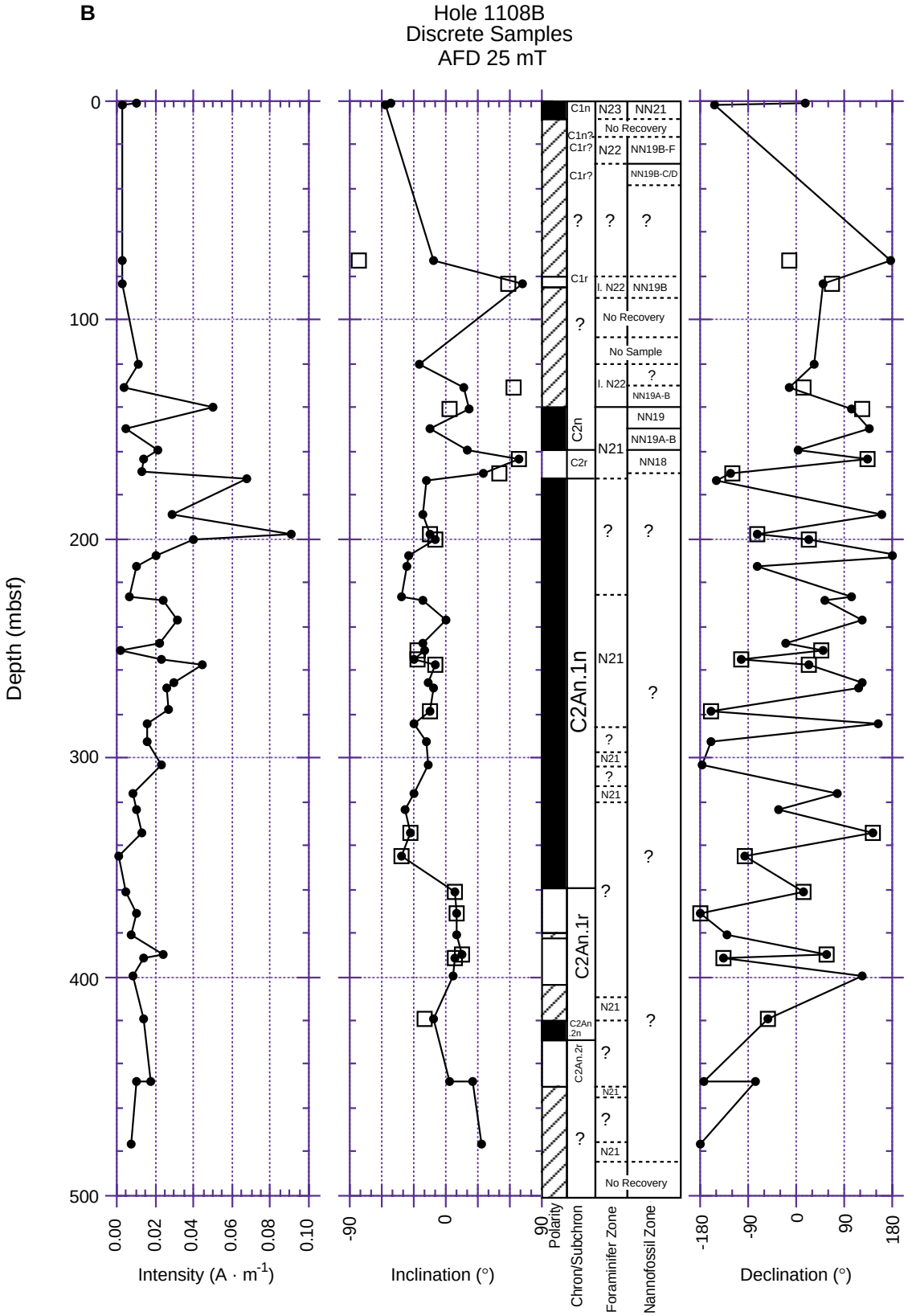

Figure F35. Depth profiles of interstitial water constituents at Site 1108. (Continued on next page.)

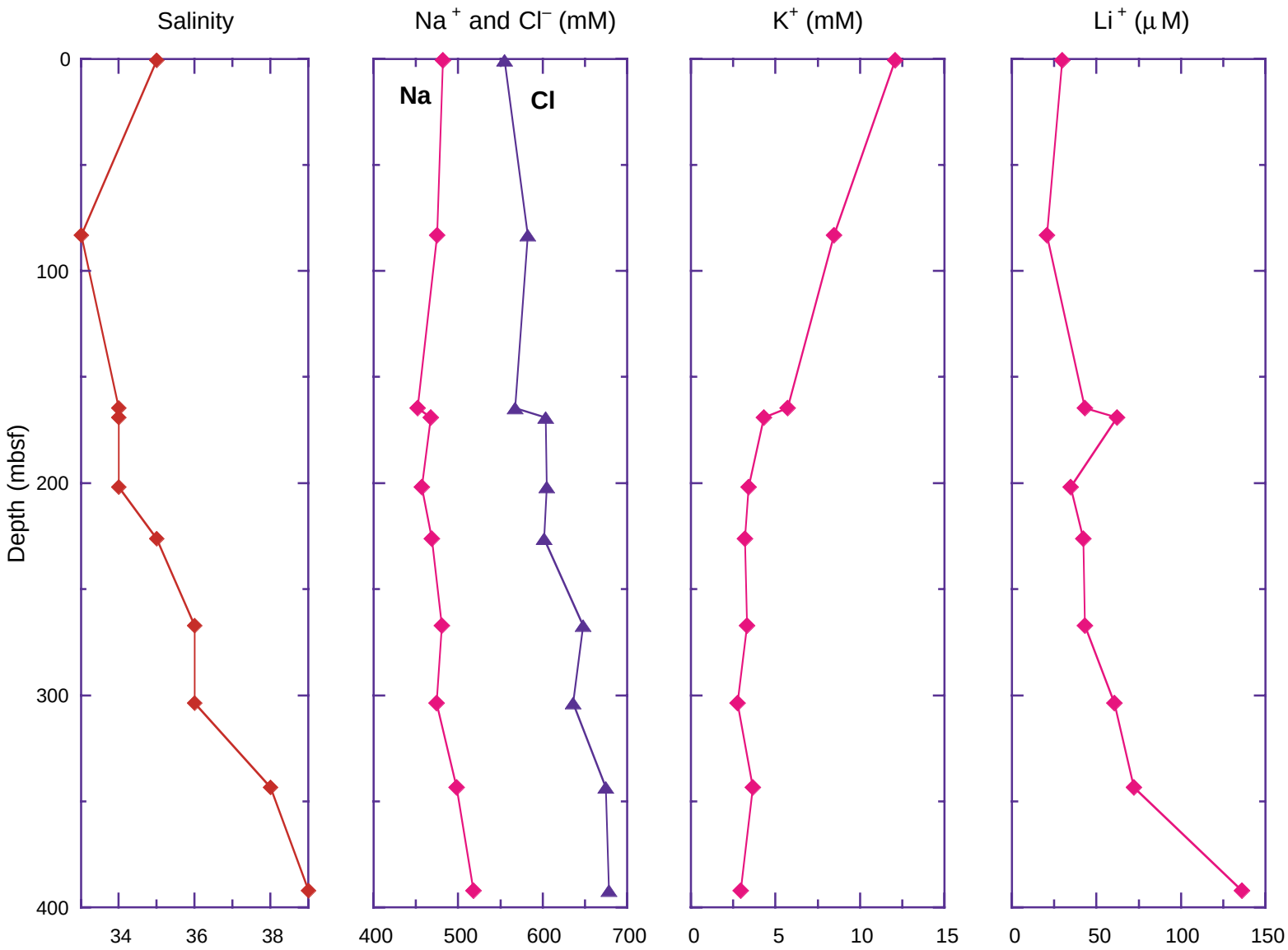

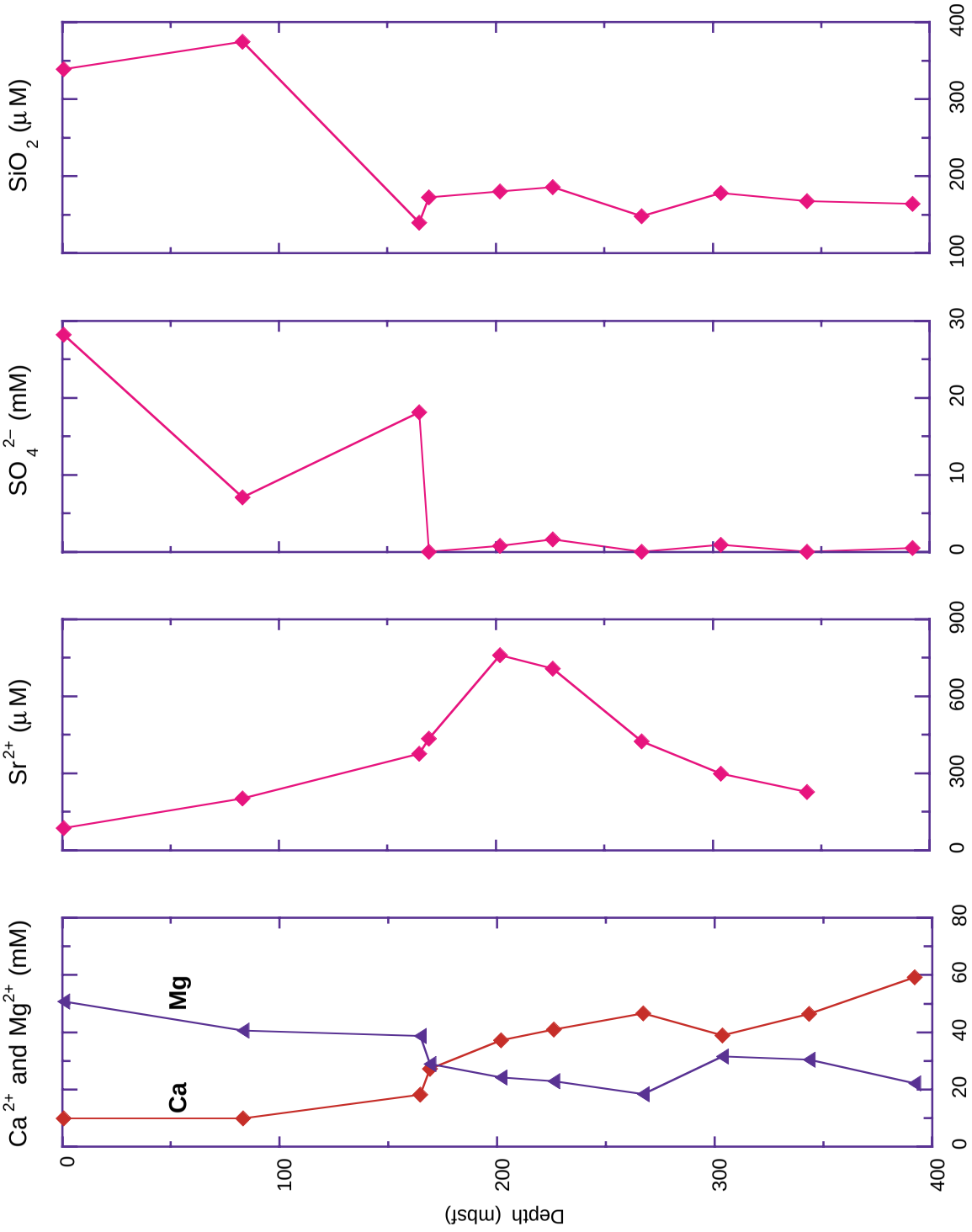

Figure F35 (continued).

Figure F36. Variations in the Ca/Mg ratio as a function of depth in interstitial water from Site 1108.

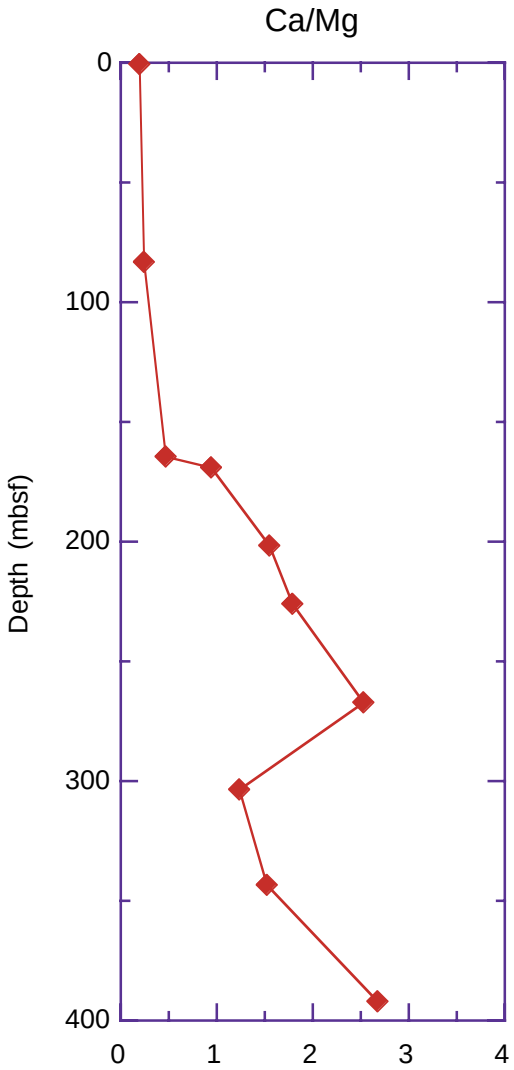

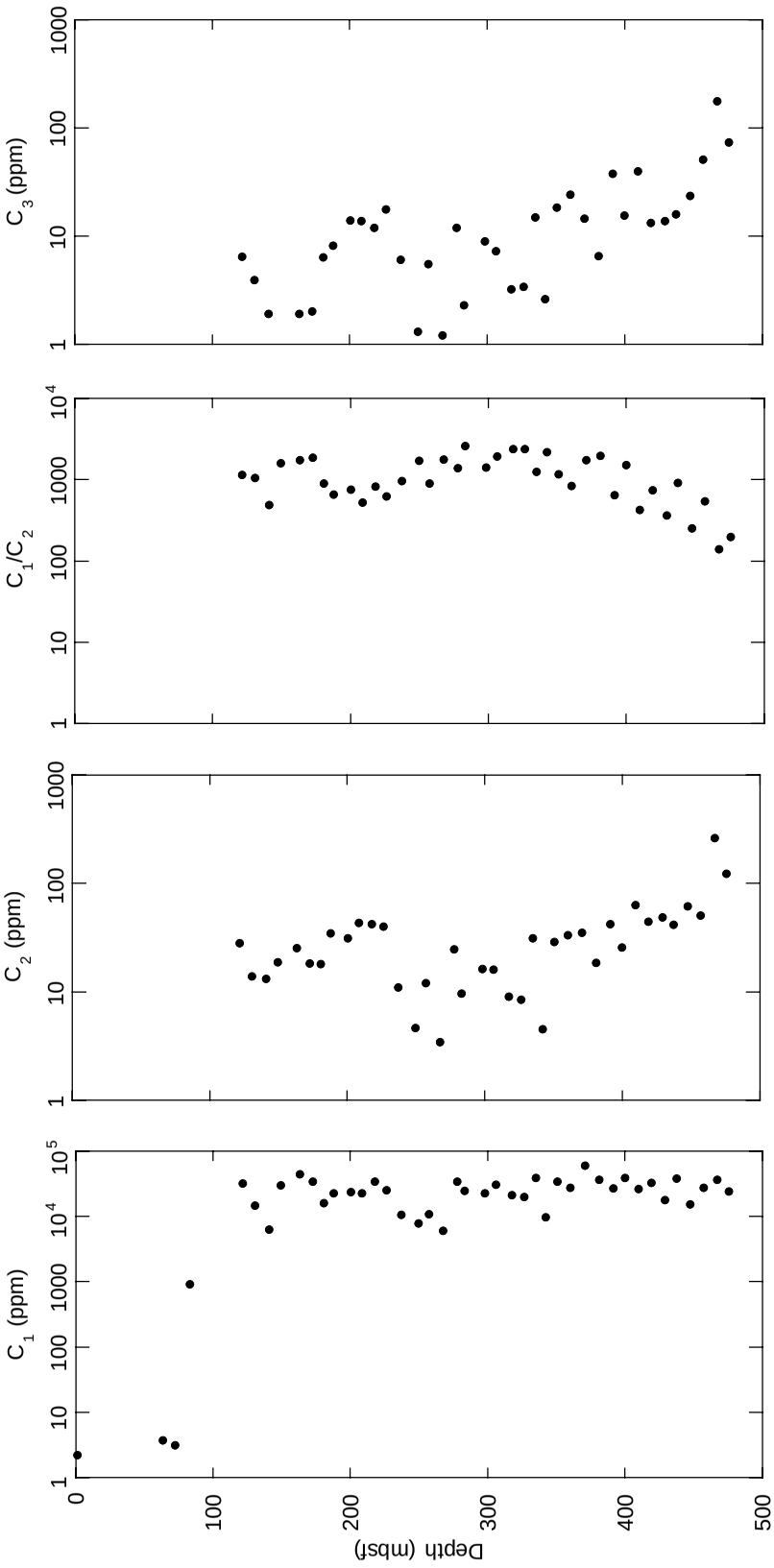

Figure F37. C_1, C_2, and C_3 hydrocarbon profiles.

Figure F38. $CaCO_3$, organic carbon, and C/N ratio profiles.

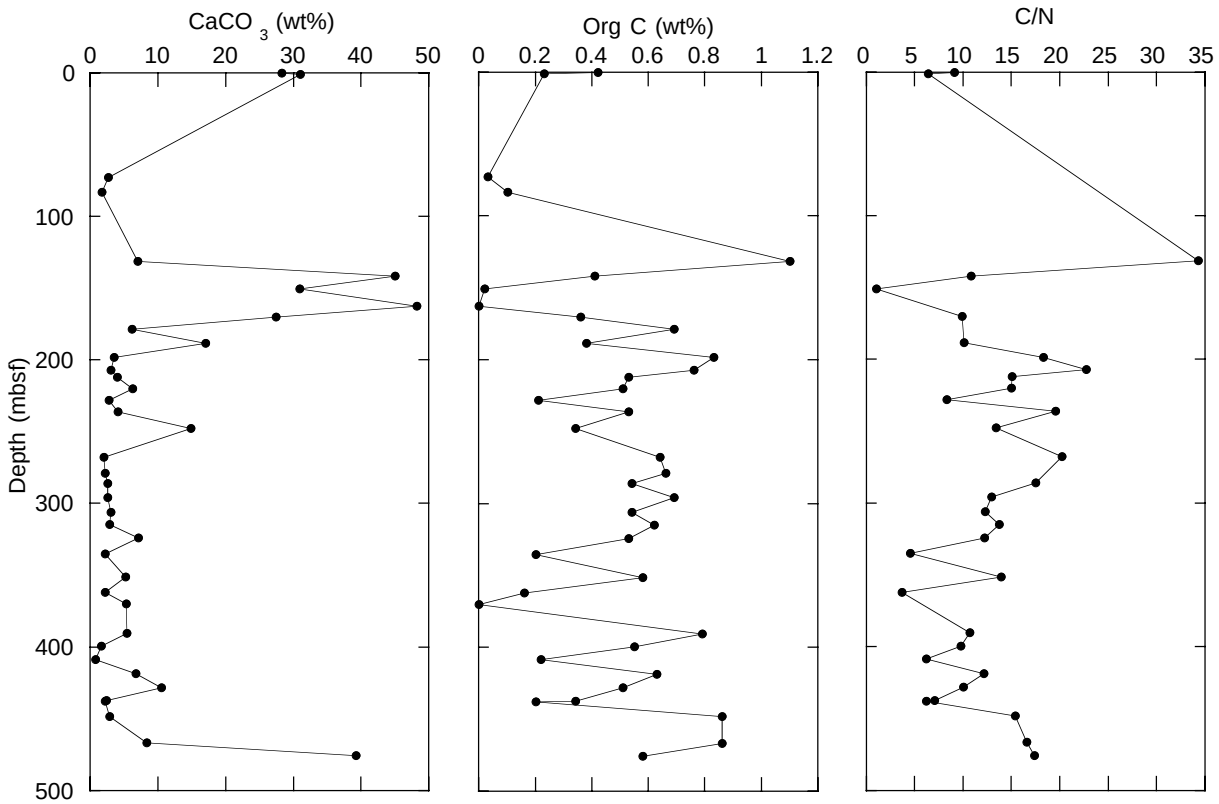

Figure F39. Hole 1108B depth distributions of total bacterial populations (solid circles) and dividing and divided cells (open circles). The solid curve represents a general regression line of bacterial numbers vs. depth in deep-sea sediments (Parkes et al., 1994), with 95% upper and lower prediction limits shown by dashed curves.

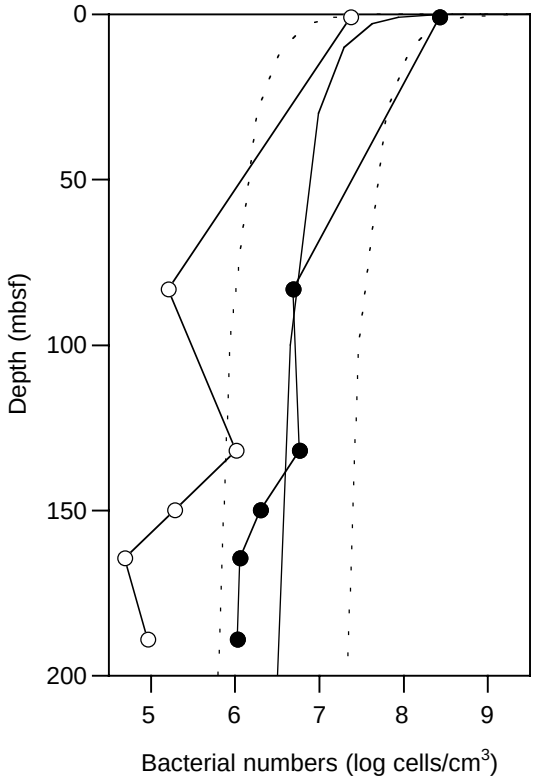

Figure F40. Site 1108 MAD-determined porosity, bulk density, and grain density.

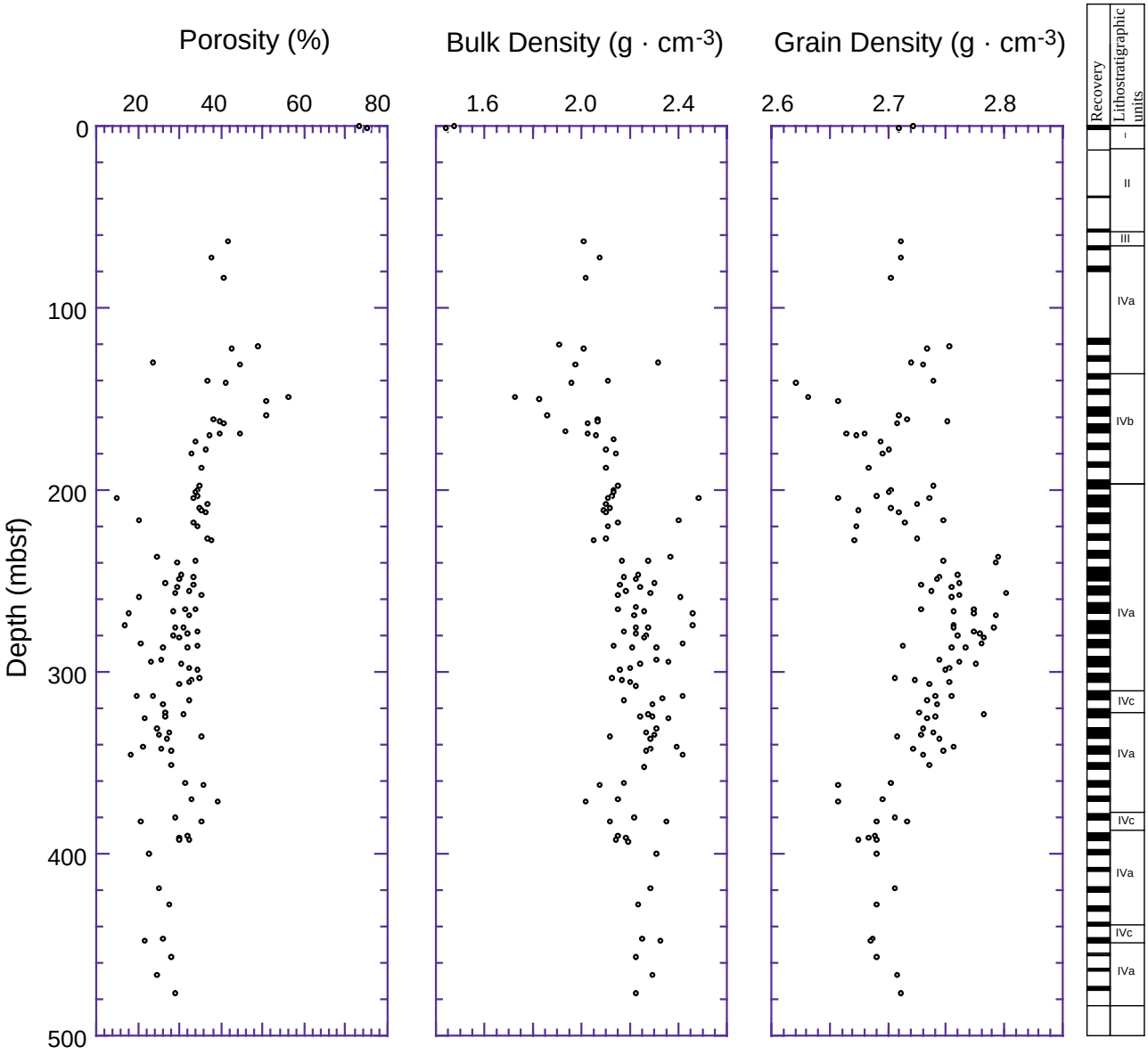

Figure F41. Density derived from GRAPE and index properties measurements.

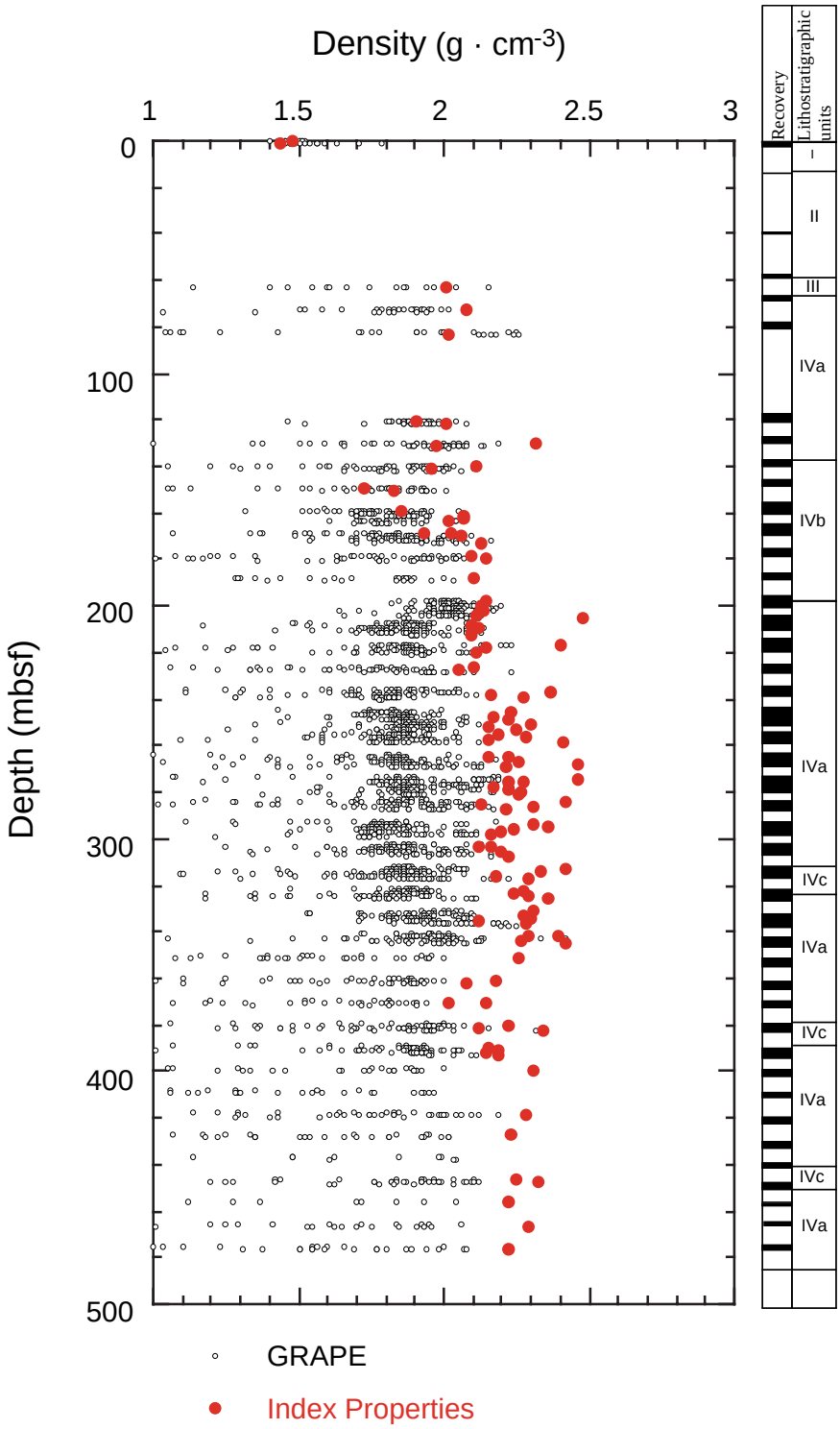

Figure F42. Regression least-squares exponential curves of porosity for (**A**) all data from Hole 1108B and (**B**) data below 63.13 mbsf.

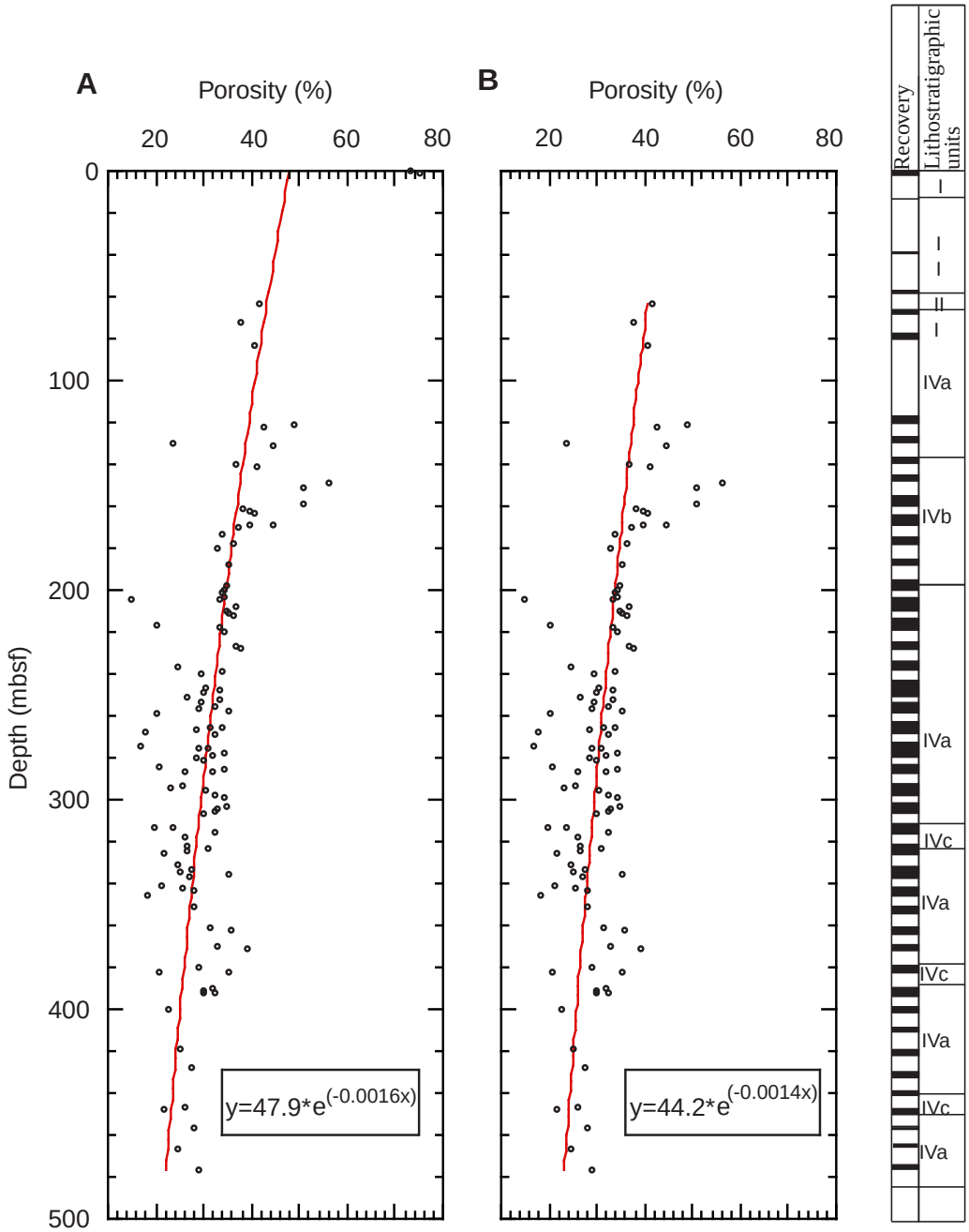

Figure F43. Site 1108 *P*-wave transverse (x, y) and longitudinal (z) velocities.

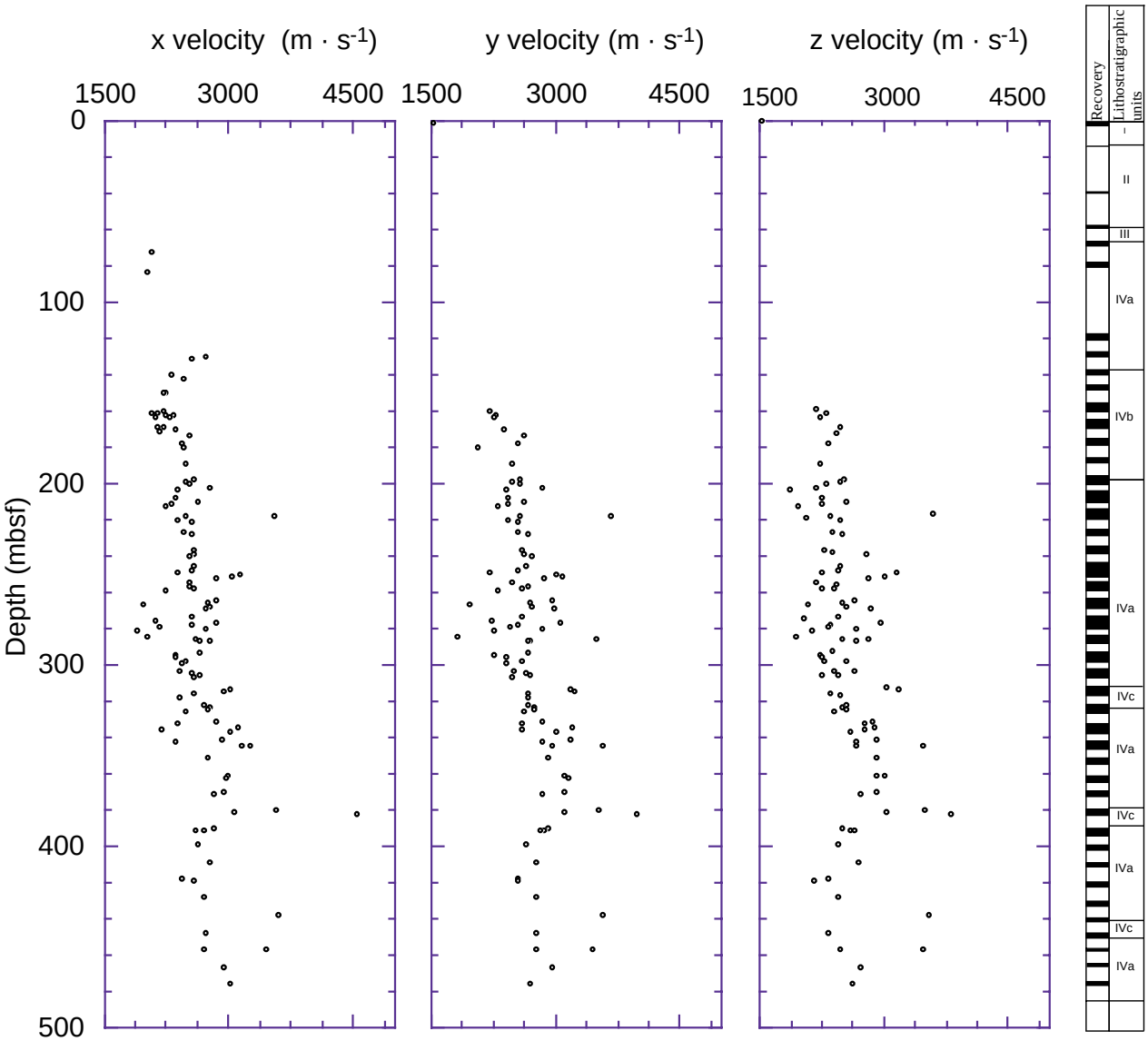

Figure F44. **A**. Longitudinal velocity vs. the average transverse velocity and **B**. *P*-wave anisotropy with depth (see **"Physical Properties,"** p. 28, in the "Explanatory Notes" chapter for method used). A positive anisotropy indicates that the transverse velocity is greater than the longitudinal velocity.

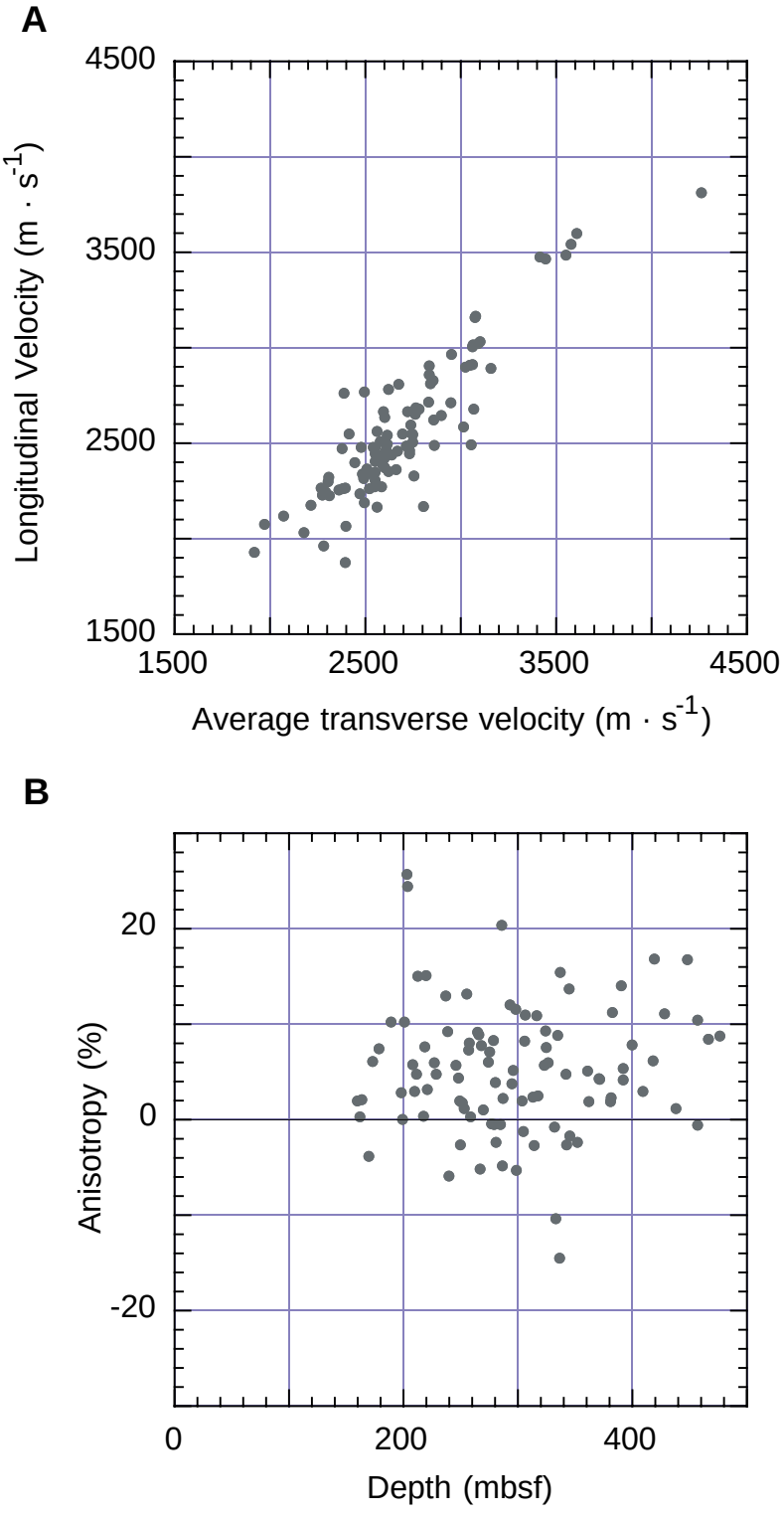

Figure F45. Site 1108 thermal conductivity.

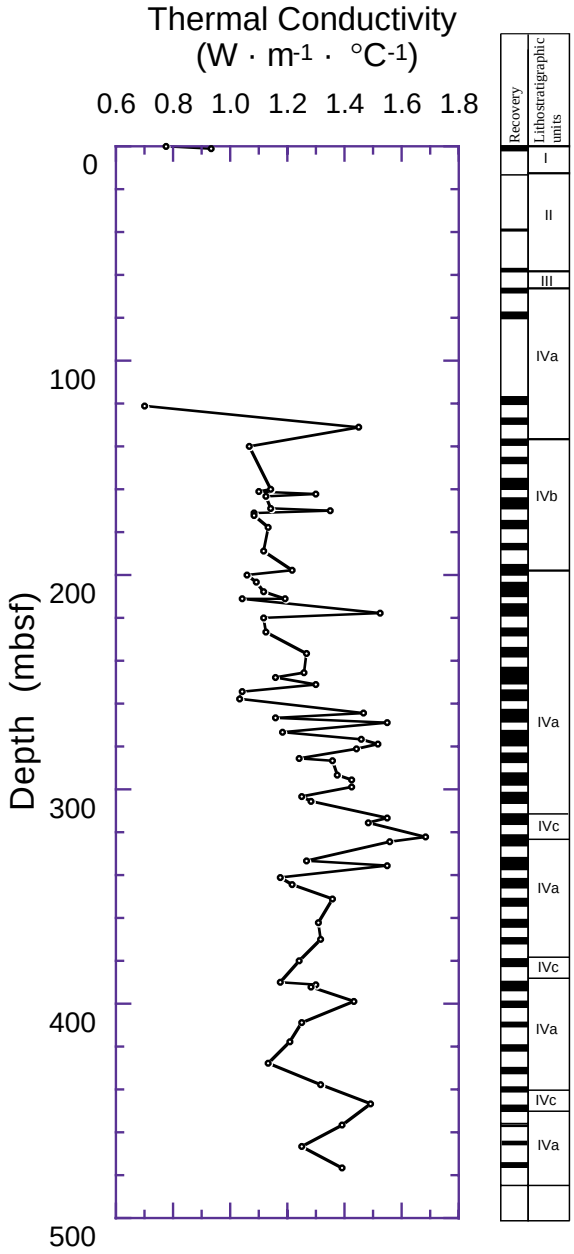

Figure F46. Site 1108 magnetic susceptibility, natural gamma ray (NGR), and remanent magnetic intensity profiles.

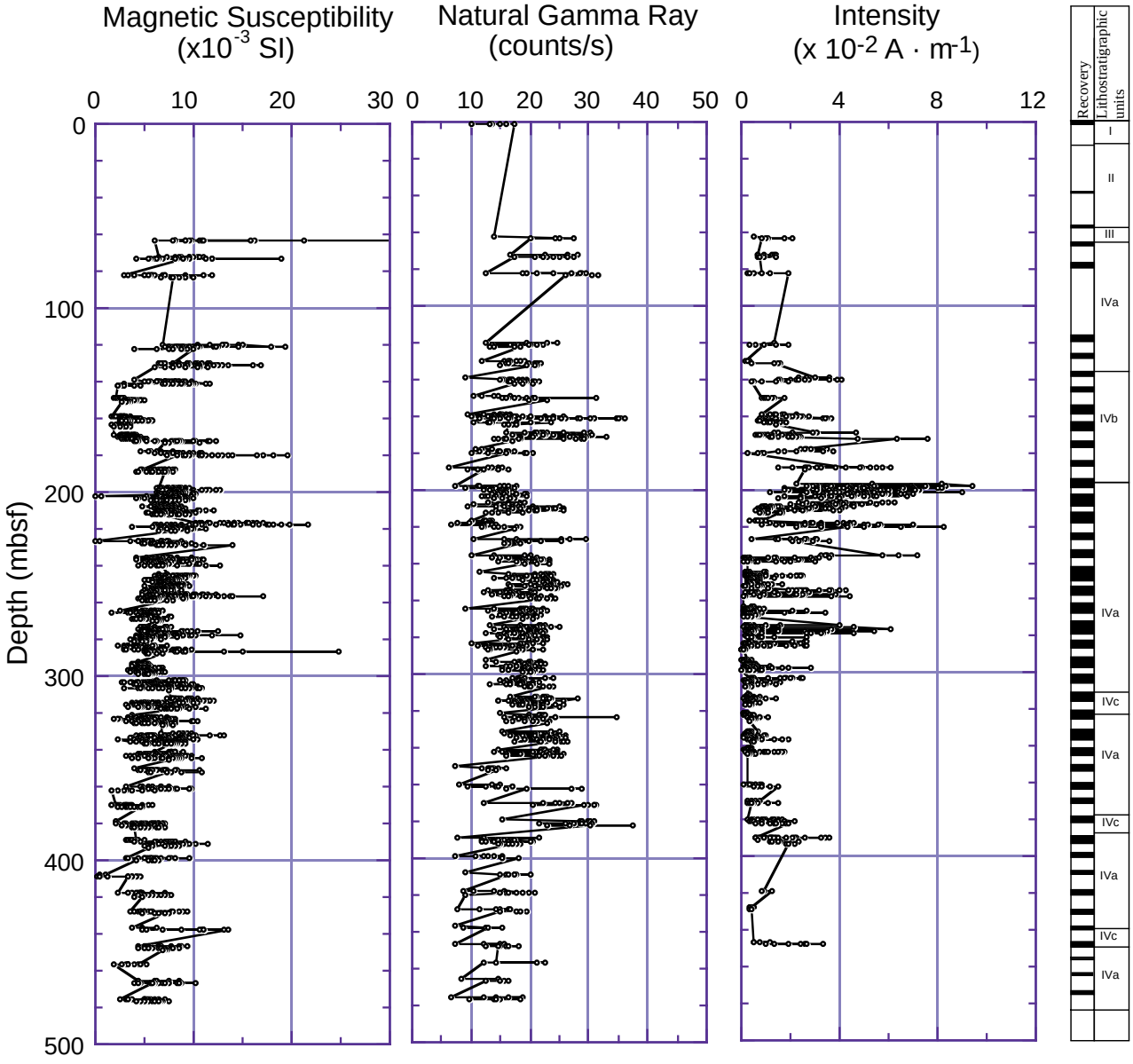

Figure F47. Detailed comparison between grain size and magnetic susceptibility at Site 1108. **A.** 216 to 221 mbsf. (Continued on next page.)

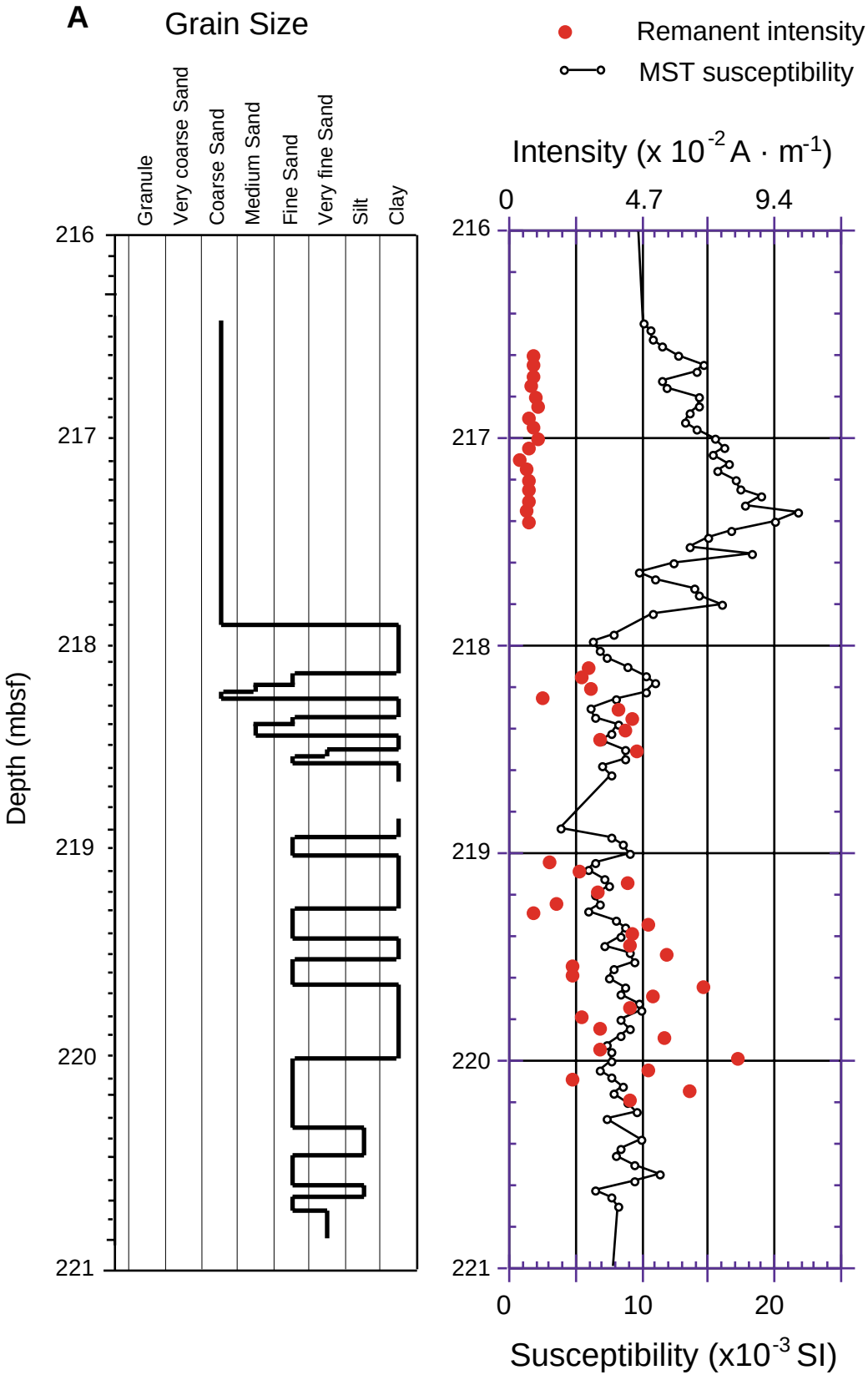

Figure F47 (continued). B. 255 to 259 mbsf.

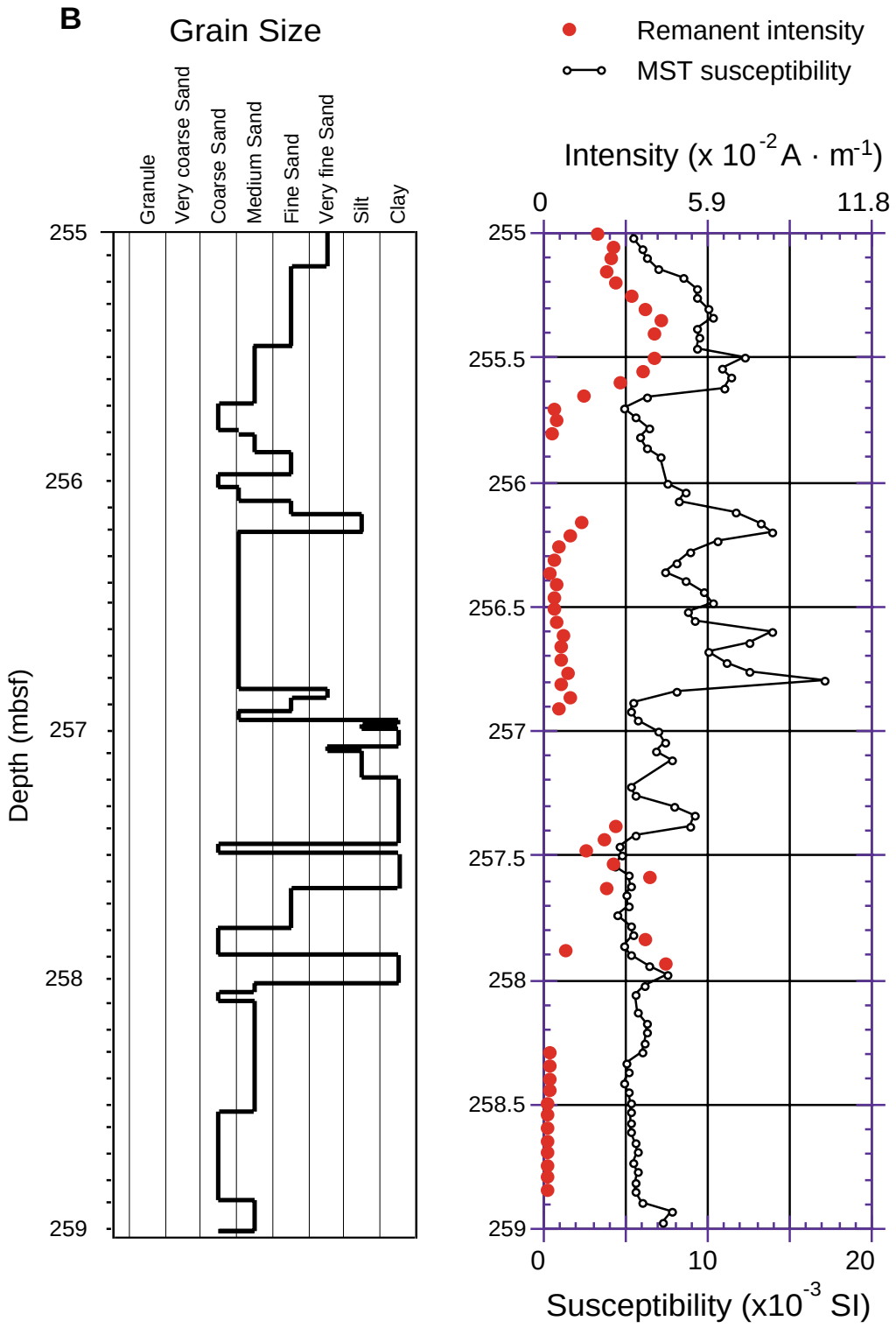

Figure F48. General comparison between grain size and natural gamma ray (NGR) in Hole 1108B. **A**. 0 to 250 mbsf. (Continued on next page.)

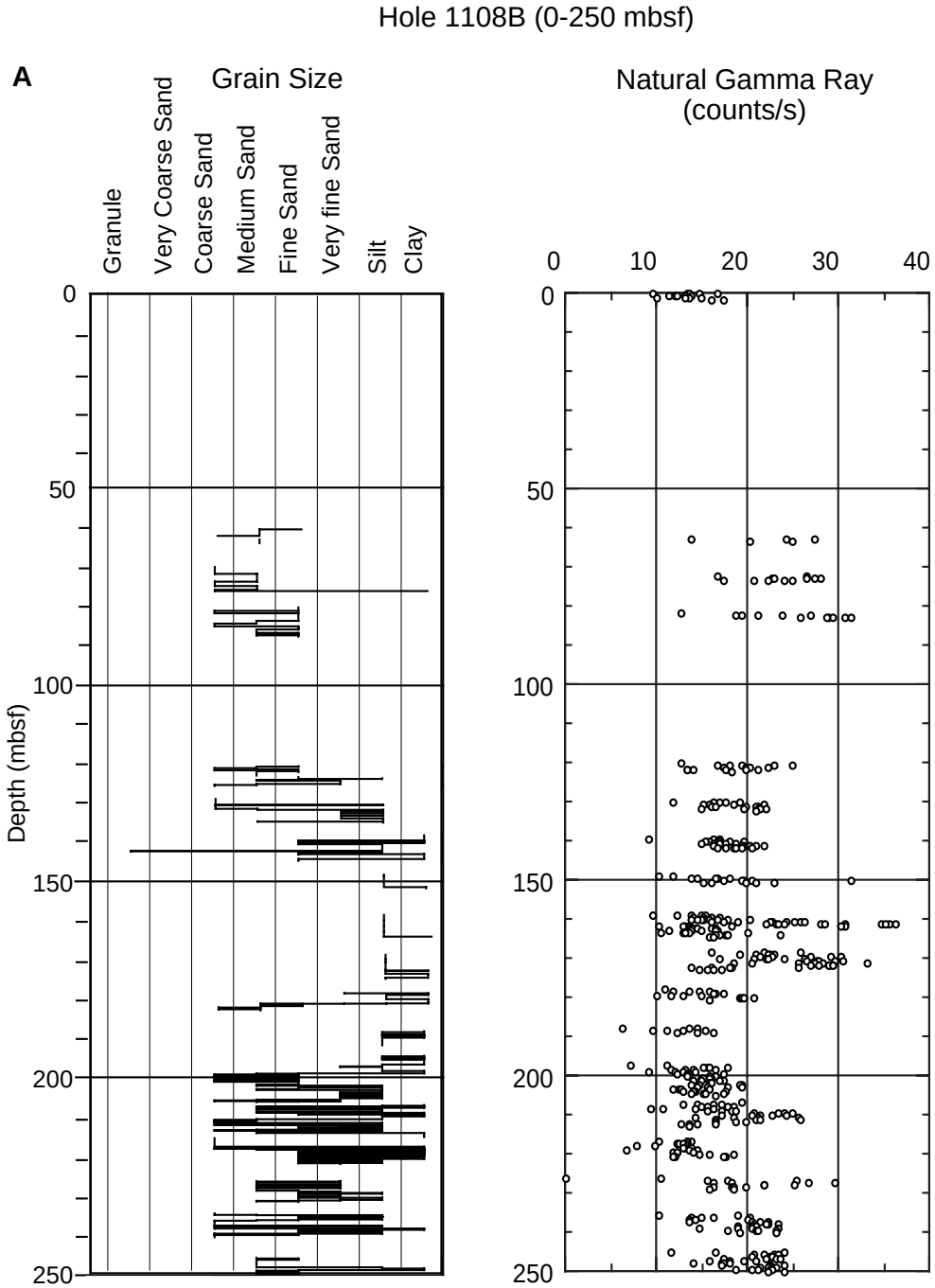

Figure F48 (continued). B. 250 to 477 mbsf.

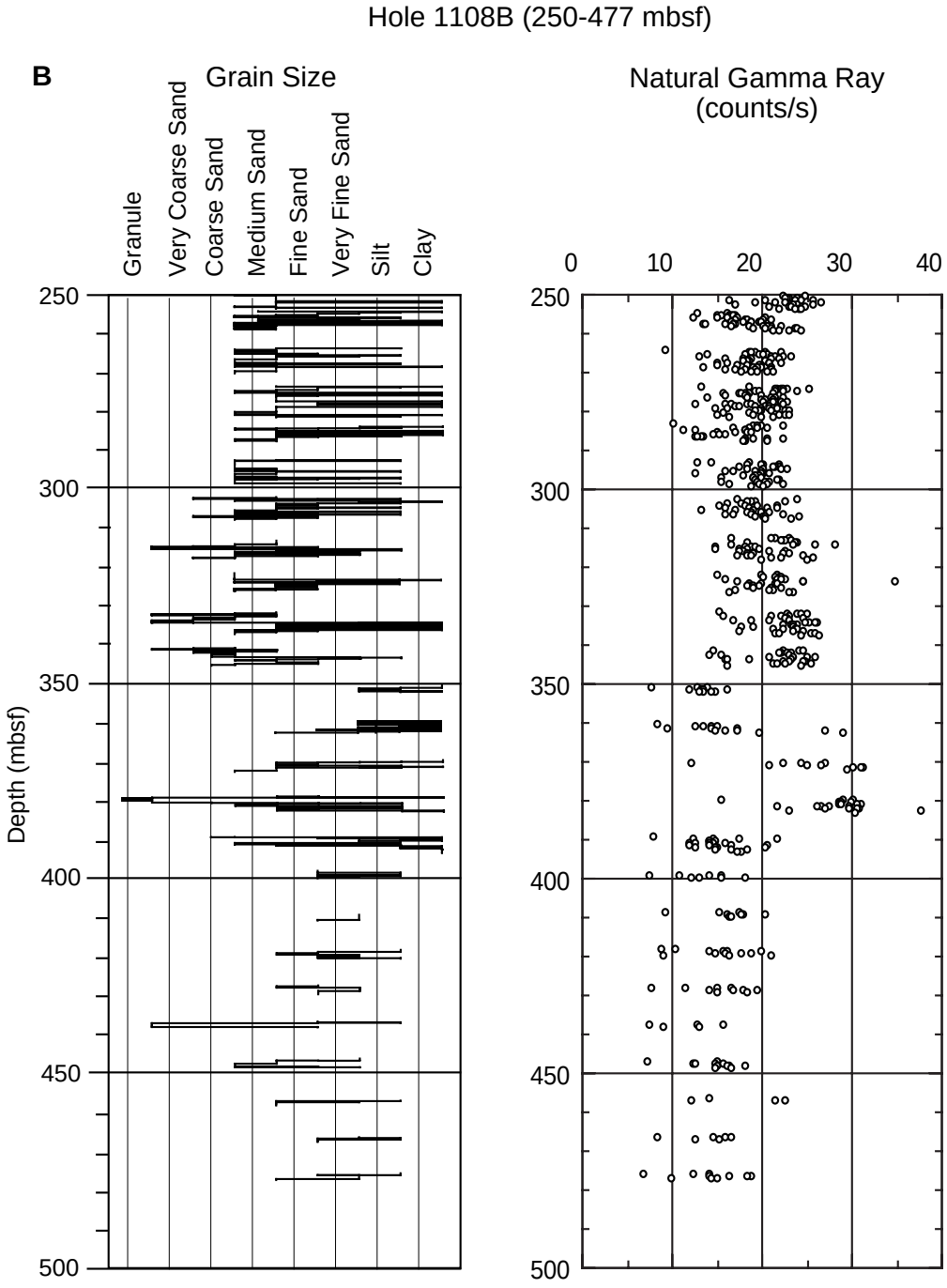

Figure F49. Hole 1108B total gamma ray (HSGR) from the HNGS. Downgoing and upgoing logs labeled in chronological order (up1 to up3).

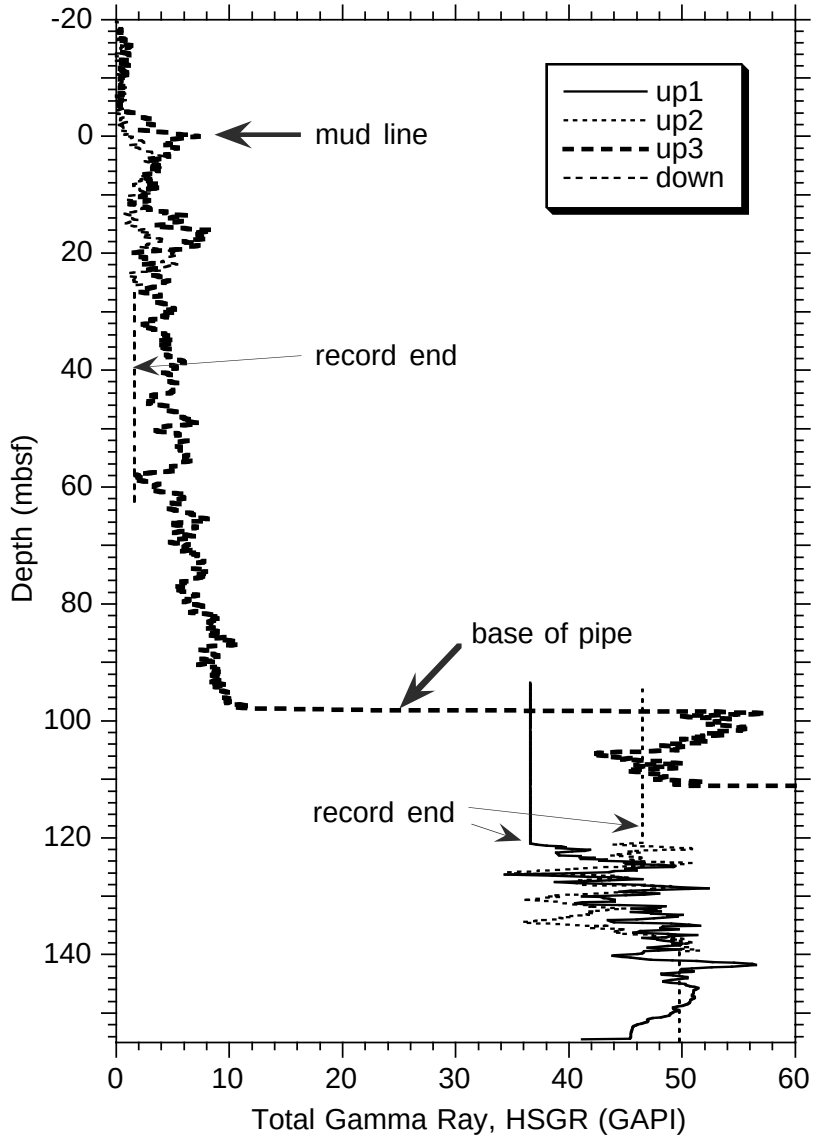

Figure F50. Hole 1108B caliper data (LCAL) from the lithodensity tool (HLDT). Logs are labeled in chronological order.

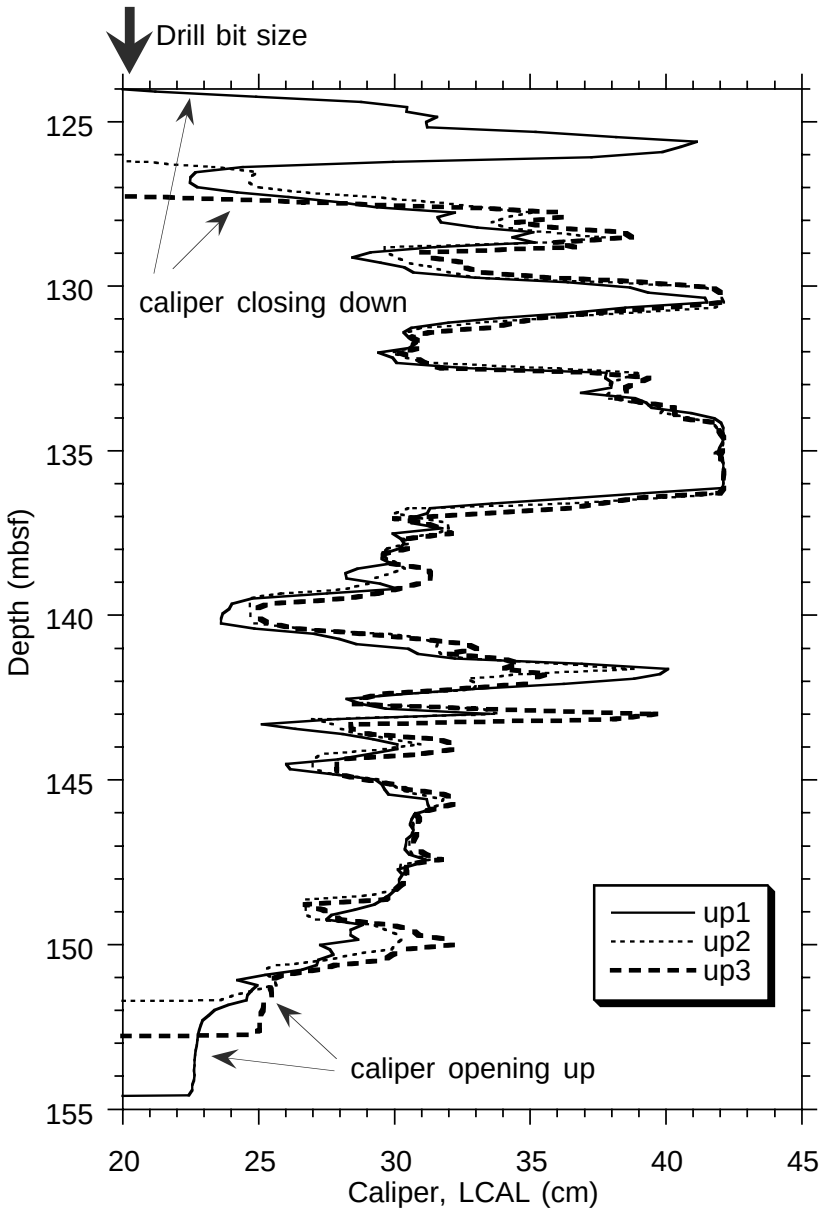

Figure F51. Hole 1108B composite log. From left to right: (1) core number and recovery intervals are shown for comparison; (2) caliper and temperature measurements from the triple combo run; (3) total natural gamma ray (HSGR) and total natural gamma ray minus uranium contribution (HCGR); (4) thorium, uranium, and potassium content; (5) resistivity from the DIT tool, consisting of deep induction (IDPH), medium induction (IMPH), and shallow spherically focused current (SFLU); and (6) neutron limestone-corrected porosity (APLC and FPLC). The temperature measurements were recorded continuously throughout the logging run. The caliper, resistivity, and the portion of the gamma-ray logs below 120 mbsf were recorded during the first pass, and the porosity and the portion of the gamma ray above 112 mbsf were recorded during the third pass.

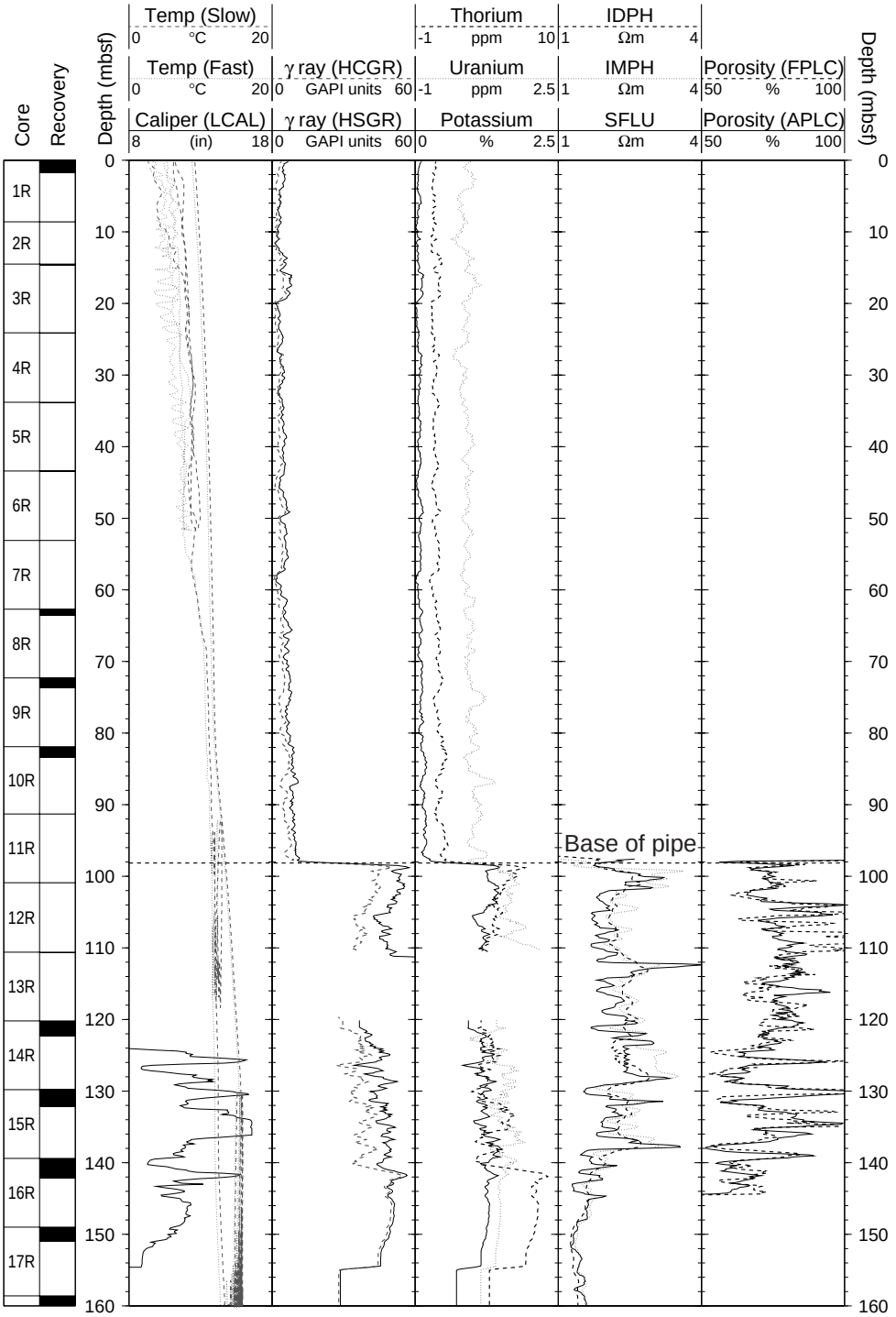

Figure F52. All temperature data from the TLT in and above Hole 1108B. Tfast and Tslow refer to the fast and slow response thermistors, respectively.

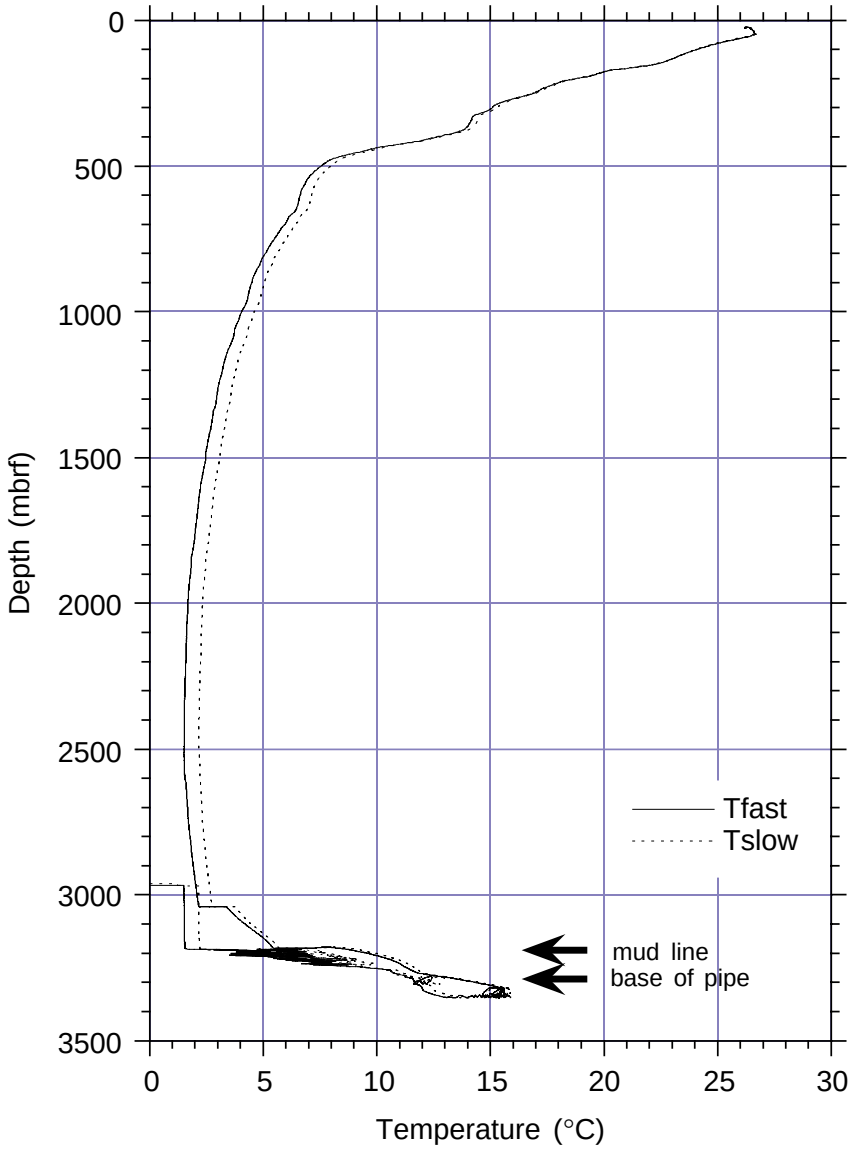

Figure F53. Borehole temperature in Hole 1108B from the TLT. Tfast and Tslow refer to the fast and slow response thermistors, respectively.

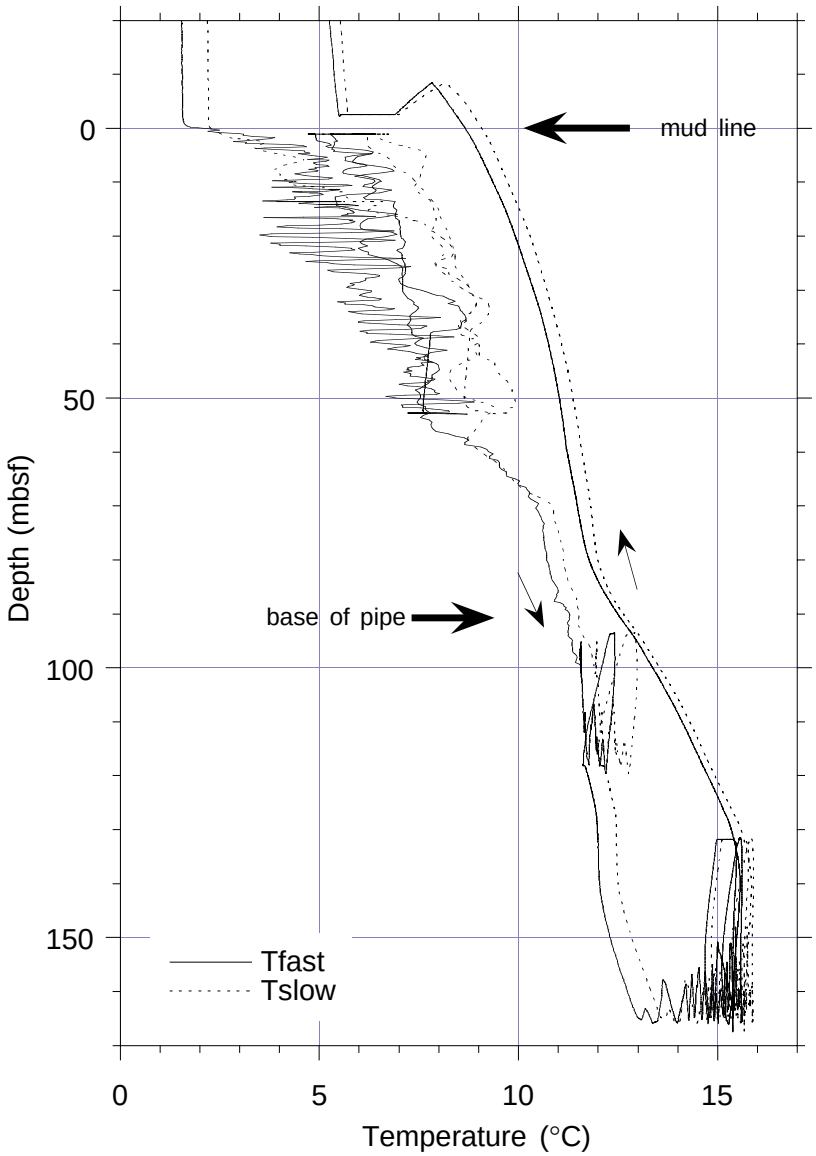

Figure F54. Temperature as a function of time for the open-hole Adara temperature run. Depth stations are marked.

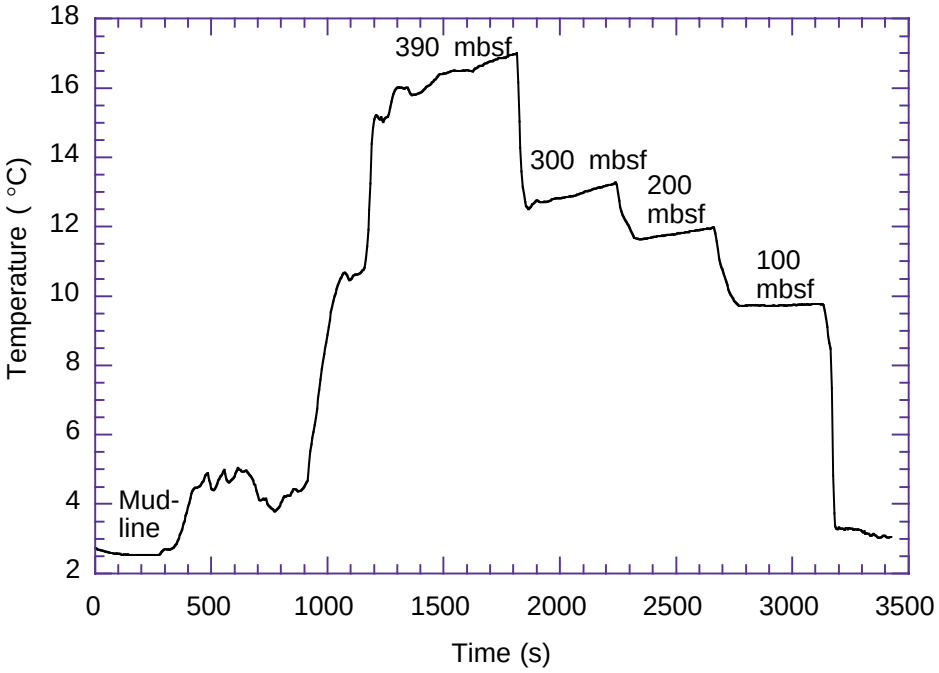

Figure F55. Temperature vs. ln[t/(t–s)] for Adara depth stations at (**A**) 100 mbsf; (**B**) 200 mbsf; (**C**) 300 mbsf; and (**D**) 390 mbsf. The equilibrium temperature is the y-intercept of the linear-regression line fitted to the data.

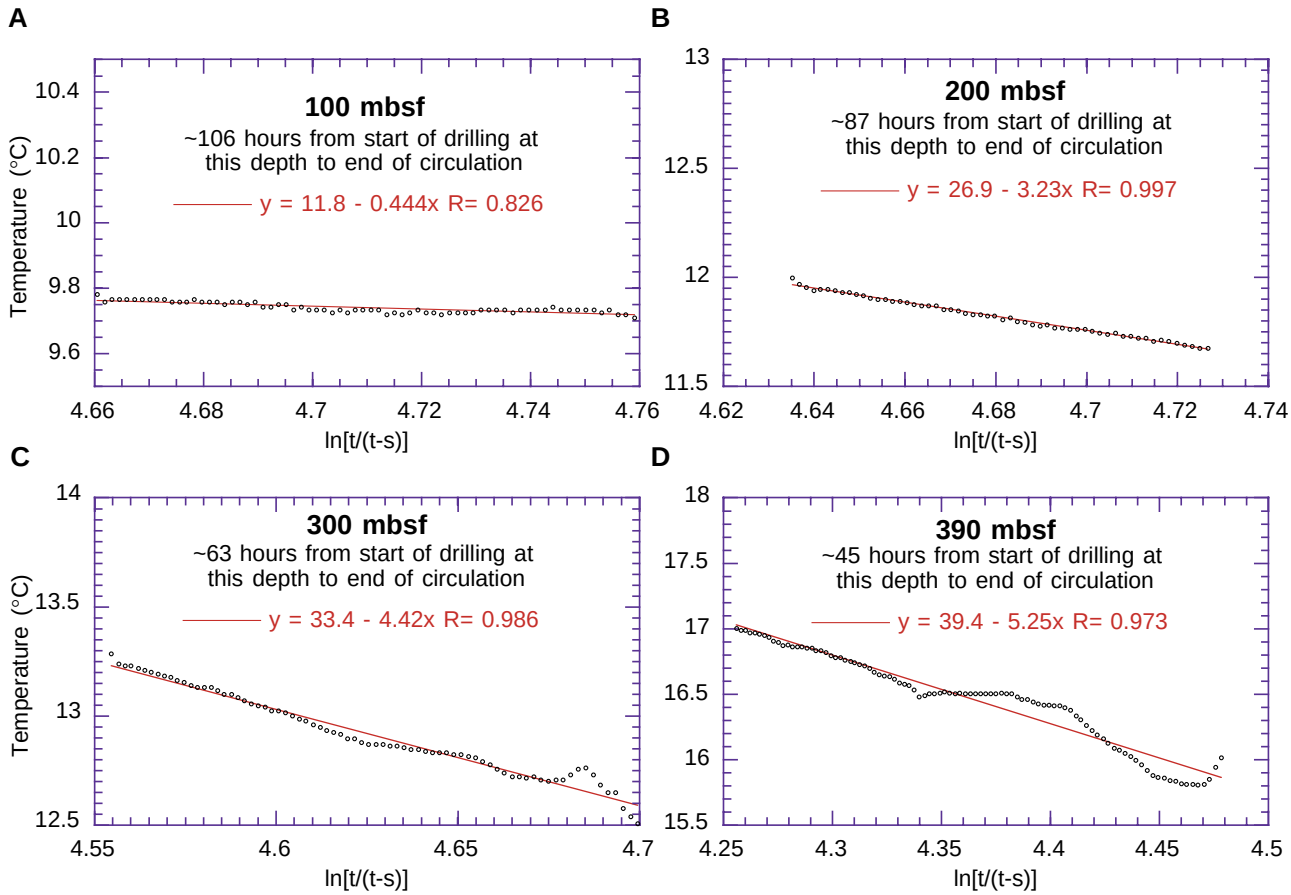

Figure F56. Temperature vs. ln[*t*/(*t*–*s*)] for data from the TLT tool during the logging run. Only data from 159.5 to 160.5 mbsf were used, and data immediately following movement of the logging string were deleted. The equilibrium temperature is the y-intercept of the linear-regression line fitted to the data.

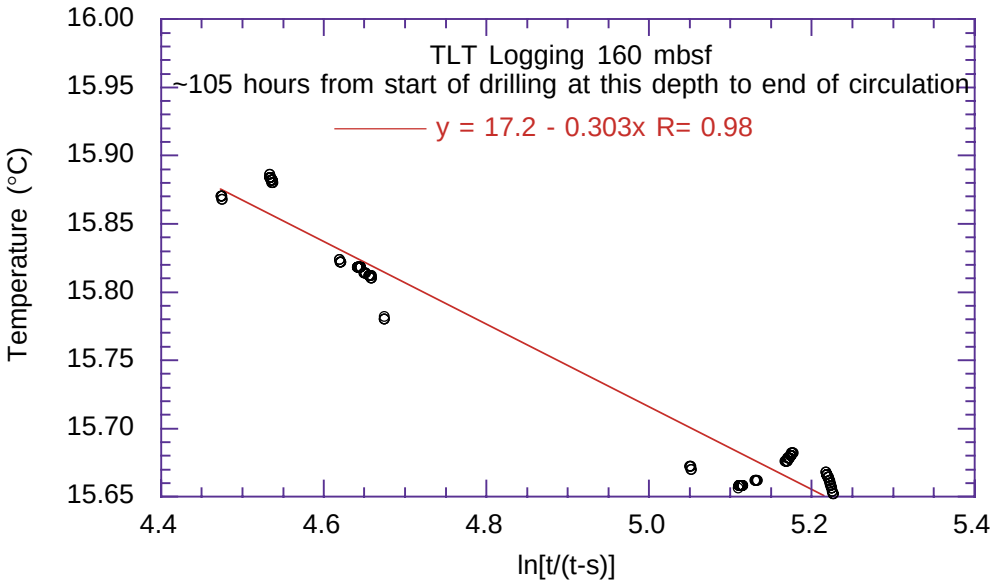

Figure F57. Approximated temperature as a function of depth, and best-fit linear regression. The solid line shows the linear regression line for all data points. Alternative interpretation (discontinuous gradient) is shown by the dashed lines.

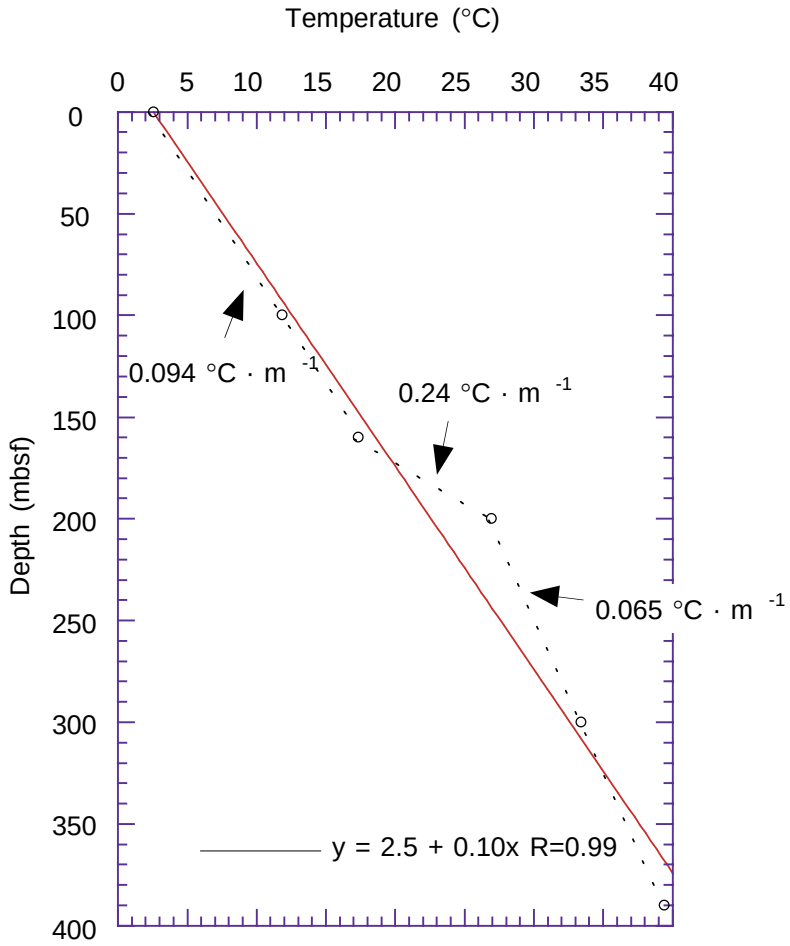

Table T1. Site 1108 coring summary. (Continued on next page.)

Hole 1108A

Latitude: 9°44.7076′S
Longitude: 151°37.5138′E
Seafloor (drill-pipe measurement from rig floor, mbrf): 3173.7
Distance between rig floor and sea level (m): 11.0
Water depth (drill-pipe measurement from sea level, m): 3162.7
Total depth (from rig floor, mbrf): 3190.00
Penetration (mbsf): 16.30
Remarks: No coring; jet-in test

Hole 1108B

Latitude: 9°44.7242′S
Longitude: 151°37.5426′E
Seafloor (drill-pipe measurement from rig floor, mbrf): 3188.3
Distance between rig floor and sea level (m): 11.1
Water depth (drill-pipe measurement from sea level, m): 3177.2
Total depth (from rig floor, mbrf): 3673.5
Penetration (mbsf): 485.20
Total number of cores: 51
Total length of cored section (m): 485.20
Total core recovered (m): 148.58
Core recovery (%): 30.6

Core	Date (June 1998)	Time (UTC +10 hr)	Depth (mbsf)	Length cored (m)	Length recovered (m)	Recovery (%)	Comment
180-1108B-							
1R	18	0220	0.0-8.6	8.6	1.80	20.9	
2R	18	0330	8.6-14.5	5.9	0.00	0.0	
3R	18	0530	14.5-24.1	9.6	0.14	1.5	
4R	18	0915	24.1-33.8	9.7	0.03	0.3	
5R	18	1100	33.8-43.4	9.6	0.09	0.9	
6R	18	1230	43.4-53.1	9.7	0.15	1.5	
7R	18	1400	53.1-62.7	9.6	0.00	0.0	No recovery
8R	18	1600	62.7-72.3	9.6	0.90	9.4	
9R	18	1720	72.3-81.9	9.6	1.47	15.3	
10R	18	1915	81.9-91.3	9.4	1.54	16.4	
11R	18	2325	91.3-100.9	9.6	0.00	0.0	No recovery
12R	19	0145	100.9-110.6	9.7	0.00	0.0	No recovery
13R	19	0530	110.6-120.2	9.6	0.03	0.3	
14R	19	0730	120.2-129.8	9.6	2.10	21.9	
15R	19	1000	129.8-139.4	9.6	2.43	25.3	
16R	19	1140	139.4-149.0	9.6	2.74	28.5	
17R	19	1310	149.0-158.6	9.6	2.02	21.0	
18R	19	1450	158.6-168.3	9.7	6.19	63.8	
19R	19	1630	168.3-178.0	9.7	4.84	49.9	
20R	19	1755	178.0-187.6	9.6	2.77	28.9	
21R	19	1945	187.6-197.2	9.6	1.69	17.6	
22R	19	2120	197.2-206.8	9.6	7.87	82.0	
23R	19	2300	206.8-216.4	9.6	6.13	63.9	
24R	20	0100	216.4-226.0	9.6	4.51	47.0	
25R	20	0245	226.0-235.6	9.6	3.10	32.3	
26R	20	0425	235.6-244.9	9.3	4.38	47.1	
27R	20	0600	244.9-254.5	9.6	8.76	91.3	
28R	20	0730	254.5-264.1	9.6	4.68	48.8	
29R	20	0920	264.1-273.4	9.3	5.75	61.8	
30R	20	1110	273.4-283.0	9.6	7.92	82.5	
31R	20	1320	283.0-292.7	9.7	4.65	47.9	
32R	20	1450	292.7-302.3	9.6	6.51	67.8	
33R	20	1635	302.3-312.0	9.7	5.28	54.4	
34R	20	1830	312.0-321.6	9.6	6.03	62.8	
35R	20	2030	321.6-331.3	9.7	4.92	50.7	
36R	20	2230	331.3-340.9	9.6	6.18	64.4	
37R	21	0110	340.9-350.5	9.6	4.36	45.4	
38R	21	0335	350.5-360.1	9.6	1.71	17.8	
39R	21	0600	360.1-369.8	9.7	2.31	23.8	
40R	21	0835	369.8-379.4	9.6	1.94	20.2	
41R	21	1120	379.4-389.0	9.6	3.48	36.3	
42R	21	1540	389.0-398.6	9.6	4.01	41.8	
43R	21	1815	398.6-408.2	9.6	1.32	13.8	

Table T1 (continued).

Core	Date (June 1998)	Time (UTC +10 hr)	Depth (mbsf)	Length cored (m)	Length recovered (m)	Recovery (%)	Comment
44R	21	2025	408.2-417.8	9.6	1.51	15.7	
45R	21	2255	417.8-427.5	9.7	2.04	21.0	
46R	22	0145	427.5-437.1	9.6	1.62	16.9	
47R	22	0520	437.1-446.7	9.6	0.96	10.0	
48R	22	0805	446.7-456.3	9.6	2.16	22.5	
49R	22	1040	456.3-465.9	9.6	0.70	7.3	
50R	22	1315	465.9-475.5	9.6	1.25	13.0	
51R	22	1600	475.5-485.2	9.7	1.61	16.6	
Totals:				485.2	148.58	30.6	

Note: UTC = Universal Time Coordinated.

Table T2. Site 1108 coring summary by section. (Continued on next five pages.)

Core No	Date (June 1998)	Time (UTC +10 hr)	Core depth (mbsf) Top	Core depth (mbsf) Bottom	Length (m) Cored	Length (m) Recovered	Recovery (%)	Section	Length (m) Liner	Length (m) Curated	Section depth (mbsf) Top	Section depth (mbsf) Bottom	Catwalk samples	Comment
180-1108A-														
No coring. Jet-in test.														
180-1108B-														
1R	17	1720	0.0	8.6	8.6	1.80	20.9							
								1	1.00	1.00	0.00	1.00	IW, WEL, WROG, WRMB	
								2	0.65	0.65	1.00	1.65	HS	
								CC	0.15	0.15	1.65	1.80	PAL	
									1.80	1.80				
2R	17	1830	8.6	14.5	5.9	0.00	0.0							
								1	0.00	0.00				
									0.00	0.00				
3R	17	2030	14.5	24.1	9.6	0.14	1.5							
								CC	0.14	0.24	14.50	14.74	PAL	
									0.14	0.24				
4R	18	0015	24.1	33.8	9.7	0.03	0.3							
								CC	0.03	0.07	24.10	24.17	PAL	
									0.03	0.07				
5R	18	0200	33.8	43.4	9.6	0.09	0.9							
								CC	0.09	0.09	33.80	33.89	PAL	
									0.09	0.09				
6R	18	0330	43.4	53.1	9.7	0.15	1.5							
								CC	0.15	0.17	43.40	43.57		
									0.15	0.17				
7R	18	0500	53.1	62.7	9.6	0.00	0.0							
								CC	0.00	0.00				
									0.00	0.00				
8R	18	0700	62.7	72.3	9.6	0.90	9.4							
								1	0.68	0.68	62.70	63.38	HS	
								CC	0.22	0.22	63.38	63.60		
									0.90	0.90				
9R	18	0820	72.3	81.9	9.6	1.47	15.3							
								1	1.31	1.31	72.30	73.61	HS	
								CC	0.16	0.16	73.61	73.77		
									1.47	1.47				
10R	18	1015	81.9	91.3	9.4	1.54	16.4							
								1	1.27	1.27	81.90	83.17	HS, IW	
								CC	0.27	0.27	83.17	83.44		
									1.54	1.54				
11R	18	1425	91.3	100.9	9.6	0.00	0.0							
								CC	0.00	0.00				
									0.00	0.00				
12R	18	1645	100.9	110.6	9.7	0.00	0.0							
								1	0.00	0.00				
									0.00	0.00				
13R	18	2030	110.6	120.2	9.6	0.03	0.3							
								CC	0.03	0.08	110.60	110.68		
									0.03	0.08				

Table T2 (continued).

Core No	Date (June 1998)	Time (UTC +10 hr)	Core depth (mbsf) Top	Core depth (mbsf) Bottom	Length (m) Cored	Length (m) Recovered	Recovery (%)	Section	Length (m) Liner	Length (m) Curated	Section depth (mbsf) Top	Section depth (mbsf) Bottom	Catwalk samples	Comment
14R	18	2230	120.2	129.8	9.6	2.10	21.9							
								1	1.16	1.16	120.20	121.36	WRSCR	
								2	0.73	0.73	121.36	122.09	HS	
								CC	0.21	0.21	122.09	122.30	PAL	
									2.10	2.10				
15R	19	0100	129.8	139.4	9.6	2.43	25.3							
								1	0.83	0.83	129.80	130.63	IW	
								2	1.42	1.42	130.63	132.05	HS, WEL	
								CC	0.18	0.18	132.05	132.23	PAL	
									2.43	2.43				
16R	19	0240	139.4	149.0	9.6	2.74	28.5							
								1	1.50	1.50	139.40	140.90		
								2	1.14	1.14	140.90	142.04	HS	
								CC	0.10	0.10	142.04	142.14	PAL	
									2.74	2.74				
17R	19	0410	149.0	158.6	9.6	2.02	21.0							
								1	1.07	1.07	149.00	150.07	HS	
								2	0.75	0.75	150.07	150.82	WEL	
								CC	0.20	0.20	150.82	151.02	PAL	
									2.02	2.02				
18R	19	0550	158.6	168.3	9.7	6.19	63.8							
								1	1.50	1.50	158.60	160.10		
								2	1.50	1.50	160.10	161.60		
								3	1.50	1.50	161.60	163.10		
								4	1.45	1.45	163.10	164.55	IW, HS, WEL	
								CC	0.24	0.24	164.55	164.79	PAL	
									6.19	6.19				
19R	19	0730	168.3	178.0	9.7	4.84	49.9							
								1	0.89	0.89	168.30	169.19	IW	
								2	0.61	0.61	169.19	169.80		
								3	1.50	1.50	169.80	171.30		
								4	1.00	1.00	171.30	172.30		
								5	0.61	0.61	172.30	172.91	HS	
								CC	0.23	0.23	172.91	173.14	PAL	
									4.84	4.84				
20R	19	0855	178.0	187.6	9.6	2.77	28.9							
								1	1.50	1.50	178.00	179.50		
								2	1.05	1.05	179.50	180.55	HS, IW	
								CC	0.22	0.22	180.55	180.77	PAL	
									2.77	2.77				
21R	19	1045	187.6	197.2	9.6	1.69	17.6							
								1	1.47	1.47	187.60	189.07	WRSCR, HS, WEL	
								CC	0.22	0.22	189.07	189.29	PAL	
									1.69	1.69				
22R	19	1220	197.2	206.8	9.6	7.87	82.0							
								1	1.50	1.50	197.20	198.70		
								2	1.50	1.50	198.70	200.20	HS	

Table T2 (continued).

Core No	Date (June 1998)	Time (UTC +10 hr)	Core depth (mbsf) Top	Core depth (mbsf) Bottom	Length (m) Cored	Length (m) Recovered	Recovery (%)	Section	Length (m) Liner	Length (m) Curated	Section depth (mbsf) Top	Section depth (mbsf) Bottom	Catwalk samples	Comment
								3	1.50	1.50	200.20	201.70		
								4	1.50	1.50	201.70	203.20	IW	
								5	1.47	1.47	203.20	204.67		
								6	0.23	0.23	204.67	204.90		
								CC	0.17	0.17	204.90	205.07	PAL	
									7.87	7.87				
23R	19	1400	206.8	216.4	9.6	6.13	63.9							
								1	1.50	1.50	206.80	208.30	HS	
								2	1.50	1.50	208.30	209.80		
								3	1.50	1.50	209.80	211.30		
								4	1.45	1.45	211.30	212.75		
								CC	0.18	0.18	212.75	212.93	PAL	
									6.13	6.13				
24R	18	1600	216.4	226.0	9.6	4.51	47.0							
								1	1.50	1.50	216.40	217.90	HS	
								2	0.94	0.94	217.90	218.84	WRKO	Orientation unknown 0-5 cm; piece fell from liner on catwalk
								3	1.50	1.50	218.84	220.34		
								4	0.40	0.40	220.34	220.74		
								CC	0.17	0.17	220.74	220.91	PAL	
									4.51	4.51				
25R	18	1745	226.0	235.6	9.6	3.10	32.3							
								1	1.50	1.50	226.00	227.50	IW, HS	
								2	1.38	1.38	227.50	228.88		
								CC	0.22	0.22	228.88	229.10	PAL	
									3.10	3.10				
26R	18	1925	235.6	244.9	9.3	4.38	47.1							
								1	1.50	1.50	235.60	237.10		
								2	1.50	1.50	237.10	238.60	HS	
								3	1.35	1.35	238.60	239.95		
								CC	0.03	0.03	239.95	239.98	PAL	All to paleontology lab
									4.38	4.38				
27R	19	2100	244.9	254.5	9.6	8.76	91.3							
								1	1.50	1.50	244.90	246.40		
								2	1.50	1.50	246.40	247.90		
								3	1.50	1.50	247.90	249.40		
								4	1.50	1.50	249.40	250.90	HS	
								5	1.50	1.50	250.90	252.40		
								6	1.23	1.23	252.40	253.63		
								CC	0.03	0.03	253.63	253.66	PAL	All to paleontology lab
									8.76	8.76				
28R	19	2230	254.5	264.1	9.6	4.68	48.8							
								1	1.46	1.46	254.50	255.96		
								2	1.22	1.22	255.96	257.18		
								3	0.91	0.91	257.18	258.09	HS	
								4	0.91	0.91	258.09	259.00		
								CC	0.18	0.18	259.00	259.18	PAL	
									4.68	4.68				

Table T2 (continued).

Core No	Date (June 1998)	Time (UTC +10 hr)	Core depth (mbsf) Top	Core depth (mbsf) Bottom	Length (m) Cored	Length (m) Recovered	Recovery (%)	Section	Length (m) Liner	Length (m) Curated	Section depth (mbsf) Top	Section depth (mbsf) Bottom	Catwalk samples	Comment
29R	20	0020	264.1	273.4	9.3	5.75	61.8							
								1	1.25	1.25	264.10	265.35		
								2	0.90	0.90	265.35	266.25		
								3	0.98	0.98	266.25	267.23	HS, IW	
								4	1.24	1.24	267.23	268.47		
								5	1.29	1.29	268.47	269.76		
								CC	0.09	0.09	269.76	269.85	PAL	
									5.75	5.75				
30R	20	0210	273.4	283.0	9.6	7.92	82.5							
								1	1.51	1.51	273.40	274.91		
								2	1.06	1.06	274.91	275.97		
								3	1.51	1.51	275.97	277.48		
								4	1.20	1.20	277.48	278.68	HS	
								5	1.13	1.13	278.68	279.81		
								6	0.52	0.52	279.81	280.33	WRSCR	
								7	0.79	0.79	280.33	281.12		
								CC	0.20	0.20	281.12	281.32	PAL	
									7.92	7.92				
31R	20	0420	283.0	292.7	9.7	4.65	47.9							
								1	1.48	1.48	283.00	284.48	HS	
								2	1.43	1.43	284.48	285.91		
								3	0.39	0.39	285.91	286.30		
								4	1.16	1.16	286.30	287.46		
								CC	0.19	0.19	287.46	287.65	PAL	
									4.65	4.65				
32R	20	0550	292.7	302.3	9.6	6.51	67.8							
								1	1.14	1.14	292.70	293.84		
								2	1.21	1.21	293.84	295.05		
								3	1.43	1.43	295.05	296.48		
								4	1.47	1.47	296.48	297.95	HS	
								5	1.03	1.03	297.95	298.98		
								CC	0.23	0.23	298.98	299.21	PAL	
									6.51	6.51				
33R	20	0735	302.3	312.0	9.7	5.28	54.4							
								1	1.33	1.33	302.30	303.63	IW	
								2	1.47	1.47	303.63	305.10		
								3	0.92	0.92	305.10	306.02		
								4	1.30	1.30	306.02	307.32	HS	
								CC	0.26	0.26	307.32	307.58	PAL	
									5.28	5.28				
34R	20	0930	312.0	321.6	9.6	6.03	62.8							
								1	1.34	1.34	312.00	313.34		
								2	1.49	1.49	313.34	314.83		
								3	1.39	1.39	314.83	316.22		
								4	1.31	1.31	316.22	317.53	HS	
								5	0.34	0.34	317.53	317.87		
								CC	0.16	0.16	317.87	318.03	PAL	
									6.03	6.03				

Table T2 (continued).

Core No	Date (June 1998)	Time (UTC +10 hr)	Core depth (mbsf) Top	Core depth (mbsf) Bottom	Length (m) Cored	Length (m) Recovered	Recovery (%)	Section	Length (m) Liner	Length (m) Curated	Section depth (mbsf) Top	Section depth (mbsf) Bottom	Catwalk samples	Comment
35R	20	1130	321.6	331.3	9.7	4.92	50.7							
								1	1.50	1.50	321.60	323.10		
								2	1.25	1.25	323.10	324.35		
								3	1.50	1.50	324.35	325.85		
								4	0.44	0.44	325.85	326.29	HS	
								CC	0.23	0.23	326.29	326.52	PAL	
									4.92	4.92				
36R	20	1330	331.3	340.9	9.6	6.18	64.4							
								1	1.01	1.01	331.30	332.31		
								2	1.11	1.11	332.31	333.42		
								3	1.47	1.47	333.42	334.89	HS	
								4	1.32	1.32	334.89	336.21		
								5	1.03	1.03	336.21	337.24		
								CC	0.24	0.24	337.24	337.48	PAL	
									6.18	6.18				
37R	20	1610	340.9	350.5	9.6	4.36	45.4							
								1	1.20	1.20	340.90	342.10		
								2	1.42	1.42	342.10	343.52	IW, HS	
								3	1.27	1.27	343.52	344.79		
								4	0.28	0.28	344.79	345.07		
								CC	0.19	0.19	345.07	345.26	PAL	
									4.36	4.36				
38R	20	1835	350.5	360.1	9.6	1.71	17.8							
								1	1.50	1.50	350.50	352.00	HS	
								CC	0.21	0.21	352.00	352.21	PAL	
									1.71	1.71				
39R	20	2100	360.1	369.8	9.7	2.31	23.8							
								1	1.16	1.16	360.10	361.26	HS	
								2	0.91	0.91	361.26	362.17		
								CC	0.24	0.24	362.17	362.41	PAL	
									2.31	2.31				
40R	20	2335	369.8	379.4	9.6	1.94	20.2							
								1	0.91	0.91	369.80	370.71		
								2	0.81	0.81	370.71	371.52	HS	
								CC	0.22	0.22	371.52	371.74	PAL	
									1.94	1.94				
41R	21	220	379.4	389.0	9.6	3.48	36.3							
								1	1.50	1.50	379.40	380.90		
								2	1.48	1.48	380.90	382.38	HS, WRSCR	
								3	0.33	0.33	382.38	382.71		
								CC	0.17	0.17	382.71	382.88	PAL	
									3.48	3.48				
42R	21	640	389	398.6	9.6	4.01	41.8							
								1	1.48	1.48	389.00	390.48		
								2	0.36	0.36	390.48	390.84		
								3	0.18	0.18	390.84	391.02		
								4	0.54	0.54	391.02	391.56	HS	
								5	0.55	0.55	391.56	392.11	IW	

Table T2 (continued).

Core No	Date (June 1998)	Time (UTC +10 hr)	Core depth (mbsf) Top	Core depth (mbsf) Bottom	Length (m) Cored	Length (m) Recovered	Recovery (%)	Section	Length (m) Liner	Length (m) Curated	Section depth (mbsf) Top	Section depth (mbsf) Bottom	Catwalk samples	Comment
								6	0.74	0.74	392.11	392.85		
								CC	0.16	0.16	392.85	393.01	PAL	
									4.01	4.01				
43R	21	915	398.6	408.2	9.6	1.32	13.8							
								1	1.13	1.13	398.60	399.73	HS	
								CC	0.19	0.19	399.73	399.92	PAL	
									1.32	1.32				
44R	21	1125	408.2	417.8	9.6	1.51	15.7							
								1	1.33	1.33	408.20	409.53	HS	
								CC	0.18	0.18	409.53	409.71	PAL	
									1.51	1.51				
45R	21	1355	417.8	427.5	9.7	2.04	21.0							
								1	1.11	1.11	417.80	418.91	HS	
								2	0.65	0.65	418.91	419.56		
								CC	0.28	0.28	419.56	419.84	PAL	
									2.04	2.04				
46R	21	1645	427.5	437.1	9.6	1.62	16.9							
								1	1.43	1.43	427.50	428.93	HS	
								CC	0.19	0.19	428.93	429.12	PAL	
									1.62	1.62				
47R	21	2020	437.1	446.7	9.6	0.96	10.0							
								1	0.66	0.66	437.10	437.76	HS	
								CC	0.30	0.30	437.76	438.06		Trace to paleontology lab
									0.96	0.96				
48R	21	2305	446.7	456.3	9.6	2.16	22.5							
								1	0.60	0.60	446.70	447.30		
								2	1.35	1.35	447.30	448.65	HS,IW	
								CC	0.21	0.21	448.65	448.86	PAL	
									2.16	2.16				
49R	22	0140	456.3	465.9	9.6	0.70	7.3							
								1	0.52	0.52	456.30	456.82		
								CC	0.18	0.18	456.82	457.00	PAL,HS	Trace to paleontology lab
									0.70	0.70				
50R	22	0415	465.9	475.5	9.6	1.25	13.0							
								1	1.00	1.00	465.90	466.90	HS	
								CC	0.25	0.25	466.90	467.15	PAL	
									1.25	1.25				
51R	22	0700	475.5	485.2	9.7	1.61	16.6							There are some sections (four working and three archive) containing fill from 0 to 485.2 mbsf; these sections have been archived at the request of the co-chiefs and staff scientist; they will be stored in the repository just after Core 180-1108B-51R
								1	1.35	1.35	475.50	476.85	HS	
								CC	0.26	0.26	476.85	477.11	PAL	
									1.61	1.61				
				Totals:	485.2	148.58	30.6							

Note: IW = interstitial water; WEL = Wellsbury microbiology; WROG = whole-round organic geochemistry; WRMB = whole-round microbiology; HS = headspace; PAL = paleontology; WRSCR = whole-round Screaton; WRKO = whole-round Kopf.

Table T3. Composition of minerals determined by X-ray diffraction in whole-rock samples, Site 1108.

Core, section, interval (cm)	Depth (mbsf)	Description	XRD identification: major (minor) minerals
180-1108B-			
1R-2, 18-19	1.18	Clay-bearing nannofossil ooze	Calcite, quartz, plagioclase, chlorite (illite)
8R-1, 25-26	62.95	Silty sand	Plagioclase, quartz (amphibole, chlorite, smectite?)
9R-1, 104-105	73.34	Sandstone	Calcite, plagioclase, quartz (chlorite, smectite?)
10R-1, 122-127	83.12	Mixed lithic sand	Plagioclase, quartz, amphibole (illite, chlorite)
14R-1, 62.5-63.5	120.82	Sandstone	Plagioclase, quartz, calcite, amphibole (chlorite, illite)
14R-2, 33-34	121.69	Sand	Quartz (plagioclase, calcite, chlorite, smectite?)
16R-2, 53-54	141.43	Silty clay	Plagioclase, quartz, calcite, chlorite, smectite? (illite, amphibole)
17R-2, 70-73	150.77	Calcareous clayey siltstone	Calcite (quartz, plagioclase)
19R-3, 47-48	170.27	Foraminifer-rich clayey siltstone	Calcite, plagioclase, quartz (aragonite, chlorite, illite, smectite?)
20R-1, 138-141	179.38	Silty claystone	Quartz, plagioclase (augite?, amphibole, chlorite, illite)
22R-4, 59.5-60.5	202.29	Sandstone	Plagioclase (quartz, calcite, chlorite, illite, smectite?)
23R-3, 125-125.5	211.05	Siltstone	Plagioclase (quartz, calcite, chlorite, illite, smectite?)
24R-3, 99-100	219.83	Sandstone	Quartz, plagioclase, chlorite (calcite, illite, amphibole)
25R-2, 18.5-19.5	227.68	Siltstone	Plagioclase, quartz, (calcite, chlorite, illite)
26R-1, 42-43	236.02	Siltstone	Quartz, plagioclase (calcite, chlorite, smectite?, amphibole)
31R-1, 40.5-41.5	283.40	Silty claystone	Plagioclase, chlorite, illite (quartz, amphibole)
32R-3, 80-81	295.85	Siltstone	Plagioclase, quartz (calcite, chlorite, smectite?, illite, amphibole)
33R-3, 81-82	305.91	Sandstone	Quartz, plagioclase, (calcite, chlorite, smectite?, illite)
34R-3, 82-83	315.65	Sandstone	Plagioclase, quartz (calcite, chlorite, smectite?, amphibole)
35R-2, 31-32	323.41	Siltstone	Plagioclase (quartz, calcite, smectite?, illite)
36R-4, 20-22	335.09	Claystone	Plagioclase (quartz, smectite?)
38R-1, 71-73.5	351.21	Claystone	Plagioclase, quartz (chlorite, smectite?, illite)
39R-2, 66-69	361.92	Silty Claystone	Plagioclase (quartz, illite, smectite?)
40R-1, 18-20	369.98	Siltstone	Plagioclase, quartz (clinoptilolite, chlorite, smectite?, illite)
42R-1, 128-129	390.28	Silty claystone	Quartz, plagioclase (chlorite, smectite?, calcite)
43R-1, 86-87	399.46	Sandy siltstone	Quartz, plagioclase (chlorite, smectite?, calcite)
44R-1, 112-112.5	409.32	Silty sandstone	Quartz, plagioclase, calcite (chlorite, smectite?)
45R-1, 81-82	418.61	Sandstone	Quartz, plagioclase (chlorite, smectite?, calcite)
46R-1, 107-107.5	428.57	Silty sandstone	Quartz, plagioclase, calcite (chlorite, illite, smectite?)
48R-2, 70-71	448.00	Silty sandstone	Quartz, plagioclase (calcite, chlorite, smectite?)
50R-1, 50-51	466.40	Sandy siltstone	Calcite, quartz, plagioclase (chlorite)
51R-1, 53-55	476.03	Sandy siltstone	Quartz, calcite, plagioclase (chlorite)

Table T4. Carbon, calcium carbonate, nitrogen, and sulfur analyses, Hole 1108B.

Core, section, interval (cm)	Depth (mbsf)	Inorganic carbon (wt%)	$CaCO_3$ (wt%)	Organic carbon (wt%)	Total nitrogen (wt%)	C/N	Total sulfur (wt%)
180-1108B-							
1R-1, 17-18	0.17	3.40	28.35	0.42	0.05	9	0.06
1R-2, 14-15	1.14	3.72	30.95	0.23	0.04	6	0.07
9R-1, 59-60	72.89	0.32	2.68	0.03			0.02
10R-CC, 5-6	83.22	0.21	1.71	0.10			0.08
15R-2, 76-77	131.39	0.84	6.97	1.10	0.03	34	0.39
16R-2, 84-85	141.74	5.40	44.98	0.41	0.04	11	0.1
17R-2, 56-58	150.63	3.72	30.95	0.02	0.02	1	0
18R-3, 73-74	162.33	5.79	48.22		0.02	0	0
19R-3, 29-30	170.09	3.29	27.43	0.36	0.04	10	0.07
20R-1, 62-63	178.62	0.74	6.13	0.69	0.04	17	0.43
21R-1, 68-69	188.28	2.04	16.97	0.38	0.04	10	0.11
22R-1, 112.5-113.5	198.32	0.41	3.45	0.83	0.05	18	0.44
23R-1, 21-22	207.01	0.36	3.03	0.76	0.03	23	0.38
23R-4, 64-65	211.94	0.48	3.98	0.53	0.04	15	0.58
24R-3, 116-117	220.00	0.75	6.22	0.51	0.03	15	0
25R-2, 38-38.5	227.88	0.33	2.74	0.21	0.03	8	0.18
26R-1, 38-39	235.98	0.49	4.09	0.53	0.03	20	0.13
27R-2, 129-130	247.69	1.78	14.80	0.34	0.03	14	0
29R-4, 44-45	267.67	0.24	1.99	0.64	0.03	20	0.56
30R-5, 3-4	278.71	0.26	2.13	0.66			0
31R-2, 132-134	285.80	0.31	2.57	0.54	0.03	18	0.41
32R-3, 72-73	295.77	0.30	2.50	0.69	0.05	13	0.3
33R-3, 78-79	305.88	0.36	2.98	0.54	0.04	12	0.46
34R-2, 138.5-139.5	314.73	0.34	2.84	0.62	0.05	14	0.25
35R-2, 110-111	324.20	0.85	7.06	0.53	0.04	12	0.07
36R-4, 21-22	335.10	0.26	2.16	0.20	0.04	5	0.12
38R-1, 73.5-74	351.23	0.62	5.15	0.58	0.04	14	0.23
39R-2, 69-70	361.95	0.26	2.15	0.16	0.04	4	0
40R-1, 18-20	369.98	0.64	5.32		0.04	0	0
42R-1, 127-128	390.27	0.65	5.38	0.79	0.07	11	0.37
43R-1, 72-73	399.32	0.19	1.60	0.55	0.06	10	0.25
44R-1, 22-23	408.42	0.09	0.77	0.22	0.04	6	0
45R-1, 68-69	418.48	0.81	6.74	0.63	0.05	12	0
46R-1, 62.5-63	428.12	1.26	10.48	0.51	0.05	10	0
47R-1, 23-24	437.33	0.28	2.32	0.34	0.05	7	0.43
47R-1, 60-61	437.70	0.26	2.19	0.20	0.03	6	0.13
48R-2, 83-84	448.13	0.34	2.80	0.86	0.06	15	0.37
50R-1, 50-51	466.40	0.99	8.29	0.86	0.05	17	0.14
51R-1, 25-26	475.75	4.70	39.16	0.58	0.03	17	0

Note: Blanks indicate values below detection limit, except for C/N ratios where blanks indicate an undefined value.

Table T5. Range chart showing the distribution of selected calcareous nannofossil species, Hole 1108B. (Continued on next page.)

Core, section, interval (cm)	Depth, (mbsf)	Abundance	Preservation	*Braarudosphaera bigelowii*	*Calcidiscus leptoporus*	*Calcidiscus macintyrei*	*Ceratolithus cristatus*	*Coccolithus pelagicus*	*Dictyococcites productus*	*Discoaster brouweri*	*Emiliania huxleyi*	*Gephyrocapsa aperta*	*Gephyrocapsa caribbeanica*	*Gephyrocapsa oceanica*	*Gephyrocapsa omega*	*Helicosphaera carteri*	*Helicosphaera carteri* var. *hyalina*	*Helicosphaera sellii*	*Pontosphaera indooceanica*	*Pontosphaera japonica*	*Pseudoemiliania lacunosa*	*Reticulofenestra minutula*	*Rhabdosphaera clavigera*	*Scapholithus fossilis*	*Scyphosphaera apsteinii*	*Scyphosphaera pulcherrima*	*Sphenolithus abies*	*Thoracosphaera heimii*	*Thoracosphaera saxea*	*Umbilicosphaera sibogae*
180-1108B-																														
1R-1, 4-6	0.04	A	G		F						C			C	R	F						C	R	F						F
1R-1, 30-32	0.30	A	G		F		R				C			A	F	F							R	R						F
1R-CC, 10-15	1.75	C	G		F		R				C			C			F					C	R	F				R		F
3R-CC, 4-7	14.54	F	M		F	r	R			r				R		F					R	R	R				r			
4R-CC, 2-3	24.12	R	P		R	r		R				R				R		R			R	R					r			
5R-CC, 8-9	33.88	B																												
10R-1, 94-96	82.84	R	P		R	R			R				R	R		R					R	F								
14R-CC, 4-7	122.13	B																												
15R-CC, 15-18	132.20	R	R		R			R					R			R						R							R	R
16R-2, 83-84	141.73	F	M		F	R		F					R			F					F	C			R				R	
16R-CC, 7-10	142.11	A	G		C	R										C					C									
17R-1, 45-47	149.45	A	M		F	R	R	F					F			F					F	C			R				R	
17R-2, 72-74	150.79	A	M	R	R	R		F					R			F		R		R	R	C			R	R			R	
17R-CC, 17-20	150.99	F	M		R			R								F					F	F								
18R-1, 99-102	159.59	C	M		F	F		F		R						F					F	C							R	
18R-3, 96-98	162.56	F	M		R	R		F								F					R				R				R	
18R-CC, 21-24	164.76	A	G		C	R										C		R			F									
19R-1, 38-39	168.68	F	M		R					R						F					F	F			R					
19R-3, 97-99	170.77	F	M		R	R		F		C						F						F								
19R-5, 59-61	172.89	R	M		R	R		R								R					R	R								
19R-CC, 20-23	173.11	C	M		F	R										F					R									
20R-1, 120-124	179.20	F	M		R			R								F		R												
20R-2, 13-16	179.63	R	M		R											R														
20R-CC, 19-22	180.74	T																												
21R-1, 48-49	188.08	F	M		F	R		R								F														
21R-1, 122-124	188.82	F	M		R			R								F														
21R-CC, 19-22	189.26	C	M		F			R								F		R			R									
22R-1, 89.5-91.5	198.10	F	M		F			R								F		R												
22R-3, 95-97	201.15	F	M		R			R								F														
22R-5, 84.5-86.5	204.05	F	M		R	R		R								R														
22R-CC, 14-17	205.04	C	M		F			F								F		R												
23R-1, 97-98.5	207.77	F	M		F			R								F														
23R-3, 96-98	210.76	R	M																											
23R-CC, 15-18	212.90	C	M		R			R								F					R									
24R-3, 108-110	219.92	F	M		F	R		F								F														
24R-CC, 14-17	220.88	R	P		R			R					R			R			R		R	R								
25R-CC, 19-22	229.07	F	M		R	R		F					R			F					R	F							R	
26R-1, 95-97	236.55	F	M		F											F					R									
26R-CC, 0-3	239.95	T	P																			R								
27R-1, 95-97	245.85	B																												
27R-3, 95-97	248.85	T	P		R					R																				
27R-CC, 0-3	253.63	R	P																			R							R	R
28R-3, 43.5-46	257.62	F	M		R											R														
28R-CC, 16-18	259.16	R	P					R		R						R					R	R							R	
29R-5, 15-18	268.62	T	M													R														
29R-CC, 7-9	269.83	R	P													R						R								
30R-1, 25-27	273.65	F	M		R											R														
30R-3, 137-139	277.34	F	M		R			R								F		R			F									
30R-CC, 10-12	281.22	F	M		R	R		F								F														
31R-CC, 17-19	287.63	B																												
32R-3, 76-77	295.81	F	M													R														
32R-4, 139-141	297.87	C	M		R			R								F														
32R-CC, 20-23	299.18	C	M		F											F														
33R-1, 47-48	302.77	C	M		F	R		R								F		R			R									
33R-CC, 23-26	307.55	B																												
34R-2, 74-76	314.08	F	M		F	R		R								R														
34R-2, 91-92	314.25	C	M		F	R		F								F		R			R									

Table T5 (continued).

Core, section, interval (cm)	Depth, (mbsf)	Abundance	Preservation	*Braarudosphaera bigelowii*	*Calcidiscus leptoporus*	*Calcidiscus macintyrei*	*Ceratolithus cristatus*	*Coccolithus pelagicus*	*Dictyococcites productus*	*Discoaster brouweri*	*Emiliania huxleyi*	*Gephyrocapsa aperta*	*Gephyrocapsa caribbeanica*	*Gephyrocapsa oceanica*	*Gephyrocapsa omega*	*Helicosphaera carteri*	*Helicosphaera carteri* var. *hyalina*	*Helicosphaera sellii*	*Pontosphaera indooceanica*	*Pontosphaera japonica*	*Pseudoemiliania lacunosa*	*Reticulofenestra minutula*	*Rhabdosphaera clavigera*	*Scapholithus fossilis*	*Scyphosphaera apsteinii*	*Scyphosphaera pulcherrima*	*Sphenolithus abies*	*Thoracosphaera heimii*	*Thoracosphaera saxea*	*Umbilicosphaera sibogae*
34R-CC, 13-16	318.00	B																												
35R-2, 49-51	323.59	F	M		R			R								F														
35R-CC, 20-23	326.49	B																												
36R-1, 95-97	332.25	B																												
36R-3, 92-94	334.34	R	P													R														
36R-5, 95-97	337.16	F	P		F	R										F					R	F								
36R-CC, 21-24	337.45	B																												
37R-2, 120-122	343.30	F	P		R	R		R								F					R	F							R	R
37R-3, 97-99	344.49	T	P																											
37R-CC, 18-19	345.25	T	P													R														
38R-1, 135.5-137.5	351.86	R	P		R				R							R						R								
38R-CC, 18-21	352.18	T	P			R																								
39R-1, 101-104	361.11	R	P		R											R					R	R						R		
39R-CC, 22-24	362.39	R	P		R			R	R							R						R							R	
40R-2, 17-18	370.88	R	M		R			R								R														
40R-CC, 20-22	371.72	C	P		F	R		F		R						F					R	F			R				F	
41R-1, 17-19	379.57	C	M		R			R								F														
41R-CC, 15-17	382.86	C	M		F	R		F								F														
42R-1, 95-97	389.95	R	M		R											R														
42R-3, 8-10	390.92	T	P		R			R																						
42R-CC, 13-16	392.98	F	M		R					R						F														
43R-CC, 16-19	399.89	R	M		R																									
44R-1, 84-85	409.04	F	M		F			R								F														
44R-CC, 16-18	409.69	C	M		F			R								F														
45R-1, 94.5-96.5	418.75	F	M		R											R														
45R-2, 24-25	419.15	R	M		R											R														
45R-CC, 25-28	419.81	R	P					R										R												
46R-1, 96.5-97.5	428.47	T	P					R																						
46R-CC, 17-19	429.10	T	P						R							R														
47R-CC, 0-1	437.76	B																												
48R-2, 6-8	447.36	T	P													R														
48R-CC, 11-13	448.76	B																												
49R-1, 25-26	456.55	T	P																											
49R-CC, 17-18	456.99	T																												
50R-CC, 22-25	467.12	B																												
51R-1, 19-21	475.69	F	P		R			R		R						R														
51R-1, 49-50.5	475.99	R	P		R											R														
51R-CC, 23-26	477.08	B																												

Notes: Abundance (number of specimens per field of view): D = dominant (>100); A = abundant (10–100); C = common (1–10); F = few (1 per 10 fields of view); R = rare (<1 per 10 fields of view); T = trace (<1 per transect of slide); B = barren. Preservation: VG = very good; G = good; M = moderate; P = poor. Distribution: C = common; F = few; R = rare; r = reworked.

Table T6. Range chart showing the distribution of selected planktonic foraminifer species, Hole 1108B.

Core, section, interval (cm)	Depth (mbsf)	Abundance	Preservation	*Bolliella adamsi*	*Bolliella calida*	*Globigerinella obesa*	*Globigerinella praesiphonifera*	*Globigerinella siphonifera*	*Globigerinita glutinata*	*Globigerinoides conglobatus*	*Globigerinoides fistulosus*	*Globigerinoides quadrilobatus*	*Globigerinoides ruber*	*Globigerinoides sacculifer*	*Globigerinoides trilobus*	*Globorotalia cavernula*	*Globorotalia crassaformis*	*Globorotalia crassaformis hessi*	*Globorotalia crassula*	*Globorotalia fimbriata*	*Globorotalia menardii*	*Globorotalia scitula*	*Globorotalia tosaensis*	*Globorotalia truncatulinoides*	*Globorotalia tumida*	*Globorotalia ungulata*	*Neogloboquadrina dutertrei*	*Neogloboquadrina humerosa*	*Orbulina suturalis*	*Orbulina universa*	*Pulleniatina obliquiloculata*	*Pulleniatina praecursor*	*Sphaeroidinella dehiscens*	*Zeaglobigerina rubescens*
180-1108B-																																		
1R-1, 30-32	0.30	A	VG	A	A	A	A	A	R	A			A	A		R			A	R					A	R	A			F	A		A	A
1R-CC, 10-15	1.75	A	VG	F	A					D			A	D					A						A	R	D			F			A	D
3R-CC, 4-7	14.54	C	G						R				A					F					F		F						D		A	1
4R-CC, 2-3	24.12																																	
5R-CC, 8-9	33.88																																	
14R-CC, 4-7	122.13	A	G																				R		A								A	
15R-CC, 15-18	132.20	C	M																						D						D		D	
16R-CC, 7-10	142.11	A	M							F	F	A	D	A			F				A		R		A			A		F	A		A	
17R-2, 72-74	150.79	A	VG																F		D				D				F		D		D	
17R-CC, 17-20	150.99	A	M								R	D	D	A			F				A			R	A			A			A		A	
18R-1, 99-102	159.59	A	VG								F						D				D		F	F	D			D	F		D		D	
18R-CC, 21-24	164.76	C	M																															
19R-1, 38-39	168.68	A	VG											F			D				A				D				F		D	F	D	
20R-CC, 19-22	180.74	R	P											R											R			R				R		
21R-CC, 19-22	189.26	R	P																															
24R-CC, 14-17	220.88	F	M																				F		A						F		D	
25R-CC, 19-22	229.07	C	M																		A				A				R				D	
26R-CC, 0-3	239.95	C	M																		A		F		F						A		A	
27R-CC, 0-3	253.63	C	M																				F								A		A	
28R-CC, 16-18	259.16	C	M																				F		F						A		A	
29R-CC, 7-9	269.83	C	P																						F								A	
30R-CC, 10-12	281.22	F	M									R	F		F		R				R		R		R			R			F		R	
32R-CC, 20-23	299.18	F	M									F	F		F		R				R		F		R						R			
33R-CC, 23-26	307.55	F	M														R				R				R							F	F	
34R-CC, 13-16	318.00	R	P									R									R												R	
35R-CC, 20-23	326.49	R	P									R									R										R		R	
37R-CC, 18-19	345.25	R	P																		R										R		R	
39R-CC, 22-24	362.39	F	P																						R						F		F	
40R-CC, 20-22	371.72	A	G														A				A				A				R		D	R	A	
41R-CC, 15-17	382.86	R	P						R			R									R				R			R				R		
44R-CC, 16-18	409.69	F	G												F		R				F	R	R		R			R		F	F		F	
46R-CC, 17-19	429.10	R	P																		R		R									R	R	
48R-CC, 11-13	448.76																																	
51R-1, 49-50.5	475.99	F	M																				F		F						F			

Notes: Abundance (number of specimens per field of view): D = dominant (>10); A = abundant (2–9); C = common (lower range of abundant); F = few (0.5–1.0); R = rare (1–3 per tray); P = present (1 per 2–3 trays); B = barren; 1 = number observed. Preservation: VG = very good; G = good; M = moderate; P = poor.

Table T7. Interstitial water geochemistry, Hole 1108B.

Core, section, interval (cm)	Depth (mbsf)	Salinity	pH	Alkalinity (mM)	Na mM)	K (mM)	Mg (mM)	Ca (mM)	Cl (mM)	SO_4 (mM)	SiO_2 (µM)	Li (µM)	Sr (µM)	Ca/Mg
180-1108B-														
1R-1, 65-70	0.65	35	7.83	3.215	482	12.1	50.6	9.9	555	28.2	339	30	86	0.19
10R-1, 122-127	83.12	33	8.21	3.172	475	8.4	40.5	9.9	582	7.1	374	21	202	0.24
18R-4, 135-145	164.45	34	7.68	0.974	452	5.7	38.7	18.2	567	18.1	139	43	374	0.47
19R-1, 79-89	169.09	34			467	4.3	28.9	27.1	603	0.0	173	62	433	0.94
22R-4, 0-15	201.70	34			457	3.4	24.1	37.2	605	0.7	180	35	759	1.54
25R-1, 0-15	226.00	35			469	3.2	22.9	40.9	601	1.6	186	42	706	1.79
29R-3, 88-98	267.13	36	8.52	1.030	480	3.3	18.4	46.4	648	0.0	148	43	424	2.53
33R-1, 123-133	303.53	36			474	2.7	31.4	38.9	636	0.9	178	61	297	1.24
37R-2, 135-142	343.45	38			498	3.6	30.4	46.4	674	0.0	167	72	225	1.52
42R-5, 40-55	391.96	39			518	2.9	22.1	59.1	678	0.4	164	136		2.67

Note: Blanks indicate no measurement.

Table T8. Composition of headspace gas in sediments, Hole 1108B.

Core, section, interval (cm)	Depth (mbsf)	C_1	C_2	$C_2^=$	C_3	$C_3^=$	*iso*-C_4	*n*-C_4	*iso*-C_5	*n*-C_5	*iso*-C_6	*n*-C_6	C_1/C_2
180-1108B-													
1R-2, 0-5	1.00	2											
8R-1, 67-68	63.37	4											
9R-1, 0-1	72.30	3											
10R-1, 126-127	83.16	92											
14R-2, 0-2	121.36	31,548	28		6								1,131
15R-2, 0-2	130.63	14,593	14		4								1,050
16R-2, 0-2	140.90	6,300	13		2								481
17R-1, 0-2	149.00	29,939	19		1								1,592
18R-4, 0-2	163.10	43,596	25		2								1,723
19R-5, 0-2	172.30	33,457	18		2								1,848
20R-2, 102-105	180.52	15,878	18		6								887
21R-1, 0-1	187.60	22,585	35		8								653
22R-2, 148-150	200.18	23,194	31		14								743
23R-1, 148-150	208.28	2,247	43		14								52
24R-1, 148-150	217.88	33,814	42		12								811
25R-1, 0-2	226.00	24,849	40		18								623
26R-2, 0-2	237.10	1,587	11		6								144
27R-4, 0-2	249.40	784	5		1								170
28R-3, 0-2	257.18	1,671	12		6								140
29R-3, 86-88	267.11	624	3		1								183
30R-4, 0-2	277.48	33,926	25		12								1,385
31R-1, 0-2	283.00	24,548	10		2								2,557
32R-4, 146-147	297.94	22,539	16		9								1,391
33R-4, 0-2	306.02	3,483	16		7								218
34R-4, 129-131	317.51	21,167	9		3								2,352
35R-4, 42-44	326.27	19,845	8		3								2,362
36R-3, 146-147	334.88	38,657	31		15								1,243
37R-2, 0-2	342.10	9,671	5		3								2,149
38R-1, 0-2	350.50	33,536	29		18								1,164
39R-1, 0-2	360.10	27,436	33		24								824
40R-2, 0-2	370.71	59,668	35		15								1,715
41R-2, 0-2	380.90	3,687	18		7								200
42R-4, 0-2	391.02	26,934	42		38		16	7		6			640
43R-1, 111-113	399.71	38,659	26		15								1,510
44R-1, 132-133	409.52	26,264	63		39		9			3			420
45R-1, 109-111	418.89	32,375	44		13		7			3			737
46R-1, 142-143	428.92	17,468	49		14								360
47R-1, 0-2	437.10	37,712	41		16		7			3			911
48R-2, 0-2	447.30	1,533	62		24		8			3			25
49R-CC, 0-2	456.82	27,152	5		6	3	22	27	59	1			5,123
50R-1, 99-100	466.89	36,358	263		175		47	2	5	19			138
51R-1, 0-2	475.50	23,944	123		73		15			6			195

Notes: All concentrations are reported in parts per million by volume. Blanks indicate values below detection limit, except for C_1/C_2 ratio where blanks indicate an undefined value.

Table T9. Total bacterial populations and numbers of dividing and divided cells in sediments, Site 1108.

Depth (mbsf)	Total bacterial population (log cells/cm^3)	Dividing and divided cells (log cells/cm^3)
0.99	8.427	7.376
83.16	6.690	5.213
132.04	6.764	6.011
150.07	6.308	5.287
164.54	6.058	4.696
189.06	6.028	4.967

Table T10. Comparison of near-surface bacterial populations, water column depth, and sediment organic carbon concentrations.

	Leg-Site	Water depth (mbsf)	Total bacterial population (cells/cm^3)	Total organic carbon (wt%)
Santa Barbara Basin	146-893	576.5	1.27×10^9	2.98
Peru Margin	112-681	150.0	1.05×10^9	1.87
Cascadia Margin	146-892	674.5	2.18×10^7	1.18
Japan Sea	128-798	900.0	7.82×10^8	1.14
Cascadia Margin	146-888	2516.3	5.32×10^8	0.99
Cascadia Margin	146-890	1326.3	6.95×10^8	0.64
Juan de Fuca Ridge	139-857	2419.3	8.28×10^8	0.45
Amazon Fan	155-934	3432.0	6.04×10^8	0.43
Lau Basin	135-834	2702.9	6.12×10^8	0.26
Amazon Fan	155-940	3195.0	5.62×10^8	0.19
Eastern Equatorial Pacific	138-851	3760.3	2.08×10^8	0.05
This study	180-1108	3188.3	2.67×10^8	0.23

Table T11. Index properties measured in cores, Site 1108 (Continued on next two pages. See table note.)

Leg	Site	Hole	Core	Type	Section	Top (cm)	Bottom (cm)	Depth (mbsf)	Water content (bulk)	Water content (dry)	Bulk density ($g \cdot cm^{-3}$)	Dry density ($g \cdot cm^{-3}$)	Grain density ($g \cdot cm^{-3}$)	Porosity (%)	Void ratio
180	1108	B	1	R	1	13.5	15.5	0.14	50.7	103.0	1.478	0.728	2.721	73.2	2.74
180	1108	B	1	R	2	43.5	47.0	1.43	53.6	115.4	1.440	0.669	2.710	75.3	3.05
180	1108	B	8	R	1	43.0	45.5	63.13	21.3	27.1	2.007	1.579	2.711	41.7	0.72
180	1108	B	9	R	1	33.5	35.5	72.64	18.6	22.9	2.074	1.688	2.711	37.7	0.61
180	1108	B	10	R	1	110.0	113.0	83.00	20.7	26.2	2.017	1.598	2.702	40.8	0.69
180	1108	B	14	R	1	37.5	39.5	120.57	26.2	35.4	1.909	1.410	2.752	48.8	0.95
180	1108	B	14	R	2	44.0	47.5	121.80	21.6	27.6	2.008	1.573	2.733	42.4	0.74
180	1108	B	15	R	1	12.0	14.5	129.92	10.4	11.6	2.319	2.077	2.719	23.6	0.31
180	1108	B	15	R	2	40.0	42.0	131.03	23.0	29.9	1.973	1.519	2.730	44.4	0.80
180	1108	B	16	R	1	47.0	49.0	139.87	17.8	21.6	2.111	1.736	2.739	36.6	0.58
180	1108	B	16	R	2	24.0	26.0	141.14	21.6	27.5	1.961	1.538	2.621	41.3	0.71
180	1108	B	17	R	1	41.0	45.0	149.41	33.4	50.2	1.726	1.149	2.631	56.4	1.29
180	1108	B	17	R	2	53.0	55.0	150.60	28.4	39.7	1.828	1.308	2.657	50.8	1.03
180	1108	B	18	R	1	60.0	62.5	159.20	27.9	38.6	1.858	1.340	2.710	50.6	1.02
180	1108	B	18	R	2	146.0	148.0	161.56	19.0	23.4	2.069	1.677	2.717	38.3	0.62
180	1108	B	18	R	3	36.0	37.0	161.96	19.6	24.4	2.067	1.661	2.751	39.6	0.66
180	1108	B	18	R	4	63.0	65.0	163.73	20.7	26.0	2.021	1.604	2.708	40.8	0.69
180	1108	B	19	R	1	10.0	11.0	168.40	23.6	30.8	1.934	1.479	2.664	44.5	0.80
180	1108	B	19	R	2	2.5	4.5	169.22	20.0	25.0	2.025	1.620	2.680	39.5	0.65
180	1108	B	19	R	3	43.0	45.0	170.23	18.6	22.8	2.057	1.675	2.673	37.3	0.60
180	1108	B	19	R	5	49.0	51.0	172.79	16.2	19.4	2.131	1.785	2.694	33.7	0.51
180	1108	B	20	R	1	9.5	11.5	178.10	17.6	21.4	2.096	1.727	2.701	36.1	0.56
180	1108	B	20	R	2	22.0	24.0	179.72	15.7	18.6	2.145	1.808	2.695	32.9	0.49
180	1108	B	21	R	1	31.0	33.0	187.91	17.1	20.7	2.100	1.740	2.683	35.1	0.54
180	1108	B	22	R	1	45.0	47.0	197.65	16.5	19.7	2.146	1.792	2.739	34.6	0.53
180	1108	B	22	R	2	128.0	130.0	199.98	16.4	19.6	2.131	1.782	2.703	34.1	0.52
180	1108	B	22	R	3	129.0	131.0	201.49	16.2	19.3	2.135	1.790	2.700	33.7	0.51
180	1108	B	22	R	4	128.0	130.0	202.98	16.5	19.8	2.121	1.771	2.690	34.2	0.52
180	1108	B	22	R	5	128.0	130.0	204.48	16.2	19.4	2.110	1.767	2.657	33.5	0.50
180	1108	B	22	R	6	15.0	17.0	204.82	6.1	6.5	2.482	2.330	2.736	14.9	0.17
180	1108	B	23	R	1	117.0	119.0	207.97	18.0	21.9	2.098	1.721	2.725	36.8	0.58
180	1108	B	23	R	2	143.0	145.0	209.73	16.9	20.3	2.117	1.759	2.703	34.9	0.54
180	1108	B	23	R	3	147.0	148.5	211.26	17.2	20.7	2.095	1.735	2.675	35.1	0.54
180	1108	B	23	R	4	125.0	127.0	212.55	17.7	21.5	2.097	1.726	2.710	36.3	0.57
180	1108	B	24	R	1	74.5	76.5	217.15	8.6	9.4	2.402	2.196	2.748	20.1	0.25
180	1108	B	24	R	2	19.0	21.0	218.09	16.0	19.0	2.149	1.806	2.715	33.5	0.50
180	1108	B	24	R	3	87.5	89.5	219.71	16.7	20.0	2.107	1.755	2.673	34.3	0.52
180	1108	B	25	R	1	69.5	71.5	226.70	17.8	21.6	2.103	1.729	2.725	36.5	0.58
180	1108	B	25	R	2	11.5	13.5	227.62	18.8	23.1	2.051	1.666	2.672	37.7	0.60
180	1108	B	26	R	1	141.0	143.0	237.01	10.6	11.8	2.364	2.114	2.795	24.4	0.32
180	1108	B	26	R	2	140.0	142.0	238.50	16.0	19.0	2.166	1.820	2.748	33.8	0.51
180	1108	B	26	R	3	87.5	89.5	239.48	13.3	15.4	2.271	1.968	2.793	29.5	0.42
180	1108	B	27	R	1	125.0	127.0	246.15	13.9	16.2	2.233	1.922	2.759	30.3	0.44
180	1108	B	27	R	2	117.0	119.0	247.57	15.7	18.6	2.171	1.830	2.744	33.3	0.50
180	1108	B	27	R	3	128.0	130.0	249.18	13.8	16.0	2.226	1.918	2.743	30.0	0.43
180	1108	B	27	R	4	126.0	128.0	250.66	11.8	13.4	2.300	2.028	2.762	26.6	0.36
180	1108	B	27	R	5	84.0	86.0	251.74	15.9	18.9	2.158	1.816	2.728	33.4	0.50
180	1108	B	27	R	6	78.0	80.0	253.18	13.4	15.5	2.244	1.943	2.754	29.5	0.42

Table T11 (continued).

Leg	Site	Hole	Core	Type	Section	Top (cm)	Bottom (cm)	Depth (mbsf)	Water content (bulk)	Water content (dry)	Bulk density ($g \cdot cm^{-3}$)	Dry density ($g \cdot cm^{-3}$)	Grain density ($g \cdot cm^{-3}$)	Porosity (%)	Void ratio
180	1108	B	28	R	1	102.0	104.0	255.52	15.1	17.7	2.187	1.857	2.738	32.2	0.48
180	1108	B	28	R	2	74.0	76.0	256.70	13.0	15.0	2.284	1.986	2.801	29.1	0.41
180	1108	B	28	R	3	13.0	15.0	257.31	16.7	20.0	2.152	1.793	2.761	35.1	0.54
180	1108	B	28	R	4	86.0	88.0	258.95	8.5	9.3	2.408	2.203	2.754	20.0	0.25
180	1108	B	29	R	1	92.0	94.0	265.02	14.4	16.8	2.226	1.905	2.774	31.3	0.46
180	1108	B	29	R	2	6.0	8.0	265.41	16.2	19.3	2.150	1.802	2.728	34.0	0.51
180	1108	B	29	R	3	83.0	85.0	267.08	13.0	15.0	2.259	1.964	2.757	28.7	0.40
180	1108	B	29	R	4	89.0	91.0	268.12	7.4	8.0	2.460	2.278	2.773	17.9	0.22
180	1108	B	29	R	5	23.0	25.0	268.70	15.1	17.7	2.215	1.882	2.792	32.6	0.48
180	1108	B	30	R	1	147.0	149.0	274.87	7.0	7.6	2.462	2.289	2.756	16.9	0.20
180	1108	B	30	R	2	84.0	86.0	275.75	14.2	16.6	2.222	1.906	2.757	30.9	0.45
180	1108	B	30	R	3	2.0	4.0	275.99	13.1	15.1	2.275	1.976	2.791	29.2	0.41
180	1108	B	30	R	4	17.0	19.0	277.65	16.2	19.3	2.173	1.822	2.773	34.3	0.52
180	1108	B	30	R	5	18.0	20.0	278.86	14.6	17.2	2.222	1.896	2.779	31.8	0.47
180	1108	B	30	R	6	27.0	29.0	280.08	12.9	14.8	2.265	1.974	2.760	28.5	0.40
180	1108	B	30	R	7	56.0	58.0	280.89	13.6	15.7	2.257	1.95	2.783	29.9	0.43
180	1108	B	31	R	1	91.0	93.0	283.91	8.8	9.7	2.416	2.203	2.781	20.8	0.26
180	1108	B	31	R	2	56.0	58.0	285.04	16.6	19.9	2.130	1.777	2.713	34.5	0.53
180	1108	B	31	R	3	35.0	37.0	286.26	11.5	12.9	2.308	2.044	2.754	25.8	0.35
180	1108	B	31	R	4	69.0	71.0	286.99	14.7	17.3	2.212	1.886	2.767	31.9	0.47
180	1108	B	32	R	1	97.0	99.0	293.67	11.3	12.7	2.307	2.047	2.744	25.4	0.34
180	1108	B	32	R	2	101.0	102.5	294.85	10.0	11.2	2.359	2.122	2.762	23.2	0.30
180	1108	B	32	R	3	92.0	94.0	295.97	14.0	16.3	2.239	1.926	2.775	30.6	0.44
180	1108	B	32	R	4	91.0	93.0	297.39	15.0	17.7	2.196	1.866	2.752	32.2	0.48
180	1108	B	32	R	5	60.0	62.0	298.55	16.1	19.2	2.162	1.813	2.750	34.1	0.52
180	1108	B	33	R	1	104.0	106.0	303.34	16.8	20.1	2.122	1.766	2.706	34.7	0.53
180	1108	B	33	R	2	29.5	31.5	303.92	15.6	18.5	2.163	1.825	2.724	33.0	0.49
180	1108	B	33	R	3	1.5	3.5	305.11	15.0	17.7	2.197	1.867	2.753	32.2	0.48
180	1108	B	33	R	4	119.0	120.5	307.20	13.9	16.1	2.221	1.913	2.735	30.1	0.43
180	1108	B	34	R	1	89.0	91.0	312.89	8.3	9.0	2.416	2.216	2.755	19.6	0.24
180	1108	B	34	R	2	51.5	53.5	313.86	10.4	11.6	2.334	2.091	2.741	23.7	0.31
180	1108	B	34	R	3	94.0	96.0	315.77	15.3	18.1	2.176	1.842	2.734	32.6	0.48
180	1108	B	34	R	4	117.0	118.5	317.39	11.7	13.2	2.293	2.025	2.743	26.2	0.35
180	1108	B	35	R	1	115.0	116.5	322.74	12.0	13.7	2.272	1.998	2.727	26.7	0.37
180	1108	B	35	R	2	76.0	78.0	323.86	14.0	16.3	2.242	1.928	2.782	30.7	0.44
180	1108	B	35	R	3	51.5	53.5	324.86	11.8	13.4	2.288	2.017	2.741	26.4	0.36
180	1108	B	35	R	4	3.5	5.5	325.89	9.5	10.5	2.360	2.137	2.733	21.8	0.28
180	1108	B	36	R	1	28.0	30.0	331.58	10.9	12.2	2.311	2.059	2.731	24.6	0.33
180	1108	B	36	R	2	64.0	66.0	332.95	12.3	14.1	2.270	1.989	2.739	27.4	0.38
180	1108	B	36	R	3	61.0	63.0	334.03	11.2	12.6	2.298	2.04	2.728	25.2	0.34
180	1108	B	36	R	4	45.0	47.0	335.34	17.0	20.5	2.116	1.756	2.708	35.1	0.54
180	1108	B	36	R	5	8.0	10.0	336.29	12.0	13.7	2.283	2.008	2.744	26.8	0.37
180	1108	B	37	R	1	65.0	67.0	341.55	9.0	9.9	2.391	2.175	2.756	21.1	0.27
180	1108	B	37	R	2	23.0	25.0	342.33	11.5	12.9	2.287	2.025	2.721	25.6	0.34
180	1108	B	37	R	3	2.0	4.0	343.54	12.7	14.6	2.264	1.976	2.748	28.1	0.39
180	1108	B	37	R	4	23.0	25.0	345.02	7.8	8.5	2.416	2.227	2.730	18.4	0.23
180	1108	B	38	R	1	114.0	116.0	351.64	12.7	14.6	2.256	1.969	2.736	28.0	0.39
180	1108	B	39	R	1	86.0	88.0	360.96	14.7	17.2	2.179	1.859	2.703	31.2	0.45

Table T11 (continued).

Leg	Site	Hole	Core	Type	Section	Top (cm)	Bottom (cm)	Depth (mbsf)	Water content (bulk)	Water content (dry)	Bulk density ($g \cdot cm^{-3}$)	Dry density ($g \cdot cm^{-3}$)	Grain density ($g \cdot cm^{-3}$)	Porosity (%)	Void ratio
180	1108	B	39	R	2	83.0	85.0	362.09	17.6	21.4	2.075	1.710	2.658	35.7	0.56
180	1108	B	40	R	1	65.0	67.0	370.45	15.6	18.6	2.148	1.811	2.696	32.8	0.49
180	1108	B	40	R	2	41.0	43.0	371.12	19.8	24.7	2.020	1.620	2.657	39.0	0.64
180	1108	B	41	R	1	99.0	101.0	380.39	13.3	15.4	2.220	1.924	2.706	28.9	0.41
180	1108	B	41	R	2	82.0	84.0	381.72	17.1	20.6	2.119	1.757	2.717	35.3	0.55
180	1108	B	41	R	3	10.0	12.0	382.48	9.0	9.9	2.346	2.134	2.691	20.7	0.26
180	1108	B	42	R	1	90.0	92.0	389.90	15.3	18.0	2.154	1.826	2.688	32.1	0.47
180	1108	B	42	R	4	35.0	37.0	391.37	14.0	16.3	2.187	1.880	2.684	29.9	0.43
180	1108	B	42	R	5	36.0	38.0	391.92	15.4	18.2	2.142	1.811	2.675	32.3	0.48
180	1108	B	42	R	6	64.0	66.0	392.75	14.1	16.3	2.190	1.883	2.691	30.1	0.43
180	1108	B	43	R	1	105.0	107.0	399.65	10.1	11.3	2.310	2.075	2.691	22.9	0.30
180	1108	B	45	R	2	10.0	12.0	419.01	11.3	12.8	2.281	2.023	2.706	25.2	0.34
180	1108	B	46	R	1	21.0	23.0	427.71	12.6	14.4	2.233	1.953	2.691	27.4	0.38
180	1108	B	48	R	1	27.0	29.0	446.97	11.9	13.5	2.252	1.985	2.686	26.1	0.35
180	1108	B	48	R	2	34.0	36.0	447.64	9.5	10.6	2.325	2.103	2.685	21.7	0.28
180	1108	B	49	R	1	37.0	39.0	456.67	12.8	14.7	2.226	1.941	2.690	27.8	0.39
180	1108	B	50	R	1	97.0	99.0	466.87	11.0	12.4	2.292	2.039	2.708	24.7	0.33
180	1108	B	51	R	1	111.0	113.0	476.61	13.3	15.4	2.223	1.926	2.711	29.0	0.41

Note: This table is also available also in ASCII format in the **TABLES** directory.

Table T12. Longitudinal (z) and transverse (x and y) velocities for cores, Site 1108. (Continued on next page. See table note.)

Leg	Site	Hole	Core	Type	Section	Top (cm)	Bottom (cm)	Depth (mbsf)	x-velocity ($m \cdot s^{-1}$)	y-velocity ($m \cdot s^{-1}$)	z-velocity ($m \cdot s^{-1}$)
180	1108	B	1	R	1	13.1	13.1	0.13	NA	NA	1528
180	1108	B	1	R	1	13.4	13.4	0.13	NA	1526	NA
180	1108	B	1	R	2	21.5	21.5	1.22	NA	NA	1524
180	1108	B	1	R	2	47.1	47.1	1.47	NA	1518	NA
180	1108	B	9	R	1	34.6	34.6	72.65	2066	NA	NA
180	1108	B	10	R	1	111.5	111.5	83.02	2024	NA	NA
180	1108	B	15	R	1	21.8	21.8	130.02	2713	NA	NA
180	1108	B	15	R	2	92.9	92.9	131.56	2544	NA	NA
180	1108	B	16	R	1	70.1	70.1	140.10	2300	NA	NA
180	1108	B	16	R	2	87.1	87.1	141.77	2459	NA	NA
180	1108	B	17	R	1	92.6	92.6	149.93	2239	NA	NA
180	1108	B	17	R	2	45.9	45.9	150.53	2204	NA	NA
180	1108	B	18	R	1	107.0	107.0	159.67	2212	2217	2172
180	1108	B	18	R	2	57.0	57.0	160.67	2073	NA	NA
180	1108	B	18	R	2	117.1	117.1	161.27	2137	NA	NA
180	1108	B	18	R	3	25.0	25.0	161.85	2324	2284	2298
180	1108	B	18	R	3	30.4	30.4	161.91	2222	NA	NA
180	1108	B	18	R	4	54.8	54.8	163.65	2117	NA	NA
180	1108	B	18	R	4	57.0	57.0	163.67	2282	2266	2228
180	1108	B	19	R	1	30.7	30.7	168.61	2244	NA	NA
180	1108	B	19	R	2	15.4	15.4	169.34	2137	NA	NA
180	1108	B	19	R	2	40.0	40.0	169.59	2367	2386	2470
180	1108	B	19	R	3	95.6	95.6	170.76	2161	NA	NA
180	1108	B	19	R	5	55.0	55.0	172.85	2542	2612	2425
180	1108	B	20	R	1	14.5	14.5	178.15	2431	2551	2314
180	1108	B	20	R	2	11.3	11.3	179.61	2454	NA	NA
180	1108	B	20	R	2	44.5	44.5	179.95	NA	2054	NA
180	1108	B	21	R	1	109.0	109.0	188.69	2479	2463	2232
180	1108	B	22	R	1	50.5	50.5	197.71	2587	2569	2507
180	1108	B	22	R	2	29.0	29.0	198.99	2475	2475	2475
180	1108	B	22	R	3	21.0	21.0	200.41	2524	2573	2303
180	1108	B	22	R	4	83.0	83.0	202.53	2762	2847	2168
180	1108	B	22	R	5	34.0	34.0	203.54	2389	2396	1872
180	1108	B	23	R	1	114.0	114.0	207.94	2357	2433	2262
180	1108	B	23	R	2	147.5	147.5	209.78	2619	2607	2538
180	1108	B	23	R	3	106.2	106.2	210.86	2308	2412	2251
180	1108	B	23	R	4	98.5	98.5	212.29	2249	2307	1960
180	1108	B	24	R	1	83.0	83.0	217.23	3557	3659	3596
180	1108	B	24	R	2	16.0	16.0	218.06	2470	2576	2339
180	1108	B	24	R	3	84.0	84.0	219.68	2381	2413	2062
180	1108	B	24	R	4	38.0	38.0	220.72	2566	2536	2474
180	1108	B	25	R	1	74.0	74.0	226.74	2459	2556	2364
180	1108	B	25	R	2	68.0	68.0	228.18	2553	2674	2493
180	1108	B	26	R	1	101.0	101.0	236.61	2579	2590	2271
180	1108	B	26	R	2	133.7	133.7	238.44	2579	2619	2371
180	1108	B	26	R	3	91.5	91.5	239.52	2531	2708	2780
180	1108	B	27	R	1	61.5	61.5	245.52	2577	2638	2464
180	1108	B	27	R	2	123.0	123.0	247.63	2566	2538	2443
180	1108	B	27	R	3	35.0	35.0	249.13	2373	2205	2245
180	1108	B	27	R	4	35.5	35.5	249.76	3135	3013	3157
180	1108	B	27	R	5	38.0	38.0	251.28	3052	3077	3012
180	1108	B	27	R	6	19.5	19.5	252.60	2833	2851	2811
180	1108	B	28	R	1	45.0	45.0	254.95	2524	2466	2187
180	1108	B	28	R	2	38.0	38.0	256.34	2529	2667	2416
180	1108	B	28	R	3	39.0	39.0	257.57	2572	2601	2388
180	1108	B	28	R	4	41.0	41.0	258.50	2228	2308	2262
180	1108	B	29	R	1	24.0	24.0	264.51	2846	2947	2643
180	1108	B	29	R	2	37.0	37.0	265.72	2737	2691	2484
180	1108	B	29	R	3	28.5	28.5	266.54	1970	1968	2074
180	1108	B	29	R	4	42.0	42.0	267.65	2783	2710	2542
180	1108	B	29	R	5	74.5	74.5	269.22	2732	2974	2825
180	1108	B	30	R	1	18.0	18.0	273.58	2566	2603	2434
180	1108	B	30	R	2	19.5	19.5	275.11	2119	2237	2030
180	1108	B	30	R	3	69.5	69.5	276.67	2855	3046	2964
180	1108	B	30	R	4	76.0	76.0	278.24	2562	2534	2346
180	1108	B	30	R	5	54.5	54.5	279.23	2174	2442	2320
180	1108	B	30	R	6	22.0	22.0	280.03	2734	2828	2676
180	1108	B	30	R	7	48.5	48.5	280.82	1889	2247	2118

Table T12 (continued).

Leg	Site	Hole	Core	Type	Section	Top (cm)	Bottom (cm)	Depth (mbsf)	x-velocity ($m \cdot s^{-1}$)	y-velocity ($m \cdot s^{-1}$)	z-velocity ($m \cdot s^{-1}$)
180	1108	B	31	R	1	126.0	126.0	284.26	2027	1806	1927
180	1108	B	31	R	2	97.0	97.0	285.45	2602	3505	2490
180	1108	B	31	R	3	29.0	29.0	286.2	2648	2696	2805
180	1108	B	31	R	4	61.0	61.0	286.91	2769	2675	2663
180	1108	B	32	R	1	9.5	9.5	292.80	2659	2661	2360
180	1108	B	32	R	2	84.5	84.5	294.70	2362	2254	2224
180	1108	B	32	R	3	65.5	65.5	295.71	2368	2391	2260
180	1108	B	32	R	4	121.5	121.5	297.70	2490	2601	2268
180	1108	B	32	R	5	45.5	45.5	298.42	2441	2389	2548
180	1108	B	33	R	1	108.0	108.0	303.38	2400	2489	2399
180	1108	B	33	R	2	46.3	46.3	304.09	2563	2635	2632
180	1108	B	33	R	3	57.5	57.5	305.68	2643	2687	2455
180	1108	B	33	R	4	11.0	11.0	306.13	2568	2474	2259
180	1108	B	34	R	1	85.7	85.7	312.86	3016	3185	3029
180	1108	B	34	R	2	62.5	62.5	313.97	2935	3221	3164
180	1108	B	34	R	3	126.3	126.3	316.09	2579	2663	2351
180	1108	B	34	R	4	110.7	110.7	317.33	2412	2667	2478
180	1108	B	35	R	1	110.7	110.7	322.71	2708	2677	2545
180	1108	B	35	R	2	68.0	68.0	323.78	2762	2735	2505
180	1108	B	35	R	3	34.7	34.7	324.70	2756	2734	2546
180	1108	B	35	R	4	9.8	9.8	325.95	2479	2618	2403
180	1108	B	36	R	1	34.0	34.0	331.64	2833	2834	2856
180	1108	B	36	R	2	60.0	60.0	332.65	2387	2601	2767
180	1108	B	36	R	3	88.0	88.0	334.3	3116	3194	2889
180	1108	B	36	R	4	107.5	107.5	335.97	2189	2585	2761
180	1108	B	36	R	5	28.5	28.5	336.50	3014	3015	2584
180	1108	B	37	R	1	61.5	61.5	341.52	2926	3169	2907
180	1108	B	37	R	2	20.5	20.5	342.31	2348	2837	2663
180	1108	B	37	R	3	96.0	96.0	344.48	3166	2965	2675
180	1108	B	37	R	4	18.0	18.0	344.97	3258	3572	3474
180	1108	B	38	R	1	99.0	99.0	351.49	2750	2915	2903
180	1108	B	39	R	1	68.0	68.0	360.78	3001	3116	2908
180	1108	B	39	R	2	46.5	46.5	361.73	2959	3161	3004
180	1108	B	40	R	1	69.0	69.0	370.49	2936	3110	2897
180	1108	B	40	R	2	10.0	10.0	370.81	2820	2840	2714
180	1108	B	41	R	1	93.0	93.0	380.33	3577	3523	3484
180	1108	B	41	R	2	14.0	14.0	381.04	3070	3110	3020
180	1108	B	41	R	3	15.0	15.0	382.53	4537	3982	3809
180	1108	B	42	R	1	97.0	97.0	389.97	2818	2900	2485
180	1108	B	42	R	4	53.0	53.0	391.55	2603	2868	2594
180	1108	B	42	R	5	6.0	6.0	391.62	2702	2821	2649
180	1108	B	43	R	1	77.5	77.5	399.38	2618	2653	2438
180	1108	B	44	R	1	87.5	87.5	409.08	2761	2766	2684
180	1108	B	45	R	1	25.5	25.5	418.06	2432	2535	2336
180	1108	B	45	R	2	17.0	17.0	419.08	2569	2550	2164
180	1108	B	46	R	1	26.5	26.5	427.77	2689	2769	2444
180	1108	B	47	R	1	52.0	52.0	437.62	3596	3558	3538
180	1108	B	48	R	2	49.0	49.0	447.74	2730	2774	2328
180	1108	B	48	R	1	43.8	43.8	456.74	2690	2769	2459
180	1108	B	49	R	1	46.5	46.5	456.77	3450	3435	3464
180	1108	B	50	R	1	42.0	42.0	466.32	2939	2955	2709
180	1108	B	51	R	1	54.0	54.0	476.04	3023	2693	2620

Notes: This table is also available also in ASCII format in the **TABLES** directory. NA = Data not available.

Table T13. Thermal conductivity values in cores, Site 1108. (Continued on next three pages. See table note.)

Leg	Site	Hole	Core	Type	Section	Top interval (cm)	Bottom interval (cm)	Top depth (mbsf)	Bottom depth (mbsf)	Middle depth (mbsf)	Thermal conductivity ($W \cdot m^{-1} \cdot °C^{-1}$)	Thermal conductivity average ($W \cdot m^{-1} \cdot °C^{-1}$)
180	1108	B	1	R	1	34.0	34.0	0.340	0.340	0.340	0.769	
180	1108	B	1	R	1	34.0	34.0	0.340	0.340	0.340	0.788	
180	1108	B	1	R	1	34.0	34.0	0.340	0.340	0.340	0.778	0.778
180	1108	B	1	R	2	32.0	32.0	1.320	1.320	1.320	0.958	
180	1108	B	1	R	2	32.0	32.0	1.320	1.320	1.320	0.916	
180	1108	B	1	R	2	32.0	32.0	1.320	1.320	1.320	0.918	0.931
180	1108	B	15	R	1	61.0	64.0	130.410	130.440	130.225	1.444	
180	1108	B	15	R	1	61.0	64.0	130.410	130.440	130.225	1.423	
180	1108	B	15	R	1	61.0	64.0	130.410	130.440	130.225	1.485	
180	1108	B	15	R	1	61.0	64.0	130.410	130.440	130.225	1.435	1.447
180	1108	B	16	R	1	47.0	49.0	139.870	139.890	139.880	1.069	
180	1108	B	16	R	1	47.0	49.0	139.870	139.890	139.880	1.069	
180	1108	B	16	R	1	47.0	49.0	139.870	139.890	139.880	1.066	
180	1108	B	16	R	1	47.0	49.0	139.870	139.890	139.880	1.068	1.068
180	1108	B	18	R	1	104.5	106.0	159.645	159.660	159.653	1.160	
180	1108	B	18	R	1	104.5	106.0	159.645	159.660	159.653	1.140	
180	1108	B	18	R	1	104.5	106.0	159.645	159.660	159.653	1.134	1.145
180	1108	B	18	R	2	147.0	148.0	161.570	161.580	161.575	1.003	
180	1108	B	18	R	2	147.0	148.0	161.570	161.580	161.575	1.260	
180	1108	B	18	R	2	147.0	148.0	161.570	161.580	161.575	0.947	
180	1108	B	18	R	2	147.0	148.0	161.570	161.580	161.575	1.185	1.099
180	1108	B	18	R	4	61.0	62.0.	163.710	163.720	163.715	1.192	
180	1108	B	18	R	4	61.0	62.0	163.710	163.720	163.715	1.218	
180	1108	B	18	R	4	61.0	62.0	163.710	163.720	163.715	1.064	
180	1108	B	18	R	4	61.0	62.0	163.710	163.720	163.715	1.020	1.124
180	1108	B	18	R	3	21.0	23.0	161.810	161.830	161.820	1.280	
180	1108	B	18	R	3	21.0	23.0	161.810	161.830	161.820	1.308	
180	1108	B	18	R	3	21.0	23.0	161.810	161.830	161.820	1.310	
180	1108	B	18	R	3	21.0	23.0	161.810	161.830	161.820	1.305	1.301
180	1108	B	19	R	1	35.5	36.5	168.655	168.665	168.660	1.183	
180	1108	B	19	R	1	35.5	36.5	168.655	168.665	168.660	1.116	
180	1108	B	19	R	1	35.5	36.5	168.655	168.665	168.660	1.138	
180	1108	B	19	R	1	35.5	36.5	168.655	168.665	168.660	1.133	1.143
180	1108	B	19	R	2	38.5	41.0	169.575	169.600	169.588	1.369	
180	1108	B	19	R	2	38.5	41.0	169.575	169.600	169.588	1.341	
180	1108	B	19	R	2	38.5	41.0	169.575	169.600	169.588	1.332	
180	1108	B	19	R	2	38.5	41.0	169.575	169.600	169.588	1.353	1.349
180	1108	B	19	R	3	121.0	124.0	171.010	171.040	171.025	1.092	
180	1108	B	19	R	3	121.0	124.0	171.010	171.040	171.025	1.076	
180	1108	B	19	R	3	121.0	124.0	171.010	171.040	171.025	1.075	
180	1108	B	19	R	3	121.0	124.0	171.010	171.040	171.025	1.078	1.080
180	1108	B	19	R	5	27.0	30.0	172.570	172.600	172.585	1.082	
180	1108	B	19	R	5	27.0	30.0	172.570	172.600	172.585	1.080	
180	1108	B	19	R	5	27.0	30.0	172.570	172.600	172.585	1.082	1.081
180	1108	B	20	R	1	13.0	14.0	178.130	178.140	178.135	1.125	
180	1108	B	20	R	1	13.0	14.0	178.130	178.140	178.135	1.113	
180	1108	B	20	R	1	13.0	14.0	178.130	178.140	178.135	1.158	1.132
180	1108	B	21	R	1	110.0	111.0	188.700	188.710	188.705	1.115	
180	1108	B	21	R	1	110.0	111.0	188.700	188.710	188.705	1.120	1.118
180	1108	B	22	R	1	48.0	49.0	197.680	197.690	197.685	1.219	
180	1108	B	22	R	1	48.0	49.0	197.680	197.690	197.685	1.212	
180	1108	B	22	R	1	48.0	49.0	197.680	197.690	197.685	1.211	
180	1108	B	22	R	1	48.0	49.0	197.680	197.690	197.685	1.215	1.214
180	1108	B	22	R	3	18.0	20.0	200.380	200.400	200.390	1.096	
180	1108	B	22	R	3	18.0	20.0	200.380	200.400	200.390	1.029	
180	1108	B	22	R	3	18.0	20.0	200.380	200.400	200.390	1.042	
180	1108	B	22	R	3	18.0	20.0	200.380	200.400	200.390	1.057	1.056
180	1108	B	22	R	5	31.0	33.0	203.510	203.530	203.520	1.093	
180	1108	B	22	R	5	31.0	33.0	203.510	203.530	203.520	1.092	
180	1108	B	22	R	5	31.0	33.0	203.510	203.530	203.520	1.074	
180	1108	B	22	R	5	31.0	33.0	203.510	203.530	203.520	1.098	1.089
180	1108	B	23	R	1	114.5	117.0	207.945	207.970	207.958	1.120	
180	1108	B	23	R	1	114.5	117.0	207.945	207.970	207.958	1.120	
180	1108	B	23	R	1	114.5	117.0	207.945	207.970	207.958	1.115	
180	1108	B	23	R	1	114.5	117.0	207.945	207.970	207.958	1.121	1.119
180	1108	B	23	R	3	149.0	150.0	211.290	211.300	211.295	1.008	
180	1108	B	23	R	3	149.0	150.0	211.290	211.300	211.295	1.081	1.045

Table T13 (continued).

Leg	Site	Hole	Core	Type	Section	Top interval (cm)	Bottom interval (cm)	Top depth (mbsf)	Bottom depth (mbsf)	Middle depth (mbsf)	Thermal conductivity ($W \cdot m^{-1} \cdot °C^{-1}$)	Thermal conductivity average ($W \cdot m^{-1} \cdot °C^{-1}$)
180	1108	B	24	R	1	84.5	86.5	217.245	217.265	217.255	1.534	
180	1108	B	24	R	1	84.5	86.5	217.245	217.265	217.255	1.571	
180	1108	B	24	R	1	84.5	86.5	217.245	217.265	217.255	1.516	
180	1108	B	24	R	1	84.5	86.5	217.245	217.265	217.255	1.491	1.528
180	1108	B	24	R	3	89.0	91.0	219.730	219.750	219.740	1.113	
180	1108	B	24	R	3	89.0	91.0	219.730	219.750	219.740	1.115	
180	1108	B	24	R	3	89.0	91.0	219.730	219.750	219.740	1.119	
180	1108	B	24	R	3	89.0	91.0	219.730	219.750	219.740	1.117	1.116
180	1108	B	25	R	1	77.0	79.0	226.770	226.790	226.780	1.102	
180	1108	B	25	R	1	77.0	79.0	226.770	226.790	226.780	1.231	
180	1108	B	25	R	1	77.0	79.0	226.770	226.790	226.780	1.066	
180	1108	B	25	R	1	77.0	79.0	226.770	226.790	226.780	1.100	1.125
180	1108	B	26	R	1	129.0	130.0	236.890	236.900	236.895	1.252	
180	1108	B	26	R	1	129.0	130.0	236.890	236.900	236.895	1.189	
180	1108	B	26	R	1	129.0	130.0	236.890	236.900	236.895	1.323	
180	1108	B	26	R	1	129.0	130.0	236.890	236.900	236.895	1.308	1.268
180	1108	B	23	R	3	92.5	93.5	210.725	210.735	210.730	1.184	
180	1108	B	23	R	3	92.5	93.5	210.725	210.735	210.730	1.202	
180	1108	B	23	R	3	92.5	93.5	210.725	210.735	210.730	1.198	
180	1108	B	23	R	3	92.5	93.5	210.725	210.735	210.730	1.198	1.120
180	1108	B	27	R	1	60.0	61.0	245.500	245.510	245.505	1.256	
180	1108	B	27	R	1	60.0	61.0	245.500	245.510	245.505	1.253	
180	1108	B	27	R	1	60.0	61.0	245.500	245.510	245.505	1.256	
180	1108	B	27	R	1	60.0	61.0	245.500	245.510	245.505	1.261	1.257
180	1108	B	27	R	3	33.0	34.0	248.230	248.240	248.235	1.153	
180	1108	B	27	R	3	33.0	34.0	248.230	248.240	248.235	1.160	
180	1108	B	27	R	3	33.0	34.0	248.230	248.240	248.235	1.162	
180	1108	B	27	R	3	33.0	34.0	248.230	248.240	248.235	1.164	1.160
180	1108	B	27	R	5	17.0	18.0	251.070	251.080	251.075	1.380	
180	1108	B	27	R	5	17.0	18.0	251.070	251.080	251.075	1.484	1.298
180	1108	B	28	R	1	41.0	43.0	254.910	254.930	254.920	1.036	
180	1108	B	28	R	1	41.0	43.0	254.910	254.930	254.920	1.048	
180	1108	B	28	R	1	41.0	43.0	254.910	254.930	254.920	1.048	
180	1108	B	28	R	1	41.0	43.0	254.910	254.930	254.920	1.049	1.045
180	1108	B	28	R	3	36.5	37.0	257.545	257.550	257.548	1.025	
180	1108	B	28	R	3	36.5	37.0	257.545	257.550	257.548	1.034	
180	1108	B	28	R	3	36.5	37.0	257.545	257.550	257.548	1.034	
180	1108	B	28	R	3	36.5	37.0	257.545	257.550	257.548	1.037	1.033
180	1108	B	29	R	1	20.0	21.5	264.300	264.315	264.308	1.474	
180	1108	B	29	R	1	20.0	21.5	264.300	264.315	264.308	1.484	
180	1108	B	29	R	1	20.0	21.5	264.300	264.315	264.308	1.468	
180	1108	B	29	R	1	20.0	21.5	264.300	264.315	264.308	1.426	1.463
180	1108	B	29	R	3	26.0	27.0	266.510	266.520	266.515	1.160	
180	1108	B	29	R	3	26.0	27.0	266.510	266.520	266.515	1.159	
180	1108	B	29	R	3	26.0	27.0	266.510	266.520	266.515	1.160	1.160
180	1108	B	29	R	5	76.0	77.0	269.230	269.240	269.235	1.550	
180	1108	B	29	R	5	76.0	77.0	269.230	269.240	269.235	1.556	1.553
180	1108	B	30	R	1	15.0	17.0	273.550	273.570	273.560	1.186	
180	1108	B	30	R	1	15.0	17.0	273.550	273.570	273.560	1.187	1.187
180	1108	B	30	R	3	67.0	68.0	276.640	276.650	276.645	1.360	
180	1108	B	30	R	3	67.0	68.0	276.640	276.650	276.645	1.506	
180	1108	B	30	R	3	67.0	68.0	276.640	276.650	276.645	1.429	
180	1108	B	30	R	3	67.0	68.0	276.640	276.650	276.645	1.532	1.457
180	1108	B	30	R	5	50.5	53.0	279.185	279.210	279.198	1.506	
180	1108	B	30	R	5	50.5	53.0	279.185	279.210	279.198	1.533	1.520
180	1108	B	30	R	7	45.0	47.0	280.780	280.800	280.790	1.451	
180	1108	B	30	R	7	45.0	47.0	280.780	280.800	280.790	1.445	
180	1108	B	30	R	7	45.0	47.0	280.780	280.800	280.790	1.452	
180	1108	B	30	R	7	45.0	47.0	280.780	280.800	280.790	1.430	1.445
180	1108	B	31	R	2	95.0	96.5	285.430	285.445	285.438	1.240	
180	1108	B	31	R	2	95.0	96.5	285.430	285.445	285.438	1.255	
180	1108	B	31	R	2	95.0	96.5	285.430	285.445	285.438	1.228	
180	1108	B	31	R	2	95.0	96.5	285.430	285.445	285.438	1.253	1.244
180	1108	B	31	R	3	31.0	32.0	286.220	286.230	286.225	1.309	
180	1108	B	31	R	3	31.0	32.0	286.220	286.230	286.225	1.346	
180	1108	B	31	R	3	31.0	32.0	286.220	286.230	286.225	1.424	
180	1108	B	31	R	3	31.0	32.0	286.220	286.230	286.225	1.342	1.355
180	1108	B	32	R	1	91.5	92.5	293.615	293.625	293.620	1.329	

Table T13 (continued).

Leg	Site	Hole	Core	Type	Section	Top interval (cm)	Bottom interval (cm)	Top depth (mbsf)	Bottom depth (mbsf)	Middle depth (mbsf)	Thermal conductivity ($W \cdot m^{-1} \cdot °C^{-1}$)	Thermal conductivity average ($W \cdot m^{-1} \cdot °C^{-1}$)
180	1108	B	32	R	1	91.5	92.5	293.615	293.625	293.620	1.414	
180	1108	B	32	R	1	91.5	92.5	293.615	293.625	293.620	1.353	
180	1108	B	32	R	1	91.5	92.5	293.615	293.625	293.620	1.394	1.373
180	1108	B	32	R	3	104.0	105.5	296.090	296.105	296.098	1.388	
180	1108	B	32	R	3	104.0	105.5	296.090	296.105	296.098	1.426	
180	1108	B	32	R	3	104.0	105.5	296.090	296.105	296.098	1.452	
180	1108	B	32	R	3	104.0	105.5	296.090	296.105	296.098	1.436	1.426
180	1108	B	32	R	5	65.0	66.5	298.600	298.615	298.608	1.277	
180	1108	B	32	R	5	65.0	66.5	298.600	298.615	298.608	1.483	
180	1108	B	32	R	5	65.0	66.5	298.600	298.615	298.608	1.466	
180	1108	B	32	R	5	65.0	66.5	298.600	298.615	298.608	1.462	1.422
180	1108	B	33	R	1	110.0	110.5	303.400	303.405	303.403	1.234	
180	1108	B	33	R	1	110.0	110.5	303.400	303.405	303.403	1.259	
180	1108	B	33	R	1	110.0	110.5	303.400	303.405	303.403	1.254	1.249
180	1108	B	34	R	1	92.0	93.0	312.920	312.930	312.925	1.492	
180	1108	B	34	R	1	92.0	93.0	312.920	312.930	312.925	1.558	
180	1108	B	34	R	1	92.0	93.0	312.920	312.930	312.925	1.495	
180	1108	B	34	R	1	92.0	93.0	312.920	312.930	312.925	1.648	1.548
180	1108	B	33	R	3	86.0	88.0	305.960	305.980	305.970	1.286	
180	1108	B	33	R	3	86.0	88.0	305.960	305.980	305.970	1.277	1.282
180	1108	B	34	R	3	97.0	98.0	315.800	315.810	315.805	1.469	
180	1108	B	34	R	3	97.0	98.0	315.800	315.810	315.805	1.491	1.480
180	1108	B	35	R	1	112.0	113.0	322.720	322.730	322.725	1.650	
180	1108	B	35	R	1	112.0	113.0	322.720	322.730	322.725	1.738	
180	1108	B	35	R	1	112.0	113.0	322.720	322.730	322.725	1.656	
180	1108	B	35	R	1	112.0	113.0	322.720	322.730	322.725	1.676	1.680
180	1108	B	35	R	3	48.0	49.0	324.830	324.840	324.835	1.535	
180	1108	B	35	R	3	48.0	49.0	324.830	324.840	324.835	1.602	
180	1108	B	35	R	3	48.0	49.0	324.830	324.840	324.835	1.529	
180	1108	B	35	R	3	48.0	49.0	324.830	324.840	324.835	1.582	1.560
180	1108	B	36	R	2	59.0	61.0	332.900	332.920	332.910	1.161	
180	1108	B	36	R	2	59.0	61.0	332.900	332.920	332.910	1.281	
180	1108	B	36	R	2	59.0	61.0	332.900	332.920	332.910	1.299	
180	1108	B	36	R	2	59.0	61.0	332.900	332.920	332.910	1.313	1.263
180	1108	B	36	R	4	105.0	106.0	335.940	335.950	335.945	1.514	
180	1108	B	36	R	4	105.0	106.0	335.940	335.950	335.945	1.636	
180	1108	B	36	R	4	105.0	106.0	335.940	335.950	335.945	1.484	
180	1108	B	36	R	4	105.0	106.0	335.940	335.950	335.945	1.551	1.546
180	1108	B	37	R	1	59.0	60.0	341.490	341.500	341.495	1.117	
180	1108	B	37	R	1	59.0	60.0	341.490	341.500	341.495	1.207	
180	1108	B	37	R	1	59.0	60.0	341.490	341.500	341.495	1.111	
180	1108	B	37	R	1	59.0	60.0	341.490	341.500	341.495	1.254	1.172
180	1108	B	40	R	1	71.0	72.0	370.510	370.520	370.515	1.308	
180	1108	B	40	R	1	71.0	72.0	370.510	370.520	370.515	1.333	1.321
180	1108	B	37	R	3	94.0	95.0	344.460	344.470	344.465	1.210	
180	1108	B	37	R	3	94.0	95.0	344.460	344.470	344.465	1.291	
180	1108	B	37	R	3	94.0	95.0	344.460	344.470	344.465	1.192	
180	1108	B	37	R	3	94.0	95.0	344.460	344.470	344.465	1.189	1.221
180	1108	B	38	R	1	94.0	95.0	351.440	351.450	351.445	1.350	
180	1108	B	38	R	1	94.0	95.0	351.440	351.450	351.445	1.366	1.358
180	1108	B	39	R	2	44.0	45.0	361.700	361.710	361.705	1.300	
180	1108	B	39	R	2	44.0	45.0	361.700	361.710	361.705	1.324	1.312
180	1108	B	41	R	1	96.0	97.0	380.360	380.370	380.365	1.025	
180	1108	B	41	R	1	96.0	97.0	380.360	380.370	380.365	1.331	
180	1108	B	41	R	1	96.0	97.0	380.360	380.370	380.365	1.306	
180	1108	B	41	R	1	96.0	97.0	380.360	380.370	380.365	1.321	1.246
180	1108	B	42	R	1	98.0	99.0	389.980	389.990	389.985	1.186	
180	1108	B	42	R	1	98.0	99.0	389.980	389.990	389.985	1.162	1.174
180	1108	B	42	R	4	53.0	54.0	391.550	391.550	391.550	1.268	
180	1108	B	42	R	4	53.0	54.0	391.550	391.550	391.550	1.315	
180	1108	B	42	R	4	53.0	54.0	391.550	391.550	391.550	1.296	
180	1108	B	42	R	4	53.0	54.0	391.550	391.550	391.550	1.307	1.297
180	1108	B	42	R	6	54.0	55.0	392.650	392.660	392.655	1.249	
180	1108	B	42	R	6	54.0	55.0	392.650	392.660	392.655	1.293	
180	1108	B	42	R	6	54.0	55.0	392.650	392.660	392.655	1.286	
180	1108	B	42	R	6	54.0	55.0	392.650	392.660	392.655	1.300	1.282
180	1108	B	43	R	1	17.0	18.0	398.770	398.780	398.775	1.392	
180	1108	B	43	R	1	17.0	18.0	398.770	398.780	398.775	1.421	

Table T13 (continued).

Leg	Site	Hole	Core	Type	Section	Top interval (cm)	Bottom interval (cm)	Top depth (mbsf)	Bottom depth (mbsf)	Middle depth (mbsf)	Thermal conductivity ($W \cdot m^{-1} \cdot °C^{-1}$)	Thermal conductivity average ($W \cdot m^{-1} \cdot °C^{-1}$)
180	1108	B	43	R	1	17.0	18.0	398.770	398.780	398.775	1.452	
180	1108	B	43	R	1	17.0	18.0	398.770	398.780	398.775	1.481	1.437
180	1108	B	44	R	1	121.0	122.0	409.410	409.420	409.415	1.163	
180	1108	B	44	R	1	121.0	122.0	409.410	409.420	409.415	1.314	
180	1108	B	44	R	1	121.0	122.0	409.410	409.420	409.415	1.285	1.254
180	1108	B	45	R	1	23.0	24.0	418.030	418.040	418.035	1.165	
180	1108	B	45	R	1	23.0	24.0	418.030	418.040	418.035	1.257	
180	1108	B	45	R	1	23.0	24.0	418.030	418.040	418.035	1.218	
180	1108	B	45	R	1	23.0	24.0	418.030	418.040	418.035	1.200	1.210
180	1108	B	46	R	1	30.0	32.0	427.800	427.820	427.810	1.124	
180	1108	B	46	R	1	30.0	32.0	427.800	427.820	427.810	1.140	
180	1108	B	46	R	1	30.0	32.0	427.800	427.820	427.810	1.137	
180	1108	B	46	R	1	30.0	32.0	427.800	427.820	427.810	1.139	1.135
180	1108	B	47	R	1	30.0	31.0	437.400	437.410	437.405	1.298	
180	1108	B	47	R	1	30.0	31.0	437.400	437.410	437.405	1.316	
180	1108	B	47	R	1	30.0	31.0	437.400	437.410	437.405	1.320	
180	1108	B	47	R	1	30.0	31.0	437.400	437.410	437.405	1.320	1.314
180	1108	B	48	R	1	29.0	31.0	446.990	447.010	447.000	1.453	
180	1108	B	48	R	1	29.0	31.0	446.990	447.010	447.000	1.492	
180	1108	B	48	R	1	29.0	31.0	446.990	447.010	447.000	1.491	
180	1108	B	48	R	1	29.0	31.0	446.990	447.010	447.000	1.522	1.490
180	1108	B	49	R	1	12.0	13.0	456.420	456.430	456.425	1.331	
180	1108	B	49	R	1	12.0	13.0	456.420	456.430	456.425	1.411	
180	1108	B	49	R	1	12.0	13.0	456.420	456.430	456.425	1.405	
180	1108	B	49	R	1	12.0	13.0	456.420	456.430	456.425	1.408	1.389
180	1108	B	50	R	1	42.0	44.0	466.320	466.340	466.330	1.186	
180	1108	B	50	R	1	42.0	44.0	466.320	466.340	466.330	1.223	
180	1108	B	50	R	1	42.0	44.0	466.320	466.340	466.330	1.364	
180	1108	B	50	R	1	42.0	44.0	466.320	466.340	466.330	1.228	1.250
180	1108	B	51	R	1	76.5	78.5	476.265	476.285	476.275	1.377	
180	1108	B	51	R	1	76.5	78.5	476.265	476.285	476.275	1.447	
180	1108	B	51	R	1	76.5	78.5	476.265	476.285	476.275	1.384	
180	1108	B	51	R	1	76.5	78.5	476.265	476.285	476.275	1.392	
180	1108	B	51	R	1	76.5	78.5	476.265	476.285	476.275	1.364	1.393

Note: This table is also available also in ASCII format in the **TABLES** directory.